Development of Regenerative Braking System and Sensor Fault Tolerant Algorithm for Electric Vehicles in Hilly Region

A

Thesis Submitted

in Partial Fulfilment of the Requirements

for the Degree of

DOCTOR OF PHILOSOPHY

By

Tako Nama

Department of Electronics and Electrical Engineering

Indian Institute of Technology Guwahati

Guwahati - 781 039, India

November 2023


भारतीय प्रौद्योगिकी संस्थान गुवाहाटी
Indian Institute of Technology Guwahati

Certificate

This is to certify that the thesis entitled "**Development of Regenerative Braking System and Sensor Fault Tolerant Algorithm for Electric Vehicles in Hilly Region**", submitted by **Ms Tako Nama (Roll no.-146102026)**, a research scholar in the *Department of Electronics and Electrical Engineering, Indian Institute of Technology Guwahati*, for the award of the degree of **Doctor of Philosophy**, is a record of an original research work carried out by her under my supervision and guidance. The thesis has fulfilled all requirements as per the regulations of the institute and has reached the standard needed for submission. The results embodied in this thesis have not been submitted to any other University or Institute for the award of any degree or diploma.

Dated:	Dr. Praveen Tripathy
Guwahati.	Associate Professor
	Dept. of Electronics and Electrical Engg.
	Indian Institute of Technology Guwahati
	Guwahati - 781 039, Assam, India.

Dated:	Dr. Anup Kumar Gogoi
Guwahati.	Ex-Professor (retired)
	Dept. of Electronics and Electrical Engg.
	Indian Institute of Technology Guwahati
	Guwahati - 781 039, Assam, India.

To my family...

Acknowledgement

I thank my supervisors, ***Prof. Anup Kumar Gogoi*** and ***Dr. Praveen Tripathy*** for giving me the opportunity to work in the field of power electronics and its implementation in electric vehicles. I have received a great deal of knowledge from them, which is not limited to technical knowledge but encompasses all other aspects of life. I am grateful for their guidance and generous support throughout my Ph.D. journey.

I thank ***Prof. Uday Shanker Dixit***, ***Prof. Somanath Majhi***, and ***Dr. Ravindranath Adda***, for their critical review and insightful comments at every stage of my research work which helped me immensely in shaping this thesis.

I thank **IIT Guwahati** and **EEE Department** for the various financial assistantships and for providing the necessary infrastructure to carry out this research. I thank all the office staff and technical staff at the EEE Department, the campus security, the hostel cooks and last but not least, the hostel cleaners for their service throughout my stay at IIT Guwahati.

I thank the past and present department colleagues and seniors; ***Dr. Prosonjit, Dr. Umesh, Dr. Mridul, Dr. Gayatri, Dr. Kamakshi, Dr. Ramyani, Dr. Alex, Dr. Amit, Abhishek, Pramit*** and ***Virral***. I truly appreciate all the help I received from them and the many enlightening interactions which made my work possible.

I extend my heartfelt gratitude to my entire family, with a special acknowledgement to my cherished sisters, ***Naniya*** and ***Meniya***, for their unwavering support and prayers. To my dear friends—***Phurpa, Beth, Gayatri, Trishna, Sarita, Ines, Ruchika, Shruti, Babina*** and ***Wendy***—thank you for turning my Ph.D. odyssey into an enriching and enjoyable experience. Your encouraging words during tough times meant a lot. The beautiful memories we created together at IIT Guwahati will forever hold a special place in my heart.

Once again, I sincerely thank everyone who, directly or indirectly, has lent their helping hands in this challenging journey, akin to a roller-coaster ride filled with highs and lows. Finally, I thank the Almighty God for being the guiding light throughout this Ph.D. course.

Tako Nama

Abstract

The world is steadily moving towards sustainable and green technology; Electric Vehicles (EVs) are one of the founding wheels of this movement. India is marching along with the global movement. EVs, especially electric two-wheelers, are booming in India's automotive industry. However, they are mostly seen driven where the roads are reasonably plain, as found in urban cities. EVs, both four and two-wheelers presence, are less felt in the highlander states of the country where the roads are hilly. The less or no visibility of EVs in the hilly region parts of India was the initial driving force behind the inception of this thesis. Hence, the author is motivated to study the hilly roads and the challenges associated with such roads on EVs. The goal behind the work done in this thesis is to make EVs, especially electric two-wheelers, more feasible for hilly roads.

Although EVs have many benefits over ICE vehicles, like being more efficient, reliable, safer, smarter, and environmentally friendly. However, their range is still a major challenge. The battery that powers the EVs has a lower energy density than gasoline fuel used in ICE vehicles. The range of EVs gets worse for hilly roads due to the presence of road gradients. If we only consider the battery power consumption, i.e. kWh per hour, the hilly region roads become unfriendly to EVs, which explains the poor visibility of electric vehicles in the hilly region of the country. Various methods have been reported in the literature to increase EV's range. One effective way to extend the range is to recover the energy spent while climbing uphill. When the EVs have reached the top of the hill, it has gained potential energy; while climbing down, some of this energy can be fed back into the source battery. This is accomplished by utilising a regenerative

braking system (RBS) over conventional friction braking during the retardation period of the wheels. Regenerative braking converts the moving wheel's kinetic energy into electrical energy and charges the source battery during the braking period of the vehicle.

This thesis presents an alternative regenerative braking circuit configuration for low-speed and high-torque applications required in hilly region roads. The proposed braking circuit is a modular add-on to the primary motor drive inverter circuit. Two control methods are designed to control the braking circuit, which are: First is a type-II compensator, accomplished using classical control theory. The second is the proposed non-linear control method based on the sliding mode control method. The proposed braking system is simulated in MATLAB/Simulink and is experimentally verified in a scaled-down laboratory test set-up. The results validate the proposed control scheme, charging of the battery, and braking action.

The BLDC motors are a popular choice for two-wheelers and other light EVs. Three Hall effect sensors are employed to detect the rotor position in a 3-phase BLDC motor. There is a possibility of sensor failure, which will hinder the motoring operation of the EV. Hence, to mitigate this problem, the thesis proposes a simple and smart algorithm that detects the fault and keeps the BLDC motor working even with the failure of one Hall effect sensor.

Overall, the thesis endeavours to provide readers with a holistic view of the road characteristics of hilly roads. Get acquainted with the challenges of such roads. Offers suggestions to solve the problems. For the engineers and technical professionals, the thesis aims to give an experience of learning and understanding the analysis and designing of a modular regenerative braking circuit that can help electric two-wheelers descend the slope of the hill at a comfortable speed while converting the potential energy to electrical energy.

Contents

List of Figures

List of Tables

List of Common Abbreviations

AC	Alternating Current
ADC	Analog to Digital Converter
ARAI	Automotive Research Association of India
ANN	Artificial Neural Network
BA	Barometer
BEV	Battery Electric Vehicle
BLDC	Brushless Direct Current
CCM	Continuous Conduction Mode
DBR	Diode Rectifier Bridge
DC	Direct Current
DSO	Digital Storage Oscilloscope
ECU	Electric Control Unit
emf	Electromotive Force
EV	Electric Vehicle
FAME	Faster Adoption and Manufacturing of Hybrid and Electric Vehicles
FUDS	Federal Urban Driving Schedule
FTC	Fault Tolerant Control
FD	Fault Diagnosis
GPS	Global Positioning System
GM	Gain Margin of Bode Plot
HEV	Hybrid Electric Vehicle
IDC	Indian Drive Cycle

IEA	International Energy Agency
ICE	Internal Combustion Engine
IRC	Indian Roads Congress
KCL	Kirchhoff's Current Law
KVL	Kirchhoff's Voltage Law
LIDAR	Light Detection and Ranging
LTI	Linear Time-Invariant
LEV	Light Electric Vehicle
LCD	Liquid Crystal Display
MATLAB	Matrix Laboratory
MOSFET	Metal Oxide Semiconductor Field Effect Transistor
NEDC	New European Drive Cycle
NYCC	New York City Cycle
OEM	Original Equipment Manufacturer
PCB	Printed Circuit Board
PMSM	Permanent Magnet Synchronous Motors
PHEV	Plug-in Hybrid Electric Vehicle
PV	Photovoltaic
PWM	Pulse Width Modulation
PM	Phase Margin of Bode Plot
RBS	Regenerative Braking Circuit
rpm	Revolution Per Minute
SMC	Sliding Mode Control
SOC	State of Charge
SRM	Switched Reluctance Motor
SPDT	Single Pole Double Throw
TERI	The Energy and Resources Institute
UC	Ultra Capacitor

List of Symbols

θ	Hill angle
ρ	Air density
λ	Flux linkages
μ_{rr}	Rolling friction coefficient
ω_m	Motor angular speed
ω_w	Wheel angular speed
ω_p	Controller pole frequency
ω_z	Controller zero frequency
ω	Cross-over frequency
ϕ_B	Phase boost
$\mathbf{A}$	Dynamic transmission matrix
$\mathbf{B}$	Input transmission matrix
$\mathbf{C}$	Output transmission matrix
$\mathbf{D}$	Direct transmission matrix
A	Frontal area of vehicle
B	Battery
C_d	Drag coefficient of the vehicle body
C	Output capacitor
$\mathrm{D_a}$	Diode
D	DC value of duty cycle
d	Instantaneous duty cycle

$\hat{d}$	Perturbation in duty cycles
E_{eq}	DC value of equivalent voltage of the battery
e_{eq}	Equivalent voltage of the battery averaged over switching time period
$\hat{e}_{eq}$	Perturbation in equivalent voltage of the battery
E_{l-l}	Line-to-line back emf
f_s	Switching frequency in Hz
F_a	Aerodynamic drag force
F_g	Force required to oppose gravitational acceleration
F_{gh}, F_{gv}	Force component of F_g
F_f	Friction force
F_t	Tractive force
g	Acceleration due to gravity
G_C	Controller transfer function
G_M	Pulse width modulator transfer functions
G_{id}	Duty cycle to braking current transfer functions
h	Altitude in meters
H_a, H_b, H_c	Hall sensor signals
I_{brake}	DC value of braking current
i_{brake}	Braking current averaged over switching time period
$\hat{i}_{brake}$	Perturbation in braking current
i^*_{brake}	Reference braking current
i_{bat}	Battery current
i_c	Capacitor current
J	Inertia constant
k_c	Controller gain
K	Sliding gain
K_b	Scaling factor
K_t	torque constant

m	Mass of scooter in kg
M	Motor
P_t	Tractive power
r	Radius of the wheel-hub motor
r_c	Parasitic resistance of the output capacitor
R_{int}	Internal resistance of the battery
r_{in}	Parasitic resistance of the input side of the braking circuit
s	Sliding surface
$\mathrm{S}_1 ... \mathrm{S}_6$	Semiconductor switches
T	Outer loop gain
T_m	Mechanical torque
T_{brake}	Braking torque
T_{gh}	Mechanical torque due to gravitational pull and vehicle weight
T_{wheel}	Wheel torque
$\mathrm{T_s}$	Switching period
u	Control law
u_{eq}	Equivalent control law
v	Scooter velocity
v_{brake}	Scooter velocity with brake force applied
V_{bat}	DC value of battery terminal voltage
v_{bat}	Battery terminal voltage averaged over switching time period
v_{coast}	scooter coasting velocity
v_c	Capacitor voltages averaged over switching time period
V_c	DC value of capacitor voltage
v_c	Capacitor voltage averaged over switching time period
$\hat{v}_c$	Perturbation in capacitor voltage
V_{dc}	Input voltage of the inverter
V_{in}	DC value of the input voltage of the converter

v_{in}	Input voltage of the converter averaged over switching time period
$\hat{v}_{in}$	Perturbation in input voltage of the converter
V_L	DC value of inductor voltage
v_L	Inductor voltage over switching time period
V_o	DC value of converter output voltage
v_o	Converter output voltage over switching time period
$\hat{v}_o$	Perturbation in converter output voltage
V_M	Peak voltage of ramp signal

1

Introduction

Contents

1.1 Introduction

With the rise in human awareness of the earth's environmental and climate issues, clean and sustainable energy has become the new desirable standard for today's technologies. A collective global effort is required to preserve the environment for a sustainable future. Electric Vehicles are one of the key players in achieving the above objectives.

An Electric Vehicle (EV) is a type of automobile that is propelled by one or more electric motors, where the energy for the motion of its body is mainly or partially provided by the electrical energy stored in rechargeable batteries or any other energy storage device, mounted in the body of the vehicle [1]. It consists of the electric motor, the energy-transmitting shaft and controller, which adjusts and controls the motor characteristics and operating conditions.

The fundamental anatomical difference between an EV and a conventional fossil fuel Internal Combustion Engine (ICE) vehicle is shown in Figure 1.1. Here, Figure 1.1 (a) shows the drive line of a four-wheeler EV; it is an assembly of an electric motor, battery pack, power converter, inverter, energy transmitting shaft, electric control unit (ECU), and battery management system. Figure 1.1 (b) shows an ICE vehicle's basic power train configuration. The main difference between the two configurations, as seen in Figure 1.1, is that instead of being driven by an IC engine in conventional petrol or diesel cars, an EV is propelled by a traction motor, which the ECU controls. The ECU takes signals from the driver via the accelerator or the brake pedal and feedback signals from sensors such as the vehicle's speed and acceleration to control the traction motor's power requirement and power flow direction.

It may seem that EVs recently became relevant in the automobile market with their commercial success and presence. However, it is interesting that EV's history dates back to the early 20th century and has more than 150 years of history. Due to limitations in power electronics, battery technology, and cheap fossil fuels, EVs lost their stand in the market in those days. The recent advancement in power electronics and battery technology has resurrected the market value that EVs lost against ICE vehicles. Today, electrification of all types of vehicles in the market is available, from light two-wheelers to heavy passenger

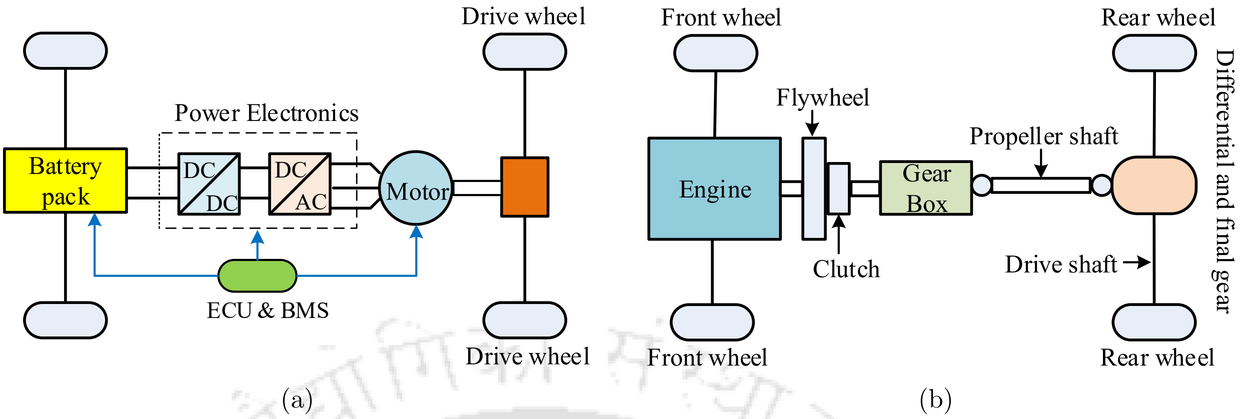

Figure 1.1: General configuration of (a) conventional electric vehicle power train (b) front-engine rear-wheel-drive conventional ICE vehicle power train.

buses. EVs have been around for over a hundred years now.

1.1.1 Benefits of EV and its Limitations

EVs have many benefits over ICE vehicles, like being more efficient, reliable, safer, smarter, and environmentally friendly. An electric motor is a hundred times simpler than an ICE. As EVs do not need a mechanical or automatic gearbox, it is also possible to eliminate every mechanical transmission using wheel-drive motors. Because of their simplicity, they are also more reliable and robust, but the most important advantage of EVs is their high efficiency (more than 90% against an average of 30% for ICEs) [2].

Despite all the above advantages, fully electric vehicles still have some problems, such as a short drive range and expensive pricing. The range of an EV is the distance covered when fully charged [1]. The battery that powers the EVs has a lower energy density than gasoline fuel used in ICE vehicles. Also, the gasoline tank can be refilled within a few minutes, while batteries require long charging times, typically in hours, to be fully charged. Researchers around the globe are looking into ways to increase the specific energy and power rating of battery packs and to come up with cheaper alternatives to overcome this challenge.

1.1.2 Classifications of EVs

One can classify EVs based on their power-train configuration as below:

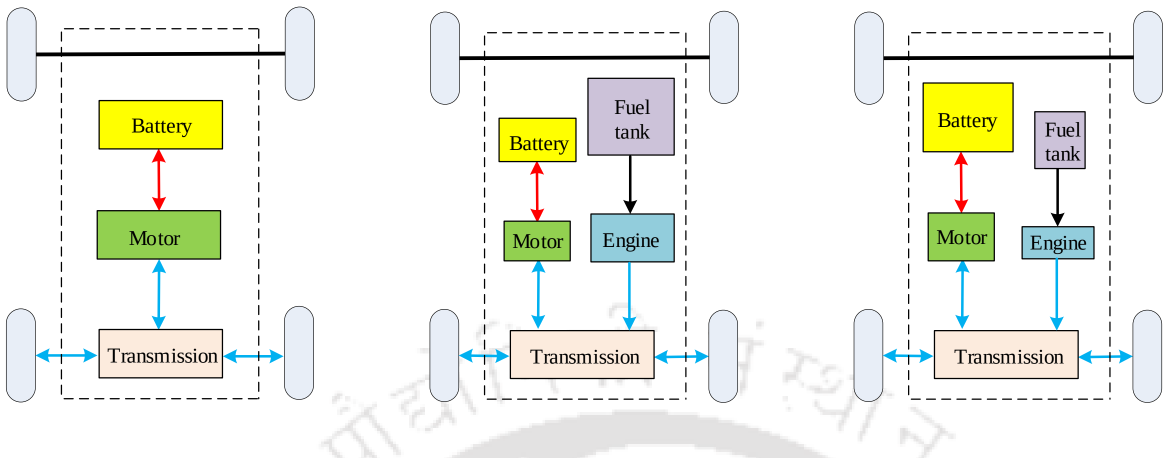

(a) (b) (c)

Figure 1.2: Block diagram of types of electric vehicle (a) BEV (b) HEV (c) PHEV.

(a) **Battery Electric Vehicles (BEV)**

An EV whose power supply purely comes from a battery falls under this category. This EV type solely depends on the electric motors for its propulsion, as shown in Figure 1.2 (a).

(b) **Hybrid Electric Vehicles (HEV)**

A hybrid vehicle refers to a vehicle with at least two power sources. A hybrid-electric vehicle indicates that a battery provides one power source and uses an electric motor for its propulsion. The other source of motive power can come from several different technologies but is typically provided by an internal combustion engine designed to run on either gasoline or diesel fuel, as shown in Figure 1.2 (b). As proposed by the Technical Committee (Electric Road Vehicles) of the International Electrochemical Commission, an HEV is a vehicle in which propulsion energy is available from two or more types of energy sources. The propulsion is from either of the two sources. There is no provision for charging the battery from the electrical grid in HEV [1].

(c) **Plug-in Hybrid Electric Vehicle (PHEV)**

Its propulsion is mainly from the battery, and the electrical grid charges its battery. In case the charge level of the battery is below a threshold, then the propulsion is through

(a) (b) (c) (d)

Figure 1.3: Few examples of EVs (a) bus (b) electric sedan (c) electric e-rickshaw (d) electric scooter, (All images under a Creative Commons License).

the ICE, Figure 1.2 (c) shows its block diagram representation.

1.1.3 Types of EVs in the Market

Today, electrification of all types of vehicles in the market is available, from light two-wheelers to heavy passenger buses. Figure 1.3 (a) shows an example of an HEV electric bus, Figure 1.3 (b) is an example of Light electric vehicle (LEV), i.e., electric car, Figure 1.3 (c) is an example of LEV three wheeler e-Rickshaw, and Figure 1.3 (d) is an example of light electric two-wheelers. However, EVs are not limited to the example shown in Figure 1.3; there are rail electric vehicles, surface, underwater electric vessels, and electric aircraft and electric spacecraft, the latest addition.

1.1.4 The Current Global Status of EVs

There is a paradigm shift in the transportation system from Transportation 1.0 to Transportation 2.0, as postulated in [4]. Transportation 1.0 refers to a conventional fossil fuel-

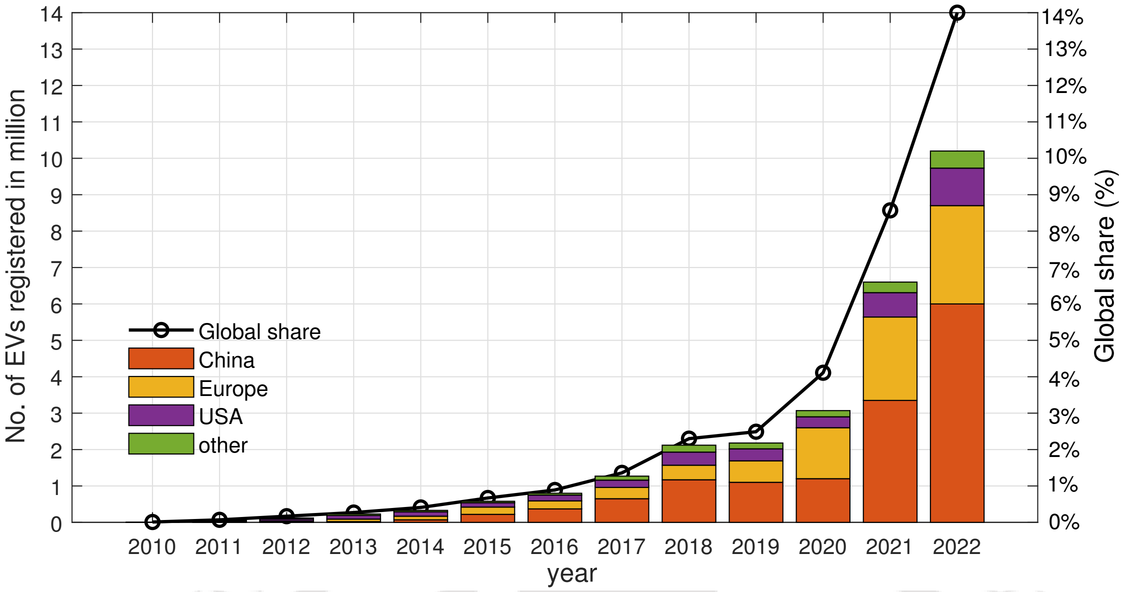

Figure 1.4: Global sales and sales market share of electric cars (four-wheelers), 2010-2022, (Data source [3]).

dependent transportation system, and Transportation 2.0 refers to the then-upcoming new generation of electrified vehicles. Currently, many traditional automobile companies are slowly shifting towards electrification.

Figure 1.4 shows EV's current global sales growth for 2010 – 2022. In 2022, 10 million registered electric cars were on the road, i.e., 55% up relative to the 6.6 million cars in 2021 [3]. The sales growth has been impressive, particularly in the previous three years, 2020 – 2022. There was a 108% boost in global electric car sales from 2020 to 2021, which is impressive, and a 64% boost from 2021 to 2022. These electric car numbers include passenger vehicles, light trucks, and light commercial vehicles (only four-wheelers). The share of electric cars in total car sales jumped from 9% in 2021 to 14% in 2022, more than ten times their share in 2017.

Figure 1.5 shows the sales distribution of BEV and PHEV within the EV global sales, indicating the popularity of BEVs. In 2022, BEV sales in China increased by 60% relative to 2021 to reach 4.4 million, and PHEV sales nearly tripled to 1.5 million.

Globally, China is the top player when it comes to EVs. China grew globally by selling nearly 3.4 million electric cars in 2021. In other words, more electric vehicles were sold in

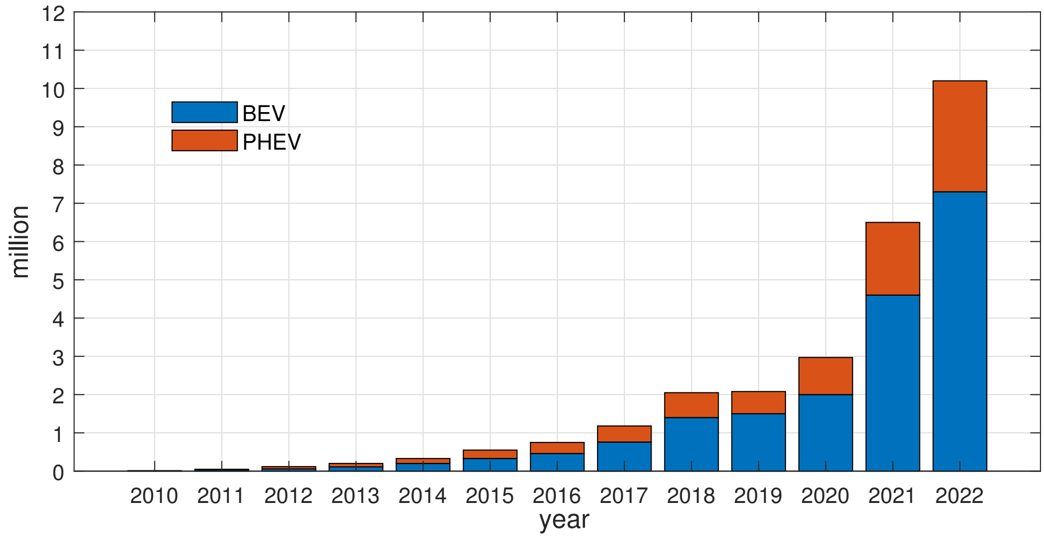

Figure 1.5: Distribution of BEV and PHEV in the global sales of electric cars, 2010-2022, (Data source [5]).

2021 in China alone than in the entire world in 2020, and in 2022, sales in China increased by 80%, accounting for 60% of global growth. Growth in Europe remained high (i.e., up 15%) and accelerated in the United States (i.e., up 55%) as reported by the International Energy Agency (IEA) in their Global EV Outlook 2023 report [5]. China, Europe, and the United States account for roughly two-thirds of the overall car market but around 90% of electric car sales.

In comparison, the overall sales in other developed countries were less than 2% in the automobile market in the same year [3]. The price premium attached to electric cars and a lack of charging infrastructure are key reasons for the sluggish growth in large developing economies such as Brazil, India, and Indonesia. However, the sales of electric two-wheelers are expanding in these countries.

The rising popularity of EVs and positive sales growth indicate the onset of transportation 2.0, and they are here to stay. These reports [3, 5] are testimony to the bright future of Transportation 2.0.

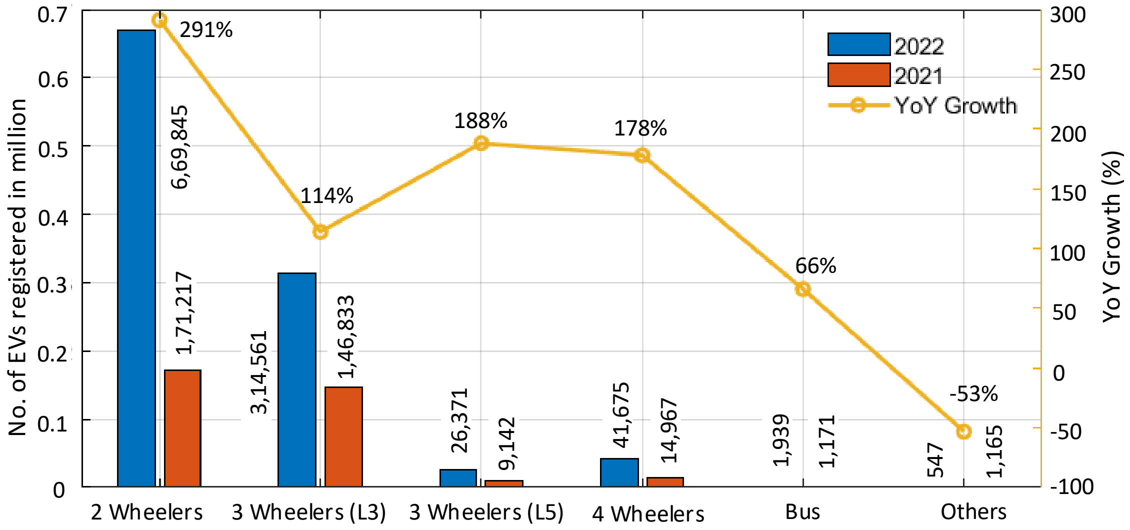

Figure 1.6: EV sales in India for the years 2021 and 2022, (Data source [6]).

1.1.5 The Status of EVs in India.

EV sales in India reached a record one million units in 2022, a jump of close to 300% against the 322, 877 units sold in 2021. Figure 1.6 shows the different EV categories sold in the years 2021 and 2022 and their year-on-year (YoY) percentage growth. The numbers do not include data for Telangana and Lakshadweep. With a total sales of 10, 54, 983 units in 2022, the EV industry has accounted for 4.7% of overall automobile sales, according to the Ministry of Road Transport and Highways (Govt. of India) data, shared through its Vahan Dashboard [6]. Among all the EVs, the high-speed electric two-wheelers (2W) showed a massive sales growth of 291% from 2021 to 2022.

Figure 1.7 shows the percentage distribution of vehicle category-wise EV sales. The data shows that registered electric two-wheelers accounted for 63% of the total EV sales, up from 50% in 2021, i.e., a total of 6, 69, 845 units out of 10, 54, 983 units in 2022. Next in the line is the low-speed (L3) three-wheelers (3W), holding a 30% share of EV sales in 2022, dropping from 43% in 2021. Then, with no significant change in % share, the four-wheeler (4W) and high-speed (L5) electric three-wheeler (3W) made 4% and 2% of the pie, respectively. The sales of electric buses show a jump from 1171 units in 2021 to 1939 units in 2022.

Figure 1.8 shows the state-wise EV sales in India for 2022. Uttar Pradesh contributes

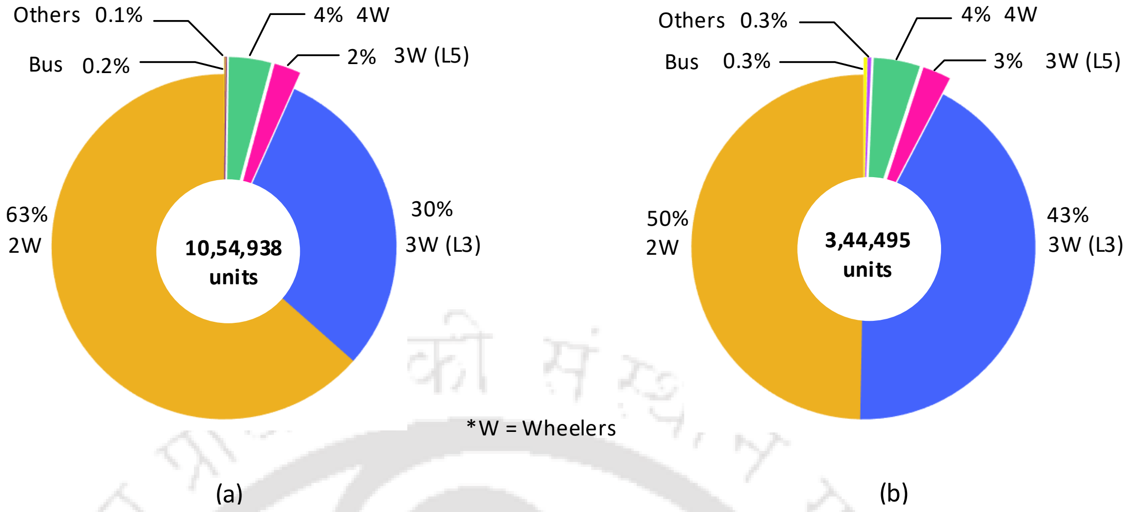

Figure 1.7: Vehicle category wise EV sales and penetration (a) for the year 2022 (b) for the year 2021, (Data source [6]).

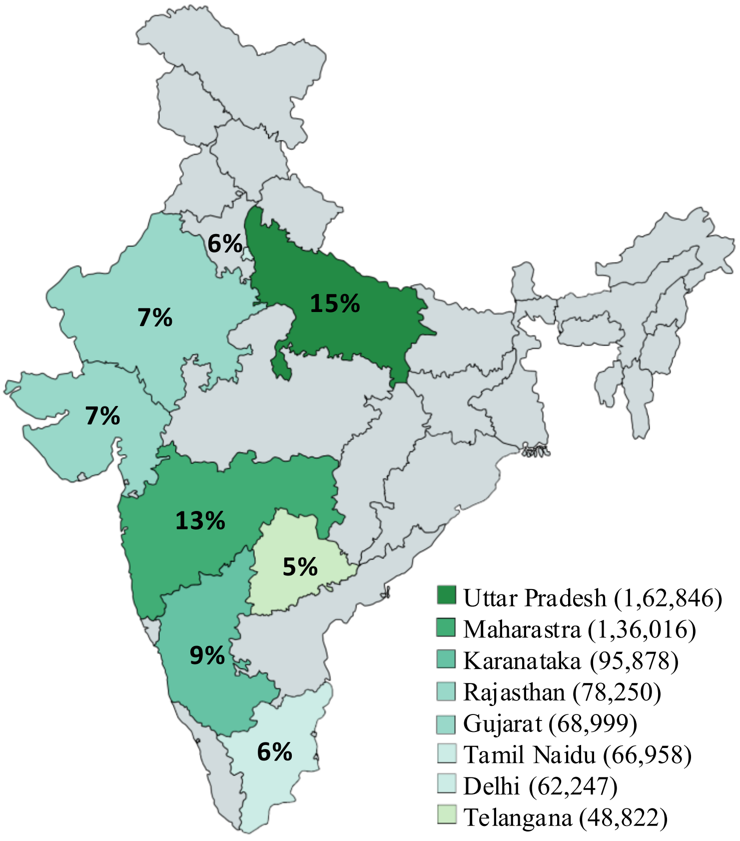

Figure 1.8: State-wise EV sales in India for the year 2022, (Data source [6]).

15%, i.e., $1,62,846$ out of the total $10,54,938$ units sold in 2022, followed by Maharastra with 13% and Karnataka with 9%. Other states are mentioned in the figure with more than or close to $50,000$ EVs each. The eight states mentioned in Figure 1.8 contributed to 68% of EVs sold in the calendar year 2022. Most EVs sold in Uttar Pradesh were the low-speed three-wheelers, famous for last-mile connectivity.

1.1.6 Electric Two-Wheelers on Hilly Region

As seen from the earlier reports, EVs, especially electric two-wheelers, are booming in India's automotive industry. However, they are mostly seen driven where the roads are reasonably plain, as found in urban cities. Out of all the electric two-wheelers sold in the country, 57% of them were in five states: Maharashtra (18%), Karnataka (13%), Gujarat (10%), Tamil Nadu (9%) and Rajasthan (8%) [6]. However, India has different geographical characteristics; parts of India have people living in hilly regions such as Arunachal Pradesh, Meghalaya, Mizoram, Himachal Pradesh, Uttrakhand, etc. These regions have different road characteristics than the plain road drives of metro cities like Delhi, Mumbai, Chennai, and Bangalore. Different road characteristic has different challenges. Electric vehicles, both four and two-wheelers presence, are less felt in these highlander states of the country where the roads are hilly. Figure 1.9 highlights these regions in the Map of India. The main motivation behind the thesis is the lack of visibility of electric vehicles in the author's home state (Arunachal Pradesh) and other hilly region cities of India.

With the world's largest pollution, India reports that one in three households owns a two-wheeler, and one in ten owns a car [7]. India spends roughly 70% of its foreign exchange earnings on oil imports [8]. Conventional ICE two-wheelers like motorcycles and scooters are popular in India. It is quite ubiquitous for both the plain region and hilly region drives. The motorcycles have gearboxes, and scooters have automatic power transmission gear in their power-train to propel themselves in such demanding routes. Our dependence on oil makes our overall economy and household budgets extremely vulnerable to volatile oil prices. Moreover, the air condition in India's cities is worsening every day. Electric two-wheelers

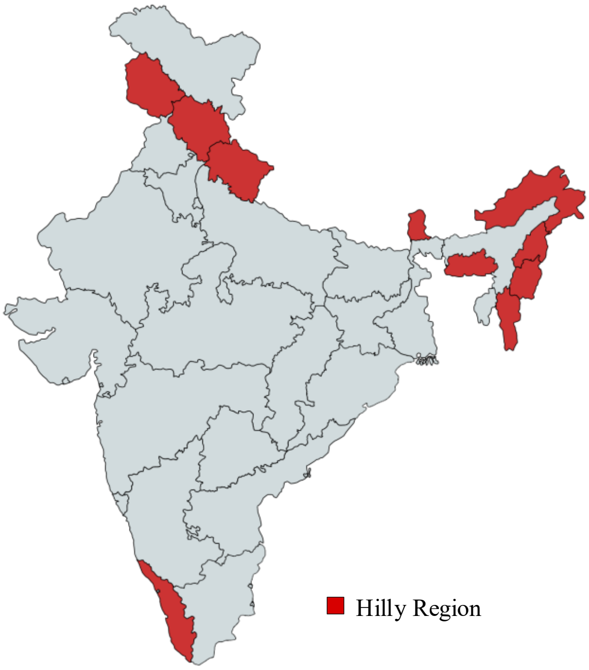

Figure 1.9: Indian map showing the hilly regions where there are fewer EVs.

can help reduce the problem of air pollution and decrease fossil fuel consumption. Today it is a well-known fact that electric vehicles have lesser carbon footprints than conventional ICE vehicles. Slowly, the trend of switching conventional ICE two-wheelers to electric two-wheelers is catching up in most countries, and India, too, is moving forward in that direction.

The main observations from the sales report:

- From the sales data in Figure 1.6, Figure 1.7, and Figure 1.8, it can be observed that electric vehicles have eventually found their place in the Indian automobile market. There is a positive ethos seen for EVs in India, and its presence is fast growing.

- The government of India is also giving due importance and prioritising the EV industry. Since 2015, under the scheme titled "Faster Adoption and Manufacturing of Hybrid and Electric Vehicles" (FAME), the government has been promoting the manufacturing and sale of EVs (two, three, and four-wheelers). By 2030, the government of India has the vision to ensure that 30% of vehicles on Indian roads are electric vehicles.

- Electric two-wheelers have dominated Indian EV sales in the past two years, 2021 –

2022. The data from [6] shows that registered electric two-wheelers accounted for 63% of the total EV sales, up from 50% in 2021. i.e. a total of $6,69,845$ units out of $10,54,983$ units in 2022.

- India has embraced EVs into its automobile market of the urban cities and is slowly making its way into other parts of the country. It is observed here that the presence of EVs, both four-wheelers and two-wheelers, needs to increase in the rural and hilly regions of the country.

Hence, the author is motivated to study the hilly roads and the challenges associated with such roads on EVs. The goal behind the work done in this thesis is to make EVs, especially electric two-wheelers, more feasible for hilly roads.

1.2 Modeling Electric Two-Wheelers on Hilly Road

This thesis considers electric two-wheelers to model and study EVs on hilly roads. Since electric two-wheelers are commonly called electric scooters, the terms electric two-wheelers and electric scooters are used interchangeably. The road characteristic in the hilly region differs from the plains. The parameter differentiating plain and hilly road drive is the road gradient, as shown in Figure 1.10 (a) and Figure 1.10 (b). The road gradient is the change in altitude divided by the horizontal distance traveled and is usually expressed in percent slope or slope angle in degree [9]. In this thesis, road gradient is referred to as the hill angle, symbolized as θ, and measured in degree (°). The roads in the hilly region have several positive slopes (*i.e.*, going uphill) and negative slopes (*i.e.*, going downhill).

The resistive force the electric scooter must overcome to be in motion is called tractive effort. These tractive forces are shown in Figure 1.10. The source battery should supply power to overcome these tractive forces. The total tractive force for a plain and uphill road is then given by (1.1)

$$F_t = F_f + F_a + F_{gh} + m\frac{dv}{dt} \tag{1.1}$$

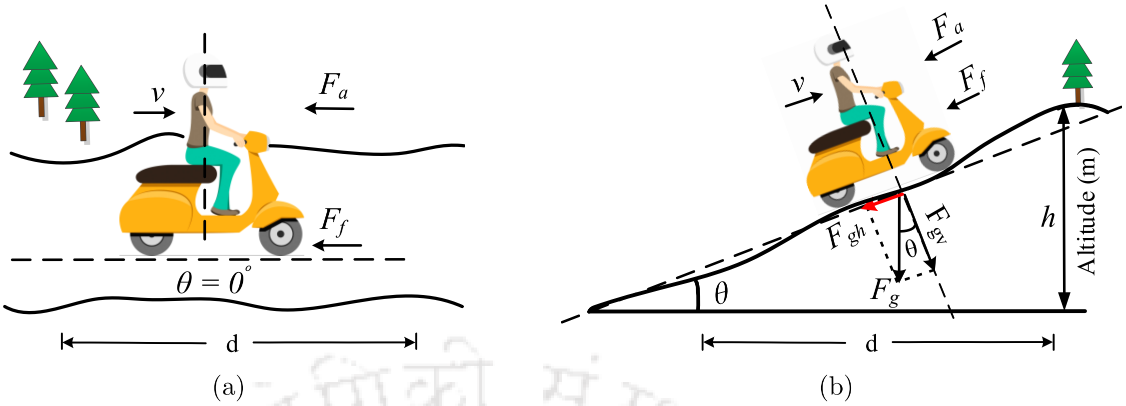

Figure 1.10: Illustrations showing the tractive forces associated with electric two-wheelers (a) in plain road (b) while climbing up the hill.

where F_f is the friction force to overcome the rolling resistance between tire and road surface and is given as

$$F_f = \mu_{rr} m g cos(\theta) \tag{1.2}$$

where m is the mass of the scooter in kg, and the passenger, μ_{rr} is the rolling friction coefficient. The value of μ_{rr} varies with different types of road; here, the value taken is for an asphalt concrete surface road. g is the acceleration due to gravity. m the mass of the kerb and passenger. The term cos(θ) in (1.2) is very small, and in some cases, it is neglected. For example, in plain road, the θ is zero; hence the cos(θ) term is absent.

The aerodynamic drag force is expressed as

$$F_a = \frac{1}{2} \rho A C_d v^2 \tag{1.3}$$

where ρ is the air density, v is the scooter speed in m/s, and C_d is the drag coefficient whose value depends on the vehicle's design.

For two-wheelers and four-wheelers, C_d values are different. Two-wheelers, such as motorcycles and scooters, have much higher values of C_d than four-wheelers. The electric vehicle designers succeeded in bringing it down for the four-wheelers as small as 0.19. Two-wheelers such as motorcycles and scooters, however, have much higher values; it is around 0.7 (typical value) [2].

The effort to climb the hill is denoted as F_g, then, F_{gh} is the vertical force component of F_g due to its weight and gravitational acceleration, which is in horizontal to the road plane as shown in Figure 1.10 is given as

$$F_{gh} = mgsin(\theta) \tag{1.4}$$

where θ is the gradient of the road or hill angle.

It is to be mentioned here that F_{gh} is absent for a plain road drive as the hill angle will be zero or close to zero and is negative when descending the hill and aids in the motion of the scooter.

The linear acceleration force is given by $m\frac{dv}{dt}$ where $\frac{dv}{dt}$ is the acceleration, it is negative during de-acceleration. This force is absent when the vehicle runs at a constant speed, then the tractive force at constant speed is given by

$$F_t = F_f + F_a + F_{gh} \tag{1.5}$$

1.2.1 The Drawback of Hilly Road for EVs

Although EVs have many benefits over ICE vehicles, as already outlined in the introduction section. However, their range is still a major challenge. The range of an EV is the distance covered when fully charged [1]. The battery (energy source) that powers the EVs has a lower energy density than gasoline fuel used in ICE vehicles. The range of the EVs further goes down when operating on hilly region roads.

Due to the road gradient, the battery has to supply more power to generate the required tractive force on an inclined road than on a plain road for a given distance to cover at the same speed. For example, if we take an electric scooter running on a plain road as seen in Figure 1.10 (a), it has to overcome only the friction force (F_f) and the aerodynamic drag force (F_a) to move forward. However, when the electric scooter climbs up the hill, besides F_a and F_f, there is an additional hill-climbing effort (F_{gh}) to overcome as shown in seen in Figure 1.10 (b). The battery should supply energy to generate the tractive forces for

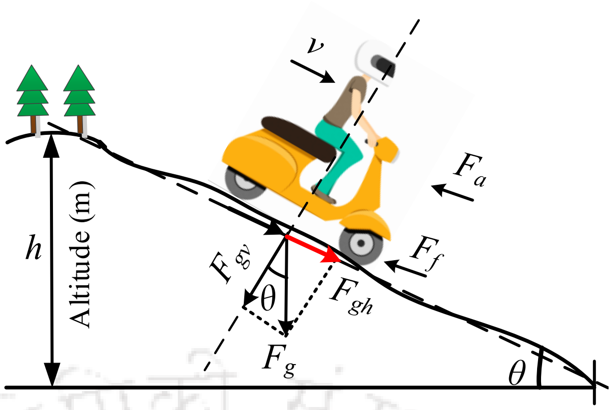

Figure 1.11: Illustrations showing the tractive forces associated with electric two-wheelers while climbing down the hill

the electric scooter to move forward. Thus, due to the hill angle, the electric scooter will consume more energy to cover the same distance at the same speed compared to that on a plain road. For hilly roads, the required tractive force is higher than for plain roads, thus increasing the power ratings of the EVs.

1.2.2 The Benefit of Hilly Roads for EVs

When the electric scooter has reached the top of the hill, it has gained potential energy (mgh); while climbing down, some of this energy can be cultivated back into the source battery. As illustrated in Figure 1.11, while descending the hill, there will be an increase in the overall scooter mass due to the rotating mass [10]. Then the F_{gh} force, which is the force component due to the weight and the gravitational acceleration, can aid to the driving force of the scooter; here, F_{gh} assist in the motion of the scooter, and the governing equation for motion without brake force is then given as

$$\frac{dv}{dt} = \frac{F_t + F_{gh} - (F_f + F_a)}{m} \tag{1.6}$$

To prevent the scooter from overspeeding, the brake force F_{brake} needs to be applied. The governing equation for motion with brake force is then given as

$$\frac{dv}{dt} = \frac{F_{gh} - (F_f + F_a + F_{brake})}{m} \tag{1.7}$$

where F_{brake} is provided by the electric braking circuit.

The electric braking that enables electric vehicles to recover energy while braking is called “Regenerative Braking”. It is “regenerative” braking because it converts the moving wheel’s kinetic energy (i.e., the mechanical energy) into electrical energy and charges the source battery during the braking period of the vehicle. In an ICE vehicle, this same energy would have been absorbed in the form of heat in friction-based braking. Regenerative braking is another advantageous feature of an electrified vehicle over ICE vehicles.

1.2.3 The Potential of Regenerative Braking on Hilly Roads

Using the typical two-wheeler and road parameters as given in Table 1.1 and using scooter dynamic Equations (1.6) and (1.7), a simple MATLAB programming was run to show the energy recovered when constant brake force is applied. Here, an electric scooter with a wheel-hub motor is considered. The simulation assumes that the electric scooter is climbing down from a height of 31 m with a hill angle of 3° with a constant gravitational F_{gh} force acting on the electric scooter.

Figure 1.12 (a) plots the waveforms of the scooter speed while coasting down the slope with a freewheel speed denoted as v_{coast}, *i.e.*, without any braking force, and the descending speed with a brake force applied, denoted as v_{brake}. As observed from the v_{coast} waveform, the scooter speed keeps increasing due to the constant F_{gh} force acting on it, and on the other hand, with an appropriate amount of brake force, the scooter speed is held to a comfortable speed v_{brake} of 20 km/h. Here, naturally, to cover the same height, the time taken to cover the distance is more when speed is brought down from v_{coast} km/h to v_{brake} km/h.

Figure 1.12 (b) plots the energy consumed to overcome the air drag by the scooter for v_{coast} and v_{brake} speed, respectively. From Figure 1.12, it can be inferred that one can also save some energy that otherwise would have been spent to overcome the air-drag force by trading off the speed. Considering the scooter descends at speed v_{brake} km/h instead of higher speed v_{coast} km/h by applying the brake force, then the amount of energy (i.e., the

Table 1.1: A typical specification of scooter dynamics

Parameters	**Values**
Mass, m	200 kg (110 kg kerb and 90 kg of the passenger)
Maximum speed	50 km/h *i.e.* 13.88 m/s
Drag coefficient, C_d	0.7
Air density, ρ	1.25 kg/m^3
Frontal area of vehicle and rider, A	0.6 m^2
Coefficient of rolling friction, μ_{rr}	0.007
Gravitational acceleration, g	9.8 m/s^2
Radius of the wheel hub motor, r	0.2 m

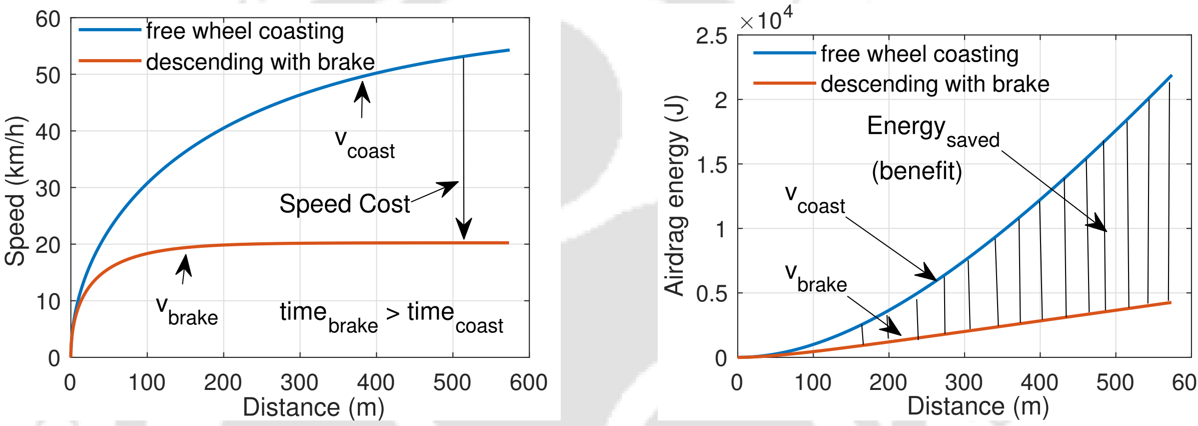

(a) (b)

Figure 1.12: Simulation results showing (a) scooter speed response with and without braking force (b) energy consumed by F_a.

saved energy) that can be recovered is given as

$$\text{Energy Saved} = \frac{1}{2}\rho A C_d (v_{coast})^2 - \frac{1}{2}\rho A C_d (v_{brake})^2 \tag{1.8}$$

The shaded area between the airdrag energy curve of the two speeds shown in Figure 1.12 (b) is the energy that is saved as the EV is operating at low speed. The benefit of applying regenerative braking while climbing down the hilly slope is that the recovered potential energy is high as less energy gets absorbed to overcome the air drag. Further, the low speed while climbing also adds to the comfort and safety of the driver. Hence, regenerative braking is an important and desirable feature for EVs designed to operate on hilly roads to help extend their driving range. Later in this thesis (Chapter 3), the design and implementation of one such regenerative braking circuit for an electric two-wheeler will be presented in detail.

1.3 Literature Survey

The literature survey has been presented in three subsections, the first related to hilly roads, the second is on regenerative braking circuits and the third on fault detections and mitigations for BLDC motors.

1.3.1 Hilly Region Drive Cycles

In EV, the electric motor is the propulsion machine that moves the vehicle forward. Besides the kerb and passenger weight, the road's gradient also acts as a load to the electric motor. Hence, the knowledge of the road gradient and practical aspects of hilly roads becomes essential for road load analysis. The road load, in simple terms, means the resistances that an EV's electric motor must overcome and keep moving forward [11]. A road load analysis of a vehicle helps us in the early stage propulsion system design of an EV. Studying the road characteristics of a hilly region requires both its Drive Cycle and hill angle data. Drive Cycle is a set of vehicle speed points versus time, representing a specific city or region [12]. Experts and researchers worldwide agree that driving features of different terrains are unique because of their road type, traffic density, and vehicle fleet compositions.

Many modular Drive Cycles are available worldwide, primarily used to test vehicle emissions and fuel consumption. A few typical examples are shown in Figure 1.13, which are all used for vehicle regulatory purposes. Figure 1.13 (a) shows the New York City Cycle (NYCC), and Figure 1.13 (b) shows the Federal Urban Driving Schedule (FUDS) used by the United States environmental protection agency. Figure 1.13 (c) shows New European Drive Cycle (NEDC), and Figure 1.13 (d) shows Japan's 10-15 mode Cycle (JP1015). These examples represent urban city driving with frequent start and stop conditions. These regulatory drive cycles represent a country or a region but don't represent a particular city and special terrain. The knowledge of the Drive Cycle helps the researchers evaluate fuel consumption [13], estimate pollutant generators, vehicle design, vehicle efficiency [14], and tooling & manufacturing of the vehicles.

In India, a standard Drive Cycle for the base emission rate study was developed in the

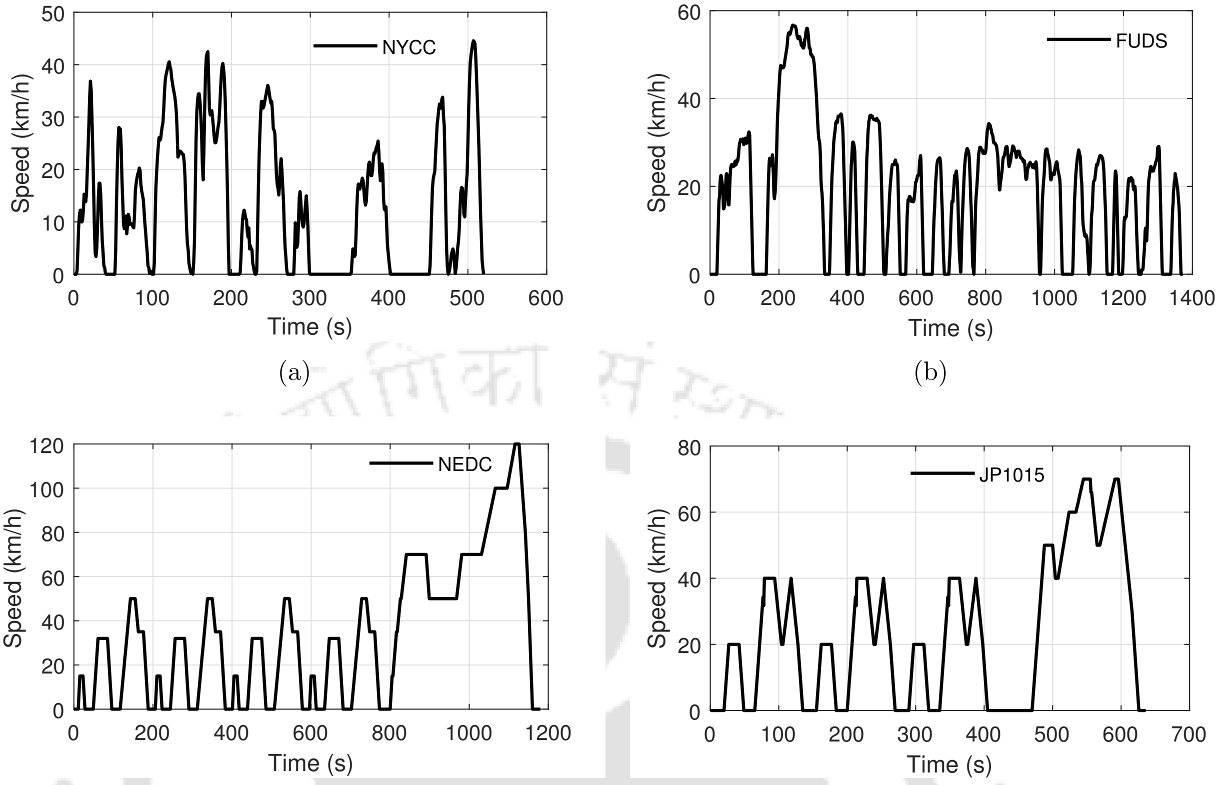

(a) (b)

(c) (d)

Figure 1.13: Examples of few common Drive Cycles (a) New York City Cycle (NYCC) (b) Federal Urban Driving Schedule (FUDS) (c) New European Drive Cycle (NEDC) (d) Japan 10-15 (JP1015).

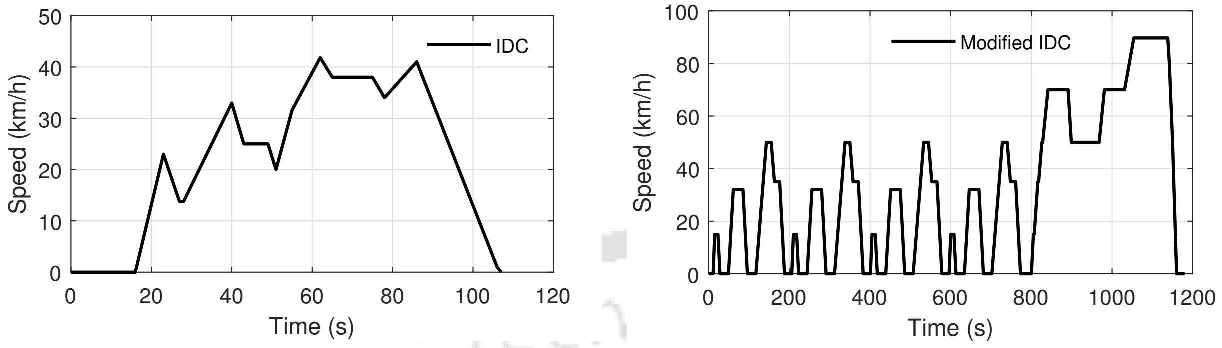

(a) (b)

Figure 1.14: Drive Cycles in India (a) IDC (b) modified IDC.

year 1985 by the Automotive Research Association of India (ARAI) called the Indian Drive Cycle (IDC), shown in Figure 1.14 (a). Since Figure 1.14 (a) was too old to represent the actual road conditions, later in the year 2000, a modified Indian Drive Cycle came into use, which is an adoption of the Europe Drive Cycle as shown in Figure 1.14 (b). However, many studies showed that the IDC does not fully represent the Indian driving condition due to wide variations in traffic density, road conditions, and driving habits in different parts of the country. Authors [15] have shown that IDC fully does not represent real-world driving. In their study, the authors [16] showed that Chennai has unique driving characteristics. Therefore, adopting a driving cycle from another country or city may not be appropriate. In 2013, The Energy and Resources Institute (TERI) presented similar work to study the real-world driving conditions in different Indian cities and compare them with the IDC for different vehicle categories. The result revealed that the driving cycle for different vehicle types (cars, two-wheelers, and buses) is distinctly different and not representative of India's actual IDC. Drive Cycle studies for two-wheelers were also presented in [17]. Their work compares motorcycle Drive Cycles in two world cities: Edinburgh in Scotland and Delhi in India. They showed how two cities have different drive characteristics from the same motorcycles.

From the literature on Drive Cycles, it can be gathered that many authors have developed real-time Drive Cycles for a particular city to represent better the road type and the vehicle's driving characteristics. However, so far, the information on the hill angle is missing in most standard Drive Cycles. For unique terrains like the hilly region, hill angle information is required to study the vehicle's operating performance. The ARAI collected the data from metro cities like Delhi, Mumbai, Chennai, Bangalore, and Pune to build the IDC; these city roads are entirely different from those of Shimla, Shillong, and Gangtok. Because if one were to superimpose road gradient on standard Drive Cycles, there would be more fuel use and emission rates than without the gradient information. The effect of long slopes and high gradients on vehicle speed is considerable, and one cannot neglect them. On average, fuel use increases by 15% to 20% when a typical light-duty vehicle is driven over a hilly road compared to a flat road [18]. The gradient information is crucial for road load analysis of any EV on a hilly road.

Now, there is no one standard way to quantify the hill angle. Many researchers have presented various gradient measurement methods for studying vehicle fuel use and emission rates as they are sensitive to the road gradient. Recent works are of online estimation on moving vehicles to facilitate the automatic driving system. Then there are traditional offline methods like maps, instruments, and drive cycle data to find the hill angle. Then there are on-board direct measurements of hill angle, which are using an instrumented car [19], sensor-based (accelerometer) [20], laser-based Light Detection and Ranging (LIDAR) method [21], or satellite-based (GPS) [9]. The sensor-based road gradient measurement for automotive patents was filled as early as 1971, as reported in [22]. The gradient measured from the accelerometer and inclinometer on moving vehicles has been shown to have limitations due to the noise arising from the vehicle suspension from the vehicle's dynamic. Methods like morphology, neural network, first-order low pass filter, and recursive least square were used to remove noise from the gradient data [23,24]. The very recent contribution of estimating road gradient employs a Global Positioning System (GPS) receiver of various kinds [25–28]. The authors [29] use a GPS receiver with an in-built barometric (GPS/BA) to collect field data and use its position and distance information to quantify road gradient and the precision of the gradient estimation from GPS/BA and Differential Global Positioning System (DGPS) based were later compared with LIDAR [29].

The literature survey on hill angle measurement tells us that GPS and sensor-based approaches give the most accurate results, but they are expensive. In the following Chapter 2 of this thesis, we present a simple method to derive hill angles using spatial location information and basic trigonometric formula. The aim is to find the vehicle speed (km/h) and hill angle (°) relationship from the Drive Cycle data practically collected from a small sample of hilly roads. Further, from the data collected, the road load characteristic is studied for synthesising the electric scooter's power and torque requirement for such hilly roads.

1.3.2 Regenerative Braking Circuits for EVs

As mentioned earlier, the EV's range is still a significant challenge, and it gets worse for hilly roads. The Sub-Section 1.2.3 explained the potential of using a regenerative braking technology to recover energy and help increase the range of electric two-wheelers. The range problem of EVs is not a new phenomenon; in the past and the present, many other studies

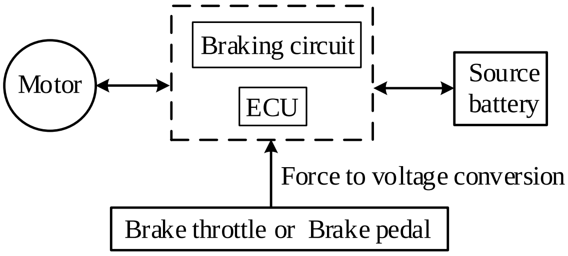

Figure 1.15: Block diagram of RBS System.

have been done to improve the EV range. In literature, different methods have been reported to increase EV's range and fuel economy. The power train of an EV classically consists of an energy source, an electric circuit (power electronics), ECU, and an electric motor, as shown in Figure 1.15. Now, the approach to tackle the range extension problem is being made from all the different parts of the EV drive line. A comprehensive topological overview of power trains for battery-powered vehicles with range extenders is given in [30,31], and some critical technologies for electric vehicles are also discussed in [32].

Since battery is the primary energy source, special attention has been given to battery technology to make it a good, lasting source. So, choosing the correct type of energy source can give a longer range, for example, Li-Ion batteries over lead acid batteries. Li-Ion batteries have been found to have a high energy density and longer lifespan compared to their other counterparts [33,34]. Work at the nascent stage combines fuel cells (with even higher energy density and quicker refill time than a battery) with source batteries to make a longer-lasting energy source [35].

EV range extension is also achieved by system-level modeling of an efficient cell balancing circuit of the battery packs [36]. Also, maintaining the battery to operate at an optimum temperature has improved the battery's life span and increased the EV range [37]. Further, opting for newer, highly efficient designed motors like SRM, PMSM, and BLDC over DC motors shows better performance and less fuel is consumed [38,39]. In [40], the design of an energy-optimal control method to improve the motor drive system's efficiency and extend the driving range of electric vehicles is studied.

So far, the methods discussed above for the range extension were to reduce and optimize power consumption or increase the capacity of the source battery. The other way to extend the EV range is to recover the energy already spent. That is the regeneration way using regenerative braking technology. Incorporating a regenerative braking system (RBS) over conventional friction braking during the retardation period of the wheels also has been reported to increase the driving range [41, 42]. Studies show a good RBS design enables the EV to increase its driving range by up to 16% to 25% [43, 44]. An RBS consists of the braking device (*i.e.*, the interface between the human and the vehicle which converts the braking force into an electrical quantity), the regenerative braking circuit, the energy storage device, and the electronic control unit (ECU) as shown in Figure 1.15. The main work done in this thesis presents a regenerative braking circuit that falls within the subset of the regenerative braking system.

The regenerative braking circuit in the RBS can be realized by using the existing inverter of the EV powertrain or by using additional components. Based on this factor, the regenerative braking circuit topology can be classified into two types, i.e., Type-I and Type-II; Type-I is for those using the same inverter circuit, and Type-II is for those using additional circuits or components.

The Type-I category employs the same inverter circuit of the EV power train as the regenerative braking circuit, as shown in Figure 1.16 (a). In these topologies, it only modifies the inverter's switching pattern during the braking phase to regulate the inverse torque and ensure that the braking energy is sent back to the battery [44–46]. The benefit of using the same motor drive inverter circuit as a regenerative braking circuit is to minimize the number of power devices and, hence, is more economical. The limiting factor of this type is that it is not suitable for low-speed and heavy-duty vehicles. The switch in the inverter needs to supply more power to the propulsion motor, and its switching frequency is low compared to the typical switching frequency used in the DC/DC converter needed to boost very low voltage.

Since this (Type-I) topology is not suitable for the low-speed application, Heydari *et al.* proposed a boundary in the braking force distribution where the combination of regenerative

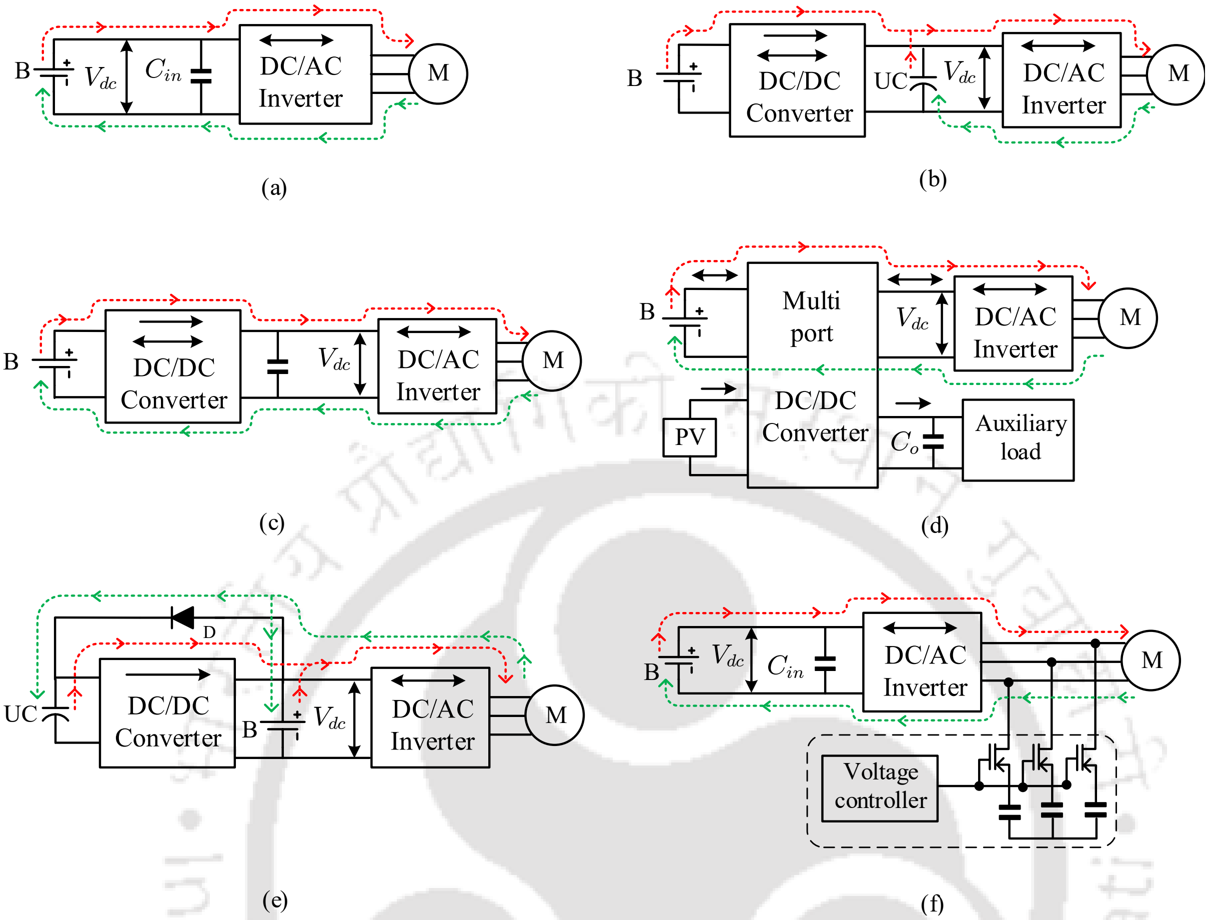

(a) (b) (c) (d) (e) (f)

Figure 1.16: State of art of regenerative braking circuit (a) Type-I topology used in [44–51], (b) Type-II topology used in [52–54] (c) Type-II topology presented in [55] (d) Type-II topology presented in [56] (e) Type-II topology presented in [57] (f) Type-II topology presented in [58, 59].

and friction braking is carried out to maximize energy recovered through the regenerative braking process which is defined using the performance map of the traction motor (TM) and its controller [47, 60]. Godfrey *et al.*, proposed new electric braking based on the stopping time and energy regeneration; here, a combination of regenerative and plugging for braking is presented using the same inverter drive circuit for low-speed application [48]. In these three papers, the optimization of regenerative braking is studied. Fuzzy logic control [49] is used to distribute braking force, Tagaki-Sugeno fuzzy model [50] and a knowledge based methodology in a hierarchical control structure [51] is studied for the stability and improvement of the braking performance.

The Type-II category uses additional circuits like DC/DC converters or components as regenerative braking circuits. This category comes with different variants as explained below.

In [52–54] a buck-boost converter is employed as a regenerative braking circuit. The block representation is shown in Figure 1.16 (b). During the braking period, the buck converter is activated, and the recovered energy during the quick deceleration period is sent to the UC. The advantage of this topology is that the voltage of the dc-link is relatively constant as the battery is connected to the dc-link, which makes the voltage control loops simple. This arrangement is suitable for quick acceleration and deceleration periods, not for hilly region braking. It's also important to note that regenerative braking using solely UCs is ineffective on steep downhills because they eventually hit their maximum voltage and become incapable of receiving any more power, as pointed out by the authors [52].

Lee *et al.* [55] uses a bidirectional DC/DC converter as a regenerative braking circuit, as shown in Figure 1.16 (c). Here, three half-bridge buck-boost converters are connected in parallel to form the DC/DC converter that is being used during the braking period. During the braking period, the DC/DC converter acts like a buck converter, and the regenerative energy is sent back to the battery. The interleaved converter has the benefit of allowing for a reduction in the converter's inductance and capacitance, which are governed by the tolerance range of current and voltage ripple. The disadvantage of this topology is that the extra three numbers of inductance increase the weight of the overall topology.

A multi-port and multi-functional converter for electric vehicle (EV) applications with regenerative charging ability is discussed in [56]. The converter exhibits bidirectional power flow functionality, making it suitable for charging the battery during regenerative braking, as shown in Figure 1.16 (d). During the braking period, the DC/DC converter acts like a buck converter to charge the battery. The advantage of this converter is its ability to accommodate energy resources with different voltage and current characteristics. The limiting factor is that the efficiency of regenerative braking is reduced as a result of the bidirectional DC/DC converter and inverter's power dissipation. Moreover, a buck converter as a braking circuit is unsuitable for low-speed applications.

The additional DC/DC converter used in [57] is a buck converter which is used during motoring mode only. During the braking period, the inverter circuit, along with the help of an additional switch and diode, acts as regenerative braking, as shown in Figure 1.16 (e). Here, during the regenerative braking process, the dc-link voltage is boosted, and the diode is forward-biased. The advantage is that the regenerative braking energy flows to the supercapacitor or the battery without any power converter, thus increasing the efficiency. The disadvantage of such an arrangement is that the voltage of the supercapacitor is always higher than the battery, which puts limitations on system design. Also, the high voltage UC is expensive compared to a high power density battery.

In [58, 59], energy recovery is done via an electromagnetic retardation. Here, the additional components, like the switch and capacitor along with the inverter circuit, form the braking circuit as shown in Figure 1.16 (f). The advantage of this type of braking circuit is that the technique is based on the resonance of the L-C circuit for AC motors and is suitable for braking operation during very low or high speeds. The limiting factor of this technique is that it does not apply to other motors that do not have sinusoidal waveforms, for example, BLDC motors with trapezoidal waveforms.

From the literature review, it is inferred that designing a regenerative braking circuit is a case of "no one size fits all," meaning based on factors like power handling, vehicle size, and terrain application, the designs call for a unique braking circuit. For example, when designing an electric braking circuit for a railed vehicle like urban rail transit trains, where braking power density is high. In such a case, using an additional DC/DC converter seems more appropriate to charge a stationary supercapacitor energy storage system [61].

Likewise, for road vehicles, the nature of braking action on a plain road, as mostly seen in urban city drives, is quite different from that of hilly road drives in hill stations. The brake is mainly applied on hilly roads to descend at a comfortable low speed and prevent the vehicle from over-speeding, as illustrated in Figure 1.17 (a). Comparing Figures 1.17 (a) and (b), it is seen that the braking time required is longer while descending a hill. For such kind of braking, a high power density and a high energy density energy storage are required like Li-Ion [62]. The regenerative braking circuit design and storage device for the hilly road demands to be different from that used in urban plain roads, where it is used to bring the

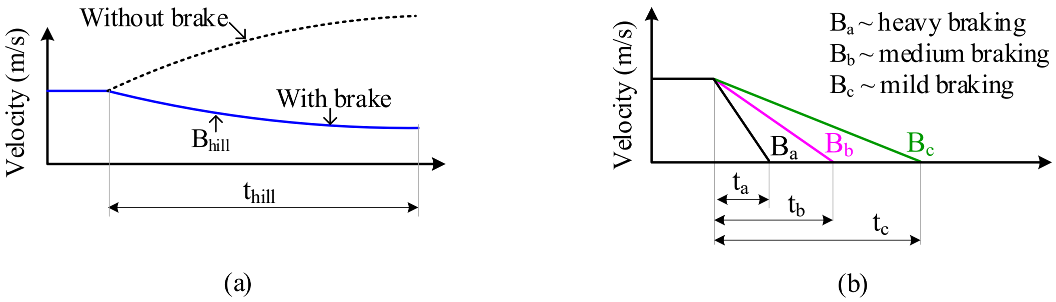

Figure 1.17: Types of braking force application; (a) braking force applied for a longer duration to descend the vehicle at low speed on the hill slope (b) braking force applied for a short period to quickly stop the vehicle, as seen in urban drives.

vehicle to a quick stop, as shown in the Figures. 1.17 (b).

In braking applications like B_a, B_b, and B_c, as shown in Figure 1.17 (b), the kinetic energy needs to be dissipated quickly for the vehicle to stop. High-power ultra capacitors (UC) are required to quickly store the braking energy developed during such regenerative braking. This combination of an additional energy storage device and the main battery is known as a hybrid energy storage system (HESS). Whenever there is a HESS scheme, they have an additional DC/DC converter to meet the demand. Various HESS configuration and their quantitative comparison are mentioned in [63, 64] and their different control strategies considering four configurations: fuel cell-battery, battery-UC, fuel cell-UC, and battery-fuel cell-UC are studied in [65]. Numerous UC-based regenerative braking circuits for EVs have been discussed above under the Type-II category. However, UCs are expensive, and their control is comparatively complex. In addition, it is also important to note that regenerative braking using UCs solely is ineffective on steep downhills because they eventually hit their maximum voltage and become incapable of receiving any more power [52].

The Type-I category of braking circuit design has less component count and is economically friendly; however, it is unsuitable for very low-speed braking and may incur more loss [58]. Efforts have been made to combine this braking circuit with friction braking for very low-speed applications by [60] and many others. Moreover, as the switch in the inverter needs to supply more power to the propulsion motor, its switching frequency is low compared to the typical switching frequency used in the boost converter. Thus limiting voltage gain in regenerative mode. In a hilly region, it is essential to have high voltage gain due to the low value of the back emf generated at low speed. In [58] for low-speed regenerative braking application, Sungchul *et al.* uses an additional electromagnetic retardation circuit with switch-capacitors connected across the motor windings of PMSM to boost the input voltage seen by the battery terminal based on the resonance of the L-C circuit. However, this technique is based on the resonance of the braking circuit for AC motors. This method is less effective for BLDC motors, which have trapezoidal waveforms.

1.3.3 Fault Detection and its Mitigations

The BLDC motors are a popular choice for two-wheelers and other light EVs. In two-wheeler applications, the motor is usually fixed in the center of the wheel and fully covered with a metal cast for its safety and sturdiness. For this type of application, the 3-phase BLDC motors are usually lightly weighted and consist of many permanent magnet poles ranging from forty to as many as ninety. Although BLDC motors are durable and reliable, like any other rotating machine, they are also susceptible to faults and wear-out failures. Various faults can jolt the operation of the whole BLDC motor drive system, which is expected in any rotating machine. The faults can be internal to the motor body, such as magnet damage, demagnetization, rotor and stator misalignment, unbalanced magnet pull, and stator winding faults, or the faults can be external, such as the inverter switch damages, controller failure, sensors, and damage to other peripheral components.

Various fault detection/diagnosis (FD) and fault tolerant control (FTC) have been proposed in the past and present to make the BLDC motor drive system more reliable and resilient towards faults. The recent trend is towards non-stop monitoring and future prediction methods using AI (Artificial Intelligence) and other soft computing methods to prevent fault occurrence and improve system performance. In [66], the authors proposed the prognosis of BLDC drive faults using the Autoregressive Integrated Moving Average (ARIMA) Algorithm for open circuit (OC) and short circuit (SC) faults in BLDC drive. In [67], online monitoring of power converter degradation using a deep learning scheme is presented. For a healthy power converter, the value of the snubber resistance must be within a specific range. Hence, the abnormality of the snubber resistors of the 3-phase inverter switch (IGBTs) of the BLDC drive was detected based on its resistance. In [68], the detection of rotor faults is studied using advanced Fourier Transform techniques. Authors in [69] presented a fault-tolerant system where the failure of a DC link sensor, current sensors, and position sensors are presented where a corresponding method of detection or diagnosis is provided for each possible sensor fault. Several review papers have been published in the literature to discuss the various fault diagnosis and condition monitoring methods available for electric machines [70] and those with permanent magnet rotors [71, 72]. Condition Monitoring of motors with the help of Motor Current Signature Analysis (MCSA) is popularly used to find rotor and stator faults [70].

Here in this thesis, the faults associated with the Hall effect sensor are studied. As explained later in Chapter 5, the whole operation of the BLDC drive depends upon the signals obtained from the Hall sensors. Sometimes, the Hall sensors might produce unwanted glitches or entirely go dead due to ageing, extreme heat, jerking, loose wire connections, etc., leading to a wrong switching sequence of the inverter switches. This situation can cause the motor speed to oscillate and vibrate due to the fluctuations in motor current, which again is caused by uneven excitation of the inverter switches. Hence, even though Hall effect sensors are reliable, less inexpensive, and easy to integrate into the motor drive system, their reliability can be further increased with a simple protection layer in terms of a good fault diagnosis and its remedy. The Fault Tolerant Control (FTC) system comprises both Fault Diagnosis (FD) and Signal Reconstruction (SR), where FD is the important part. Various FD and SR methods have been proposed in the past and present to improve the reliability of Hall-sensor-based BLDC motor drives. The nature of the fault in the Hall effect sensor system may vary; for example, case one where all three Hall sensors are healthy, but a fault may arise due to the misalignment in the sensor position or due to some delay or damage in the signal conditioning circuit, and the second case is dealing with the unhealthy Hall sensor, i.e., one or more of the Hall sensor is damaged. There is complete obstruction of the signal in the latter case. Below is a brief literature survey specific to the Hall effect sensor system faults for both cases.

In [73] based on the principle of minimum deviation, a pre-calibration method to identify and eliminate the offset of the permanent magnet poles, the delay time caused by the Hall signal conditioning circuit, and the offset of the sensor signal identification due to armature response under different loads were presented. Here, based on the pre-calibration results, a self-adaptive position information prediction algorithm based on the Sage–Husa method was able to correct the rotor position information of the BLDC motor. In [74], the effects of one Hall sensor misalignment in its placement on the BLDC motor are presented. Here, adding a phase delay to one of the Hall sensors simulation was conducted to study its effect on commutation circuit switching timings, rotor speed, electromagnetic torque, switching cycle duration, and phase current. In [75], a microcontroller calculates the switching points based on signals from Hall sensors, with the option for tuning using an external optimization algorithm. The control strategy allows for applying a correction algorithm that significantly enhances the commutation of BLDC drives, particularly in unbalanced Hall sensors. The author developed both the computation of sensor misalignment and the correction method to enhance the functionality of BLDC motor drive systems with closed-loop speed control. In [76], the author deduced the Hall signal using the line voltage zero crossing information, making it a sensor-less operation. The work is presented in simulation to show that the sensorless operation can take over in case of any Hall sensor failure.

In the works presented in [77] and [78], authors Scelba et al., uses a hybrid vector-tracking observer to compensate for faulty signals of the Hall effect sensors. Here, the Hall sensor signals are modified into a stationary reference frame, and each combination of almost rotating space vector states of the modified signals is used for fault detection. In the same line of work, the authors in [79] presented an improved FTC, wherein the vector-tracking observer was enhanced by making it direction-sensitive, leading to better performance during steady state and transients. However, using such vector tracking comes at the cost of processing time, demanding extra computational resources, making them sluggish for high-speed and acceleration and decelerations operation. Recent FTC methods have been proposed in [80–82] to identify the faults of Hall sensors and perform the necessary reconstruction at high speeds and fast acceleration/ deceleration. The fast fault diagnostic (FFD) method in [80] combines a simple fault detection and reconstruction technique with a static acceleration coefficient (i.e., constant threshold). This method offers improved dynamic performance at the time of fault. While one sensor fault was detected in [79], two sensor failures could be detected in [80]. However, because the diagnosis approach in [80] is based on a constant threshold, it might function poorly in situations involving significant accelerations or decelerations or a sudden shift in load. Ebadpour et al. advance the approach introduced in reference [80] by introducing an innovative Fast Fault-Tolerant Control (FFTC) technique in [82]. In addition to promptly identifying various faults and efficiently reconstructing faulty Hall signals, the novel FFTC method exhibits resilience in the face of extreme acceleration/deceleration transients. This resilience is achieved through the incorporation of a dynamic acceleration coefficient, which is based on motor speed. In the FTC method presented in [81], combinatory circuits are designed to detect faults in Hall effect sensors. A simple combinatory circuit facilitates the construction of the faulty sensor signal, dependent solely on the duration of the preceding sector.

The literature review shows that many FTC algorithms enhance the overall performance of BLDC motor drive systems even in the presence of Hall sensor faults, both in steady-state conditions and during transient conditions. But it requires complex computation.

1.4 Motivation of the Thesis

Based on the shortcomings as seen in the literature survey, the motivation to carry out the research work is as follows:

- The standard available Drive Cycles of India fall short to wholly represent the hilly region road. The hill angle information needs to be included in standard Drive Cycle data. The literature shows that many authors have developed real-time Drive Cycles to better represent a particular city's road type and vehicle driving characteristics.

Hence, a local hilly road survey is needed to get the speed and gradient pattern.

- From the literature review of regenerative braking circuits, it is inferred that designing a regenerative braking circuit is a case of “no one size fits all,” meaning based on factors like power handling, vehicle size, and terrain application, the designs call for a unique braking circuit. Hilly roads consist of longer slopes, which require the vehicle to coast down at a safe speed. For hilly region applications, it is essential to have high voltage gain due to the low value of the back emf generated at low speed. Hence, a regenerative braking circuit for low-speed and more extended braking period applications, which can work for all three-phase motors, is needed.

- From the literature review on fault detection and mitigation, it is observed that the methods suggested demand substantial computational resources for implementing co-ordinate transformations, state and vector observers, or requiring additional circuits. Hence, there is a need to have a simple and smart Hall effect sensor system that detects the fault and keeps the BLDC motor working despite the damage of Hall effect sensors.

1.5 Objective of the Thesis

Based on the motivation discussed above, the objective and contribution of the thesis are:

- To present a simple and cost-effective procedure to find the two-wheeler’s speed variation pattern with the road gradient for hilly roads. The data are further used for analysis in developing and designing the electric scooter regenerative braking systems.

- To propose a new modular regenerative braking circuit and its control scheme for low-speed and more extended braking period applications, which can work for all three-phase motors, be it BLDC or PMSM.

- To develop the small-signal model of the proposed regenerative braking circuit. Furthermore, to analyzes its steady-state and dynamic-state performance.

- To design and develop a Type-II compensator current controller for regulating the proposed regenerative braking circuit. Its implementation and hardware validations.
- To design and develop a robust Sliding Mode control current controller for regulating the proposed regenerative braking circuit. Its implementation and hardware validations.
- To develop a simple and smart Hall effect sensor system that detects the fault and keeps the BLDC motor working despite the damage to Hall effect sensors.

Overall, the author hopes to provide readers from diverse backgrounds with a comprehensive understanding of how hilly roads impact electric two-wheelers. It aims to familiarise readers with the challenges of navigating these rugged terrains and offers suggestions to address these issues, making electric vehicles more practical for such conditions. The central focus of the thesis is to present practical solutions for the difficulties faced by electric two-wheelers on hilly roads, thereby enhancing their feasibility in challenging terrain.

1.6 Structure of the Thesis

The remaining of the thesis is organized as follows:

Chapter 2: Drive Characteristic of Hilly Region

This chapter presents a cost-effective and straightforward procedure to find the road gradient from the data (speed, altitude, time, distance) collected from an ICE scooter using a GPS-based app on a smartphone in Shillong City. Further, from the data collected, the road load characteristic is studied for synthesizing electric scooter's power and torque requirements for hilly roads. Further, from the data collected, the road load characteristic is studied for synthesizing electric scooter's power and torque requirements for such hilly roads. The results show that the torque demand increases with the hill angle value, leading to a trade-off between scooter speeds and power. For an electric scooter to be suitable for such an aggressive road, it should have a high-power motor with a high current rating and high current capacity battery banks.

Chapter 3: Regenerative Braking Circuit for Electric Two-Wheelers in Hilly Region

This chapter presents a modular regenerative braking circuit for electric scooters operating at low speeds. The proposed modular regenerative braking circuit's configuration, operation, and control scheme are explained in the chapter. Here, using the state-space averaging technique, the small-signal modeling of the braking circuit is done, and a Type-II current controller is designed to track the braking current reference. The operation of the proposed regenerative braking circuit and the vehicle's overall motor drive-train are validated through simulation and experiment.

Chapter 4: Robust Control of the Proposed Regeneration Braking Circuit

This chapter is in the continuation of Chapter 3; the only significant difference is that, here, in this chapter, the close-loop feedback controller of the braking circuit is new. Seeing the benefits of the Sliding Mode (SM) controller, here in this chapter, an SM current controller is designed and implemented to regulate the braking current of the proposed regenerative braking circuit, which is established in Chapter 3. The new controller (i.e., its design and control scheme) will be implemented using MATLAB/Simulink. Further, it is experimentally verified in the same scaled-down laboratory test setup used in Chapter 3.

Chapter 5: Application of a Smart Hall-Effect Sensor System for 3-Phase BLDC Drives

The work done in this chapter provides a smart method to detect the rotor position of a 3-phase BLDC motor. Such motors require three Hall effect sensor numbers for detecting the rotor position. The information on the rotor position provided by these sensors is then used to obtain the accurate firing sequences of the six switches of the 3-phase inverter in a 3-phase BLDC drive system required to accomplish the electronic commutation process of the motor. If one of the hall effect sensors stops working due to some damage, then the six firing sequences cannot be obtained, and the motor's commutation process is hindered. The proposed work provides intelligence to the hall sensor system to generate the necessary six-firing sequence to operate the motor, even when one hall sensor suddenly stops working in the middle of the run. This scheme is helpful for emergency operations before replacing the damaged hall effect sensor.

Chapter 6: Conclusion and future Scope

Finally, this chapter summarises the thesis, the major conclusions, and the recommendations for future research.

2

Drive Characteristic of Hilly Region

Contents

2.1 Introduction

A road load analysis of a vehicle helps us in the early stage design of the propulsion system of an EV. Studying a hilly region's road characteristics requires its Drive Cycle and hill angle data. The available standard Drive Cycle of India is unsuitable to represent the characteristics of a hilly region road. For the study of the hilly roads, the information on the hill angle needs to be included in standard Drive Cycle data. The literature shows that many authors have developed real-time Drive Cycles to better represent a particular city's road type and vehicle driving characteristics. Hence, this chapter collects the Drive Cycle of Shillong City, a hill station located in the Meghalaya state of the NorthEastern region of India. From the data collected, the average speed pattern of two-wheelers on hilly roads concerning the hill angle is computed further to facilitate the road load analysis of such hilly roads.

The literature survey on hill angle measurement tells us that GPS and sensor-based approaches give the most accurate results but are expensive. In this chapter, we present a simple method to derive hill angles using spatial location information and basic trigonometric formula. The aim is to find the vehicle speed (km/h) and hill angle (°) relationship from the Drive Cycle data collected from a small sample of hilly roads. Further, from the data collected, the road load characteristic is studied for synthesizing the electric scooter's power and torque requirement for such hilly roads. The work done in this chapter helps in finding the potential of regenerative braking in hilly regions and its associated challenges.

2.2 Methodology and Data Collection

This section explains a simple and affordable method to collect the Drive Cycle data. Figure 2.1 shows the steps involved in the methodology. The steps involved are route selection, data collection, data processing, and computation, further briefly explained below.

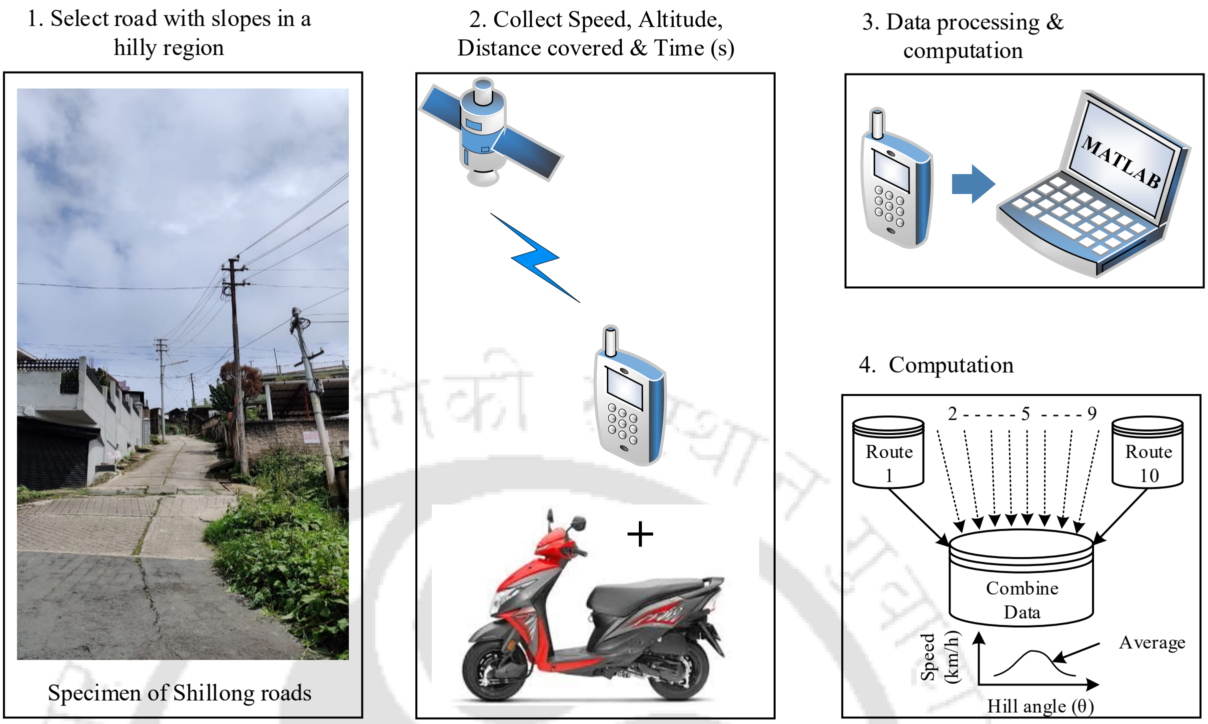

Figure 2.1: Steps involved in the methodology approached.

2.2.1 Route Selection

Shillong City is considered for the data collection of a hilly region Drive Cycle. Shillong is the capital of Meghalaya, situated at an elevation of 4,908ft to 6,449 ft above sea level [83]. Shillong is one of the most popular hill stations in Northeast India. The slope comes under the bracket of exceptional gradient type by IRC:SP:73-2015 and IRC:SP:84-2014. This type of road is different from the highway roads, and it is observed that they often do not always follow the Indian Road Congress (IRC) rules, and roads are even steeper in some parts of the local streets. Ten routes were selected based on the presence of the slopes by visual inspection. Figure 2.1 (a) shows a sample route of Shillong colony roads. As seen, the slope of the roads is visible just from visual inspection.

2.2.2 Device Used to Collect Data

Currently, motorcycles and scooters are the two most popular traditional ICE-powered two-wheelers on these roads. Figure 2.2 shows a typical example of motorcycle and scooters. A conventional ICE scooter in India, such as the TVS scooty pep and Honda kinetic, is

(a) (b)

Figure 2.2: Example (a) motorcycle (b) scooter, (pictures under a Creative Common License).

four hp to eight hp power. This thesis does not compare the electric scooters with the ICE scooters. However, due to the unavailability of high-powered electric scooters at the time of data collection, the driving activity to collect the data was carried out on a conventional ICE gasoline scooter named Honda Dio, as shown in Figure 2.2 (b) and whose values are given in Table 2.1. Later this Drive Cycle data collected on the ICE scooter is analyzed, and the authors discuss the suitable motor power ratings and design modifications so that the electric scooters almost emulate their performance with that of ICE scooters on hilly roads.

With the driver and co-passenger carrying the smartphone device. Using a smartphone, iPhone 7, and an App, the data was collected. The app "Speedometer 55 Pro" actively tracks and records data; the data logged are speed, altitude, distance, and time at a 1 Hz sampling rate, which is saved in the black box of the app and later transferred to a computer for analysis. This app uses the GPS longitude & latitude location to give the altitude. Figure 2.3 shows the Speedometer 55 Pro app dashboard screen, which shows the barometric vertical speed indicator in graph form along with the altitude data points.

Table 2.1: Specification of Honda Dio scooter

Parameters	**Values**
IC Engine type	Single Cylinder, Air-cooled, 4-Stroke
Mass	200 kg = (105 kg of the kerb weight) + (95 kg of the passenger)
Net torque	8.91 Nm @ 5500 rpm
Maximum power	8 bhp @ 7000 rpm
Maximum speed	83 km/hr
Wheel base	1238 mm

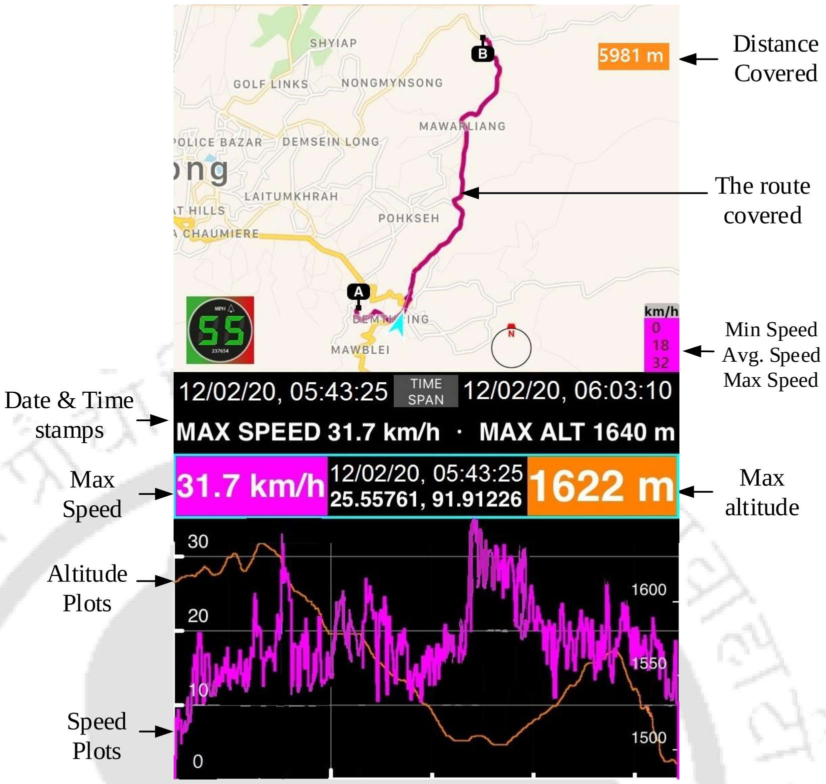

Figure 2.3: Speedometer 55 Pro dashboard.

2.2.3 Data Processing

At the end of each trip, data is exported in a .csv file from the mobile phone to the computer and checked for any discrepancies. MATLAB2018b is used for processing the data and analysis. With the help of its in-built linear regression functions and filters, it becomes quite convenient to work with a large volume of data. A moving average filter is applied to the elevation data to remove abrupt spikes in data. The driver need not necessarily adhere to this speed profile collected. The speed profile is unique to each driver, but the effect of GPS altitude points to the speed will mostly remain the same.

2.2.4 Drive Cycle Characteristic

The analysis is carried out in each route to find the driving characteristic of all the ten routes using the parameters given in the literature. The parameters are distance travelled, average speed, and maximum speed.

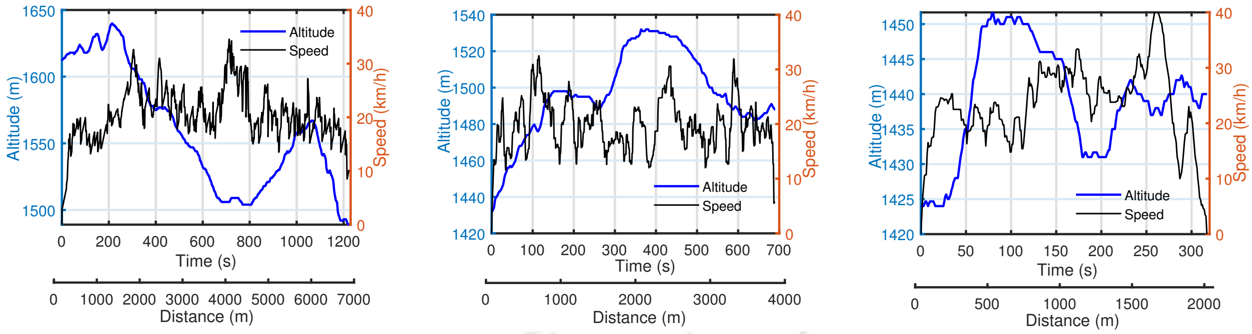

(a) Route one (R1)
(b) Route two (R2)
(c) Route three (R3)

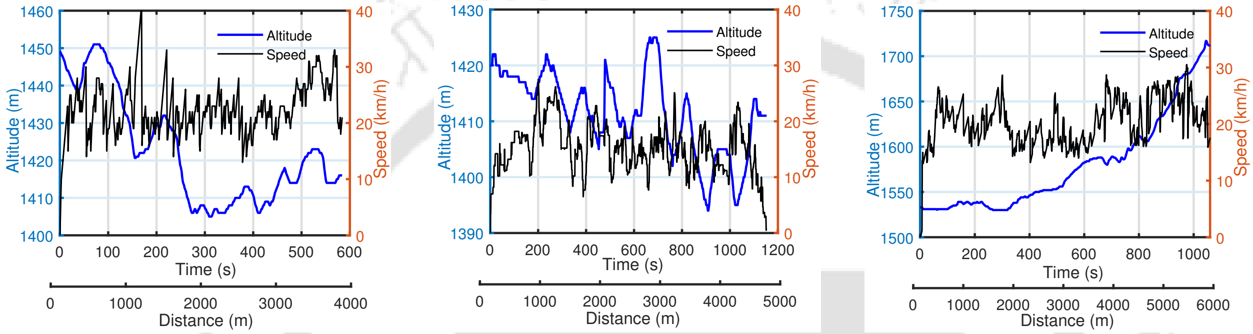

(d) Route four (R4)
(e) Route five (R5)
(f) Route six (R6)

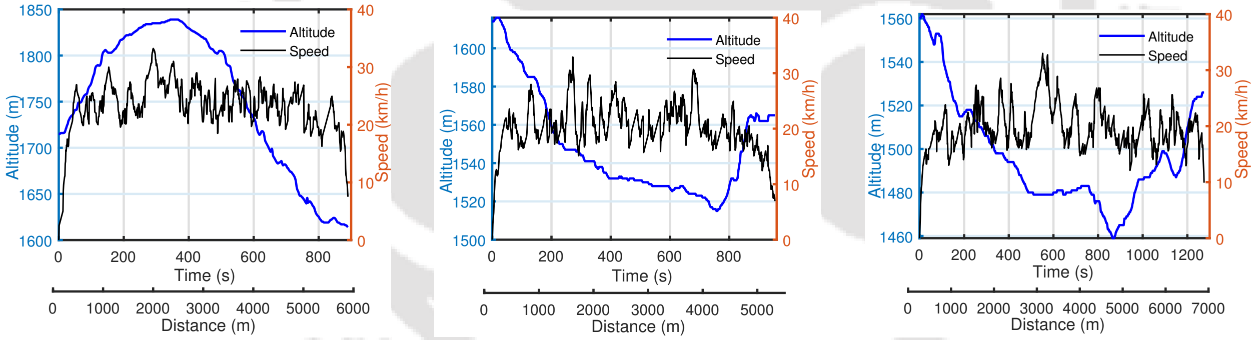

(g) Route seven (R7)
(h) Route eight (R8)
(i) Route nine (R9)

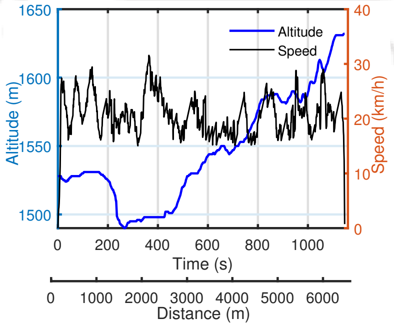

(j) Route ten (R10)

Figure 2.4: Shillong Drive Cycles data plots: (a) Nonghthymmai-Mawblei-Umpling-polo, (b) Pokesh-laimu-wards lake, (c) Wards lake-Golf links, (d) Art café to Nehu, (e) DB Museum-laimu, (f) Laimu-BTW Mawblei, (g) Mawblei-Nonghthymmai, (h) Nonghthymmai to Malki, (i) Malki-PB-Laimu, (j) Laimu-Goroline-Nongrim Hill.

Table 2.2: Shillong drive characteristic

Route no.	Trip Distance (km)	Trip Time (m)	Avg. Speed (km/h)	Max. Speed (km/h)
R1	7.0	20.4	20.2	34.0
R2	3.8	11.0	20.2	33.0
R3	2.0	06.0	24.0	38.0
R4	3.6	10.0	22.5	36.5
R5	4.8	19.2	16.6	36.0
R6	6.0	17.6	20.5	30.0
R7	5.7	15.0	24.0	31.2
R8	5.3	16.0	20.2	32.7
R9	7.0	21.30	19.7	38.3
R10	6.6	19.20	20.5	31.5

The driving characteristics of each route are tabulated in Table 2.2. From the preliminary analysis of these ten drive cycles, we get an idea about the nature of the speed profile in Shillong City. Since driving at high speeds above 50 km/h on hilly roads is dangerous, the average driving speed is about 20-22 km/h. Figure 2.4 shows plots of altitude and speed with respect to time and distance, respectively.

2.3 Hill Angle Calculation

This section explains the calculation of the hill angle from the altitude and distance data. As explained in the previous section, the data collected from the speedometer pro 55 App gives the altitude and distance data points. Using this spatial location information and implementing the basic trigonometric formula, we find the hill angle (θ). Taking a segment from the length of the distance covered as shown in Figure 2.5, the hill angle becomes the arc-tangent of its altitude and base as given by (2.1)

$$\theta_i = tan^{-1}\left(\frac{\text{Altitude}_i}{\text{Base}_i}\right) \tag{2.1}$$

where i is the index number and the Base$_\text{i}$ is calculated by simply applying the Pythagoras equation as given in (2.2).

$$\text{Base}_i = \sqrt{(\Delta D_i)^2 - (\text{Altitude}_i)^2} \tag{2.2}$$

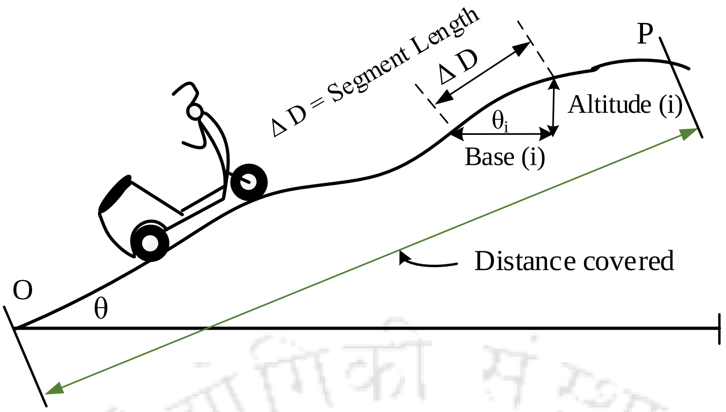

Figure 2.5: The segment length illustration.

where ΔD is the segment length selected from the hypotenuse side of the triangle; a small portion of the distance travelled by scooter in one trip, selection of ΔD length, affects the hill angle of the road as seen in the expressions (2.1) and (2.2). The length of ΔD is taken such that it is greater than five times the vehicle body length [9]. There should be finite data points between OP refer Figure 2.5. The number of data points is inversely proportional to the vehicle's speed. At a higher speed, lesser data are recorded and vice-versa. Since the scooter's body length is 1.8m, for comparison study purposes, four different segment length was chosen, and regressive simulation analysis was done to compare the hill angle value generated for all ten routes.

Figure 2.6 shows the altitude, speed, and calculated hill angle plotted against the distance covered for route one (R1). It can be inferred from the hill angle vs. distance plot that there is no significant difference in the hill angle values from different segment lengths, i.e., $(\Delta \mathrm{D} = 10\ \mathrm{m}, 20\ \mathrm{m}, 30\ \mathrm{m}, 50\ \mathrm{m})$ as shown in Figure 2.6. The final choice for the segment length taken is 20 m, which is further used for the road load analysis of electric scooters in the next section. This technique of calculating gradient angle with the help of GPS App data of altitude and speed might have ±5% error [21] [84]. However, it is reasonable for representation and theoretical study purposes.

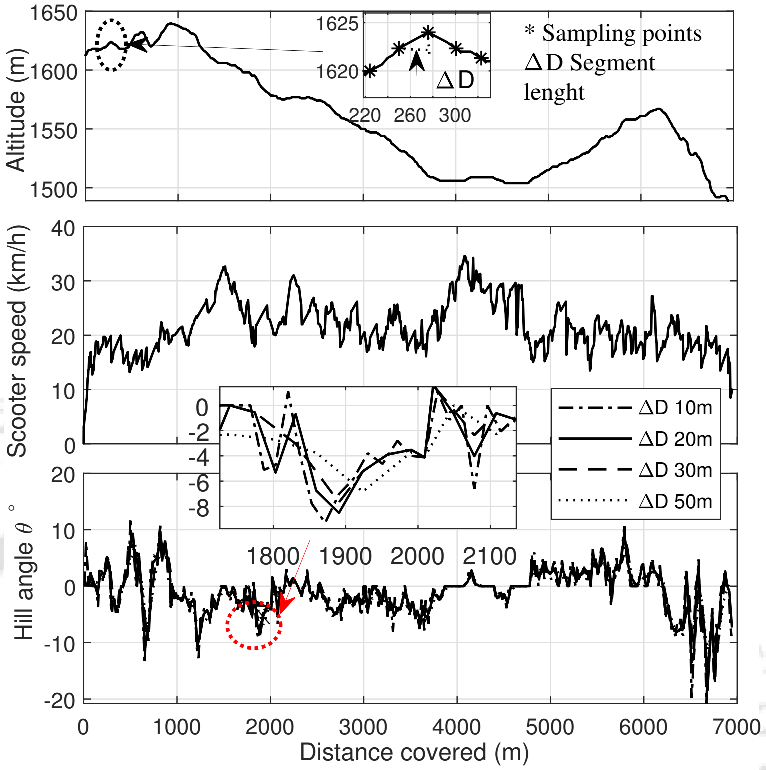

Figure 2.6: Hill angle vs. distance covered plot for R1 route.

2.3.1 The Vehicle Speed vs. Hill Angle Analysis

From the speed and hill angle data, the mean, maximum, and minimum scooter speeds are calculated using classical descriptive statistic methods. The scooter speed data and the hill angle data of all ten routes are put into one data bin. Figure 2.7 (a) shows all the scooter speed data of all the ten routes spread across its hill angle data. Next, a MATLAB code is written to segregate the data into sixty-five separate data bins. The criteria to create the bin is the range of hill angle, keeping a difference of 0.5° between each bin starting from 0°. Both hill angle and speed data are collected to its sixty-five designated bins, As example $0 = 0°$ is assign to bin one, then $0 < \theta \leq 0.5°$ is bin two, $0 > \theta \geq -0.5°$ is bin three, $0.5 < \theta \leq 1.0°$ is bin four, $-0.5 > \theta \geq -1.0°$ is bin five, and in this fashion till $15.5 < \theta \leq 16°$ and $-15.5 > \theta \geq -16°$ bins are created, resulting into sixty-five separate bins hill angle data. Simultaneously sixty-five bins for speed data with associative index numbers are also created. Then in each bin, the maximum, minimum, and average speed is

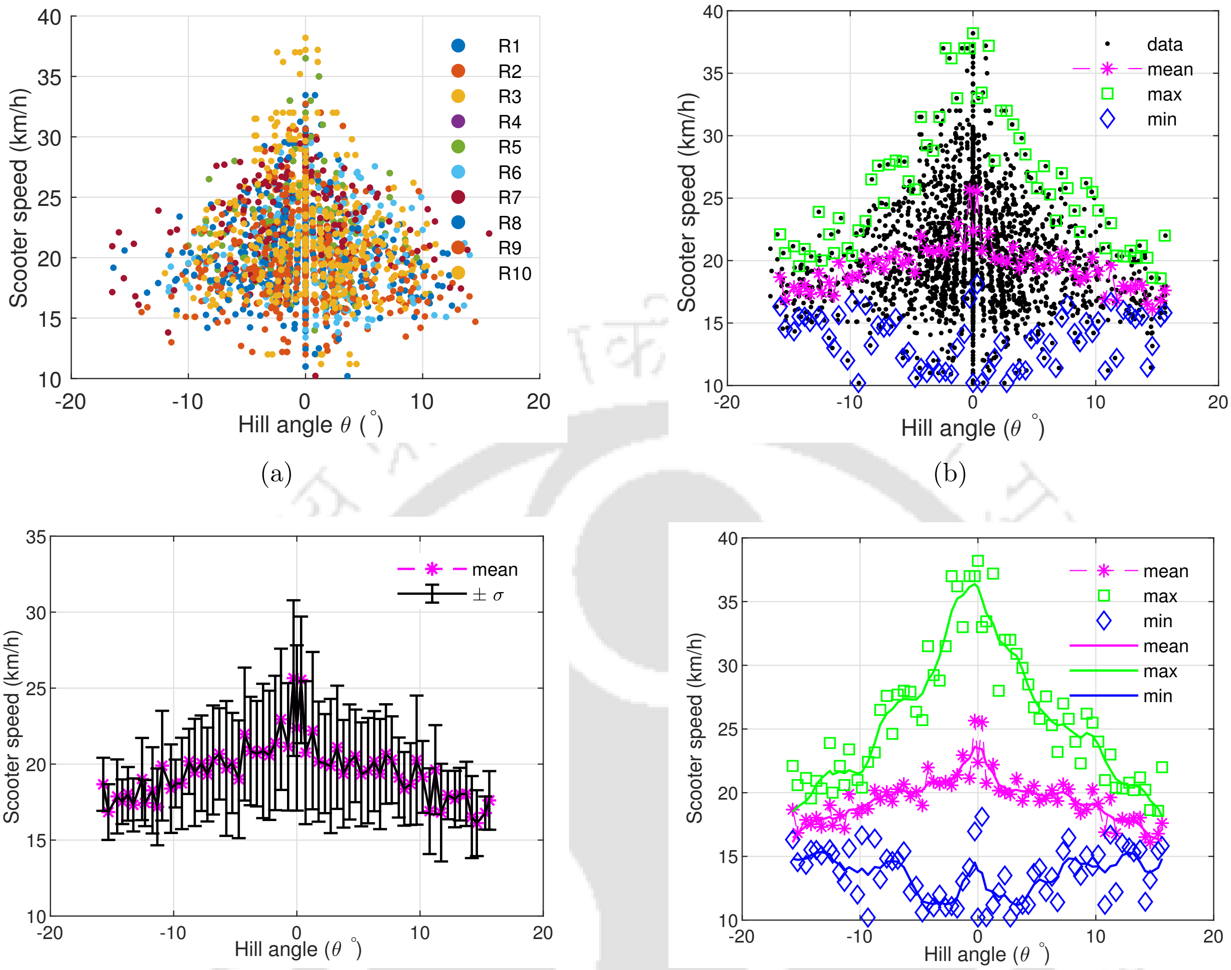

(a)

(b)

(c)

(d)

Figure 2.7: Results after data processing and computation in MATLAB (a) combine data of scooter speed of all the ten routes plotted against the hill angle (b) shows the min, max and mean scooter speed against mean hill angle of each bin (c) standard deviation in the scooter speed from its mean value at each bin (d) the min, max and mean scooter speed against mean hill angle is outlined

calculated. The mean of the θ value of a bin is used to represent the gradient of the road.

Figure 2.7 (a) is the scatter plot of scooter speed vs. hill angle, collected from the ten different routes of Shillong city. It is inferred from the data that scooter speed varies inversely to the hill angle. The scooter speed distribution across the hill angle exhibits a bell-shaped distribution pattern. This pattern of normal distribution is observed in many naturally occurring phenomena. Here, too it is natural that when the hill angle increase, the load seen by the scooter increases and the scooter has to trade off some speed in order to meet the load demand.

Figure 2.7 (b) shows the mean, the minimum, and the maximum value of the speed of each theta bin plotted along with all the scattered data of the sixty-four bins of scooter speed spread across bin mean θ value. This result tells us that in a plain area where the hill angle value is small, the max scooter speed is high, and when the hill angle value is high, the max scooter speed value is low. It is interesting to note that the data shown were collected from an ICE Scooter, yet the maximum speed seen is less than 50 km/h despite its top speed being 80 km/h. That shows the speed trend in hilly regions where riders generally drive slower due to safety reasons and sloppy roads. Next, the standard deviation of speed data from its mean is also found for each bin. Figure 2.7 (c) plots the mean speed and the standard deviation of the scooter speed with respect to the hill angle. Figure 2.7 (d) shows the outlined mean, minimum, and maximum value of the speed against the hill angle value. The scattered data are smoothened using the filter in MATLAB. This data will be used for further road load analysis.

2.4 Road Load Analysis

In this section, the data presented in the previous section, as shown in Figure 2.7, are used to calculate the road load in terms of tractive efforts. The road load, in simple terms, means the resistances that an electric vehicle's electric motor must overcome to keep the vehicle moving forward. Figure 2.8 shows a simplified force diagram of an electric scooter. While climbing up the hill, the road load consists of rolling resistance, friction resistance, aerodynamic resistance, and hill-climbing resistance. Hence, for an electric scooter to make its foothold in a hilly region, it must overcome the resistance while climbing uphill. This resistive force that the electric scooter has to overcome to be in motion is called tractive effort. The source battery should supply power to overcome these tractive resistive forces. The total tractive force for the uphill motion at constant speed is given by (2.3)

$$F_t = F_f + F_a + F_{gh} \tag{2.3}$$

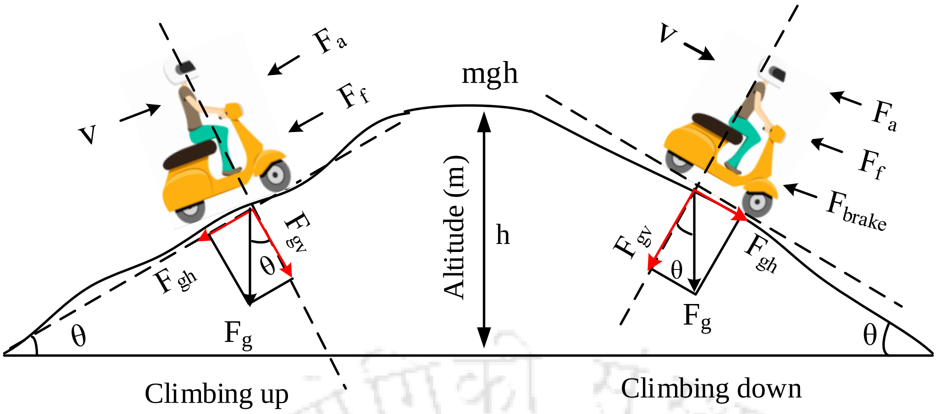

Figure 2.8: Simplified force diagram of an electric scooter on hill.

where F_f is the friction force to overcome the rolling resistance between the tire and the road surface. F_a is the aerodynamic drag force, and F_{gh} is the effort to climb the hill at a constant speed. F_f, F_a and F_{gh} are defined by Equations (1.2),(1.3) and (1.4) respectively in Chapter 1. Here the speed and hill angle data from the previous section is used to find the tractive forces.

The torque at the scooter wheel with radius 'r' is then given by

$$T_{wheel} = F_t r \tag{2.4}$$

The tractive power (P_t) required to overcome the resistive force is then expressed as

$$P_t = F_t v \tag{2.5}$$

when expanded

$$P_t = F_f v + F_a v + F_{gh} v \tag{2.6}$$

$$P_t = P_f + P_a + P_{gh} \tag{2.7}$$

where P_f is the power required to overcome the rolling resistance between the tire and the road surface. p_a is power spent to overcome the aerodynamic drag force, and P_{gh} is power spent to overcome the effort to climb the hill at a constant speed.

Next, using (2.3), (2.4), (2.5), (2.5) and values given in Table 2.3 computation is done

Table 2.3: Road load parameters

Parameters	**Values**
Mass, m	200 kg (110 kg of the scooter and 90 kg of the passenger)
Drag coefficient, C_d	0.7
Air density, ρ	1.25 kg/m^3
Frontal area of vehicle and rider, A	0.6 m^2
Coefficient of rolling friction, μ_{rr}	0.007
Gravitational acc. constant , g	9.8 m/s^2
Radius of the wheel hub motor	0.2 m

on MATLAB programming to find the force and power values. Here, taking speed and hill angle data, the torque and the power associated with each data point are computed.

2.5 Results and Discussions

Figure 2.9 shows the traction power profile of the ICE Honda city scooter using the road parameters given in Table 2.3. From Figure 2.9 (a), it is observed that the mean value of the demand or generated torque decreases as the speed increase, whereas from Figure 2.9 (b), it is observed that the torque demand increase with the rise in hill angle and the generated torque also increases with increase in hill angle with negative slope, i.e., when the vehicle is climbing downhill. The effect of the hill angle on the propulsion power requirement is plotted in Figure 2.9 (c) and Figure 2.9 (d); it can be seen that with the increase in the theta value, the propulsion power also increases. The results show that hilly roads like those in Shillong City are high power-demand drive cycles due to their high torque demand. Figure 2.9 (e) shows the power required to overcome the friction force, air drag force, and gravitational forces by the vehicle for the data points associated with the maximum total power. We can see the P_{gh} is proportional to the θ value. The P_f and P_a remain the same and are independent of the θ value. Hence we can see most of the power is spent to overcome the gravitational force. Vehicles running on plain roads need not overcome the effect of gravitational force.

Results and the findings on the electric scooter's drive-train design based on the road

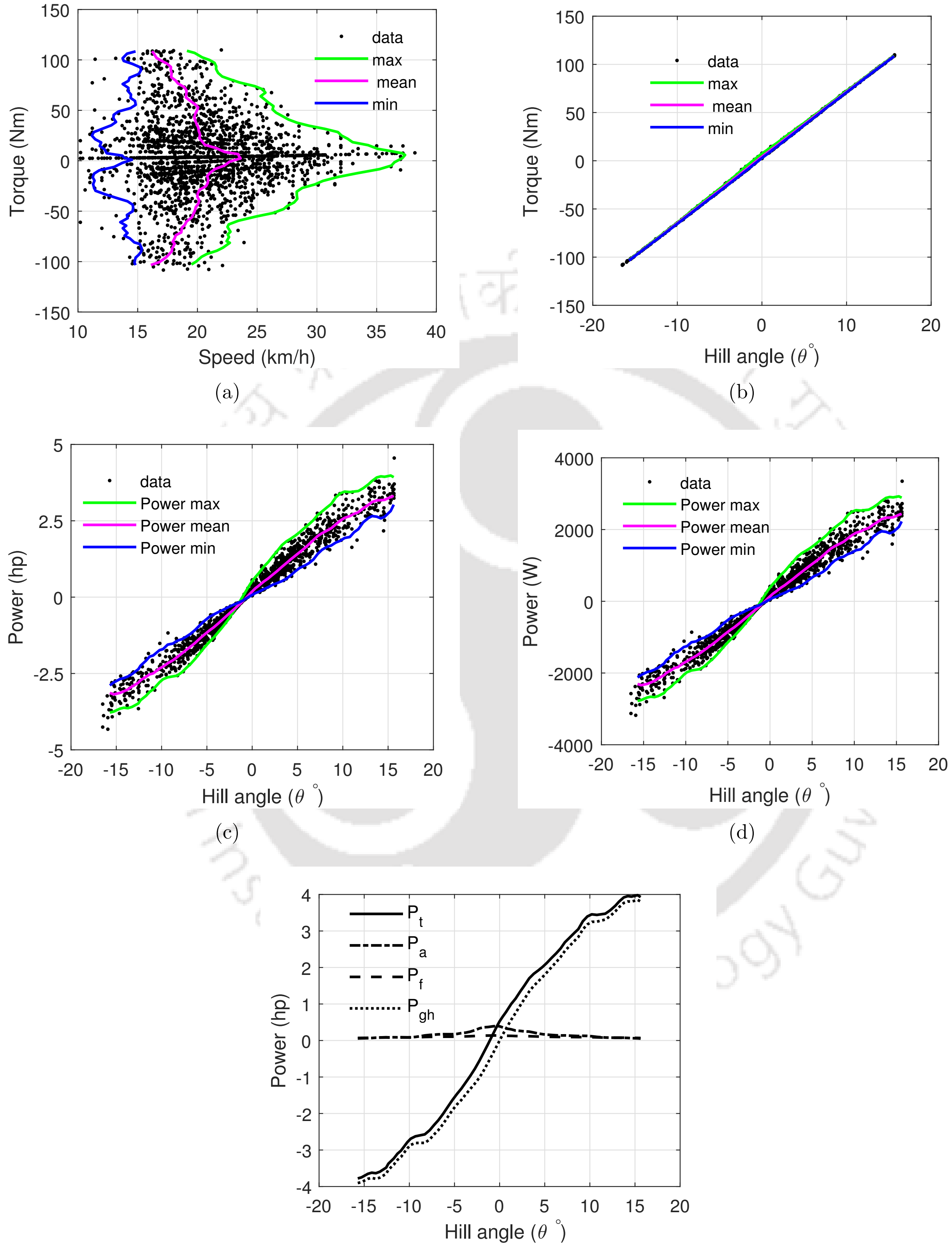

(a)

(b)

(c)

(d)

(e)

Figure 2.9: Plot showing (a) wheel torque variations w.r.t scooter speed (b) wheel torque requirement w.r.t hilly road (c) calculated power w.r.t hill angle in hp (d) calculated power w.r.t hill angle in W (e) various tractive power for the max average speed vs. max average hill angle profile.

load analysis are done from data collected on the ICE Honda Dio scooter, and are presented below:

- The less use of electric scooters in hilly regions is explained by Figure 2.9 (a) and Figure 2.9 (b). This is due to the high torque and current demand for such roads. Further, it is observed that the torque demand increases with the increase in the hill angle value and is proportional to an electric motor's current demand. Hence, it requires a battery with high power and energy capacity. Presently, the electric scooters in the market are typically designed for plain roads.
- Due to the road gradient, the battery has to supply more power and energy to overcome the tractive resistive force on an inclined road compared to a plain road.
- Also, in Figure 2.9 (a), the motor can act as a generator in the negative torque region. This indicates an opportunity to harness the kinetic energy back to the battery source by applying regenerative braking.
- From the power vs. hill angle plot, it can be said that a low-power motor below 1 kW is not suitable for the hilly road with a hill angle greater than 5°. For a hill angle greater than 5° and less than 10°, a medium power rating motor of 2 kW may be needed, whereas for a hill angle greater than 10° will require a 4-5 kW motor for a smooth ride of the electric vehicle.

2.6 Summary

This chapter presents a simple method to derive hill angle (θ) using spatial location information and basic trigonometric formula. The work shows the scooter speed and hill angle relationship from the drive cycle data practically collected from Shillong City in an ICE scooter. Further, from the information on the hill angle, the road load characteristic is studied for synthesizing the power and torque requirement of electric scooters for such hilly roads. The results found that for an electric scooter to be suitable for such a high torque-demanding road, it should have a high-power motor and high current capacity battery banks.

With proper design of the motor core, winding conductor for high current capacity, and using a battery with high power and energy, it is possible to develop scooters that may find much acceptance in the hilly region.

If we only consider the battery power consumption, *i.e.* kWh per hour, the hilly region roads become unfriendly to EVs because it stresses their range. The battery (energy source) that powers the EVs has a lower energy density than gasoline fuel used in ICE vehicles. The range of the EVs further goes down when operating on hilly roads. In the next chapter, we study that with the assistance of a regenerative braking circuit while descending the hill, the potential energy that the electric scooter gains when reaching the hilltop can be recovered back to the battery, which can give some respite to the EV range problem.

3

Regenerative Braking Circuit for Electric Two-Wheelers in Hilly Region

Contents

3.1 Introduction

As briefly discussed in Chapter 1, the roads in the hilly region challenge the EVs in terms of their increased torque capacity while climbing up the hill, requiring more energy and power from the battery. While climbing downhill, the gained potential energy is lost as heat in a conventional drum or disc-type brake device. Thus significantly reducing the range of the EVs. However, with the design of a suitable regenerative braking system, a portion of stored potential energy gained while climbing up can be recouped to charge the battery.

While descending the hill, there is a freewheel motion of the vehicle due to the gravitational acceleration acting on the vehicle. The friction and air drag force tries to oppose the motion of the vehicle, thus reducing the available potential energy for its conversion to electrical energy through the regenerative electric braking system. Due to the freewheel motion, the propulsion motor can start acting like a generator, leading the motor windings to induce a back-emf. This induced back-emf can then be utilised to develop the electromagnetic torque to oppose the machine's external mechanical torque, thus providing the brake force.

The magnitude of the induced voltage in the motor winding is directly proportional to the speed of the EV. While descending on a hilly road often requires the vehicle's speed to be low for safety purposes. Thus, achieving regenerative braking at low speed is the major challenge with the electric braking system in the hilly region, as the voltage generated is very low compared with the conventional regenerative braking system used on the plain road. Therefore, an intermediary circuit with high voltage gain is required to boost the low voltage to the required level to charge the battery.

In Sub-Section 1.3.2 of Chapter 1, a comprehensive literature review on the current and previous state of regenerative braking circuit topologies are given in detail, supported by its simple block diagram representation in Figure 1.16. From the literature review, it was inferred that the designs call for a unique braking circuit based on factors like power handling, vehicle size, and terrain application. Hence, as seen, different regenerative braking circuit topologies are available. These braking circuit topologies were classified into two types, i.e., Type-I and Type-II; Type-I is for those using the same inverter circuit, and Type-II is for those using additional circuits or components.

On hilly roads, the braking time required is longer while descending a hill; for such kind of braking, a high power density and a high energy density energy storage is required. Type-II regenerative braking using solely UCs is ineffective on steep downhills because they eventually hit their maximum voltage and become incapable of receiving any more power, as pointed out by the authors [52]. The Type-I category of braking circuit design has less component count and is economically friendly; however, it is unsuitable for very low-speed braking and may incur more loss [58]. In [58] for low-speed regenerative braking application, Sungchul *et al.* uses an additional electromagnetic retardation circuit with switch-capacitors connected across the motor windings of PMSM to boost the input voltage seen by the battery terminal based on the resonance of the L-C circuit. However, this technique is based on the resonance of the braking circuit for AC motors. This method is less effective for BLDC motors which have trapezoidal waveforms.

Hence, to overcome the abovementioned limitations, this chapter presents a new modular regenerative braking circuit configuration and its control scheme for low-speed and more extended braking period applications, which can work for many types of three-phase motors such as BLDC, PMSM etc. The configuration of the proposed regenerative braking circuit is mentioned in the following sub-section.

3.1.1 The Proposed Regenerative Braking Circuit

The proposed regenerative braking circuit configuration is shown in Figure 3.1. It consists of the classical components; a three-phase diode bridge rectifier and DC/DC boost converter. To the best of our knowledge, the proposed combined configuration has not been used earlier in a regenerative braking scheme.

The main features of the proposed regenerative braking circuit are:

- The unique feature of the topology is that the regenerative circuit remains connected

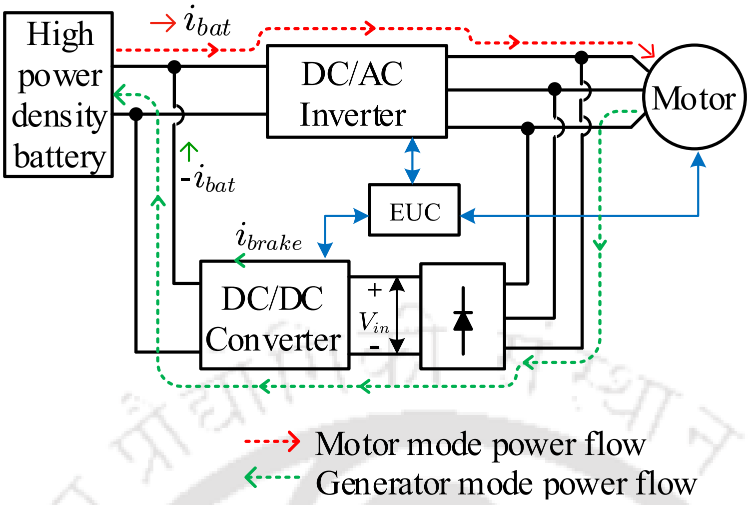

Figure 3.1: Block diagram of the proposed regenerative braking circuit and its configuration.

all the time, and the switching between the motoring and regenerative modes is done by enabling or disabling the gate pulse to the inverter or the boost converter. Thus, the modes could be switched almost instantly.

- As the switch in the inverter needs to supply more power to the BLDC motor, its switching frequency is low compared to the typical switching frequency used in the boost converter. Thus present topology supports high switching frequency with improved voltage gain. This helps in developing an effective regenerative system for hilly terrain.
- Here, no separate energy source is used, thus making the regenerative system more compact and cost-effective.
- Though the system has one additional switch and some passive components, but they operate only at the time of the regenerative braking, thus increasing the durability and the robustness of the system.
- Due to its modular design, it can be integrated into the existing electric scooter, which uses mechanical braking with minor modifications.

The other contributions of the chapter are designing the current controller for the proposed regenerative braking circuit and experimentally implementing it on a motor drive train in a scaled-down laboratory test set-up. This includes the small-signal modeling of the braking circuit using the state-space averaging technique and the design of the Type-II current controller to track the braking current reference using and bode-plot technique. The motoring and regenerative modes are switched by turning the gate pulses on or off to the inverter or DC/DC boost converter, which removes the need for a separate switch in the power circuit, hence increasing reliability and reducing cost. The MATLAB/Simulink computing environment will be used to simulate the operation of the proposed regenerative braking circuit, along with the overall motor drive-train of the vehicle.

The remaining chapter is organised as follows; the system background and its working are explained in Section 3.2, where a short mathematical modeling of the system is presented. Then in Section 3.3, controller design is explained in detail. In Section 3.4, the simulation of the proposed circuit and its control scheme is verified, followed by experimental validation in Section 3.5. Finally, the chapter ends with a conclusion.

3.2 System Background

This chapter considers an electric scooter with a wheel-hub BLDC motor for modeling and study purposes. The proposed system will consist of two power-driveline: the first for the motoring mode, *i.e.*, and the normal forward scooter mode; here, the power flows from the battery-inverter-motor as shown in Figure 3.2 (b). The second one is for the regeneration mode, which is the regenerative braking action mode, and the power flows from the motor-rectifier-converter-battery, as shown in Figure 3.2 (c). The proposed regenerative braking circuit is an add-on circuit to the existing EV motor drive-train. The overall control architecture of the proposed driving system is shown in Figure 3.2 (d). The traction system consists of a control hierarchy; the higher level control on a physical level (human level interface) and the lower level control on an electronic level.

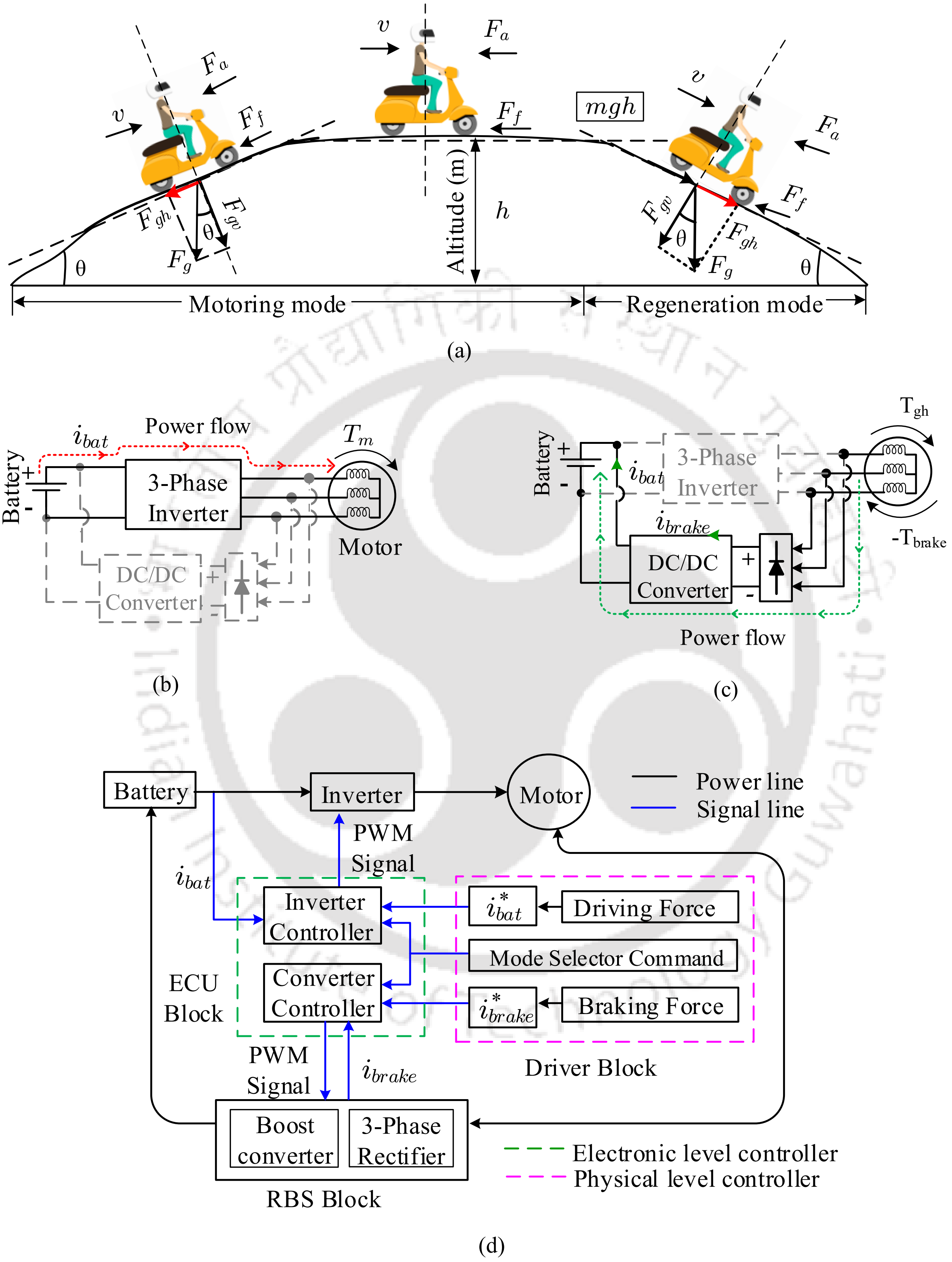

Figure 3.2: Schematic diagram showing (a) tractive forces associated while climbing up and down a hilly road (b) circuit configuration of the motoring mode power-drive train (c) circuit configuration of the generator mode power-drive train (d) single-line diagram of the control architecture showing the control hierarchy.

3.2.1 Working of the Proposed System

The regenerative braking process starts when the rider initiates the braking action by pressing the brake button. The brake device can be either a foot-pressed brake pedal or a thumb-pressed pedal mounted on the accelerator throttle; these devices convert the physical brake force into equivalent electrical quantity [49], [85]. The output voltage of the braking device is then scaled into a braking current reference and sent to the electronic control unit (ECU) block. When the braking command is given, the boost converter controller gets activated, and the inverter controller is deactivated. The close loop feedback is designed to track the braking current (I^*_{brake}) such that the required braking torque (T_{brake}) is produced and the braking force is available on the wheel-hub motor.

For ease of mathematical modeling, the system can be divided into three levels, *i.e.*, the physical level is the outermost layer, the machine level is the second layer, and the innermost layer is the circuit level as shown in Figure 3.3. The time constant of the dynamics associated with all three levels are significantly different and hence, can be separately modeled to describe the working of an electric scooter. Subsequently, the modeling of all the three-level is explained briefly as per the requirement of the work. The modeling process involves approximation to complex chemical level phenomena and also neglecting insignificant circuit or physical phenomena. In the next few sub-sections, a brief explanation of the fundamental principle and modeling of the proposed regenerative braking circuit's various building blocks are presented.

3.2.2 Modeling of Braking Force, Braking Torque and Braking Current

In Sub-Section 1.2 of Chapter 1, the electric scooter's physical level vehicle equations were already derived. Here we start with the machine and circuit level equations. As shown in Figure 3.2 (a) and Figure 3.3 (a), the F_{gh} aids the scooter's motion while climbing downhill. The wheel-hub BLDC motor experiences a mechanical (load) torque due to F_{gh}.

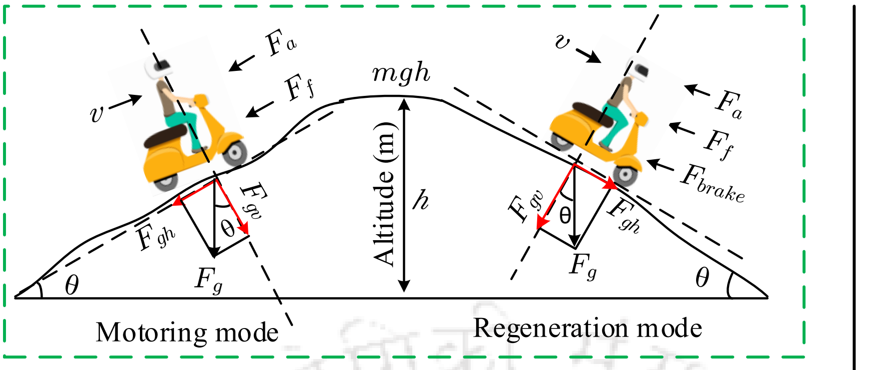

(a) Physical level

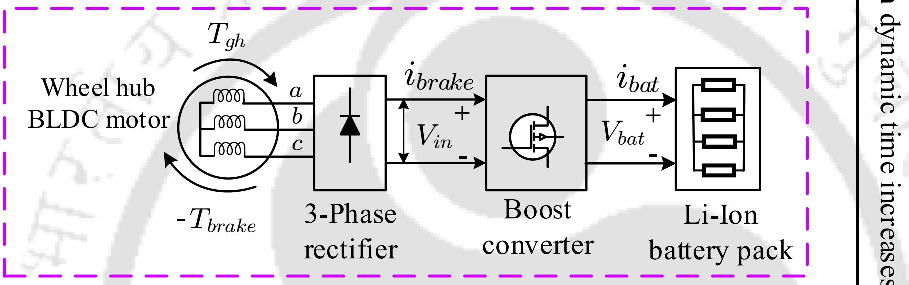

(b) Machine level

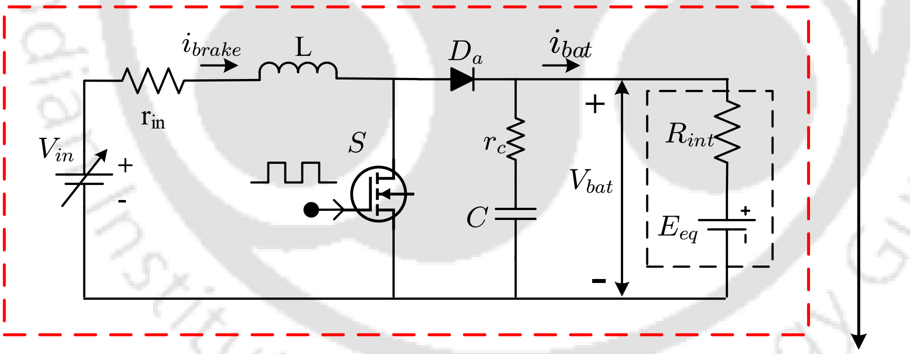

(c) Circuit level

Figure 3.3: System division into three layers based on the reaction time (a) vehicle physical level with time dynamics of approximately 0.3 s (b) machine level with dynamics in milliseconds (c) circuit level with dynamics in microseconds

This mechanical torque which aids in the motion of the motor, is then as

$$T_{gh} = [F_{gh} - (F_f + F_a)]r \tag{3.1}$$

where r is the radius of the wheel-hub motor.

To prevent the scooter from overspeeding, the rider provides the braking force (F_{brake})

by pressing an electric brake pedal, thus reducing the T_{gh} as given in the equation below

$$T_{gh} = [F_{gh} - (F_f + F_a + F_{brake})]r \tag{3.2}$$

The electric brake pedal is a linear Hall effect sensor-based device that converts the input force into electrical quantity in volts. The output voltage of the braking device is then scaled into braking current reference (I^*_{brake}).

$$I^*_{brake} = K_b F_{brake} \tag{3.3}$$

where K_b is the scaling factor .

The braking circuit will draw braking current (I_{brake}), which will develop the electromagnetic torque (T_{brake}) in the motor. T_{brake} is the braking torque developed in the motor, which opposes the external driving torque T_{gh} and is given as,

$$T_{brake} = K_t I_{brake} \tag{3.4}$$

where K_t is torque constant of the motor.

The negative sign of T_{brake} as shown in Figure 3.3 (b) indicates that it is the opposing electromagnetic torque. The magnitude of T_{brake} is proportional to the armature current flowing in the motor winding, and I_{brake} is the rms value of the armature current.

As shown in Figure 3.3 (b), I_{brake} flows from the motor terminal to the rectifier terminal to the converter and then to the source battery. The power drive train of the electric scooter during the regenerative braking mode consists of the BLDC motor, the 3-phase rectifier, the boost converter and the Li-Ion battery as shown in Figure 3.3 (b).

In a wheel-hub motor, the rotor angular speed (ω_m) is the same as the wheel angular speed (ω_w). The angular acceleration due to F_{gh} force is then given as

$$T_{gh} - T_{brake} = J\frac{d\omega_m}{dt} \tag{3.5}$$

where J is the inertia constant. When T_{brake} becomes equal to T_{gh}, the motor speed reaches a constant value, i.e., to its steady state.

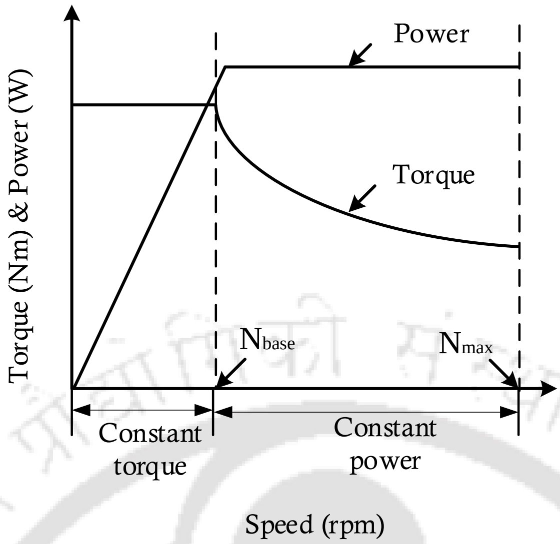

Figure 3.4: Electric motor characteristic in the constant operation of maximum power.

3.2.3 Induced Voltage in Wheel-Hub Motor

The brushless DC (BLDC) motors are the most widely used motors when it come to the application of two-wheelers [86]. These motors consist of a permanent magnet rotar.

Here, it is essential to mention that the battery current rating limits the maximum speed that a motor can go in an electric scooter application. In the constant power region, as shown in Figure 3.4, once the maximum current is hit, maximum torque is reached, further increase in the speed will be at the cost of reduced torque. This is the reason in plain road drive, where the torque requirement is less, the vehicle can run at a higher speed, and while in hilly region roads, the speed is limited due to higher torque requirement [62]. The scooter's speed can range from as low as 10 km/h to a maximum of 50 km/h on hilly roads.

Due to T_{gh}, whilst descending the slope, the wheel hub-motor acts like a 3-phase generator. The rms line-to-line back emf induced in the stator winding of the wheel-hub BLDC motor due to the available free motor rpm is then given as

$$E_{l-l} = \sqrt{3}E_{phase} = \sqrt{6}\pi f \lambda \tag{3.6}$$

where λ is the flux linkages in wb-turns, f is the frequency in Hz of the induced voltage in the machine windings.

The frequency is directly proportional to the motor rpm hence the induced voltage is also directly proportional to the speed of the motor angular speed as

$$E_{l-l} \propto \omega_m \tag{3.7}$$

The stator terminal voltage of the three phase machine is then expressed as

$$V_{l-l} = \underbrace{E_{l-l}}_{\propto \omega_m} - \underbrace{i_{rms} r_s}_{\text{drop in armature}} \tag{3.8}$$

where E_{l-l} is the induced voltage, i_{rms} is the armature current and r_s is the stator resistance.

As shown in Figure 3.3 (b) the stator terminals of the motor are connected to the input of 3-phase diode rectifier bridge (DBR) to convert the AC output voltage from the motor terminal to a DC voltage (V_{in}). Here, V_{in} is the input to the braking circuit. The output voltage of the DBR is derived in [87] and the expression is given below

$$V_{in} = \frac{3\sqrt{2}}{\pi} V_{l-l} \tag{3.9}$$

It is inferred from (3.7), (3.8) and (3.9) that V_{in} seen by the DC/DC boost converter based braking circuit is a varying voltage dependent on the speed of the wheel-hub motor.

3.2.4 Modeling of the Regenerative Braking Circuit

The DC/DC boost converter is the primary energy-transferring circuit of the proposed braking circuit configuration. The mathematical modelling of the braking circuit using the differential equation governing the system will be presented in the sub-section. In the braking circuit, the energy transfer from the input to the load side is regulated by adjusting the turn-on period of the pulse width modulation (PWM) signal provided to the power MOSFET switch (S). As shown in Figures. 3.5 (b) & (c), when S is ON, the braking energy is transferred from the motor line to the inductor by charging it; here, the braking energy is stored in its magnetic field of the inductor (L). When S is OFF, the inductor energy is transferred to the battery, and the inductor is discharged. The energy transfer to the battery over the braking

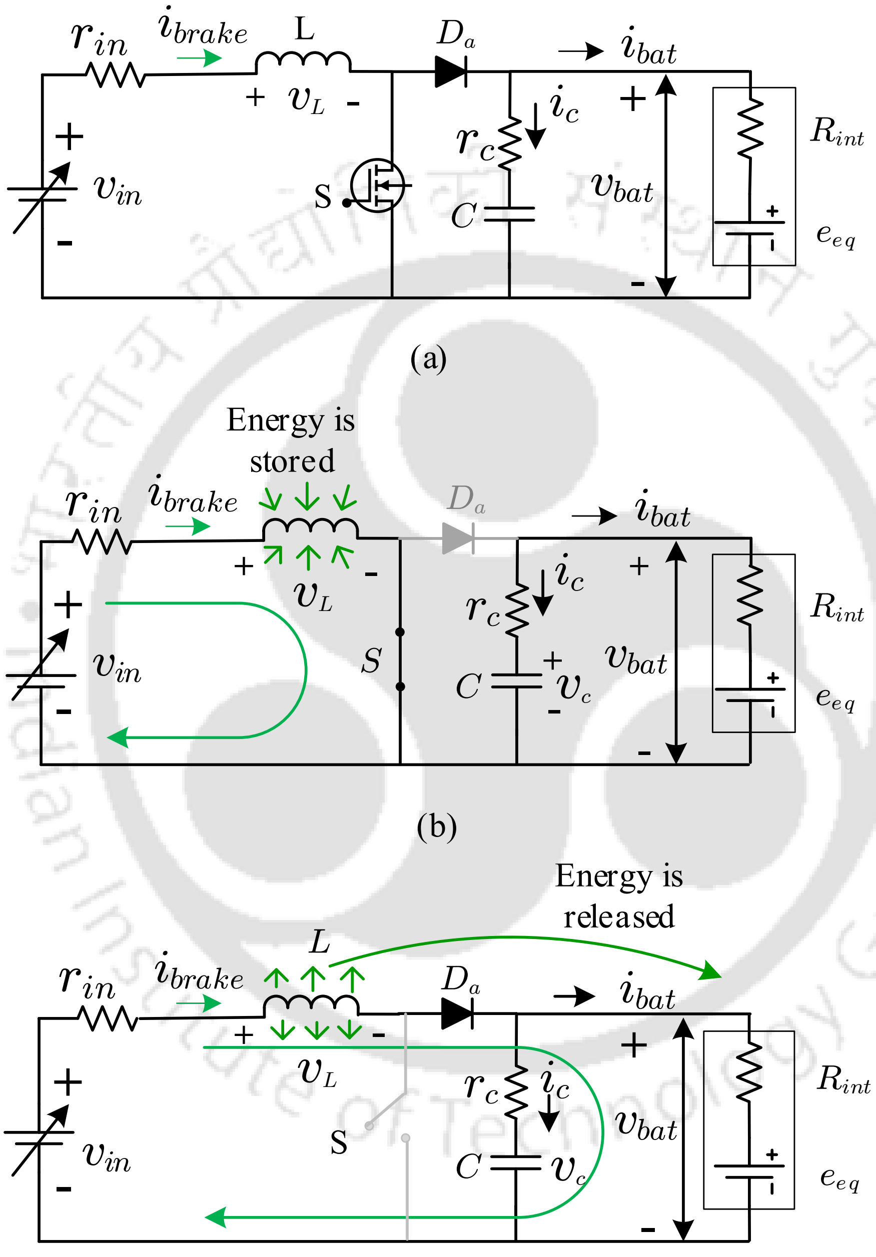

(a)

(b)

(c)

Figure 3.5: Equivalent circuit of (a) DC/DC boost converter (b) switch is ON, (c) switch is OFF.

period (neglecting the internal resistance drop losses in the battery) is expressed as

$$E_{bat} = \int_{t_1}^{t_2} (v_{bat} i_{bat}) dt \tag{3.10}$$

where v_{bat} is the terminal voltage of the battery and i_{bat} is the battery charging current. The steady-state values over one switching period are expressed in the next sub-section.

Assumptions and Exemptions

- The DC/DC boost converter modeling is done considering a DC input voltage v_{in}, which is the rectified output voltage of the three-phase diode bridge rectifier.
- The internal resistances of the input side (3-phase rectifier) is considered as r_{in} in series with the input voltage v_{in}.
- A linear approximation of the converter model is made for the dynamic state modeling. This allows the non-linear behavior of the power converter circuits to be approximated with a linear time-invariant (LTI) model that is valid around an operating point of interest.
- The motor side dynamic modeling is neglected here and can be considered for future advanced modeling.
- Developing a general model for any electrochemical storage device like a battery that accounts for its chemistry and physics characteristics is a complex task. Here, in this chapter, a simple equivalent electric circuit model of a battery is considered, as shown in Figure 3.3 (c) and Figure 3.5 (a). The model consists of a source (E_{eq}) and an internal resistance (R_{int}). The expression for equivalent voltage source and internal resistance are provided in [64].

  The terminal voltage (V_{bat}) of the battery using steady-state model is given as

$$V_{bat} = E_{eq} - R_{int} I_{bat} \tag{3.11}$$

where

$$E_{eq} = (1.965 + 0.12 * SOC).n_c \tag{3.12}$$

$$R_{int} = \frac{n_c}{C_{10}} \left(\frac{4}{1 + |I_{bat}|^{1.3}} + \frac{0.27}{|SOC|^{1.5}} + 0.02 \right) .(1 - 0.007.\Delta T) \tag{3.13}$$

Here, SOC is the state of charge of the battery, C_{10} is the battery capacity in ampere hours, ΔT is the change in the temperature from its nominal value, and n_c is the number of cells.

3.2.4.1 Steady State Equations

The steady-state model of the boost converter is obtained using the Inductor Volt Second Balance and Capacitor Charge Balance. The circuit equation during the ON period, i.e., the switch S is on, using the KVL in loop ① is given as

$$v_L = v_{in} - r_{in} i_{brake} \tag{3.14}$$

$$L \frac{di_{brake}}{dt} = v_{in} - r_{in} i_{brake} \tag{3.15}$$

Applying KCL at node ‘a’ as shown in Figure. 3.5 (b) we have,

$$i_c = -i_{bat} \tag{3.16}$$

$$i_c = -\frac{(v_{bat} - e_{eq})}{R_{int}} \tag{3.17}$$

i.e.

$$v_{bat} = e_{eq} + i_{bat} R_{int} \tag{3.18}$$

During the OFF period, applying KVL in the outer loop as shown in Figure. 3.5 (c), we get,

$$v_L = v_{in} - r_{in} i_{brake} - v_{bat} \tag{3.19}$$

$$L \frac{di_{brake}}{dt} = v_{in} - r_{in} i_{brake} - v_{bat} \tag{3.20}$$

Applying KCL at node ‘a’ as shown in Figure. 3.5 (c) we have,

$$i_c = i_{brake} - i_{bat} \tag{3.21}$$

$$i_c = i_{brake} - \frac{(v_{bat} - e_{eq})}{R_{int}} \tag{3.22}$$

Now, according to Inductor Volt Second Balance (flux balance), at steady state, the integral of applied inductor voltage over one switching period (T_s) is zero.

$$\int_0^{T_s} v_L(t)dt = 0 \tag{3.23}$$

Then applying Inductor Volt Second Balance to (3.14) and (3.19) and using the small siganl approximation of the v_{in}, v_{bat} and i_{brake} signals we get

$$(V_{in} - r_{in}I_{brake})DT_s + (V_{in} - r_{in}I_{brake} - V_{bat})(1-D)T_s = 0 \tag{3.24}$$

where D is the turn-on period of the PWM signal, also commonly known as the duty ratio. The width of D ranges from $(0 < D < 1)$, i.e., for example, 0.4 duty ratio means 40% of the width of the PWM signal is HIGH, and 60% of the PWM width of the signal is LOW. $(1-D)$ gives the turn-off period.

Simplifying (3.24) we get

$$V_{in} - r_{in}I_{brake} = V_{bat}(1-D) \tag{3.25}$$

The steady-state mean voltage of the boost converter with the battery as the load is given by

$$V_{bat} = \frac{V_{in} - I_{brake}r_{in}}{(1-D)} \tag{3.26}$$

Next, applying Capacitor Amp Second Balance (charge balance) along with the small ripple approximation to (3.17) and (3.22), we get

$$\int_0^{T_s} i_c(t)dt = -\frac{(V_{bat} - E_{eq})}{R_{int}}DT_s + I_{brake} - \frac{(V_{bat} - E_{eq})}{R_{int}}(1-D)T_s = 0 \tag{3.27}$$

Capacitor Amp Second Balance (charge balance) states that at steady state, the integral of the capacitor current over one switching period is zero.

Simplifying (3.27) we have

$$(1-D)I_{brake} = \frac{(V_{bat} - E_{eq})}{R_{int}} \tag{3.28}$$

Substituting the value of V_{bat} from (3.26) to (3.28) we have

$$(1-D)I_{brake}R_{int} = \frac{V_{in} - I_{brake}r_{in}}{(1-D)} - E_{eq} \tag{3.29}$$

further simplifying (3.29), we have the steady state braking current given as

$$I_{brake} = \frac{\frac{V_{in}}{(1-D)^2} - \frac{E_{eq}}{(1-D)}}{R_{int} + \frac{r_{in}}{(1-D)^2}} \tag{3.30}$$

Again, applying Capacitor Amp Second Balance (charge balance) to (3.16) and (3.21), we get

$$-DI_{bat} + (1-D)I_{brake} - (1-D)I_{bat} = 0 \tag{3.31}$$

The steady-state battery current is given by

$$I_{bat} = (1-D)I_{brake} \tag{3.32}$$

Substituting i_{brake} in (3.32) we have

$$I_{bat} = \frac{\frac{V_{in}}{(1-D)} - E_{eq}}{R_{int} + \frac{r_{in}}{(1-D)^2}} \tag{3.33}$$

(3.26), (3.30), and (3.33) are the expressions of the steady-state battery terminal voltage, battery braking current, and battery current. The relationship between the braking current and the charging current is expressed by (3.32).

3.2.4.2 Dynamic State Equations

The proposed regenerative braking circuit is designed to provide the braking torque whenever the rider/driver gives the braking force, which is proportional to the braking current. This is accomplished by designing a feedback system that varies the converter's control input (i.e., the duty cycle) such that the braking current of the circuit is regulated to follow the reference braking current. To design the controller of the system, we need the dynamic model of the switching converter. Here in the upcoming section, we first derive a set of equations, also known as an average state-space equation, that describes the complete dynamics of the converter based on the averaging method. Further, a small-signal averaged model is derived by introducing perturbation and linearization to the averaged state-space equation. The linearized state equation is utilized to get the transfer function between the duty cycle and braking current [87–89]. The small-signal model enables us to apply classic control theory to power electronics circuits, which requires an LTI representation such as a transfer function or a state-space system model. In Appendix A, the fundamentals of the state-space equations and Small Signal Perturbation and Linearization of a PWM converter are given in detail.

State Equations of the Braking Circuit

During the ON period, applying KVL in loop ① as shown in Figure. 3.5 (b) the rate of change of the braking current i.e. the inductor current, is derived as

$$\frac{di_{brake}}{dt} = \frac{v_{in}}{L} - \frac{r_{in}}{L} i_{brake} \tag{3.34}$$

Similarly, applying KVL in loop ②, the rate of change in the capacitor voltage is given by

$$\frac{dv_c}{dt} = -\frac{v_c}{C(r_c + R_{int})} + \frac{e_{eq}}{C(r_c + R_{int})} \tag{3.35}$$

The output equation is given by

$$v_o = \frac{R_{int}}{(r_c + R_{int})} v_c + \frac{r_c}{(r_c + R_{int})} e_{eq} \tag{3.36}$$

The Equations (3.34), (3.35) and (3.36) can be written in matrix form as

$$\begin{bmatrix} \frac{di_{brake}}{dt} \\ \frac{dv_c}{dt} \end{bmatrix} = \begin{bmatrix} -\frac{r_{in}}{L} & 0 \\ 0 & -\frac{1}{C(r_c+R_{int})} \end{bmatrix} \begin{bmatrix} i_{brake} \\ v_c \end{bmatrix} + \begin{bmatrix} \frac{1}{L} & 0 \\ 0 & \frac{1}{C(r_c+R_{int})} \end{bmatrix} \begin{bmatrix} v_{in} \\ e_{eq} \end{bmatrix} \tag{3.37}$$

$$\begin{bmatrix} v_o \end{bmatrix} = \begin{bmatrix} 0 & \frac{R_{int}}{r_c+R_{int}} \end{bmatrix} \begin{bmatrix} i_{brake} \\ v_c \end{bmatrix} + \begin{bmatrix} 0 & \frac{r_c}{(r_c+R_{int})} \end{bmatrix} \begin{bmatrix} v_{in} \\ e_{eq} \end{bmatrix} \tag{3.38}$$

The state-space equations when the switch S is ON is given as

$$\dot{\boldsymbol{x}} = \mathbf{A}_{on}\boldsymbol{x} + \mathbf{B}_{on}\boldsymbol{u} \ , \quad \boldsymbol{y} = \mathbf{C}_{on}\boldsymbol{x} + \mathbf{D}_{on}\boldsymbol{u} \tag{3.39}$$

where

$$\mathbf{A}_{on} = \begin{bmatrix} -\frac{r_{in}}{L} & 0 \\ 0 & -\frac{1}{C(r_c+R_{int})} \end{bmatrix}, \quad \mathbf{B}_{on} = \begin{bmatrix} \frac{1}{L} & 0 \\ 0 & \frac{1}{C(r_c+R_{int})} \end{bmatrix} \tag{3.40}$$

$$\mathbf{C}_{on} = \begin{bmatrix} 0 & \frac{R_{int}}{r_c+R_{int}} \end{bmatrix}, \quad \mathbf{D}_{on} = \begin{bmatrix} 0 & \frac{r_c}{(r_c+R_{int})} \end{bmatrix} \tag{3.41}$$

Similarly, the dynamic equations for inductor current and capacitor voltage when the switch S is OFF are shown in Figure. 3.5 (c) and the corresponding equations are given as

$$\frac{di_{brake}}{dt} = \frac{v_{in}}{L} - \frac{\left(r_{in} + \frac{r_c R_{int}}{(r_c+R_{int})}\right)}{L} i_{brake} - \frac{\frac{R_{int}}{(r_c+R_{int})}}{L} v_c - \frac{\frac{r_c}{(r_c+R_{int})}}{L} e_{eq} \tag{3.42}$$

$$\frac{dv_c}{dt} = \frac{\frac{R_{int}}{(r_c+R_{int})}}{C} i_{brake} - \frac{\frac{1}{(r_c+R_{int})}}{C} v_c + \frac{\frac{1}{(r_c+R_{int})}}{C} e_{eq} \tag{3.43}$$

The output voltage is given by

$$v_o = \frac{r_c R_{int}}{(r_c + R_{int})} i_{brake} + \frac{R_{int}}{(r_c + R_{int})} v_c + \frac{r_c}{(r_c + R_{int})} e_{eq} \tag{3.44}$$

Equations (3.42), (3.43) and (3.44) in matrix form we have

$$\begin{bmatrix} \frac{di_{brake}}{dt} \\ \frac{dv_c}{dt} \end{bmatrix} = \begin{bmatrix} -\frac{\left(r_{in}+\frac{r_c R_{int}}{(r_c+R_{int})}\right)}{L} & -\frac{R_{int}}{L(r_c+R_{int})} \\ \frac{R_{int}}{C(r_c+R_{int})} & -\frac{1}{C(r_c+R_{int})} \end{bmatrix} \begin{bmatrix} i_{brake} \\ v_c \end{bmatrix} + \begin{bmatrix} \frac{1}{L} & -\frac{r_c}{L(r_c+R_{int})} \\ 0 & \frac{1}{C(r_c+R_{int})} \end{bmatrix} \begin{bmatrix} v_{in} \\ e_{eq} \end{bmatrix} \tag{3.45}$$

$$\begin{bmatrix} v_o \end{bmatrix} = \begin{bmatrix} \frac{r_c R_{int}}{(r_c+R_{int})} & \frac{R_{int}}{(r_c+R_{int})} \end{bmatrix} \begin{bmatrix} i_{brake} \\ v_c \end{bmatrix} + \begin{bmatrix} 0 & \frac{r_c}{(r_c+R_{int})} \end{bmatrix} \begin{bmatrix} v_{in} \\ e_{eq} \end{bmatrix} \tag{3.46}$$

The state-space equations when the switch S is OFF are given as

$$\dot{\boldsymbol{x}} = \mathbf{A}_{off}\boldsymbol{x} + \mathbf{B}_{off}\boldsymbol{u}\ , \quad \boldsymbol{y} = \mathbf{C}_{off}\boldsymbol{x} + \mathbf{D}_{off}\boldsymbol{u} \tag{3.47}$$

where

$$\mathbf{A}_{off} = \begin{bmatrix} -\frac{\left(r_{in}+\frac{r_c R_{int}}{(r_c+R_{int})}\right)}{L} & -\frac{R_{int}}{L(r_c+R_{int})} \\ \frac{R_{int}}{C(r_c+R_{int})} & -\frac{1}{C(r_c+R_{int})} \end{bmatrix}, \qquad \mathbf{B}_{off} = \begin{bmatrix} \frac{1}{L} & -\frac{r_c}{L(r_c+R_{int})} \\ 0 & \frac{1}{C(r_c+R_{int})} \end{bmatrix} \tag{3.48}$$

$$\mathbf{C}_{off} = \begin{bmatrix} \frac{r_c R_{int}}{(r_c+R_{int})} & \frac{R_{int}}{(r_c+R_{int})} \end{bmatrix}, \qquad \mathbf{D}_{off} = \begin{bmatrix} 0 & \frac{r_c}{(r_c+R_{int})} \end{bmatrix} \tag{3.49}$$

Now, by taking the average over one switching period to get the average state-space equations.

Average State-Space Equation

Now, the averaged state-space equation is written as

$$\frac{d\mathbf{x}}{dt} = \mathbf{Ax} + \mathbf{Bu} \quad \mathbf{y} = \mathbf{Cx} + \mathbf{Du} \tag{3.50}$$

where the average state-space matrices are calculated using the value of $\mathbf{A}_{on}$, $\mathbf{B}_{on}$, $\mathbf{C}_{on}$, $\mathbf{D}_{on}$, $\mathbf{A}_{off}$, $\mathbf{B}_{off}$, $\mathbf{C}_{off}$ and $\mathbf{D}_{off}$ from Equations (3.40), (3.41), (3.48) and (3.49), then, inserting it into (A.2), are given by

$$\mathbf{A} = \begin{bmatrix} -\frac{1}{L}\left(r_{in} + \frac{r_c R_{int}(1-d)}{(r_c+R_{int})}\right) & -\frac{1}{L}\frac{R_{int}(1-d)}{(r_c+R_{int})} \\ \frac{R_{int}(1-d)}{C(r_c+R_{int})} & -\frac{1}{C(r_c+R_{int})} \end{bmatrix}, \qquad \mathbf{B} = \begin{bmatrix} \frac{1}{L} & -\frac{r_c(1-d)}{L(r_c+R_{int})} \\ 0 & \frac{1}{C(r_c+R_{int})} \end{bmatrix}$$

$$\mathbf{C} = \begin{bmatrix} \frac{r_c R_{int}(1-d)}{(r_c+R_{int})} & \frac{R_{int}}{(r_c+R_{int})} \end{bmatrix}, \qquad \mathbf{D} = \begin{bmatrix} 0 & \frac{r_c}{(r_c+R_{int})} \end{bmatrix}$$

The dynamic equations governing the braking circuit can then be given by

$$\begin{bmatrix} \frac{d\left\langle i_{brake}\right\rangle}{dt} \\ \frac{d\left\langle v_c\right\rangle}{dt} \end{bmatrix} = \begin{bmatrix} -\frac{1}{L}\left(r_{in} + \frac{r_c R_{int}(1-d)}{(r_c+R_{int})}\right) & -\frac{1}{L}\frac{R_{int}(1-d)}{(r_c+R_{int})} \\ \frac{R_{int}(1-d)}{C(r_c+R_{int})} & -\frac{1}{C(r_c+R_{int})} \end{bmatrix} \begin{bmatrix} \left\langle i_{brake}\right\rangle \\ \left\langle v_c\right\rangle \end{bmatrix} + \begin{bmatrix} \frac{1}{L} & -\frac{r_c(1-d)}{L(r_c+R_{int})} \\ 0 & \frac{1}{C(r_c+R_{int})} \end{bmatrix} \begin{bmatrix} \left\langle v_{in}\right\rangle \\ \left\langle e_{eq}\right\rangle \end{bmatrix} \tag{3.51}$$

$$\begin{bmatrix} \left\langle v_o\right\rangle \end{bmatrix} = \begin{bmatrix} \frac{r_c R_{int}(1-d)}{(r_c+R_{int})} & \frac{R_{int}}{(r_c+R_{int})} \end{bmatrix} \begin{bmatrix} \left\langle i_{brake}\right\rangle \\ \left\langle v_c\right\rangle \end{bmatrix} + \begin{bmatrix} 0 & \frac{r_c}{(r_c+R_{int})} \end{bmatrix} \begin{bmatrix} \left\langle v_{in}\right\rangle \\ \left\langle e_{eq}\right\rangle \end{bmatrix} \tag{3.52}$$

3.2.4.3 Perturbation and Linearisation

The linearization of the dynamic model as given in equations (3.51) and (3.52) is done using the perturbation of states and input variables such as $\left\langle i_{brake}\right\rangle = I_{brake} + \hat{i}_{brake}$, $\left\langle d\right\rangle = D + \hat{d}$ etc. For details, refer to A.2 of Appendix A. We get the linearised model as given below

$$\begin{bmatrix} \frac{d\hat{i}_{brake}}{dt} \\ \frac{d\hat{v}_c}{dt} \end{bmatrix} = \begin{bmatrix} -\frac{1}{L}\left(rR_{in} + \frac{r_c R_{int}(1-D)}{(r_c+R_{int})}\right) & -\frac{1}{L}\frac{R_{int}(1-D)}{(r_c+R_{int})} \\ \frac{R_{int}(1-D)}{C(r_c+R_{int})} & -\frac{1}{C(r_c+R_{int})} \end{bmatrix} \begin{bmatrix} \hat{i}_{brake} \\ \hat{v}_c \end{bmatrix} + \begin{bmatrix} \frac{1}{L} & -\frac{r_c(1-D)}{L(r_c+R_{int})} \\ 0 & \frac{1}{C(r_c+R_{int})} \end{bmatrix} \begin{bmatrix} \hat{v}_{in} \\ \hat{e}_{eq} \end{bmatrix} + \begin{bmatrix} \frac{r_c R_{int}}{L(r_c+R_{int})} I_{brake} + \frac{R_{int}}{L(r_c+R_{int})} V_c + \frac{r_c}{L(r_c+R_{int})} E_{eq} \\ -\frac{R_{int}}{C(r_c+R_{int})} I_{brake} \end{bmatrix} \begin{bmatrix} \hat{d} \end{bmatrix} \tag{3.53}$$

$$\begin{bmatrix} \hat{v}_o \end{bmatrix} = \begin{bmatrix} \frac{r_c R_{int}(1-D)}{(r_c+R_{int})} & \frac{R_{int}}{(r_c+R_{int})} \end{bmatrix} \begin{bmatrix} \hat{i}_{brake} \\ \hat{v}_c \end{bmatrix} + \begin{bmatrix} 0 & \frac{r_c}{(r_c+R_{int})} \end{bmatrix} \begin{bmatrix} \hat{v}_{in} \\ \hat{e}_{eq} \end{bmatrix} + \begin{bmatrix} -\frac{r_c R_{int}}{(r_c+R_{int})} I_{brake} \end{bmatrix} \begin{bmatrix} \hat{d} \end{bmatrix} \tag{3.54}$$

Rearranging the placing of the duty cycle variable $\hat{d}$ in (3.53) and (3.54) such that it can be included in the input matrix **U** of the above expression is rewritten as

$$\begin{bmatrix}\frac{d\hat{i}_{brake}}{dt}\\[2mm] \frac{d\hat{v}_c}{dt}\end{bmatrix} = \begin{bmatrix} -\frac{1}{L}\left(r_{in}+\frac{r_cR_{int}(1-D)}{(r_c+R_{int})}\right) & -\frac{1}{L}\frac{R_{int}(1-D)}{(r_c+R_{int})}\\ \frac{R_{int}(1-D)}{C(r_c+R_{int})} & -\frac{1}{C(r_c+R_{int})}\end{bmatrix}\begin{bmatrix}\hat{i}_{brake}\\ \hat{v}_c\end{bmatrix}+$$

$$\begin{bmatrix}\frac{1}{L} & -\frac{r_c(1-D)}{L(r_c+R_{int})} & \frac{r_cR_{int}}{L(r_c+R_{int})}I_{brake}+\frac{R_{int}}{L(r_c+R_{int})}V_c+\frac{r_c}{L(r_c+R_{int})}E_{eq}\\ 0 & \frac{1}{C(r_c+R_{int})} & -\frac{R_{int}}{C(r_c+R_{int})}I_{brake}\end{bmatrix}\begin{bmatrix}\hat{v}_{in}\\ \hat{e}_{eq}\\ \hat{d}\end{bmatrix} \tag{3.55}$$

$$\begin{bmatrix}\hat{v}_o\end{bmatrix} = \begin{bmatrix}\frac{r_cR_{int}(1-D)}{(r_c+R_{int})} & \frac{R_{int}}{(r_c+R_{int})}\end{bmatrix}\begin{bmatrix}\hat{i}_{brake}\\ \hat{v}_c\end{bmatrix}+\begin{bmatrix}0 & \frac{r_c}{(r_c+R_{int})} & -\frac{r_cR_{int}}{(r_c+R_{int})}I_{brake}\end{bmatrix}\begin{bmatrix}\hat{v}_{in}\\ \hat{e}_{eq}\\ \hat{d}\end{bmatrix} \tag{3.56}$$

where using (A.6) steady-state value of I_{brake} and V_c is calculated and expressed as

$$I_{brake} = \frac{\frac{V_{in}}{(1-D)^2}-\frac{E_{eq}}{(1-D)}}{R_{int}\left(\frac{r_c}{(r_c+R_{int})(1-D)}+\frac{R_{int}}{r_c+R_{int}}\right)+\frac{r_{in}}{(1-D)^2}} \tag{3.57}$$

$$V_c = \frac{R_{int}(1-D)V_{in}+\left(r_{in}+\frac{r_cR_{int}(1-D)}{(r_c+R_{int})}-\frac{r_cR_{int}(1-D)^2}{(r_c+R_{int})}\right)E_{eq}}{R_{int}\left(\frac{r_c}{(r_c+R_{int})(1-D)}+\frac{R_{int}}{(r_c+R_{int})}\right)+\frac{r_{in}}{(1-D)^2}} \tag{3.58}$$

3.2.4.4 Small-Signal Open-Loop Transfer Function

Next, from the newly derived average state-space equation, the open loop transfer function of the plant can be found using (A.10), (A.11), (A.12), and (A.13) derived in Appendix A. For our interest, the small-signal open-loop functions between the output variables and input variables are derived using (A.13) and rewritten here as

$$\hat{\mathbf{y}}(s) = [\mathbf{C}(s\mathbf{I}-\mathbf{A})^{-1}\mathbf{B}+\mathbf{D}]\hat{\mathbf{u}}(s)$$

which is expressed as

$$\begin{bmatrix}\hat{i}_{brake}\\ \hat{v}_c\end{bmatrix} = \begin{bmatrix}1 & 0\\ \frac{r_cR_{int}(1-D)}{(r_c+R_{int})} & \frac{R_{int}}{(r_c+R_{int})}\end{bmatrix}\begin{bmatrix}s+\frac{1}{L}\left(r_{in}+\frac{r_cR_{int}(1-D)}{(r_c+R_{int})}\right) & \frac{1}{L}\frac{R_{int}(1-D)}{(r_c+R_{int})}\\ -\frac{R_{int}(1-D)}{C(r_c+R_{int})} & s+\frac{1}{C(r_c+R_{int})}\end{bmatrix}^{-1}$$
$$\begin{bmatrix}\frac{1}{L} & -\frac{r_c(1-D)}{L(r_c+R_{int})} & \frac{r_cR_{int}}{L(r_c+R_{int})}I_{brake}+\frac{R_{int}}{L(r_c+R_{int})}V_c+\frac{r_c}{L(r_c+R_{int})}E_{eq}\\ 0 & \frac{1}{C(r_c+R_{int})} & -\frac{R_{int}}{C(r_c+R_{int})}I_{brake}\end{bmatrix}\begin{bmatrix}\hat{v}_{in}\\ \hat{e}_{eq}\\ \hat{d}\end{bmatrix}+ \tag{3.59}$$
$$\begin{bmatrix}0 & 0 & 0\\ 0 & \frac{r_c}{(r_c+R_{int})} & -\frac{r_cR_{int}}{(r_c+R_{int})}I_{brake}\end{bmatrix}\begin{bmatrix}\hat{v}_{in}\\ \hat{e}_{eq}\\ \hat{d}\end{bmatrix}$$

Duty cycles to braking current transfer functions:

The duty cycle to braking current transfer function $G_{id}(s)$ is found by solving (3.59) and setting the input voltage and battery voltage variations to zero *i.e.* $\hat{v}_{in} = \hat{e}_{eq} = 0$.

$$G_{id}(s) = \frac{\hat{i}_{brake}}{\hat{d}} = \frac{(r_c+R_{int})(sn_1+n_0)}{(R_{int}^2(1-D)^2+r_cR_{int}(1-D)+r_{in}R_{int}+r_cr_{in})(s^2m_2+sm_1+m_0)} \tag{3.60}$$

where

$$n_1 = CE_{eq}r_c^2r_{in}+CE_{eq}r_{in}R_{int}^2+Cr_cR_{int}^2V_{in}+Cr_c^2r_{in}V_{in}+CR_{int}^2V_{in}(1-D) \\ +2CE_{eq}r_cr_{in}R_{int}+Cr_cR_{int}V_{in}(1-D)$$

$$n_0 = E_{eq}r_cr_{in} - E_{eq}R_{int}^2(1-D)^2 + E_{eq}r_{in}R_{int} + r_cR_{int}V_{in} + 2R_{int}^2V_{in}(1-D)$$

$$m_2 = CLr_c^2+CLR_{int}^2+2CLr_cR_{int}$$

$$m_1 = Cr_{in}r_c^2+Cr_cR_{int}^2(1-D)+Cr_c^2R_{int}(1-D)+2Cr_{in}r_cR_{int}+Lr_c+Cr_{in}R_{int}^2+LR_{int}$$

$$m_0 = R_{int}^2(1-D)^2+r_cR_{int}(1-D)+r_{in}R_{int}+r_cr_{in}$$

The $G_{id}(s)$ is also called an open-loop plant transfer function. This transfer function describes how variations in the control input $\hat{d}(s)$ lead to a change in the braking current $\hat{i}_{brake}(s)$. A MATLAB program was used to derive (3.60) from the state-space equation (3.59).

3.3 Controller Design

As briefly explained earlier in Sub-Section 3.2.1, the traction system consists of a control hierarchy: the higher level control on a physical level (human level interface) and the lower level control on an electronic level. The overall control architecture of the proposed driving system is shown in Figure 3.2 (d). Hence, the system control design includes

- The switching between motoring and regeneration mode
- Controller design to track the braking current reference

The regenerative braking process starts when the rider initiates the braking action by pressing the brake button. The brake device can be either a foot-pressed brake pedal or a

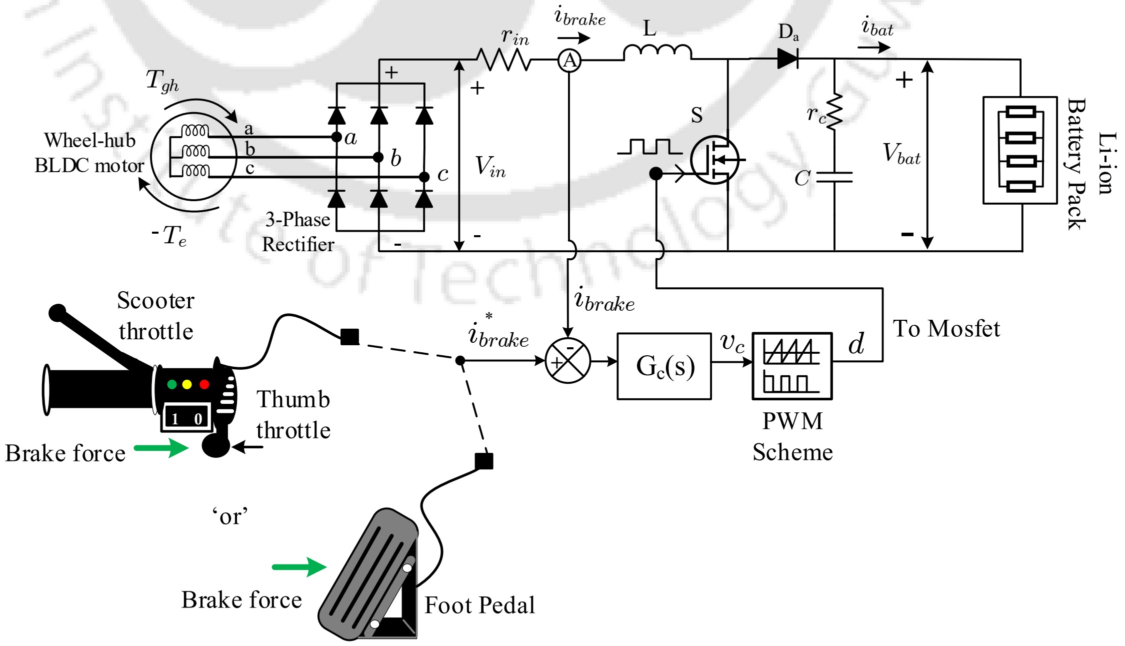

Figure 3.6: Representative block diagram of the braking circuit configuration with a feedback loop.

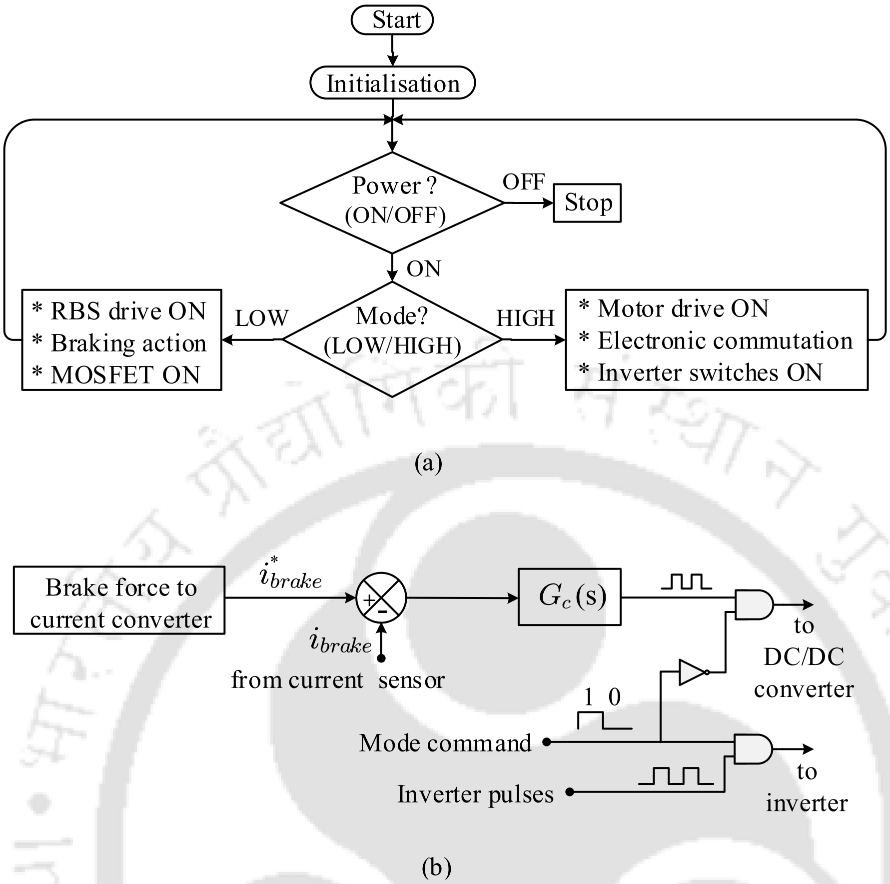

Figure 3.7: Algorithm design to switch between the two modes (a) flow chart (b) its implementation with logic gates.

thumb-pressed pedal mounted on the accelerator throttle; these devices convert the physical brake force into equivalent electrical quantity, as shown in Figure 3.6. The output voltage of the braking device is then scaled into a braking current reference and sent to the controller block. When the braking command is given, the converter controller gets activated.

3.3.1 Switching Between Two Modes

The motor drive controller and the regenerative braking circuit controller are designed to be complementary, meaning only one mode will be active at any given moment; the algorithm is outlined in Figure 3.7 (a). This control is done on the physical level, i.e. with human involvement. The rider initiates the braking action by pressing the brake pedal or pressing a switch button mounted on the accelerator throttle. Once the rider gives the signal, the regenerative braking mode action begins. For the simulation and hardware experiment

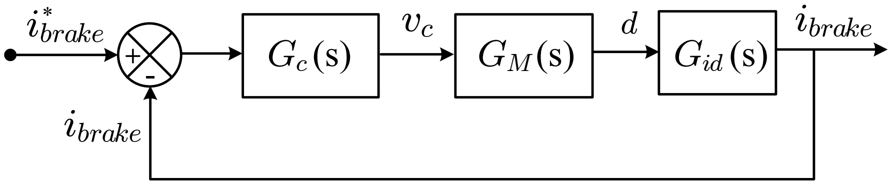

Figure 3.8: Functional block diagram of a unity feedback system.

purposes, the proposed algorithm is implemented by the logic gate and is shown in Figure 3.7 (b), which enables or disables the gate pulse to switch between the modes.

3.3.2 Closed-Loop Current Control of the Braking Circuit

The design of any closed-loop system is based on the techniques that use the feedback property. The feedback is a property of the system that allows the controlled output and input commands to be compared. If there is a difference, an error signal appears, bringing the two into correspondence. For the proposed braking circuit, a unity feedback loop is designed to regulate the braking current of the braking circuit, *i.e.* to track the barking current (I^*_{brake}) such that the required braking torque (T_{brake}) is available on the wheel-hub motor.

Figure 3.8 shows the functional block diagram of the feedback system shown in Figure 3.6, where G_C denotes the controller transfer function, G_M denotes the PWM transfer function and G_{id} denotes current-control plant transfer function. From Figure 3.8, the control problem can be described as:

"*For a given command variable i.e.* i^*_{brake}, *finding an appropriate input i.e.* d, *so that the controlled variable i.e.* i_{brake} *follows the command* i^*_{brake}."

Here, the Type-II compensator is chosen as the controller G_C. In control theory, the compensators are pole-zero combinations that alter the gain and phase characteristic of an open-loop frequency response of a system.

3.3.2.1 Type-II Compensator

The Type-II compensator is a lead-type compensator which consists of a pole at the origin and a pole-zero pair. It is also called an integral-single-lead compensator. The pole at the origin acts as an integral part, and the pole-zero pair acts as the lead part of the controller. However, the integral part of the Type-II compensator provides high gain at low frequency and thus reduces the dc error. The integral part introduces $-90°$ phase lag and therefore reduces the stability. The phase lag is compensated and reduced by the lead part of the Type-II compensator, leading to wider bandwidth and faster response. The maximum phase boost of the Type-II compensator is $90°$. The transfer function of G_C and G_M is given by

$$G_C(s) = \frac{k_c(1+\frac{s}{\omega_z})}{s(1+\frac{s}{\omega_p})} \quad \& \quad G_M = \frac{1}{V_M} \tag{3.61}$$

where k_c, ω_z, ω_p are the controller gain, controller zero, and controller pole, respectively, and V_M is the peak voltage of ramp signal.

The amplitude of the compensator transfer function at a given frequency ω is given by

$$|G_C(j\omega)| = \frac{k_c}{\omega}\sqrt{\frac{1+\left(\frac{\omega}{\omega_z}\right)^2}{1+\left(\frac{\omega}{\omega_p}\right)^2}} \tag{3.62}$$

The phase at a given frequency ω is given by

$$\angle G_c = -\frac{\pi}{2} + tan^{-1}\left(\frac{\omega}{\omega_z}\right) - tan^{-1}\left(\frac{\omega}{\omega_p}\right) \tag{3.63}$$

The asymptotic bode plot of Type-II compensator is shown in the Figure 3.9. If the pole and zero coincide with each other. In the zero slope region, the phase boost (ϕ_B) tends towards $90°$. The phase boost increases when the pole and zero are separated. Thus, by varying the pole-zero location, the phase boost varies from $0°$ to $90°$.

The frequency at which maximum phase boost occur can be found by derivating (3.63)

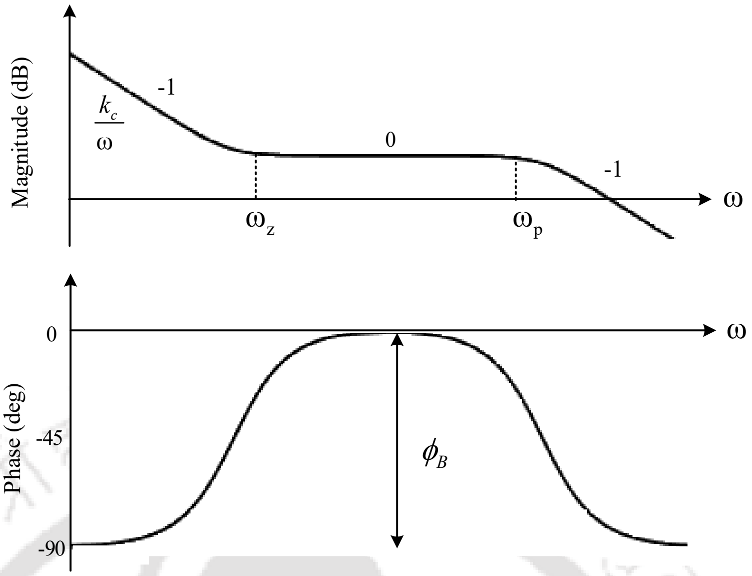

Figure 3.9: Type-II compensator asymptotic bode plot.

$$\frac{d}{dt}\left(-\frac{\pi}{2}+tan^{-1}\left(\frac{\omega}{\omega_z}\right)-tan^{-1}\left(\frac{\omega}{\omega_p}\right)\right)=0 \tag{3.64}$$

Solving (3.64), the frequency at which maximum phase boost occur is given by

$$\omega_m=\sqrt{\omega_z\omega_p} \tag{3.65}$$

The maximum phase boost occurs at geometric mean of pole-zero frequencies [90, 91]. Therefore, this geometric mean frequency ω_m is considered to be the crossover frequency ω_c in the design of compensator.

Inserting (3.65) value in ω of (3.62), and after simplification the compensator gain can be given as:

$$|G_C|=\frac{k_c}{\omega_z} \tag{3.66}$$

3.3.2.2 Design of Compensator Pole and Zero

The pole and the zero of the compensator is located such that it can provide the maximum phase boost.

The maximum phase shift is calculated as

$$\angle G_c|_{\omega_c} = -\frac{\pi}{2} + tan^{-1}\left(\frac{\omega_c}{\omega_z}\right) - tan^{-1}\left(\frac{\omega_c}{\omega_p}\right) \tag{3.67}$$

The maximum phase reduction is called as phase boost and is given by

$$\phi_B = \angle G_c|_{\omega_c} - \left(-\frac{\pi}{2}\right) = tan^{-1}\left(\frac{\omega_c}{\omega_z}\right) - tan^{-1}\left(\frac{\omega_c}{\omega_p}\right) \tag{3.68}$$

Using trigonometry

$$tan^{-1}\left(\frac{\omega_c}{\omega_z}\right) + tan^{-1}\left(\frac{\omega_c}{\omega_p}\right) = \frac{\pi}{2} \tag{3.69}$$

$$tan^{-1}\left(\frac{\omega_c}{\omega_p}\right) = \frac{\pi}{2} - tan^{-1}\left(\frac{\omega_c}{\omega_z}\right) \tag{3.70}$$

in (3.68), the phase boost ϕ_B is written as

$$\phi_B = 2tan^{-1}\left(\frac{\omega_c}{\omega_z}\right) - \frac{\pi}{2} \tag{3.71}$$

which gives

$$\frac{\omega_c}{\omega_z} = tan\left(\frac{\phi_B}{2} + \frac{\pi}{4}\right) \tag{3.72}$$

Using (3.72) and (3.65) the location of compensator zero and pole is found to be

$$\omega_z = \frac{\omega_c}{tan\left(\frac{\phi_B}{2} + \frac{\pi}{4}\right)}, \quad \omega_p = \frac{\omega_c^2}{\omega_z} = tan\left(\frac{\phi_B}{2} + \frac{\pi}{4}\right)\omega_c \tag{3.73}$$

3.3.3 Stability of the Close-Loop System

The stability of the closed-loop system can be evaluated based on the approximated outer loop gain $T(s)$. From Figure 3.8 the loop gains $T(s)$ is defined as the product of the small-signal gains in the forward and feedback paths of the feedback loop [87]. $T(s)$ is expressed as

$$T(s) = G_C(s)G_M(s)G_{id}(s) \tag{3.74}$$

The design of G_c involves calculating compensator gain and finding the location of compensator pole, zero. The aim of compensator design is to build the overall loop transfer

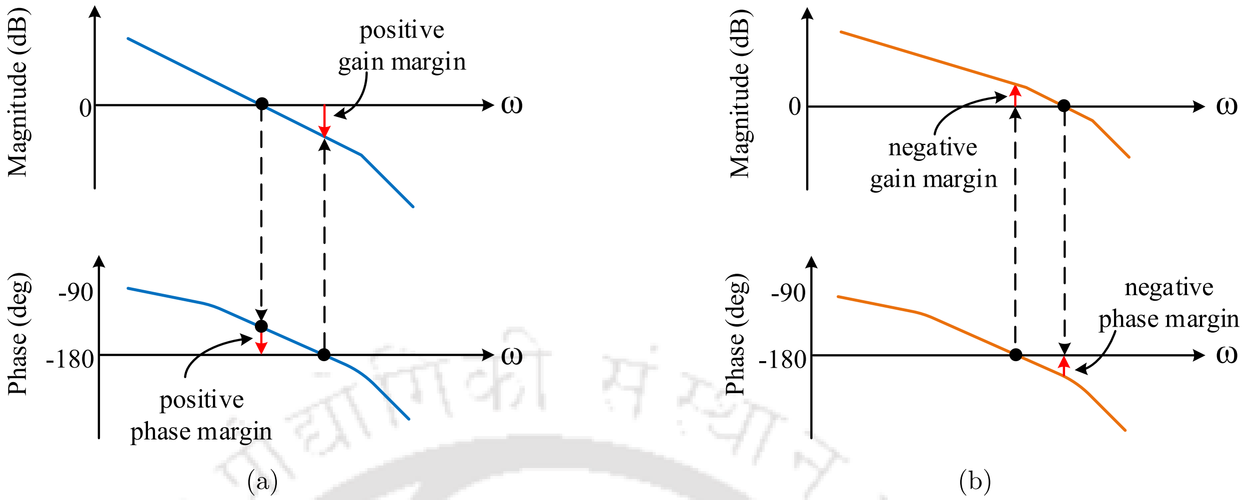

Figure 3.10: Gain margin and phase margin of (a) stable system (b) unstable system.

function to satisfy stability criteria. The Nyquist stability criteria for the closed loop system is $T(j\omega) = -1$ and results into

$$|G_C(j\omega)G_M G_{id}(j\omega)| = 1 \tag{3.75}$$

$$\angle G_C(j\omega)G_M G_{id}(j\omega) = -\pi \tag{3.76}$$

In the compensator design technique using a Bode plot, (3.75) and (3.76) stability criterion means we have to keep extra gain margin at the phase crossover frequency and extra phase margin at the gain crossover frequency which is graphically shown in Figure 3.10. The gain margin (GM) in the Bode plot tell us how far the overall loop gain T(s) is from the 0 dB at phase crossover frequency and the phase margin (PM) tells us how far the phase of T(s) is from $-180°$ at gain crossover frequency. Figure 3.10 (a) and Figure 3.10 (b) shows the graphical representation of a stable system and unstable system respectively.

The stability criterion can thus be stated as: the critical point which separates stable from unstable systems is when the open-loop phase shift is $-180°$ and the open-loop gain is 1 [92]. The choice of gain crossover frequency and the location of poles and zeros of the compensator will decide the bandwidth and stability margin.

3.3.4 Open-Loop Frequency Response of the Braking Circuit

Using the transfer function $G_{id}(s)$ *i.e.* the linearised small-signal model of the converter plant, we next plug in the numerical values and construct the bode plot to see the open-loop characteristic of the braking circuit.

Plugging in the values given in Table B.1 into (3.60) and using MATLAB programming code, the Bode diagrams and pole-zero map of the small-signal transfer function of the control-to-braking current G_{id} are achieved. Figure 3.11 is the Bode plot of the control-to-braking current transfer function G_{id}. Figure 3.12 is the plot of the poles and zeros of the continuous-time system G_{id} where x and o indicate the poles and zeros, respectively.

The salient points of open-loop transfer function G_{id} are:

- From the magnitude of the G_{id} is shown in the Bode plot Figure 3.11. The transfer function contains a low-frequency dc gain of 55 dB, gain crossover frequency is at $f_{gc} = 13.4$ kHz, and phase margin PM $= 90$.
- The transfer function doesn't have a phase crossover frequency. Therefore, the gain margin GM of the system would be infinite.
- At a frequency near 50 Hz, the transfer function has a slope of -1, i.e., attenuation of 20 dB/decade Figure 3.11.
- The roots of transfer function polynomial have two real and unequal poles and one zero as shown in pole-zero map Figure 3.12. Thus, the system is over-damped.
- It is observed from Figure 3.12, that the poles and zeros of G_{id} lies in the left-half of the s-plane, *i.e.*, open loop system is stable.

From the open-loop characteristic, it is confirmed that the open-loop system is stable. Thus, the closed-loop stability depends on the design of the controller transfer function G_c.

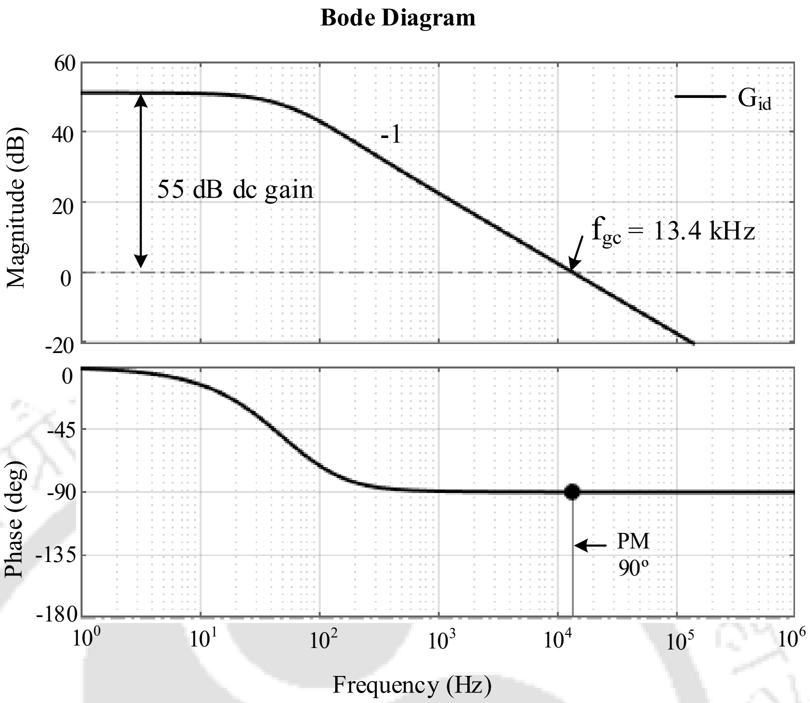

Figure 3.11: Bode plot of the control-to-braking current transfer function G_{id}.

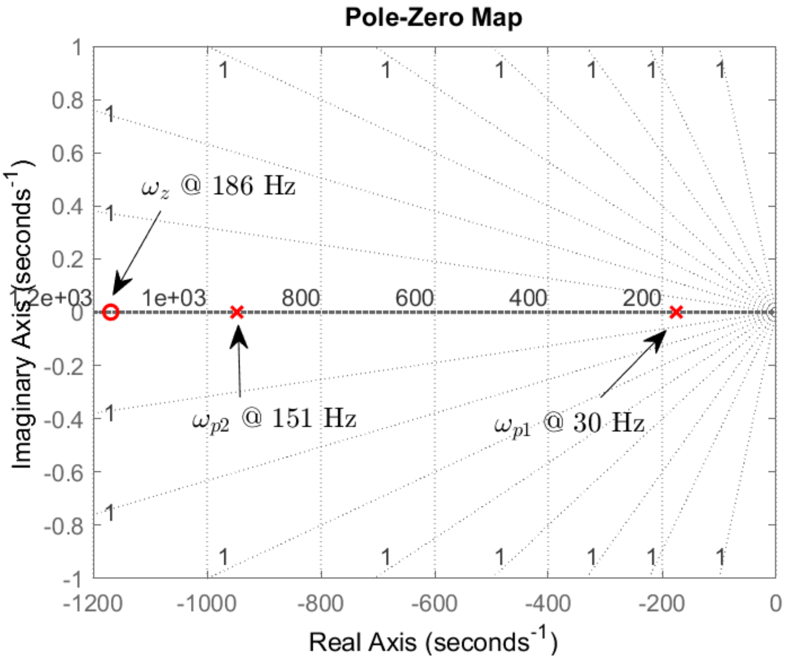

Figure 3.12: Plot of the poles and zeros of the continuous-time system G_{id}. Here, x and o indicate the poles and zeros, respectively.

3.3.5 Design Procedure of a Type-II Compensator

The design criteria in placing the compensator pole and zero is such that the loop gain transfer function crossover frequency should be high with a phase margin greater than 45° and a gain margin greater than 20 dB. These criteria ensure good stability and transient performances. The design procedure is as follows:

- Preliminary step: To plot the open-loop frequency response of the converter plant using a linearised small-signal model as explained in subsubsection 3.3.4.
- Step 1: Choose the gain crossover frequency ω_c: This is the frequency at which we would like the overall loop gain to be unity. Generally, ω_c is chosen to be high because the higher the cross-over frequency, the faster the transient response.
- Step 2: Calculate the required phase boost: Consider a desired phase margin (PM), the required phase boost is calculated as

  $$\phi_B = PM - 90^\circ - \angle G_{id}(s)|_{\omega_c} \tag{3.77}$$

  A phase margin of 90° would make the system stable. A phase margin of 30° or less will oscillate the system during the transient period and be more reactive to environmental variations [90]. Depending on the system requirement, compromise should be made between stability and fast transient response.
- Step 3: Calculate the compensator pole and zero: The compensator pole and zero are calculated using (3.73)
- Step 4: Calculate the compensator gain k_c: The compensator gain is calculated using loop gain equation at ω_c which is given as:

  $$T(s) = |G_C(s)|_{\omega_c}|G_M(s)|_{\omega_c}|G_{id}(s)|_{\omega_c} = 1 \tag{3.78}$$

  $$|G_c|_{\omega_c} = \frac{1}{|G_{id}(s)|_{\omega_c}|G_M(s)|_{\omega_c}} \tag{3.79}$$

  There is unity gain from the peak voltage ramp signal, hence $G_M(s)|_{\omega_c} = 1$ then,

$$|G_c|_{\omega_c} = \frac{1}{|G_{id}(s)|_{\omega_c}} \tag{3.80}$$

From (3.66) and (3.80) we have compensator gain equation

$$k_c = \frac{\omega_z}{|G_{id}|_{\omega_c}} \tag{3.81}$$

- Step 5: The controller is given as:

$$G_C(s) = \frac{k_c(1+\frac{s}{\omega_z})}{s(1+\frac{s}{\omega_p})} \tag{3.82}$$

3.3.5.1 Examples of Compensator Design

First, we plot the Bode plot of the open-loop transfer function G_{id}, as shown in Figure 3.11. Next, the crossover frequency is chosen at 10 kHz, which is 1/10th of the switching frequency (f_s = 100 kHz). The magnitude of G_{id} at 10 kHz is 2.48 dB, i.e. the absolute magnitude is $|G_{id}| = 1.3305$, the phase angle $\angle G_{id}$ at 10 kHz is $-89.9°$.

The transfer function of G_{id} is given by

$$G_{id}(s) = \frac{\hat{i}_{brake}(s)}{\hat{d}(s)} = \frac{8.929 \times 10^4 s + 1.082 \times 10^8}{s^2 + 1122s + 1.524 \times 10^5} \tag{3.83}$$

Case one: for desired PM of 60°, using (3.77), $\phi_B = 59.9°$

Similarly using (3.73), $\omega_z = 1.6895 \times 10^4$ rad/sec, $\omega_p = 2.3368 \times 10^5$ rad/sec and $k_c = 1.2698 \times 10^4$. The transfer function is given by

$$G_C(s) = \frac{1.2698 \times 10^4 \left(1 + \frac{s}{1.6895 \times 10^4}\right)}{s\left(1 + \frac{s}{2.3368 \times 10^5}\right)} = \frac{0.7516s + 1.2698 \times 10^4}{4.279 \times 10^{-6}s^2 + s} \tag{3.84}$$

Figure 3.13 (a) shows the bode plot of compensated TF ($G_{id}G_CG_m$), controller TF (G_C) and uncompensated plant TF (G_{id}). From the bode plots, it is observed that the designed compensator gives an $PM = 62°$ at $f_{gc} = 10$ kHz and the low frequency gain is high.

Case two: for desired PM of 80°, using (3.77), $\phi_B = 79.9°$

Similarly using (3.73), $\omega_z = 5.5523 \times 10^3$ rad/sec, $\omega_p = 7.1102 \times 10^5$ rad/sec and $k_c = 4.1733 \times 10^3$. The transfer function is given by

$$G_C(s) = \frac{4.1733 \times 10^3 \left(1 + \frac{s}{5.552 \times 10^3}\right)}{s\left(1 + \frac{s}{7.110 \times 10^5}\right)} = \frac{0.7516s + 4.173 \times 10^3}{1.406 \times 10^{-6}s^2 + s} \tag{3.85}$$

Figure 3.13 (b) shows the bode plot of compensated TF ($G_{id}G_CG_m$), controller TF (G_C) and uncompensated plant TF (G_{id}). From the bode plots, it is observed that with the designed compensator gives an $PM = 82°$ at $f_{gc} = 10$ kHz, and the low frequency gain is high.

Case three: for desired PM of 85°, using (3.77), $\phi_B = 84.90°$

Similarly using (3.73), $\omega_z = 2.7982 \times 10^3$ rad/sec, $\omega_p = 1.4108 \times 10^6$ rad/sec and $k_c = 2.1032 \times 10^3$. The transfer function is given by

$$G_C(s) = \frac{2.1032 \times 10^3 \left(1 + \frac{s}{2.7982 \times 10^3}\right)}{s\left(1 + \frac{s}{1.4108 \times 10^6}\right)} = \frac{0.7516s + 2.103 \times 10^3}{7.088 \times 10^{-7}s^2 + s} \tag{3.86}$$

Figure 3.13 (c) shows the bode plot of compensated TF ($G_{id}G_CG_m$), controller TF (G_C) and uncompensated plant TF (G_{id}). From the bode plots, it is observed that the designed compensator gives an $PM = 86°$ at $f_{gc} = 10$ kHz, and the low frequency gain is high.

Case four: for desired PM of 89°, using (3.77), $\phi_B = 88.90°$

Similarly using (3.73), $\omega_z = 603.16$ rad/sec, $\omega_p = 6.5453 \times 10^6$ rad/sec and $k_c = 453.35$. The transfer function is given by

$$G_C(s) = \frac{453.35 \left(1 + \frac{s}{603.16}\right)}{s\left(1 + \frac{s}{6.5453 \times 10^6}\right)} = \frac{0.7516s + 453.3}{1.528 \times 10^{-7}s^2 + s} \tag{3.87}$$

Figure 3.13 (d) shows the bode plot of compensated TF ($G_{id}G_CG_m$), controller TF (G_C) and uncompensated plant TF (G_{id}). From the bode plots, it is observed that the designed compensator gives an $PM = 90°$ at $f_{gc} = 10$ kHz, and the low frequency gain is high.

The design criteria in placing the controller pole and zero is such that the loop gain TF crossover frequency should be high with phase margin (PM) greater than 45° and gain margin (GM) greater than 20 dB. From the above examples, we conclude that

- In Figure 3.13 (a), there is a good phase margin of 62° at the gain crossover frequency. In the low-frequency region of about 146 Hz, there is a small oscillation or ‘dip’ in the

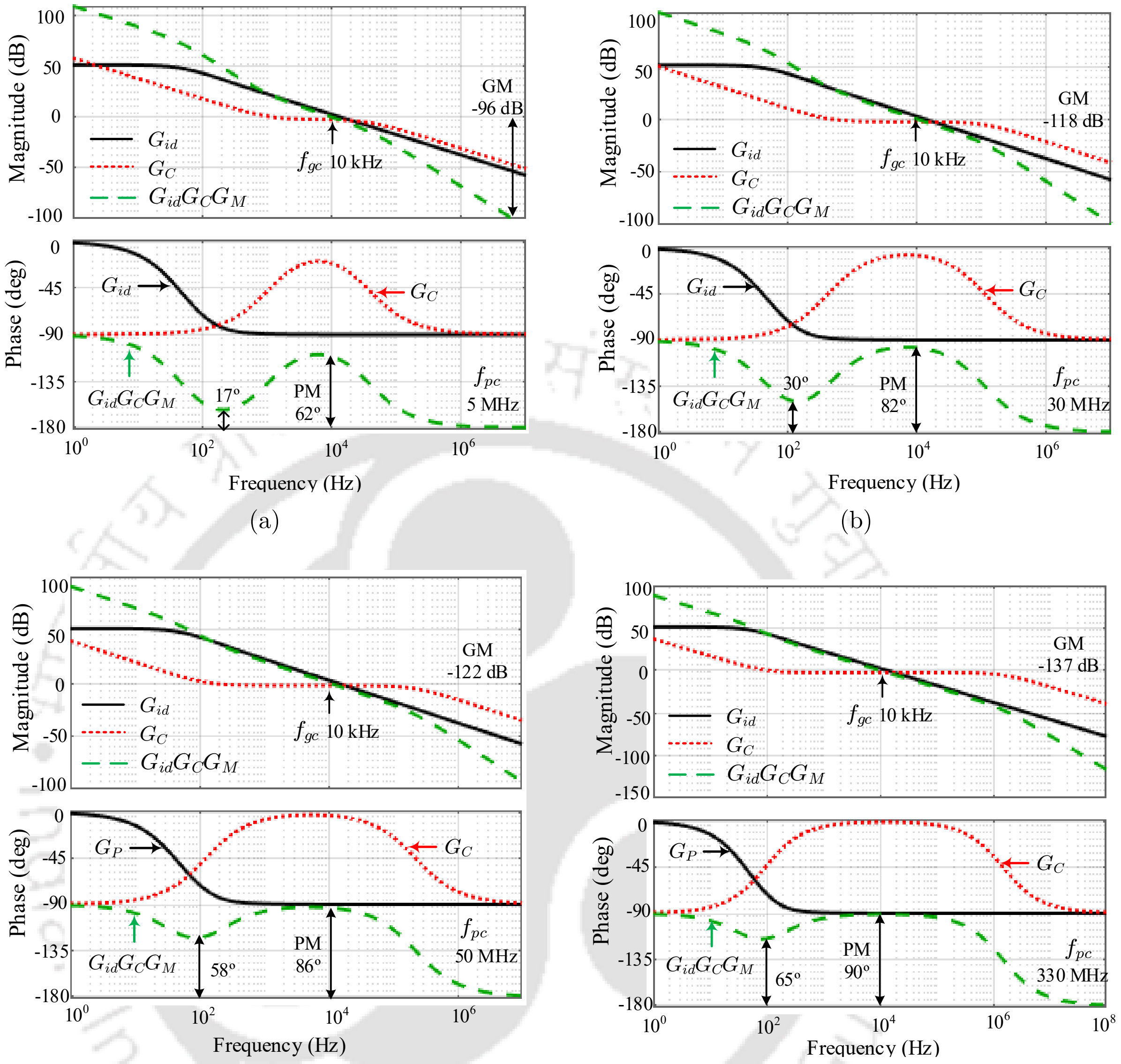

(a) (b) (c) (d)

Figure 3.13: Bode plot of open-loop transfer function of G_{id}, G_{id}, and $G_{id}G_cG_m$: (a) desired PM = 60° (b) desired PM = 80° (c) desired PM = 85° and (d) desired PM = 89°

phase waveform; here, in the dip region, the phase shift is very close to $-180°$ only $-17°$ apart. However, at 146 Hz, we have enough good gain value of 50 dB, and the system is stable. For extra precautions, to be on the safer side, the phase shift in the low-frequency dip region of the phase plot can be reduced (taken away from $-180°$) by rearranging the zero and pole locations.

- We can observe from Figure 3.13 (a) to Figure 3.13 (d) that as we increase the desired phase margin from 60° to 89°, we can see that the pole location at the high-frequency region of the compensated system is also increased. This leads to higher bandwidth and reduces the phase shift in the low-frequency region near the dip point region. However, increasing the phase margin comes with a penalty; a higher phase margin can lead to a slower transient response.

After completing the compensation design in the frequency domain, the compensated system is then simulated to check the time domain responses. Based on the results of this check, it may be necessary to repeat the whole design process. Therefore, for regulating the braking circuit, the controller parameter given in (3.86) is further used for the Simulation and Hardware experiments, which are calculated using the PM $= 85°$ at the gain crossover frequency, $f_{gc} = 10$ kHz. These criteria ensure good stability and transient performances, as shown in Figure 3.13 (c).

3.4 Simulation Study

This section verifies the control strategy and Type-II current compensator designed in the preceding section via simulation in the MATLAB/Simulink environment. The simulation aims to show the dynamic response of the proposed regenerative braking circuit and validate its working and topology. Figure 3.14 shows the simulation set-up arrangement of the inverter model, BLDC motor, rectifier, and Li-Ion battery blocks taken from the MATLAB/Simulink library. The parameters for the BLDC motor and boost converter used for the simulation are given in Table B.1 and Table B.2, respectively, of Appendix B. The work presented in this Chapter is about modeling the power train, which involves modeling the motor and regenerative braking circuit rather than the complete vehicle drive-line. Hence, some of the assumptions and settings for the present simulation are as follows :

- The BLDC motor is driven with mechanical torque (T_m) as its input. The T_m is positive during the motoring mode, and for the regenerative mode, T_m is negative. This negative T_m emulates the effect of T_{gh} due to the F_{gh}. T_{gh} force is assumed to be a constant force during the regenerative mode. Using

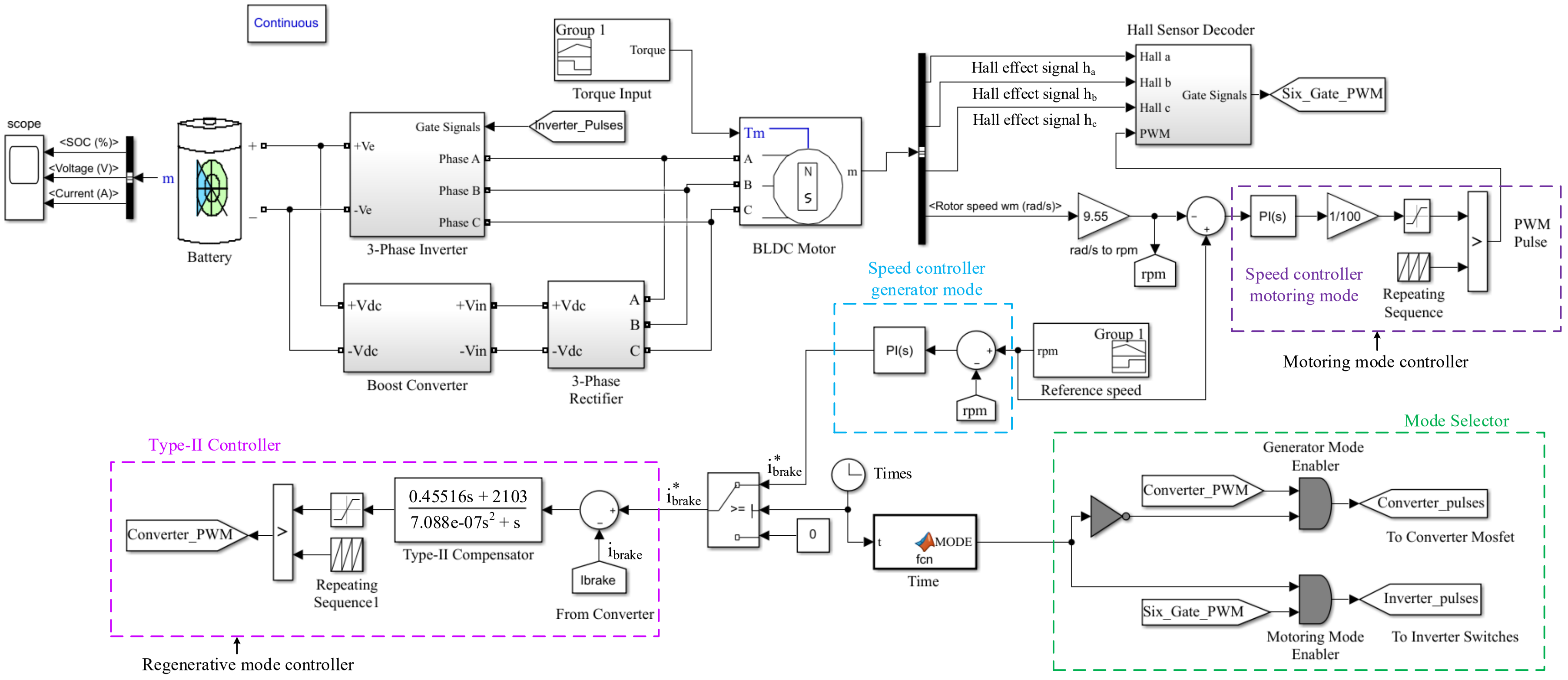

Figure 3.14: Simulation block diagram of the regenerative braking system configuration and its controller in a MATLAB/Simulink environment.

- In the real-world physical drive scenario, the rider is both the reference speed generator and the regulator. Depending on the brake force given by the rider, the speed is slowed and maintained. For the simulation purpose, to emulate the rider's braking action, a PI controller block is used to regulate the speed to produce the braking current reference from the difference between the actual motor speed and the reference speed input. The desired reference motor speed is generated using a signal builder.

- The simulation is for 6 s, just enough to show the dynamic behaviors. That is because of power electronics components like the MOSFET with a switching frequency of 100 kHz; the simulation time step is 1×10^{-6}, which slows the computational speed.

3.4.1 Implementing the Controller in Simulation

The implementation of the controller scheme, which is explained in Section 3.3, is done using simple inbuilt Simulink blocks. The controller design to track the braking current reference, as shown in closed-loop functional block diagram in Figure 3.8 is achieved using a second order transfer function block. Here the error signal, which is the difference between the i^*_{brake} and i_{brake} is sent to the controller transfer function block. The controller transfer function (G_c) value used for the simulation is taken from Equation 3.86 derived in Subsection 3.3.5. To generate the PWM pulse, the output signal (v_c) from the controller transfer function block is then compared with a saw-tooth waveform from a repeating sequence block as shown in the Type-II controller block in the Figure 3.14 using a comparator. The repeating sequence generates a periodic saw-tooth waveform of a fixed frequency (100 kHz). The comparator output is HIGH when v_c is higher than the saw-tooth signal and LOW when the v_c is lower than the saw-tooth waveform. The peak of v_c is unity, and for safety purposes, a saturation block is used to contain the pulse width modulation *i.e.*, the duty ratio between 0.1 to 0.8.

During the motoring mode, the speed control of the BLDC motor is achieved using a PI controller block and repeating sequence block to generate the PWM pulse for the inverter switch. The six commutation states of the inverter to drive the BLDC motor are obtained by using the hall sensor information, which gives the motor rotor positions. Table B.3 in Appendix B shows the six commutation states from three hall effect sensors used in this work.

Next, to implement the transition between motoring mode and generating mode, a NOT and AND gates are used as outlined in the mode selector block in Figure 3.14, which is the implementation of Figure 3.7 (b). A Simulink function block is used to time the motoring mode and generator mode period, i.e., to generate the command to start and stop the regeneration mode. In actual operations, the human driver will give the brake commands.

3.4.2 Simulation Results

Figure 3.15 shows the various waveforms of the simulated dynamic responses. Figure 3.15 (a) plots the mode command signal input, which is the command given to the controller to switch between the motoring mode and the regeneration mode. As seen from Figure 3.15 (a), initially, the mode signal is HIGH, indicating the motoring mode, *i.e.*, the normal forward motion. In this mode, the motor controller is active, the inverter pulses are ON, the regenerative braking circuit is inactive, and the DC/DC converter pulses are OFF. Then, at 2 s, the mode signal is turned LOW, indicating regeneration mode is ON. In this mode, the regenerative braking circuit is active, the DC/DC converter pulses are ON, the inverter pulses are OFF, and the motor controller is inactive. Then again, at 4.5 s, the system is back to motoring mode. As shown in Figure 3.15 (a), the simulation results show that the control strategy to switch between motoring and regeneration mode is working and effective.

Other than the mode command signal, the simulation has two predefined inputs: T_m and ω_m^* as shown with dotted lines in Figures 3.15 (b) and (c), respectively. As seen from the Figure 3.15 (b) plot during the motoring mode, the T_m is a positive 3 Nm which acts as the load to the motor. At 2 s, when the regeneration braking commences, the T_m is -3 Nm; the negative T_m value emulates the effect of the free torque due to the gravitational acceleration force F_{gh}. The motor generates T_{brake} equal to $k_t I_{brake}$ to reach the desired speed. The response waveform of T_{brake} is shown in Figure 3.15 (b).

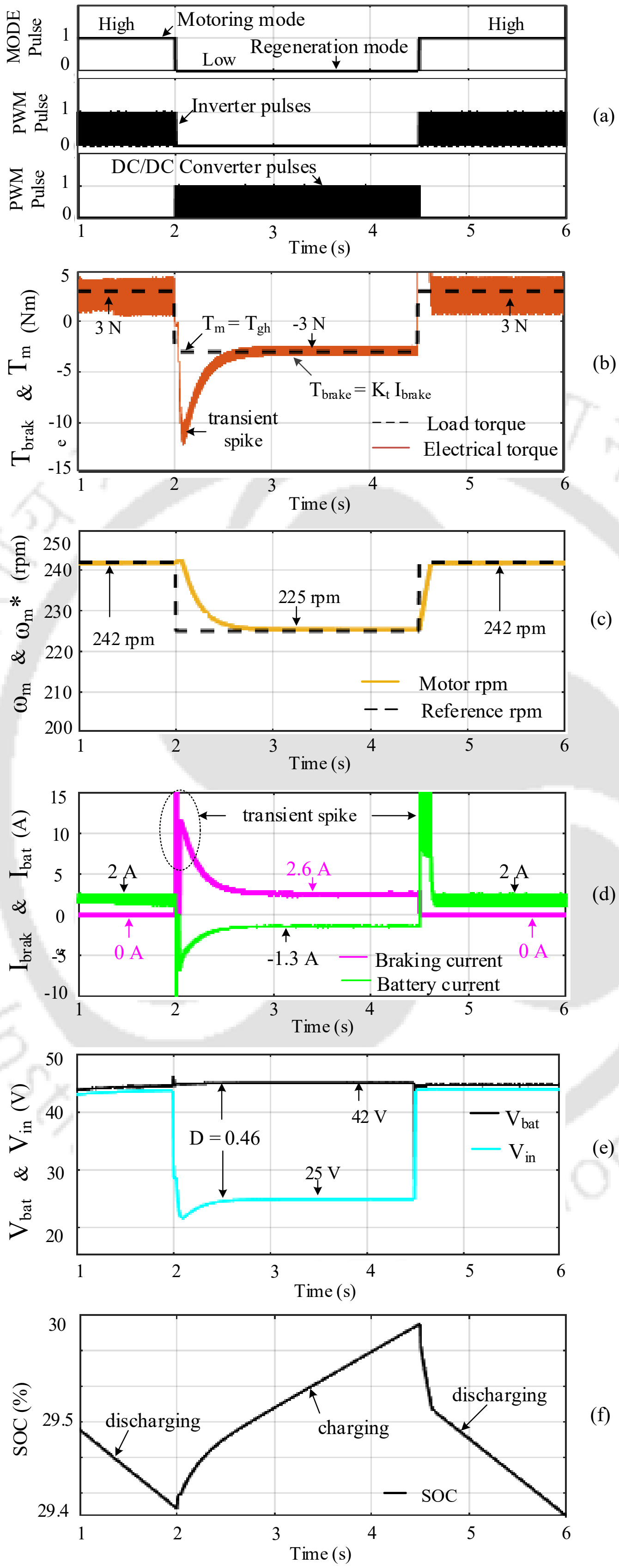

Figure 3.15: Simulated dynamic response waveforms (a) mode selector signal, inverter pulses, and DC-DC converter pulses (b) T_m and T_{brake} (c) ω_m and ω_m^* (d) I_{brake} and I_{bat} (e) V_{in} and V_{out} (f) battery SOC.

At 2 s, the regenerative braking commences upon receiving the braking command. The converter controller then tracks the braking current reference. The desired braking current starts flowing in the circuit, generating the desired braking torque required to oppose T_{gh} due to the slope. As seen from Figures. 3.15 (b) and (d) for $T_{gh} = -3$ Nm input, the braking current drawn is 2.6 A ($T_{gh}/k_t; k_t = 1.165$) and braking torque 3 Nm is generated.

Due to the opposing electromagnetic braking torque, the speed of the motor drops from 242 rpm to 225 rpm, as shown in Figure 3.15 (c). The voltage generated corresponding to 225 rpm is 25 V, as shown in Figure 3.15 (e). The duty cycle given by the converter controller is 0.46. The boost converter will boost the input voltage 25 V to a voltage slightly higher than the battery voltage (42 V, SOC 30%) so that the required current can flow to charge the battery.

Figure 3.15 (d) plots the braking and battery charging current, respectively. The negative battery current indicates the charging of the battery, which can also be validated from the battery SOC profile given in Figure 3.15 (f). During the motoring period, the SOC decreases as the power is supplied for the traction effort, and during the regenerative braking mode, the SOC increases, indicating there is a rise in the charge in the battery.

The above discussion shows that the control strategy (mode selection) and Type-II compensator perform as desired by the designer. The dynamic response shows that the designed controller gives us a good transient response, steady-state performance, and stability. The simulation results validate that the proposed regenerative braking circuit topology effectively tracks the braking current and generates the braking torque to slow down the speed of the motor and simultaneously charge the battery.

3.4.3 Steady-State Analysis and Discussion

This subsection is about the steady-state analysis of the developed regenerative braking system. Regenerative braking is applied to have a comfortable speed during the descends of the electric scooter on an inclined road, thus charging the electric scooter. From (3.26), the duty cycle (D) is then derived as

$$D = \frac{V_{bat} - V_{in} + (I_{brake} r_{in})}{V_{bat}} \tag{3.88}$$

From (3.32), we see that the charging current is a function of the duty cycle of the PWM signal and the braking current. Again from (3.88), it is seen that the value of the duty cycle is a function of the input voltage of the converter (proportional to the speed of the scooter), the braking current drawn, the available battery voltage, which in turn is dependent on the state of charge (SOC) of the battery. Thus, it can be observed that the value of the duty cycle is a function of battery voltage, input voltage, and braking current.

Figure 3.16 (a) shows the duty cycle variation with the change of input voltage for a braking current of $I_{brake} = 3$A, which is proportional to braking torque. Here, the magnitude of the input voltage is directly proportional to the descending speed of the scooter. In the present simulation, the constant of proportionality is assumed to be one, i.e., the electric vehicle's speed in km/h is equal to the input DC voltage to the regenerative braking circuit. The simulations presented in Figure 3.16 (a) are for the battery $SOC = 30\%$ and 50%. From Figure 3.16 (a), it is observed that as the input voltage (Vin) decreases, the duty cycle increases linearly. Furthermore, as the SOC of the battery increases, there is an increase in the duty cycle. A more detailed analysis of the results is presented in Table 3.1. From Table 3.1, it can be seen that as the duty cycle increases, the efficiency of the regenerative circuit decreases.

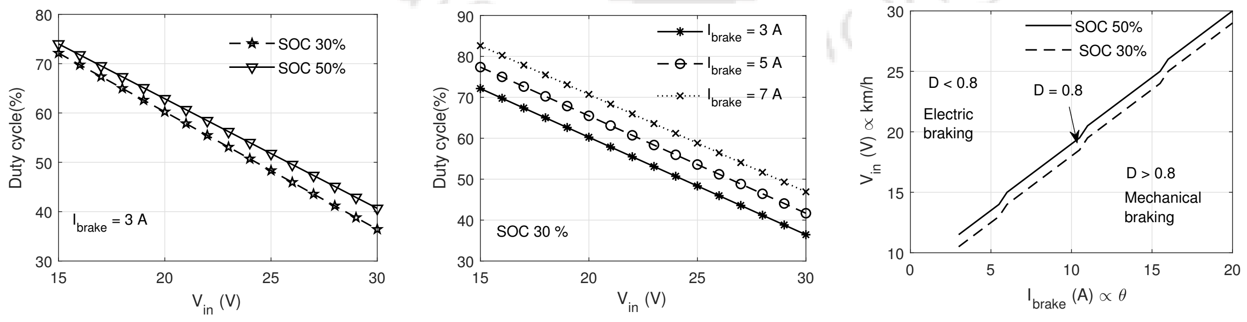

(a) (b) (c)

Figure 3.16: Steady-state calculated results showing (a) duty cycle D as a function of input voltage V_{in} at a fixed value of braking current I_{brake}, (b) and at different value I_{brake}. (c) shows the minimum speed the scooter should attain for a given hill angle for the regenerative circuit to function.

Table 3.1: Case one: Different scooter speed with same braking current.

V_{in} (V)	P_{in} (W)	SOC 50% (V_{out} = 45 V)				SOC 30% (V_{out} = 42 V)			
		D	I_{bat} (A)	P_{out} (W)	η (%)	D	I_{bat} (A)	P_{out} (W)	η (%)
30	90	0.40	1.80	81	90	0.36	1.92	86.4	96
25	75	0.51	1.47	66	88	0.48	1.56	70.22	93
20	60	0.62	1.14	51	85	0.60	1.20	54.0	90
15	45	0.74	0.78	35	77	0.72	0.82	37.0	82

Similarly, Figure 3.16 (b) shows the variation of the duty cycle for different braking currents, i.e., $I_{brake} = 3, 5$, and $7A$ at the battery $SOC = 30\%$. It is observed that as the braking current increases, there is an increase in the duty cycle for the same input voltage value. The roads with high hill angles require more braking torque T_{brake}, i.e., more braking current I_{brake}. This is mainly due to the high value of T_{gh} and the tendency of the rider to slow down on a steep slope, resulting in low input voltage, high duty cycle, and low efficiency. So, even though there is a high potential to harvest energy on the road with a higher hill angle or steeper slopes, the efficiency of converting this potential energy to electrical energy is low.

Since input voltage is inversely proportional to the duty cycle and the braking current is directly proportional to the duty cycle, then for a given hill angle, there is a minimum speed limit below which the duty cycle crosses 0.8. This speed value at which the duty cycle hits 0.8 is a critical point beyond which it is wiser to switch to mechanical braking. For higher efficiency, a DC/DC boost converter's duty cycle is usually operated below 0.8 [87]. Figure 3.16 (c) plots input voltage/speed vs. the braking current/slope at the value where D hits 0.8. Here, V_{in} is calculated as a function of I_{brake} at D equal to 0.8 by using (3.88). The V_{in} value tells the minimum speed for the scooter on a hilly road for a given hill angle value for the boost converter to work efficiently.

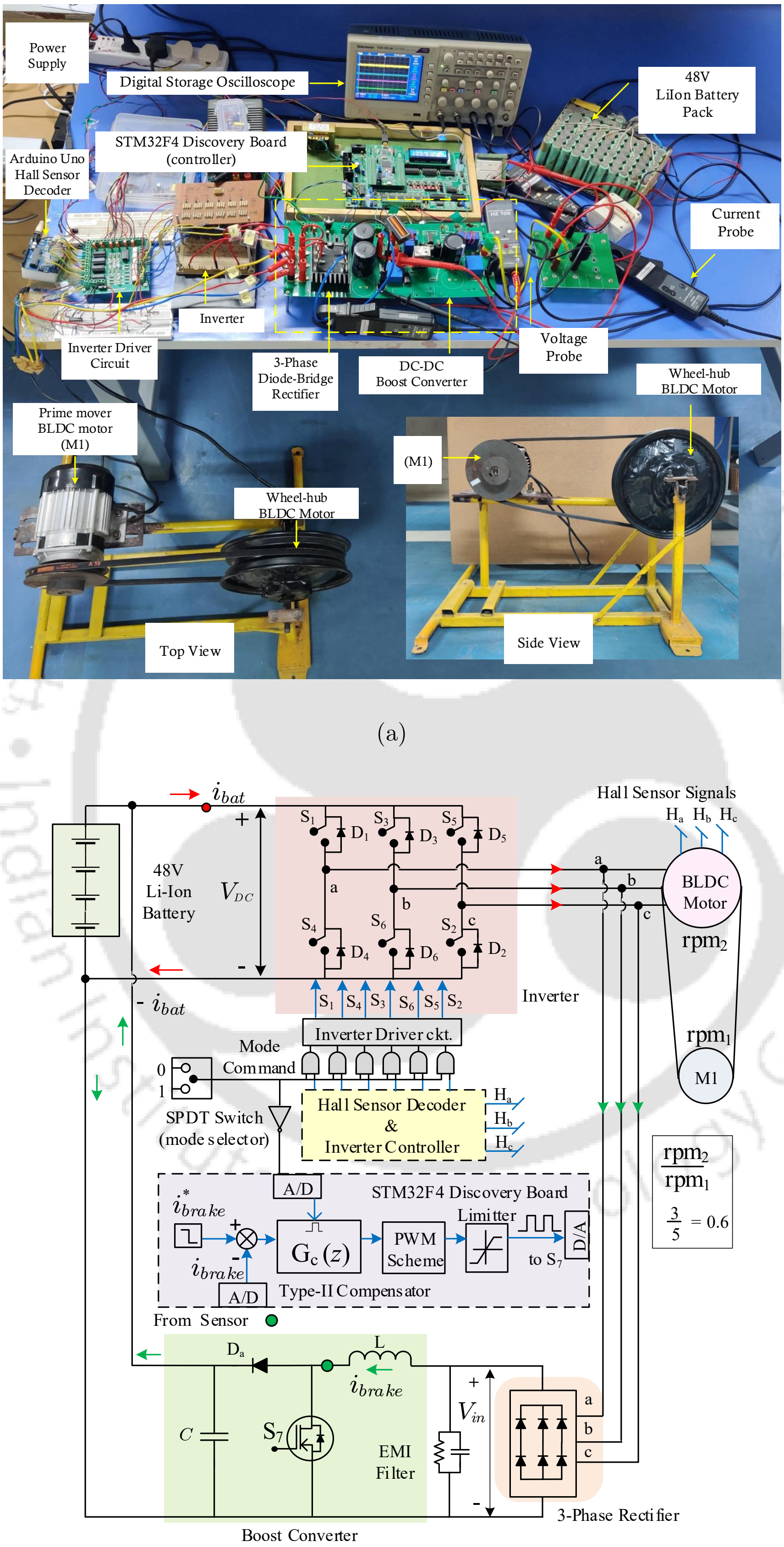

(a)

(b)

Figure 3.17: Hardware set-up (a) laboratory experimental test set-up (b) simple equivalent circuit connection of the experimental test set-up.

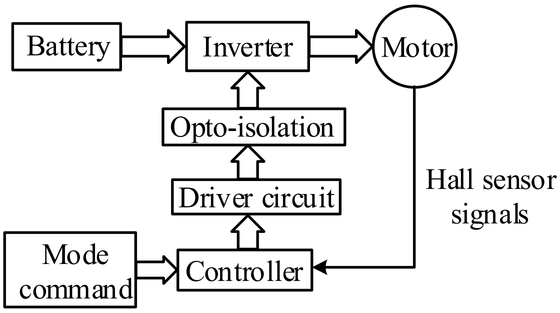

Figure 3.18: Block diagram representation of the hardware set-up during motoring mode

3.5 Hardware Implementation

This section will explain the implementation of the proposed braking system and its control strategy on a physical system. The overall hardware set-up is shown in Figure 3.17 (a), and its schematic layout of the hardware connection is shown in Figure 3.17 (b). The experimental setup is designed for a reduced power scale. As explained at the start of the chapter, the proposed regenerative braking system consists of two power drivelines, one for the motoring mode and the other for the regenerating mode. The two power trains consist of the following:

(i) The motoring mode power train consists of a Li-Ion battery pack (48 V, 12 Ah), a 3-phase in-wheel BLDC hub motor (1.8 kW), a 3-phase inverter module, an inverter driver circuit, signal conditioning circuit and an Arduino Uno as the controller which generates the PWM signal and also decodes the three hall sensors to provide the six commutation state for the inverter.

Figure 3.18 shows the block diagram of the motoring mode power train, with the schematic and circuit connections in Figure B.1 (Appendix B). Hardware specifications are listed in Table B.4 (Appendix B).

(ii) The regenerating mode powertrain consists of the 3-phase in-wheel BLDC hub motor (1.8 kW), a 3-phase rectifier, a DC/DC boost converter, a signal conditioning circuit, and an STM32F4 Discovery kit as the controller, which generates the PWM for the semiconductor switch (MOSFET) of the converter circuit. Next, to emulate the down-

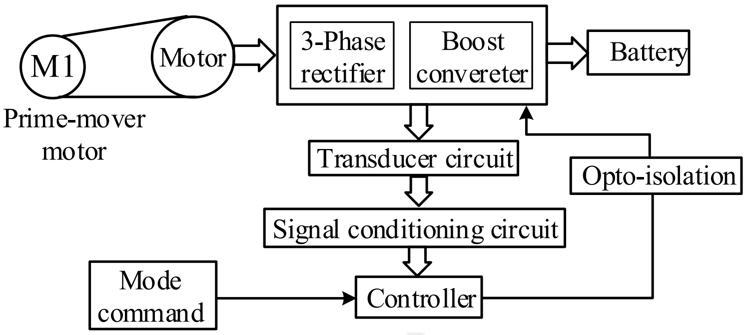

Figure 3.19: Block diagram representation of the hardware set-up during regenerative braking mode

hill driving condition, another BLDC motor, powered by another set of a 48 V battery and a 3-phase inverter, is used. The second BLDC motor is the prime mover machine to provide free rotating motion due to the hill angle. The prime mover BLDC motor is denoted as M1, and its speed is controlled with a potentiometer; it is connected to the BLDC hub motor through a belt, as shown in Figure 3.17 (a), and (b). The ratio between the wheel hub motor and the M1 is 0.6.

Figure 3.19 shows the block diagram of the hardware set-up for the regenerative braking power train, with the schematic and circuit connections in Figure B.4 (Appendix B). Hardware specifications are listed in Table B.5 (Appendix B).

3.5.1 Implementing the Controller in Hardware

In Section 3.3, the controller design was explained, and in Sub-Section 3.4.1, its implementation in the simulation environment was explained. This section gives the realization of the controller in the physical system, i.e., the hardware system.

In the hardware system, the switching between motoring and regeneration modes is actualized by an SPDT switch, as pictorially shown in Figure 3.17 (b). The working of the mode selection has already been explained briefly in Sub-Section 3.3.1, where Figure 3.7 (a) and Figure 3.7 (b) presented the mode selection algorithm and its implementation with logic gates, respectively.

From Figure 3.17 (b), we can see that the mode selector switch's 5 V (HIGH) and 0 V (LOW) signal act as input to the logic gate 7400 ICs (NAND gate) and 7404 IC (NOT gate)

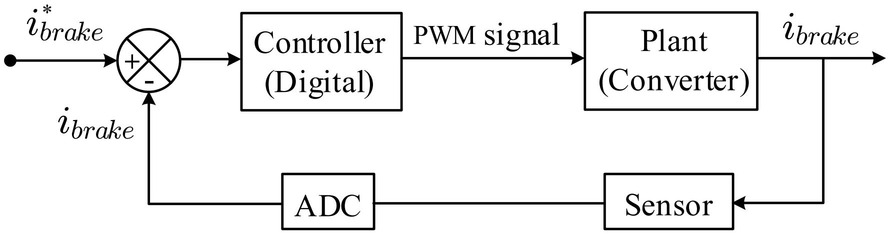

Figure 3.20: Block diagram for the hardware implementation of the controller feedback system with digital controller.

simultaneously. The mode selector mode by default is in the HIGH state (Motoring mode). The six commutation signals to the inverter circuits from the microcontroller get multiplied by the command mode signal SDPT switch in the 7400 ICs.

When the mode selector signal is 0 V, all the NAND gate output signals are LOW, and the inverter switches are in OFF mode. Simultaneously, the NOT gate will invert the 0 V to the HIGH signal and turn ON the regenerative mode. Upon receiving the HIGH signal, the DC/DC boost converter controller will start the Type-II compensator based digital controller, enabling the regenerative braking action. Similarly, when the mode selector signal is 5 V, the six commutation states via the NAND gate reach the inverter switches, and the motoring action occurs. Meanwhile, the NOT gate will invert the 5 V to LOW signal and turn OFF the regenerative mode.

Next, the control action is to adjust the duty cycle of the power switch based on the difference between the reference braking current and the sensor feedback signal. While Figure 3.8 in Sub-Section 3.3.2 showed the functional block diagram of the closed-loop system design, Figure 3.20 shows its hardware implementation with a digital controller. As shown in Figure 3.20 the controlled variable (braking current) is connected to a sensor that scales down the high current from the plant to a low-level voltage signal. The low-level voltage signal is further sent to the signal conditioning circuit before being fed to the microcontroller. The microcontroller understands the information only in digital form; hence, the sensor's analog (continuous) output needs to be converted to a digital (sampled) form, which is done by an analog-to-digital converter (ADC) device. Modern microcontroller boards come with built-in ADC in their peripherals. A schematic diagram showing the detailed connections of

Figure 3.20 with hall effect voltage and current transducers along with the signal conditioning circuit is given in Figure B.6 of Appendix B.

In this work, the controller hardware platform uses a Nitech's STM32F4 kit. The kit consists of two boards:

- Daughterboard: This board is ST Discovery card for STM32F407VGT6 microcontroller manufactured by ST Microelectronics.
- Motherboard: This board is developed to provide buffering and signal conditioning of various signals of discovery card. This board consist of buffer ICs, push button keys, an LCD display, and an RS-232 port.

This kit has a 32-bit microcontroller (ARM Cortex M4) along with peripheral units from the embedded system. The digital controller means that the controller is developed as embedded software on a microcontroller. The control algorithm can be implemented by writing code in programming languages such as C, C ++, and Assembly in an IDE and then loaded to the microcontroller, or the code can automatically be generated with special package programs from the model-based block design in MATLAB/Simulink environment. Here, the Matlab/Simulink Waijung blockset was used to create the code for the controller. Waijung is an embedded coder target that enables code generation for the STM32F4 Discovery kit, i.e., it easily deploys the MATLAB/Simulink models to the hardware controller. The Waijung blockset library needs to be separately installed in the Simulink Library. The "STM32F4 Target" block set included in the Waijung blockset is used to develop applications.

Figure 3.21 shows the block diagram of the code embedding procedure. The first step is to add the Waijung block set to MATLAB/Simulink new file. Then, the Simulink model built with the Waijung blockset is compiled using the Waijung interface. At the same time, this interface allows the user to monitor the compilation process. The ST-Link Utility and ST-Link/V2 USB drives need to be installed on the computer to transfer code from the computer to the STM32F4 Discovery board.

A continuous to discrete conversion by standard bilinear transformation method was

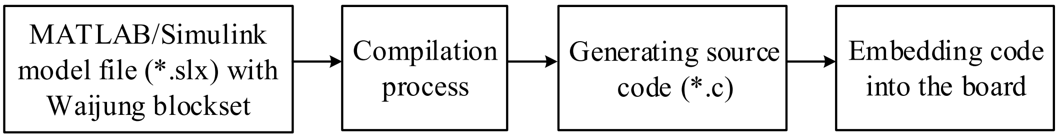

Figure 3.21: Block diagram showing the steps involved in code embedding process.

performed on MATLAB to convert the Type-II controller TF in (3.86) with a sampling rate of 5 kHz. The discretized Type-II controller TF is then derived as

$$G_c(z) = \frac{0.5245z^2 + 0.06201z - 0.4625}{z^2 - 0.03901z - 0.961} \tag{3.89}$$

Figure B.7 in Appendix B shows the implementation of the controller algorithm with Waijung block set models in MATLAB/Simulink environment.

3.5.2 Experiment to Study the BLDC Motor rpm and its Induced Voltage (V_{in}) During Generator Mode

The first experiment aimed to study the characteristic of wheel hub BLDC motor speed and its induced voltage (rms) in a no-load condition, meaning the regenerating braking circuit is not connected to the output ends of the machine terminals, as shown in Figure 3.22. Here, the main wheel hub BLDC motor is driven by another BLDC motor through a pulley belt, as shown in the hardware set-up Figure 3.17 (a). From a potentiometer, the speed of the M1 is varied from 300 rpm to 500 rpm. M1 motor drives the BLDC wheel hub motor through the belt from 180 rpm to 300 rpm, and the corresponding induced voltage across the three-phase rectifier was measured using a voltmeter.

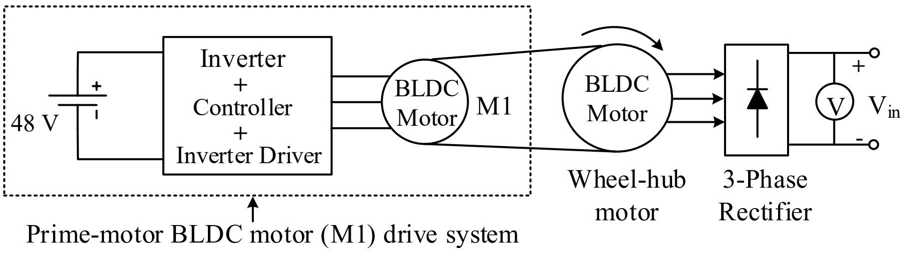

Figure 3.22: Block diagram representation of the experimental set-up to measure the induced voltage of the machine.

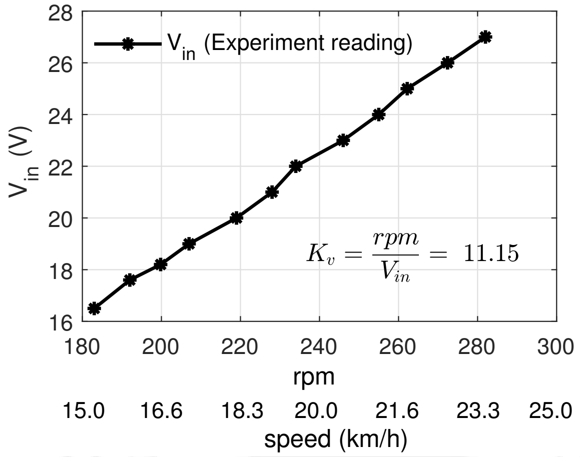

Figure 3.23: Voltage relationship with motor rpm and scooter speed.

Figure 3.23 shows the measured values of the induced voltage (rms), which is the V_{in} to the boost converter. On the y-axis of Figure 3.23 is the V_{in} corresponding to the wheel-hub motor rpm, and on the x-axis of the graph is the motor rpm. The estimated scooter speed, which was calculated using the relationship (3.90) is also shown below the motor rpm.

$$\text{Scooter speed in km/h} = (\text{rpm})\left(\frac{\pi}{30}\right)\text{r}\left(\frac{3600}{1000}\right) \tag{3.90}$$

The voltage induced is proportional to the scooter's speed. The voltage constant (K_v) for this motor is 11.15. Here, the purpose of this experiment was to get the correlation between the mechanical rotation of the wheel hub motor and its induced voltage for this specific BLDC motor under test, which is plotted in Figure 3.23.

3.5.3 Experiment to Study the Working of the Braking Circuit and the Effect of Motor rpm on Duty Cycle

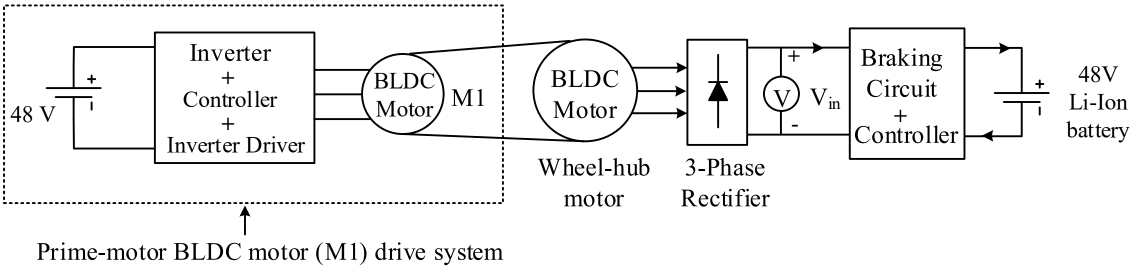

Figure 3.24: Block diagram representation of the experimental set-up to test the working of the regenerative braking circuit.

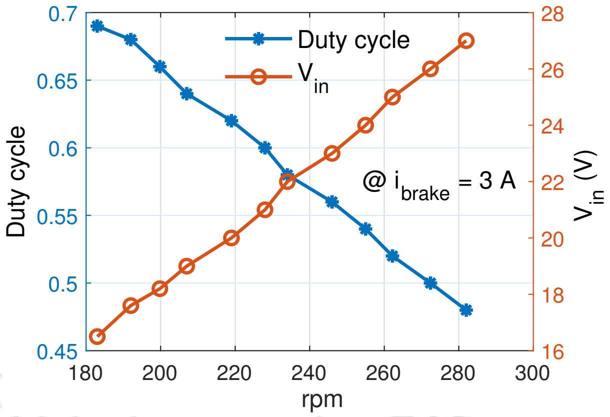

Figure 3.25: Duty cycle variation for fixed braking current and varying motor rpm.

Next, the boost converter and the Li-Ion battery are connected to the rectifier output, as shown in Figure 3.24. In this experiment, the braking current reference was fixed at 3 A, which means the braking torque generated is also fixed. The speed of the wheel-hub motor is changed from 180 rpm to 282 rpm, generating varying V_{in} from 16 V to 27 V. The controller of the boost converter regulates the PWM duty cycle accordingly to boost V_{in} to get the required $I_{brake} = 3$ A *i.e.*, same braking torque. Figure 3.25 plots the duty cycle generated by the controller against the variation in the V_{in} and motor speed. When the speed is 282 rpm, 0.48 of the PWM duty can boost V_{in} to get the required $I_{brake} = 3$ A, and when the speed is 180 rpm, then 0.69 will do the same. These results correspond with the theoretical analyses of the steady-state study.

3.5.4 Experiment to Show the Dynamic Behaviour of the Proposed Braking System

Figure 3.26 shows the block diagram representation of the experimental setup. Here, both the motoring and regenerative mode power train are connected. The experiments aim to demonstrate the switching between two modes and check the Type-II compensator's performance in the transient condition. Figure 3.27 shows a few DSO-captured images from the experiments, which are further explained below.

In Figure 3.27 (a), initially, the wheel hub motor is freely rotated at 247 rpm with the help of motor 1 (M1), and both the motoring mode circuit and the regenerative mode circuit

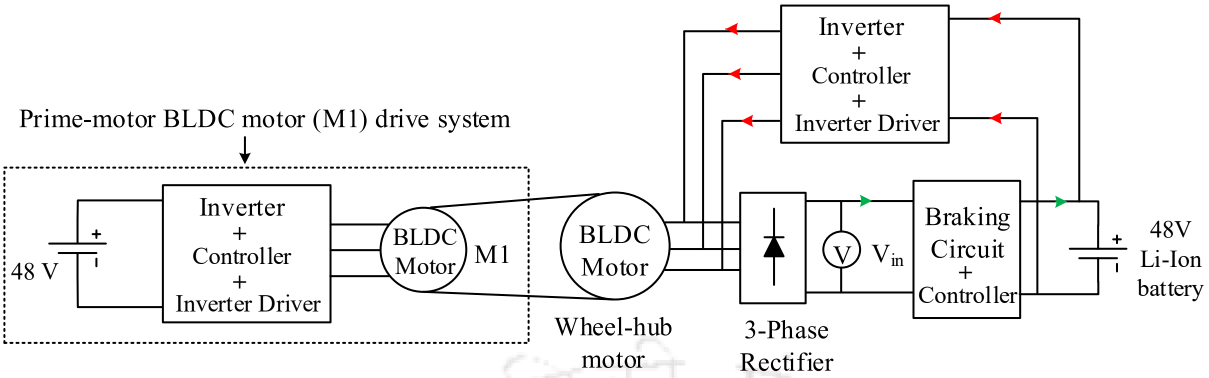

Figure 3.26: Block diagram representation of the experimental set-up showing both the motoring mode and regenerative mode power train connection.

are inactive. Then, after some moment has elapsed, the regenerative braking circuit is turned ON by manually switching the SPDT switch. The DC/DC current controller regulates itself to track the reference current, set at 3 A. It can be observed from the speed waveform that as the braking circuit draws a 3 A current, the speed drops to 230 rpm from 247 rpm. The 3 A current generates a reverse torque, which opposes the free mechanical torque, thus decreasing the motor speed. The boost converter sees an input voltage of 25 V for 230 rpm. The duty cycle of the PWM was measured to be 0.51 for input voltage 25 V and battery voltage 44 V. Furthermore, it is observed that the charging current of the battery is 0.95 A. Similarly, keeping everything else the same, Figure 3.27 (b) and Figure 3.27 (c) are the results captured by DSO for different motor speeds. It is inferred from Figure 3.27 (a), Figure 3.27 (b), and Figure 3.27 (c) that for the same braking current, the higher motor speed results in higher recovery of energy. A higher charging current is observed with higher input voltage since the battery charging current increases with the decrease in the duty cycle for the same braking current.

Figure 3.28 (a) shows the capture of a case of a step-change in the braking current reference. It is seen from the motor speed plot that as the braking current increases from 3 A to 4 A, the motor speed decreases from 238 rpm to 204 rpm. The controller regulates the duty cycle from 0.48 to 0.57 as the input voltage drops from 26 V to 21 V to boost the output voltage close to the battery voltage. This figure validates the Type-II compensator controller's performance to track the change in reference current. Figure 3.28 (b) shows the

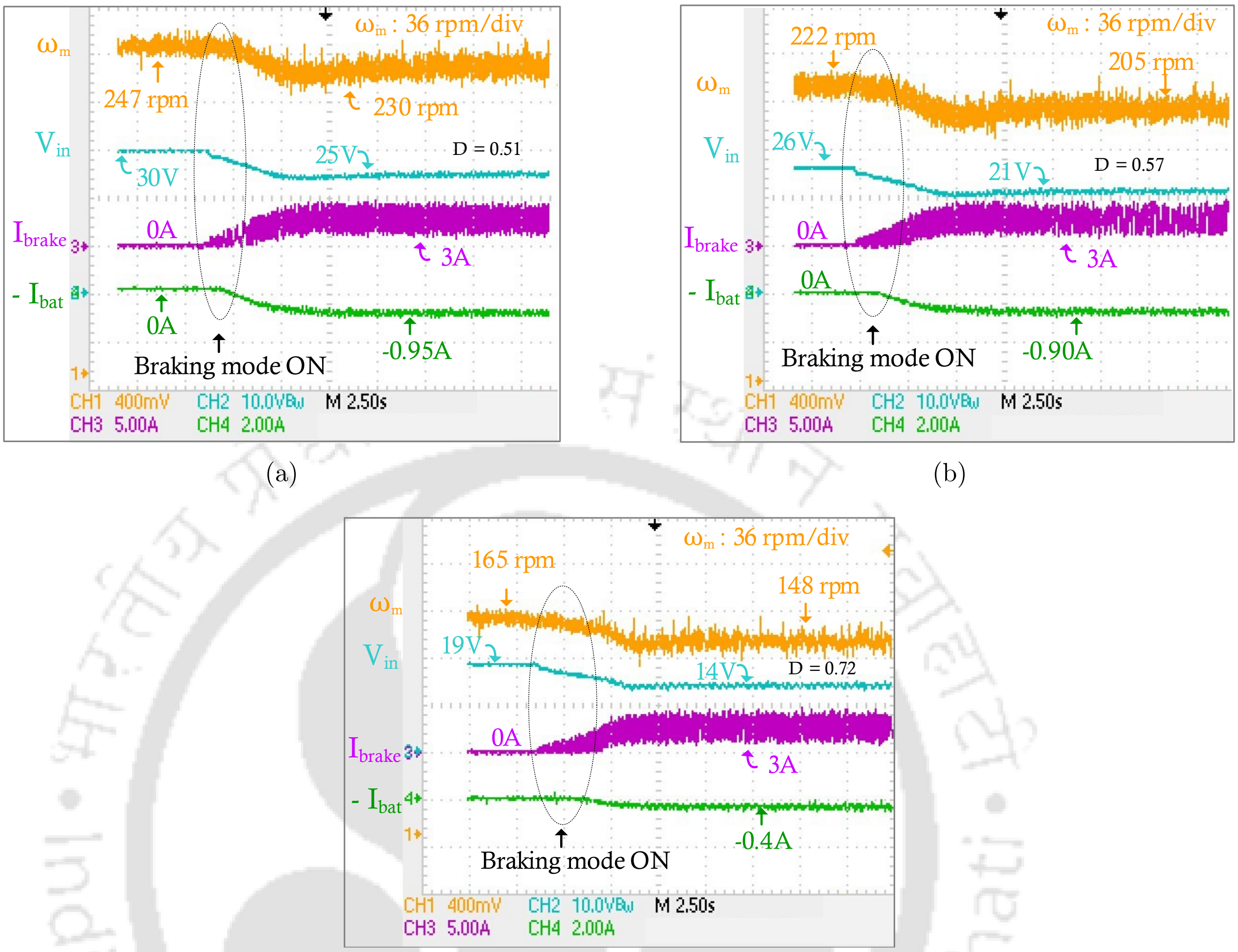

(a) (b)

(c)

Figure 3.27: Experimental results showing the braking action (a) from 247 rpm to 230 rpm with 3A braking current (b) from 222 rpm to 205 rpm with 3A braking current (c) from 165 rpm to 148 rpm with 3A braking current.

successful transition between the motoring and regenerative braking modes. Initially, the set-up is run in the motoring mode at no-load condition, and a 0.20 duty ratio is given to the inverter pulses. It is seen during the motoring mode the motor-driveline draws a no-load positive battery current of 0.2 A, which is pulsating in nature. During the motoring mode, zero braking current flows as the regenerative braking circuit is at an OFF state. Once the regenerative mode command is given, the braking current OF 3 A and the battery current of 0.52 A are observed. The braking current generates the braking torque, due to which the speed drops from 190 rpm to 168 rpm. Hence, we can see that switching between the two modes is fast and effective.

In conclusion, the experimental results validate the fast switching technique between the

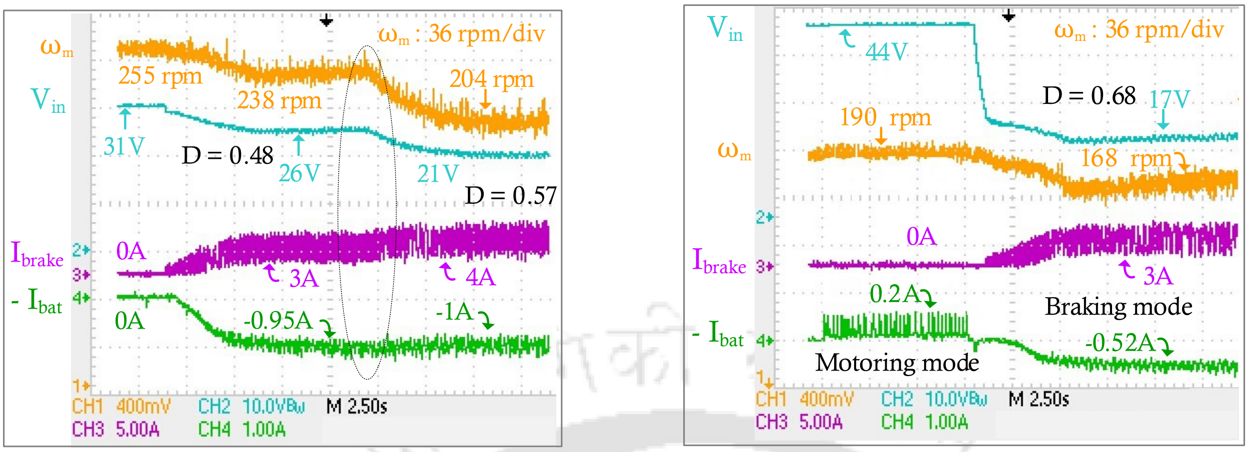

(a) (b)

Figure 3.28: Experimental results showing the braking action (a) from 238 rpm to 204 rpm with a step-change in the barking current reference from 3A to 4A (b) result showing the transition between the motoring mode and braking mode.

two driving modes, i.e., motoring and regenerating. The hardware implementation of the Type-II compensator performs satisfactorily by tracking the reference current and providing the required braking torque. The transient response (in the DSO captured results) shows that the compensator gives us a good transient response, steady-state performance, and stability. Overall, the results from Figure 3.27 to Figure 3.28 validate the feasibility and operation of the proposed regenerative braking system and its control.

3.6 Summary

Overall, this chapter contributes to the design, analysis, mathematical modeling, simulation, and hardware implementation of the control scheme for the proposed modular regenerative braking system. The proposed regenerative braking circuit can also be integrated into an existing electric scooter, which does not have a regenerative braking system. This is mainly due to the modular nature of the proposed regenerative braking system. The control technique offers fast switching between the two driving modes, i.e., motoring and regenerative braking, by enabling or disabling the gate pulses to the inverter or the boost converter. This switching method increases reliability and reduces the cost of the circuit by eliminating power switches to switch between motoring and regenerative braking modes. Since the proposed regenerative system uses the same source battery for both driving modes, i.e., motoring and regenerative braking, thus reducing the cost and weight of additional energy sources.

In motoring mode, the switches used in the inverter circuits are typically in the range of 10 kHz; hence, the Type I regenerative braking circuit uses approximately the same frequency for regenerative braking. Thus increasing the ripple in current and reducing the voltage gain. Whereas the proposed configuration uses a separate braking circuit, the braking circuit is designed at 100 kHz, thus increasing the voltage gain and is suitable for low-speed braking. The feasibility and the working of the proposed regenerative braking circuit are validated through simulations in MATLAB/Simulink. Further, the results are also experimentally verified on a developed prototype of a scaled-down laboratory test set-up. The results show successful braking action and the charging of the battery at a very low speed in the range of 25 km/h to 15 km/h, as required on hilly roads. These results also validate the compensator design used in the boost converter, which is the power-transferring circuit of the regenerative braking system. Further, the present work can be extended by including the energy efficiency study of the regenerative braking system.

4

Robust Control of the Proposed Regeneration Braking Circuit

Contents

4.1 Introduction

Chapter 3 presented the overall system design, analysis, mathematical modeling, simulation, and hardware implementation, showing the working of the proposed modular regenerative braking system. This chapter is in the continuation of Chapter 3; the only significant difference is that, here, in this chapter, the close-loop feedback controller of the braking circuit is new.

In the previous chapter, a Type-II compensator was designed using a linearised small-signal model of the proposed regenerative braking circuit. Since implementing Type- II controllers is simple, one can implement it on low-cost microcontrollers. It uses linear approximations of the nonlinear model of the power converter circuits to get a linear time-invariant (LTI) model. This LTI model is valid around an operating point of interest. All physical systems are inherently nonlinear when large signals are considered, and linear models of these systems can be approximated if the signal is small [93]. Although small-signal models are useful for analysis, they have intrinsic shortcomings like

- When there is a large transient, the converter's behavior cannot be appropriately captured because of the small-signal assumptions. Accuracy is compromised in large-signal processes. Based on this limitation, the controllers based on small-signal modeling are inadequate for larger signal disturbances in the system [94].

- The small-signal model cannot provide information on the converter's stability across the whole operating range [95]. The controller's stability cannot be guaranteed when system uncertainties exist, and this may require that the control gains be repeatedly tuned to ensure desired performances [96].

- Moreover, linear controller design methods are heavily dependent on the accuracy of the mathematical modeling of the plant, the parameters, and controller gains. The mathematical model of complex systems is prone to discrepancies in their output-input transfer function model due to unknown external disturbances, plant parameter variations, and unmodeled dynamics.

These shortcomings have driven power electronics researchers to pursue two lines of research: the search for more precise linear models or simplified nonlinear models for the controller design [97–102]; and the investigation into the potential use of various types of nonlinear controllers for DC-DC converters to improve their controllability and performances for a wide operating range [94].

In the literature, various non-linear control schemes, such as adaptive control, fuzzy logic control, artificial neural network (ANN) control, sliding mode (SM) control, and one-cycle control, have been reported to control the DC/DC converters. The advantage of non-linear controllers is that the size of the signal variations is not limited, and both the small and large signal variations are considered around the operating point [95]. This Chapter develops a sliding mode (SM) control-based controller for the regenerative braking system. The advantages of SM control over other non-linear control techniques are well documented in [94, 103]. The main advantages of SM control are

- That it guarantees stability and robustness against parameter uncertainties in the system [103]. Because the SM control process responds only to how the controlled variable's trajectory behaves, unseen parametric variations and external disturbances do not affect the trajectory.
- In addition, compared to other nonlinear control systems, the SM control method is comparatively simple to apply because it has a high degree of design flexibility.
- The SM control considers both small and large signal variations around the operating point [104–106].

Due to these above merits, SM control is well suited for many nonlinear systems, leading to its widespread industrial use in applications such as electrical drivers, automotive control, furnace control, etc. [107]. In this chapter, we are concerned with applying SM control to a specific class of variable structure engineering systems known as power electronics converters. Although power converters are physically static devices, due to their switching operation, they are a periodic time-variant system. Because of this switching nature, power converters

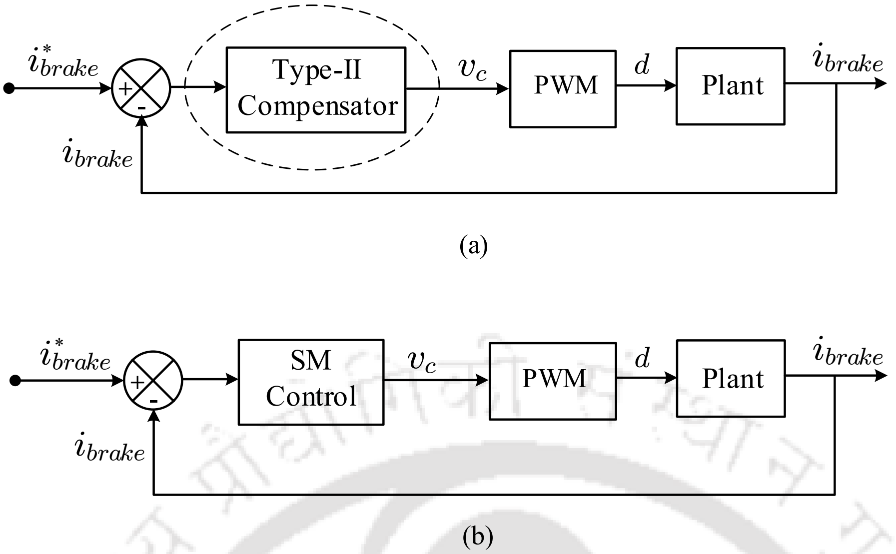

Figure 4.1: Closed loop schematic block diagram of (a) Type-II compensator (b) Sliding Mode control feedback system.

make it a perfect candidate for variable structure systems. Since the inception of SM control was for variable structure systems, applying SM control to power converters is natural. Moreover, SM control is easy to implement and considers small and large signal variations around the operating point, which is essential for DC/DC converters.

4.1.1 Objective of the Chapter

Seeing the benefits of the SM controller, here in this chapter, an SM current controller is designed and implemented to regulate the braking current of the proposed regenerative braking circuit, which was well established in Chapter 3. The overall control architecture of the proposed driving system is given in Figure 3.2 (d) of Chapter 3. The control hierarchy of the driveline system consists of (a) the switching between motoring and regeneration modes and (b) the controller design to track the braking current reference; both were explained in Section 3.3. Keeping everything else the same in the driveline system, only the close-loop current controller of the braking circuit is replaced, i.e., the Type-II compensator is replaced by a sliding mode control, as shown in Figure 4.1. The new controller (its design and control scheme) will be implemented using MATLAB/Simulink. Further, it is experimentally verified in the same scaled-down laboratory test setup used in Chapter 3.

Also, the system background, braking circuit working explanation, and system modeling remain the same as in Chapter 3. In this chapter, we start directly with the SM controller design for the braking circuit, preceded by a general theory of the SM control theory and its implementation.

The chapter structure is organized as follows: First, a brief introduction to SM control theory is explained in Section 4.2. Next, the design of the SM controller for the proposed braking circuit is given in Section 4.3. In Section 4.4, the simulation of the SM controller is verified, followed by experimental validation in Section 4.5. Finally, the chapter ends with a conclusion.

4.2 General Theory of Sliding Mode Control

Primarily, SM control was developed for the control of variable structure systems. The initial works on SM control were for ship-course control and the control of DC generators [94,103]. Since then, the research community and engineers have shown considerable interest in its advancement and application in different fields. SM control can be defined as:

a time-varying state-feedback control law that switches from one continuous structure to another at a high frequency based on the current position of the state variable in the state space, with the goal of forcing the dynamics of the system under control to follow precisely the pre-determined path in the state-space which is called sliding surface. [94].

For further explanation, let us consider the following affine state-space equation of a non-linear system

$$\dot{\mathbf{x}}(t) = A\mathbf{x}(t) + B\mathbf{x}(t) \cdot u(t), \tag{4.1}$$

where $\mathbf{x}(t)$ is the state-variable vector in an n-dimensional space R^n; $A(\cdot)$ and $B(\cdot)$ are smooth vector fields in the same space; and $u(t)$ is the discontinuous control action expressed as

$$u(t) = \begin{cases} U^+ & \text{if} \quad s(x,t) > 0 \\ U^- & \text{if} \quad s(x,t) < 0 \end{cases} \quad ; \tag{4.2}$$

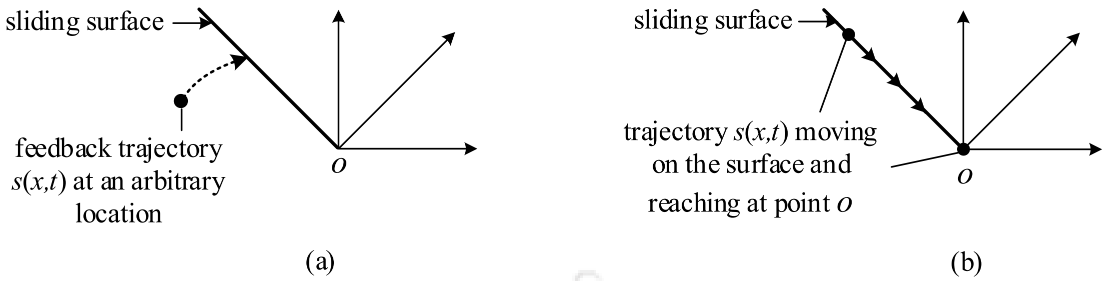

Figure 4.2: Graphical representation of SM control process in a three-dimensional space: (a) in reaching phase, the system trajectory $s(x,t)$ moves toward the sliding surface from an arbitrary location (b) in the sliding phase, the trajectory $s(x,t)$ keeps moving on the sliding surface, reaching the equilibrium point and staying there.

where U^+ and U^- are either scalar values or scalar functions of $\mathbf{x}(t)$; and $s(x,t)$ is the instantaneous feedback-tracking trajectory of the system and is a function of the state variables. The designer can design the sliding surface $s(x,t)$. It is designed in such a way that it reduces the complexity of the controller and its implementation. For most of the control problems, $s(x,t)$ is either a linear or nonlinear combination of the controlled variables or the difference between the feedback value and the reference value of the controlled variable.

Once the system trajectory reaches the sliding surface $s(x,t) = 0$, the equilibrium point acts as an attractor, and the trajectory will eventually reach the equilibrium point. The sliding surface is also known as the switching surface, as depending on the sign of $s(x,t)$, the control action switches as described in (4.2).

Figure 4.2 shows the graphical representation of the idea of the sliding mode control. Where point 'O' represents an equilibrium point, the system's trajectory settles upon touching this point. The system's trajectory is brought to this point with the help of the control action. Before the system trajectory reaches the sliding surface, a control action is directed towards the sliding surface, called the reaching phase, as illustrated in Figure 4.2 (a). Once the trajectory reaches the sliding surface, the system enters the sliding phase and remains on the sliding surface. Finally, it reaches the equilibrium point as shown in Figure 4.2 (b). This whole regime in the sliding surface, i.e., combining the reaching phase and sliding phase, is called the sliding mode operation, and the control process adopting this regime is called sliding mode control.

Hence, from the brief explanation above, it can be inferred that in the SM control theory, the control problem is to design the control input u such that:

(i) Firstly, the trajectory of the controlled variable should reach the sliding surface.

(ii) Secondly, the switching of the control function should be such that the trajectory remains on the sliding surface and finally settles at a desired point.

In a nutshell, SM control is a control process that responds only to how the controlled variable's trajectory behaves. The trajectory is not affected by to unseen parametric variations and external disturbances. The controlled trajectory will follow and, in due course, converge to the equilibrium point to attend to the steady-state condition by keeping the sliding surface as its reference path.

4.2.1 Types of Implementation

Based on the requirement of the application, SM control can be implemented in a few ways, as discussed below.

4.2.1.1 Relay and Signum Functions

The conventional way of implementing the SM control is shown in Figure 4.3 (a). Which is based directly on the control law described in (4.2), a discontinuous function realized using a switch relay.

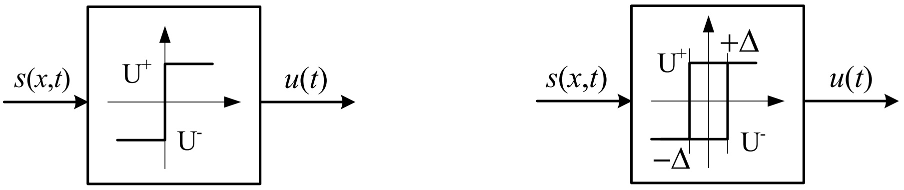

(a) (b)

Figure 4.3: A block diagram representation of (a) relay function in SM control (b) hysteresis function in SM.

For control applications which involve binary decisions, i.e. $U^+ = 1$ and $U^- = -1$ signum function is used as relay i.e.

$$u(t) = sgn(s(x,t)), \tag{4.3}$$

where the signum function $sgn(.)$ is defined as

$$u(t) = \begin{cases} 1 & \text{if} \quad s(x,t) > 0 \\ 0 & \text{if} \quad s(x,t) = 0 \\ -1 & \text{if} \quad s(x,t) < 0 \end{cases} \tag{4.4}$$

For digital logic control applications, (4.4) can be replaced by

$$u(t) = \begin{cases} 1 & \text{if} \quad s(x,t) > 0 \\ 0 & \text{if} \quad s(x,t) \leq 0 \end{cases} \tag{4.5}$$

The implementation of SM control using this method is straightforward. The outcome of such direct implementation of the control law is that the system operates at an infinite high switching frequency, leading to an unwanted chattering effect that might concern some applications. Hence, a system that requires restricting its operating frequency can instead opt for the hysteresis function method.

4.2.1.2 Hysteresis Functions

For the implementation of the SM control using the hysteresis function, we can redefine (4.2) as

$$u(t) = \begin{cases} U^+ & \text{if} \quad s(x,t) > \Delta \\ U^- & \text{if} \quad s(x,t) < \Delta \\ \text{Previous state} & \text{otherwise} \end{cases} ; \tag{4.6}$$

where Δ is a small positive value, now the hysteresis band with the boundary conditions $s(x,t) = \Delta$ and $s(x,t) = -\Delta$ will control the switching frequency of the system, providing some delay in the time period for the states switching as shown in Figure 4.3 (b) and thus solving the practical problem of very high-frequency switching operation. Due to the hysteresis band, the trajectory $s(x, t)$ of the system will now oscillate (controlled) specifically near $\pm\Delta$ of the sliding manifold. The chattering effect now becomes a function of Δ and controllable.

4.2.1.3 Equivalent Control Functions

Instead of the conventional way of implementing the SM control as given on (4.2) directly to switch or relay functions, alternatively, it is also possible to implement the SM control using a derived equivalent control [78].

In the equivalent control method, the discrete control input signal u can be replaced by a smooth function denoted as the equivalent control signal u_{eq}. i.e., if we only consider the low-frequency continuous component of the switching action, which is bounded by $U^- < u_{eq}(t) < U^+$ then, the equivalent control function $u_{eq}(t)$ is the ideal averaged control function nearly equivalent to an ideal SM-controlled trajectory. It is derived using the invariance conditions by setting the time differentiation of the sliding surface, i.e., $\dot{s} = 0$. Theoretically, implementing the equivalent control function will result in a system that operates with ideal SM control without high-frequency chattering.

The concept of the equivalent control function is fundamental in applying SM control to control power converters based on a PWM control technique. In [98], the authors suggested that under SM control operation, the control signal of equivalent control approach u_{eq} in SM control is equivalent to the duty ratio d of a PWM controller. Later in [108], the proof was given where a geometric framework was used to map the PWM feedback control onto SM control. The authors established the relationship $u_{eq} = d$; It was shown that at the high switching frequency, i.e., as it tends to infinity, an SM-controlled system's averaged dynamics are equivalent to a PWM-controlled system's averaged dynamics.

Figure 4.4 shows a PWM-based SM controller, where a pulse-width modulator employs an equivalent control (derived by applying the SM control technique) to generate a control signal to be compared with the fixed-frequency ramp in the modulator. The difference

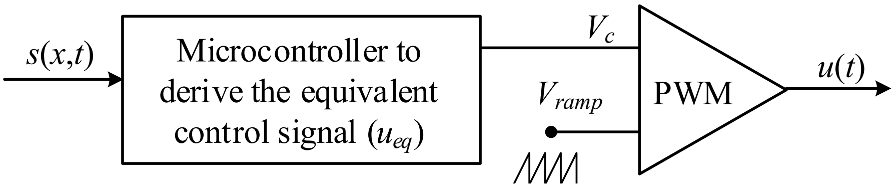

Figure 4.4: A block diagram representation showing the application of equivalent control function in a PWM-based SM controller.

between classical PWM controllers and PWM-based SM controllers is the formulation of the control signal V_c. SM controllers are based on the SM control law, whereas classical PWM controllers are based on the linear control law [94]. Here in this chapter, we will be using an equivalent control function to derive the duty ratio of our PWM-based SM controller.

4.3 The Controller Design for the Braking Circuit

From the above brief explanation of SM control theory, we understand that SM controller is a complete state-feedback control law that requires sensing its instantaneous variable values that appear in the dynamic equation of the desired control variable. Here, for our case, Figure 4.5 shows the simple schematic representation of the SM controller feedback structure, with the current and voltage sensors and their feedback signal sent to the controller block.

The first step in designing an SM controller for a converter is developing the mathematical modeling of the converter in terms of the desired control variables (i.e., voltage and current). In a PWM control implementation technique, the ON and OFF period of the converter switch gives rise to two independent physical states, leading to two state-space equations. The average of the two states is finally taken in developing the state-space equation. The converter switch is ON for dT_s interval and OFF for $(1-d)T_s$ interval, Where T_s is the switching period of one cycle of the PWM signal and d is the duty ratio of the PWM signal.

Previously in Chapter 3, the converter's average state-space equations were derived and given in (3.51) and (3.52). In a linear control system, the effort is made to replicate the exact mathematical model since the controller gains are indirectly derived from it. Hence,

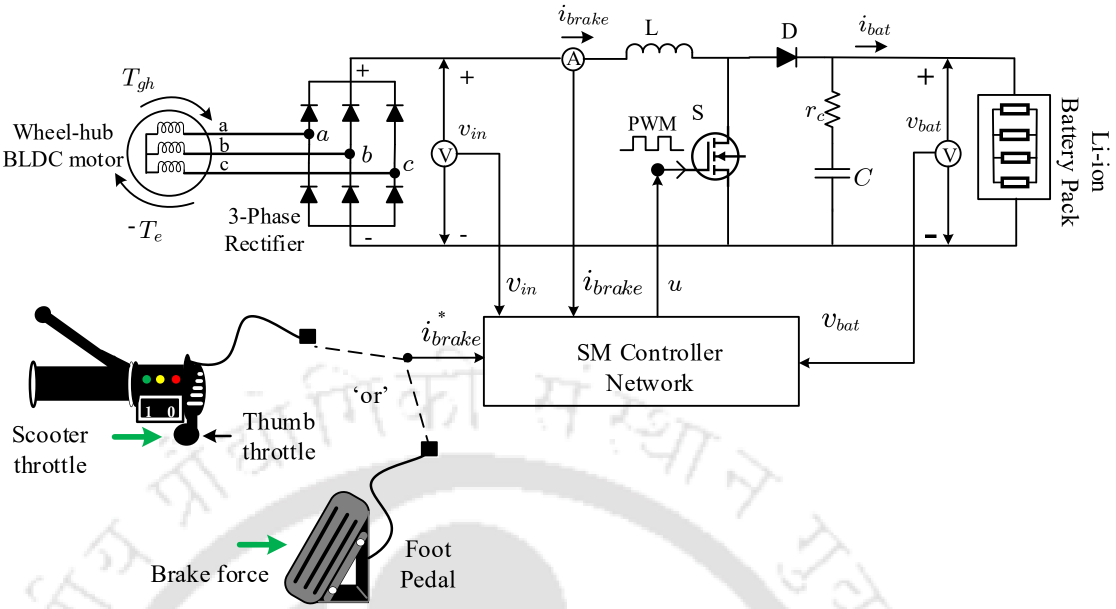

Figure 4.5: Representative block diagram of the braking circuit configuration with SM controller feedback structure.

in equations (3.51) and (3.52), the parasitic resistances and internal resistance (r_{in}, r_c and R_{int}) are considered and modelled. For the transient state analysis of the SM control, the effect of r_{in}, r_c and R_{int} is small and can be neglected; this gives a less accurate model, but the major advantage of SM control is its robustness towards model uncertainties. Hence, a simple model could be used in the present work to design SM control.

Figure 4.6 shows the simplified ON and OFF circuit diagram of the braking circuit, a simple boost converter. The input voltage seen is the rectified DC voltage v_{in}. Here, the output voltage is equal to the equivalent terminal voltage of the battery, i.e., $v_{bat} = e_{eq}$, as the R_{int} is neglected. To further simplify the model, v_{bat} is assumed to be the voltage drop across the load resistance R_L.

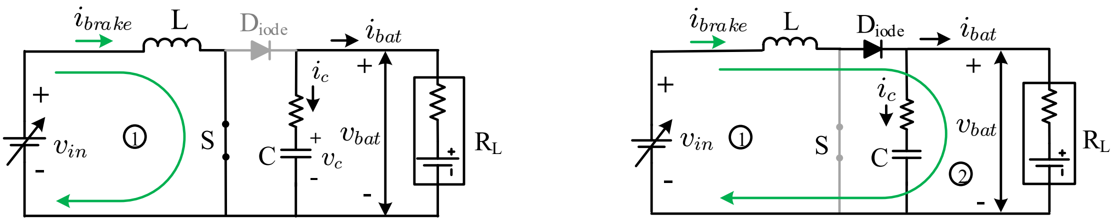

(a) (b)

Figure 4.6: Equivalent circuit diagram of the braking circuit: (a) switch S is ON, (b) switch S is OFF.

The state-space equations when the switch S is ON is given as

$$\dot{\boldsymbol{x}} = \mathbf{A}_{on}\boldsymbol{x} + \mathbf{B}_{on}\boldsymbol{u}\ , \quad \boldsymbol{y} = \mathbf{C}_{on}\boldsymbol{x} + \mathbf{D}_{on}\boldsymbol{u} \tag{4.7}$$

i.e.

$$\begin{bmatrix} \frac{di_{brake}}{dt} \\ \frac{dv_c}{dt} \end{bmatrix} = \begin{bmatrix} 0 & 0 \\ 0 & -\frac{1}{(C+R_L)} \end{bmatrix} \begin{bmatrix} i_{brake} \\ v_c \end{bmatrix} + \begin{bmatrix} \frac{1}{L} \\ 0 \end{bmatrix} \begin{bmatrix} v_{in} \end{bmatrix} \quad ; \quad \begin{bmatrix} v_o \end{bmatrix} = \begin{bmatrix} 0 & 1 \end{bmatrix} \begin{bmatrix} i_{brake} \\ v_c \end{bmatrix} \tag{4.8}$$

The state-space equations when the switch S is OFF is given as

$$\dot{\boldsymbol{x}} = \mathbf{A}_{off}\boldsymbol{x} + \mathbf{B}_{off}\boldsymbol{u}\ , \quad \boldsymbol{y} = \mathbf{C}_{off}\boldsymbol{x} + \mathbf{D}_{off}\boldsymbol{u} \tag{4.9}$$

i.e.

$$\begin{bmatrix} \frac{di_{brake}}{dt} \\ \frac{dv_c}{dt} \end{bmatrix} = \begin{bmatrix} 0 & -\frac{1}{L} \\ \frac{1}{C} & -\frac{1}{(C+R_L)} \end{bmatrix} \begin{bmatrix} i_{brake} \\ v_c \end{bmatrix} + \begin{bmatrix} \frac{1}{L} \\ 0 \end{bmatrix} \begin{bmatrix} v_{in} \end{bmatrix} \quad ; \quad \begin{bmatrix} v_o \end{bmatrix} = \begin{bmatrix} 0 & 1 \end{bmatrix} \begin{bmatrix} i_{brake} \\ v_c \end{bmatrix} \tag{4.10}$$

Now, the averaged state-space equation is written as

$$\frac{d\mathbf{x}}{dt} = \mathbf{Ax} + \mathbf{Bu} \quad \mathbf{y} = \mathbf{Cx} + \mathbf{Du}$$

Taking the value of $\mathbf{A}_{on}, \mathbf{B}_{on}, \mathbf{C}_{on}, \mathbf{D}_{on}, \mathbf{A}_{off}, \mathbf{B}_{off}, \mathbf{C}_{off}$ and $\mathbf{D}_{off}$ from Equations (4.8) and (4.10), and inserting it into (A.2) the average state-space matrices is calculated and the averaged state-space equation of the braking circuit is given by

$$\begin{bmatrix} \frac{di_{brake}}{dt} \\ \frac{dv_c}{dt} \end{bmatrix} = \begin{bmatrix} 0 & -\frac{(1-d)}{L} \\ \frac{(1-d)}{C} & -\frac{1}{C+R_L)} \end{bmatrix} \begin{bmatrix} i_{brake} \\ v_c \end{bmatrix} + \begin{bmatrix} \frac{1}{L} \\ 0 \end{bmatrix} \begin{bmatrix} v_{in} \end{bmatrix} \quad ; \quad \begin{bmatrix} v_o \end{bmatrix} = \begin{bmatrix} 0 & 1 \end{bmatrix} \begin{bmatrix} i_{brake} \\ v_c \end{bmatrix} \tag{4.11}$$

Equation 4.11 is the average state space equation needed for the SM controller design.

Then, the dynamic average model of the braking current (i.e., the desired variable that needs to be controlled) is given by

$$\frac{di_{brake}}{dt} = \frac{v_{in}}{L} - \frac{v_{bat}}{L} + \frac{v_{bat}}{L}d \tag{4.12}$$

Equation 4.12 is the dynamic equation of the braking current that is used to design the SM control law.

4.3.1 Designing the SM Control Law

In dynamic equation (4.12), the duty ratio 'd' is the control input. For PWM-based SM control applications in power converters, the equivalent control signal 'u_{eq}' in SM control is equivalent to the PWM control signal 'd' duty cycle, i.e., according to the equivalent control method implementation of the SM control [104, 108]. Hence (4.12) can be re-written as

$$\frac{di_{brake}}{dt} = \frac{v_{in}}{L} - \frac{v_{bat}}{L} + \frac{v_{bat}}{L}u \tag{4.13}$$

From the dynamic equation of the braking current (4.13), the control objective becomes clear, that is: *to find an expression for control input u such that it enforces the inductor current i_{brake} to track the reference current i^*_{brake} asymptotically.* For this purpose an error variable $\tilde{i}_{brake}$ is defined, then $\tilde{i}_{brake} = i^*_{brake} - i_{brake}$. It is desired that $\tilde{i}_{brake}$ should approach zero at an exponential rate *i.e.*, $\tilde{i}_{brake} \to 0$ as $t \to \infty$.

The error variable is then described as the *sliding surface* ($s = \tilde{i}_{brake}$) in the state space *i.e.* the instantaneous error variable's trajectory. There are no fixed formulas to define a sliding surface, but there are two guidelines;

(i) choose s such that $s = 0$ helps achieve the control objective.

(ii) make sure that u appears in the first derivative of s, which can also be stated as s must have relative degree one.

The control action u is designed such that it stabilizes the system defined by (4.13) by always keeping the sliding surface $s = \tilde{i}_{brake} = 0$. Then, the gradient of the switching surface is taken as

$$\dot{s} = \frac{di^*_{brake}}{dt} - \frac{v_{in}}{L} + \frac{v_{bat}}{L} - \frac{v_{bat}}{L}u \tag{4.14}$$

Taking $\dot{s} = 0$, the expression for the equivalent control law is expressed as

$$u_{eq} = \left[\frac{di^*_{brake}}{dt} - \left(\frac{v_{in}}{\hat{L}} - \frac{v_{bat}}{\hat{L}}\right)\right]\frac{\hat{L}}{v_{bat}} \tag{4.15}$$

where v_{in} and v_{bat} are the measured value from the sensor. $\hat{L}$ is the nominal value of the inductor accurately measured from the LCR meter.

The equivalent control law simply means if the u_{eq} value is put in (4.14) then $\dot{s} = 0$. Now, taking (4.15), the control law is defined as

$$u = (\bar{u}_{eq} + K\ \mathrm{sgn}(s))\,\frac{\hat{L}}{v_{bat}} \tag{4.16}$$

where K is the sliding gain, sgn is the signum switching function, and $\bar{u}_{eq}$ is given by

$$\bar{u}_{eq} = \left(\frac{di^*_{brake}}{dt} - \hat{f}\right) \tag{4.17}$$

where

$$\hat{f} = \frac{v_{in}}{\hat{L}} - \frac{v_{bat}}{\hat{L}} \tag{4.18}$$

4.3.1.1 Prove of Stability Condition

Now, to ensure that 's' is zero and always remains in the switching surface, a positive definite Lyapunov's function (V) is chosen and expressed as

$$V = \frac{1}{2}s^2 \tag{4.19}$$

By Lyapunov's theorem, the first derivative of the V should be a negative definite, then $\dot{s}$ will be asymptotically stable, and s will go to zero as time tends to infinity. Hence, for a stable system

$$\dot{V} = s\dot{s} \leq -\eta\,|s| \qquad \text{where} \quad \eta > 0 \tag{4.20}$$

where η is a design parameter and is chosen to be a positive number.

To check the sliding condition, (4.16) is substituted in (4.14) and then the reduced equation is as given below

$$\dot{s} = \frac{di^*_{brake}}{dt} - (f + \bar{u}_{eq} + K\ \mathrm{sgn}(s)) \tag{4.21}$$

where

$$f = \frac{v_{in}}{L} - \frac{v_{bat}}{L} \tag{4.22}$$

Now placing the $\bar{u}_{eq}$ from (4.17) in (4.21) and expanding it, (4.21) is reduced to

$$\dot{s} = (\hat{f} - f) - K\ \mathrm{sgn}(s) \tag{4.23}$$

In order for the control law to stabilize the system the control law must meet the sliding condition given below

$$\frac{d}{dt}\left(\frac{1}{2}s^2\right) = s\dot{s} \leq -\eta\,|s| \tag{4.24}$$

Now taking the product of (4.23) with sliding surface s

$$\dot{s}s = s(\hat{f} - f) - K\,|s| \tag{4.25}$$

If K is chosen as $K = F + \eta$, where $F \geq |\hat{f} - f|$ and $\eta > 0$ then

$$\dot{s}s = s(\hat{f} - f) - |\hat{f} - f|\,|s| - \eta\,|s| \tag{4.26}$$

For $|\hat{f} - f| > (\hat{f} - f)$, it can be observed from (4.26) that $\dot{s}s \leq -\eta\,|s|$. Hence, it can be said that the control law defined by (4.16) stabilizes the system defined by (4.14). Since the value of $|\hat{f} - f| = |\tilde{f}|$ is unknown, F is chosen as $F = |\hat{f}|$ which is always greater than $|\tilde{f}|$. To avoid chattering instead of the signum function, the saturation function has been used. Hence, the control law can be rewritten as:

$$\boxed{u = (\bar{u}_{eq} + K\ \mathrm{sat}\,(s))\,\frac{\hat{L}}{v_{bat}}} \tag{4.27}$$

Equation 4.27 is the final SM control law that governs the control action to guide the system trajectory to the sliding surface and generate the magnitude of the control signal ranging from 0 to 1, which acts as the input to the PWM scheme to eventually give us the

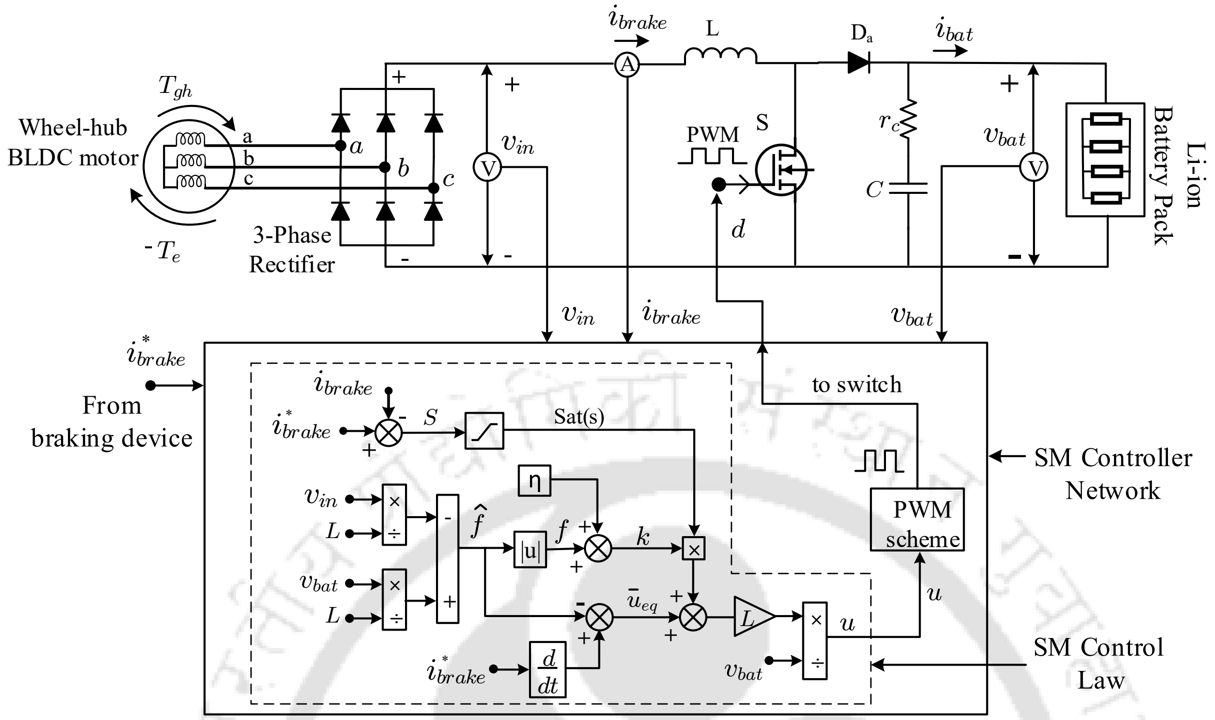

Figure 4.7: Block diagram of the braking circuit configuration with SM controller feedback structure and implementation of SM control law given in (4.27)

duty of the PWM waveform to operate the converter switch. Figure 4.7 shows the block diagram representation of the braking circuit configuration with SM controller feedback structure and implementation of SM control law given in (4.27).

Next, in the following section, the proposed SM control law will be validated in the MATLAB/Simulink environment, followed by experimental validation. The simulation environment and the hardware setup are the same as described in Chapter 3.

4.4 Implementing the SM Controller in Simulation

Figure 4.8 shows the simulation set-up arrangement of the motoring and generator mode power-train drivelines. The initial settings and assumptions made for the simulation study are the same as given in Section 3.4 of Chapter 3. Except the controller block is changed, as seen in Figure 4.8. The parameters for the BLDC motor and boost converter used for the simulation are given in Table B.1 and Table B.2, respectively, of Appendix B.

The implementation of the controller network as illustrated in Figure 4.7 is achieved using inbuilt Simulink mathematical blocks. Figure 4.9 shows the MATLAB/Simulink mathemati-

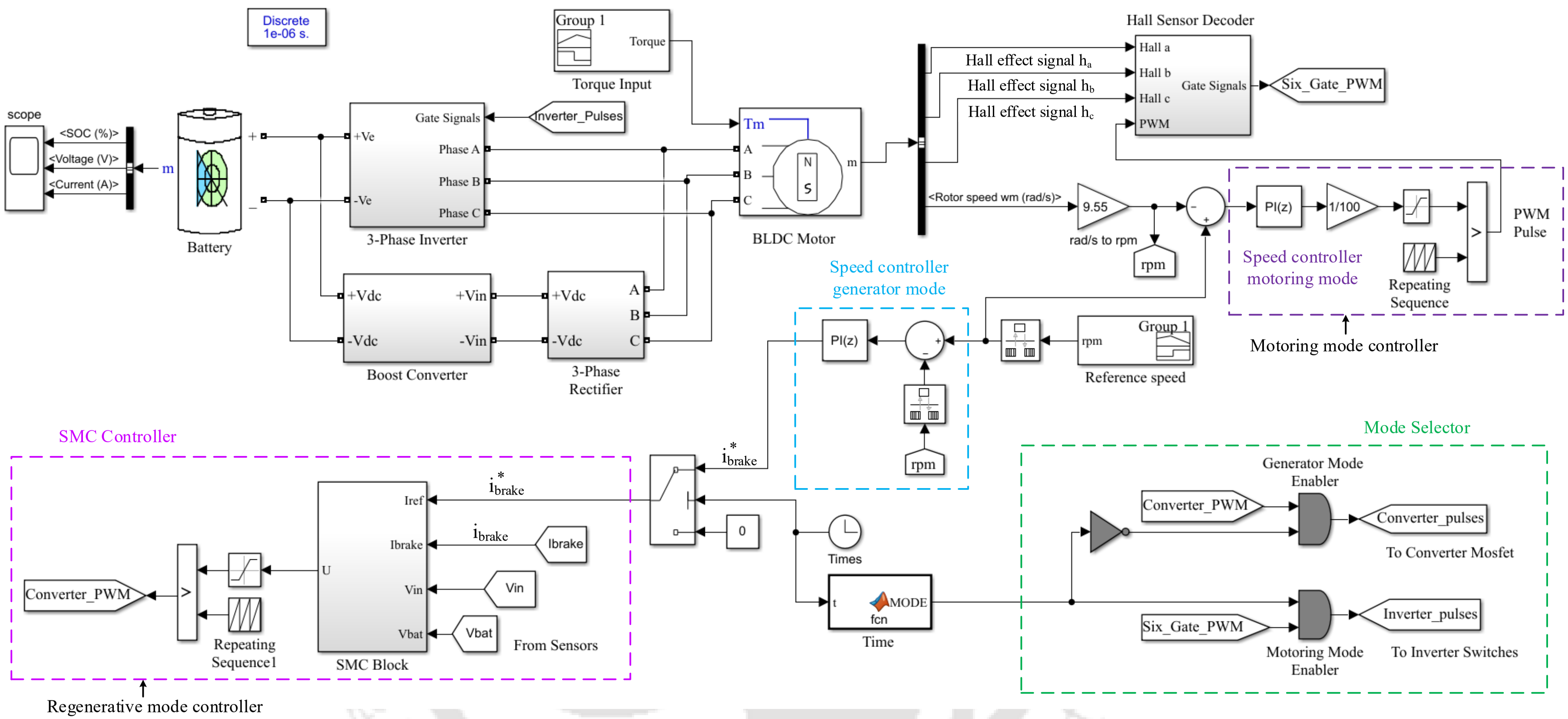

Figure 4.8: Simulation block diagram of the regenerative braking system configuration and its SM controller in a MATLAB/Simulink environment.

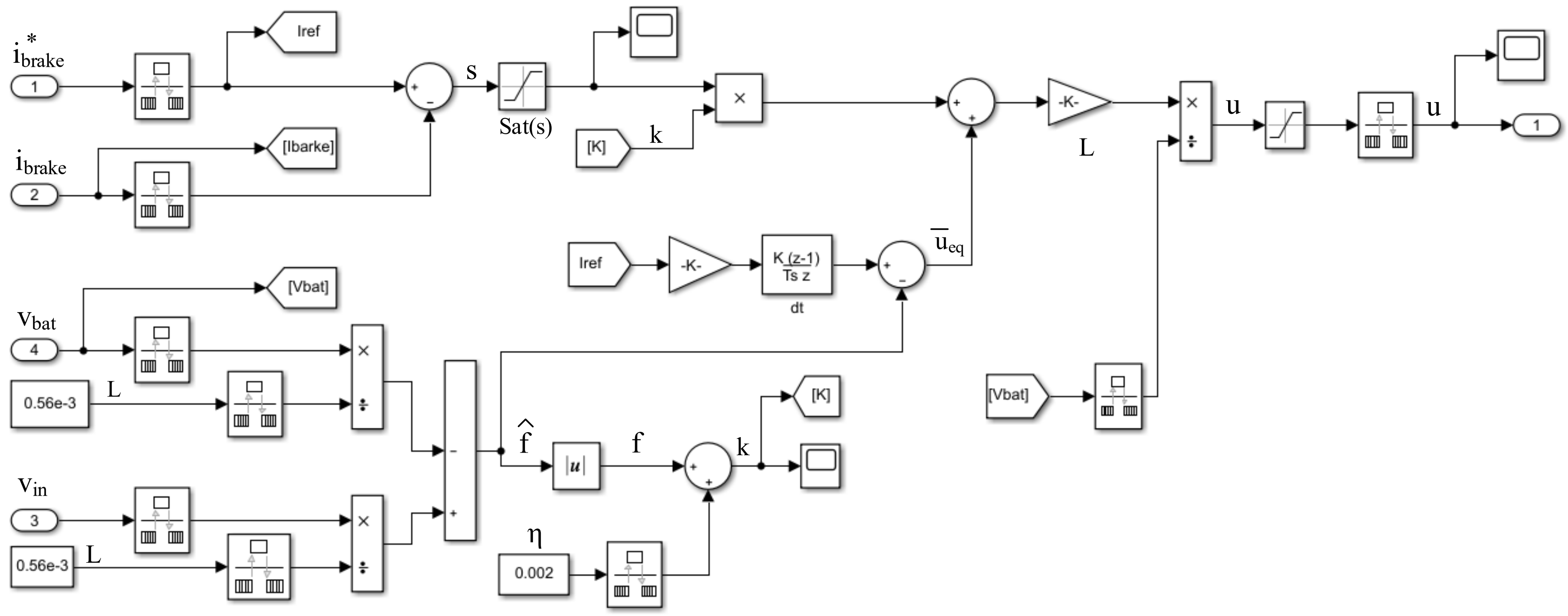

Figure 4.9: The mathematical block model for the implementation of SM control law given in (4.27) in a MATLAB/Simulink environment.

cal block models for the implementation of SM control law given in (4.27). The instantaneous values of i_{brake}, v_{bat}, and v_{in} are sensed from the converter with the help of current and voltage sensors. Here, the sliding surface, which is the difference between the i^*_{brake} and i_{brake}, is sent to the controller saturation function block. The rest of the arrangements made in the Figure 4.9 are the exact implementation of the control law (4.27). To generate the PWM pulse, the output signal (u) from the SM control law is then compared with a saw-tooth waveform generated from a repeating sequence block as shown in Figure 4.8. The repeating sequence generates a periodic saw-tooth waveform of a fixed frequency (100 kHz). The comparator operates as, i.e., its output is HIGH when u is higher than the saw-tooth signal and LOW when the u is lower than the saw-tooth waveform. The peak of u is unity, and for safety purposes, a saturation block is used to contain the pulse width modulation *i.e.*, the duty ratio between 0.1 to 0.8.

During the motoring mode, the speed control of the BLDC motor is achieved using a PI controller block and repeating sequence block to generate the PWM pulse for the inverter switch. The six commutation states of the inverter switch to drive the BLDC motor are obtained using the rotor position provided by the hall sensor. Table B.3 in Appendix B shows the six commutation states from three hall effect sensors used in this work.

Next, to implement the transition between motoring mode and generating mode, a NOT and AND gates are used as outlined in the mode selector block in Figure 4.8, which is the implementation of Figure 3.7 (b). A Simulink function block is used to set the time of the motoring mode and generator mode period, i.e., to generate the command to start and stop the regeneration mode; in real-time, the human driver will give the brake command.

4.4.1 Simulation Results

The simulation results aim to validate the working of the SM controller; hence, only dynamic responses will be analyzed. Figure 4.10 shows the simulation results of the dynamic responses. The simulation is for a short 6 s, just enough to show the dynamic behaviors. That is because of power electronics components like the MOSFET with a switching frequency of

100 kHz; the simulation time step is 1×10^{-6}, which slows the computational speed.

Figure 4.10 (a) plots the mode command signal input given to the simulation system to change between motoring and regeneration modes. The control strategy given is such that at the onset, the mode signal is HIGH, indicating the motoring mode, *i.e.*, the forward motion. In this mode, the motor controller is active, and the inverter pulses are ON, while the regenerative braking circuit is inactive, and the converter pulses are OFF. Then, at 2 s, the mode signal is turned LOW, indicating regeneration mode is ON. Here, in this mode, the regenerative braking circuit is active, the converter pulses are ON, the inverter pulses are OFF, and the motor controller is inactive. Then again, at 4.5 s, the system returns to motoring mode.

Figure 4.10 (b) plots the torque profile, where T_m reference torque shown with dotted lines. During the motoring mode, the T_m is a positive 3 Nm, which acts as the load to the motor. At 2 s, when the regeneration braking commences, the T_m is -3 Nm; the negative T_m value emulates the effect of the free torque due to the gravitational acceleration force F_{gh}. The motor generates braking torque T_{brake} to reach the desired speed. At steady state, it is equal to the T_{gh}, i.e., the torque produced by the gravitational force acting in the direction of motion of the electric vehicle. The dynamic response of T_{brake} is shown in Figure 4.10 (b).

Figure 4.10 (c) plots the motor speed profile. The ω_m^* is the reference speed and is shown with dotted lines. A PI controller is used to regulate the speed and to map its error to the braking current reference (i_{brake}^*). Figure 4.10 (f) plots the converter current profile. At 2 s, the regenerative braking commences upon receiving the braking command and braking force applied by the rider. The SM converter controller will track the braking current reference. The desired braking current starts flowing in the circuit, generating the desired braking torque required to oppose T_{gh} due to the slope. As seen from Figures 4.10 (b) and (d) for $T_{gh} = -3$ Nm input, the braking current drawn is 2.6 A (T_{gh}/kt; kt $= 1.165$) and braking torque 3 Nm is generated.

Due to the opposing electromagnetic braking torque, the speed of the motor drops from 242 rpm to 225 rpm as shown in Figure 4.10 (c). The voltage generated corresponding to

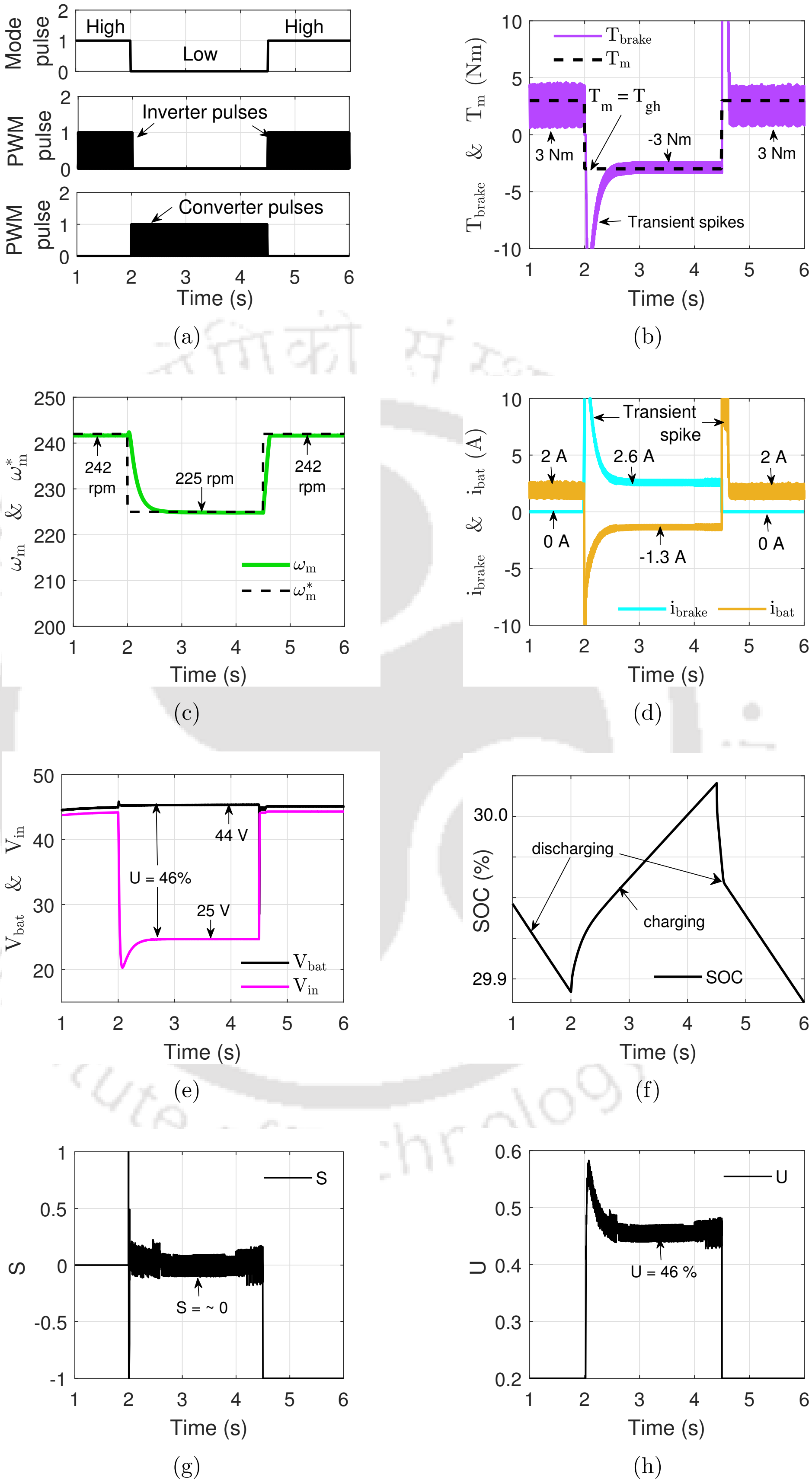

Figure 4.10: Simulation waveforms of the dynamic response (a) mode selector signal, inverter pulses, and converter pulses (b) T_m and T_{brake} (c) ω_m and ω_m^* (d) control input (e) battery SOC (f) i_{brake} and i_{bat} (g) v_{in} and v_{bat} (h) sliding surface.

225 rpm is 25 V, as shown in Figure 4.10 (e). The duty cycle generated by the converter controller is then based on (3.9), and is 46%. The boost converter will boost the input voltage 25 V to that of the battery voltage (42 V, SOC 30%) and let the current flow to charge the battery.

The battery charging current along with the braking current is shown in Figure 4.10 (f). The negative battery current indicates the charging of the battery, which can also be validated from the battery SOC profile given in Figure 4.10 (f). During the motoring period, the SOC decreases as the power is supplied for the traction effort, and during the regenerative braking mode, the SOC increases, indicating a rise in the charge in the battery.

The sliding surface and control input is shown in Figure 4.10 (g) and Figure 4.10 (h) respectively. As postulated, the sliding surface, which is the error difference between the braking reference current and the actual braking current, always remains close to zero. The control input, which is the duty cycle of the PWM signal, is given to the switch of the boost converter for quick convergences to its desired value.

The above discussion shows that the control strategy (mode selection) and SM controller give the desired performance. The DC/DC boost converter-based braking circuit draws the braking current to generate torque and slow the motor speed. The dynamic response shows that the designed controller gives a very good transient response, steady-state performance, and stability. Hence, the simulation results in Figure 4.10 show that the SM control-based controller provides the necessary braking torque and simultaneously charges the battery.

4.4.2 Robustness of the Proposed SM Controller to the Parameter Variation

The robustness of the proposed SM controllers is evaluated by varying the parameter, i.e., the inductance of the inductor of the regenerative braking circuit. The inductor is changed by ±50% to its nominal value. In the simulation, the regenerative circuit is turned ON at time $t = 2$ sec and is turned off at $t = 4.5$ sec, as shown in Figure 4.11. Figure 4.11 (a) shows the variation of i_{brake} for the nominal value of the inductance, inductance increased by 50%

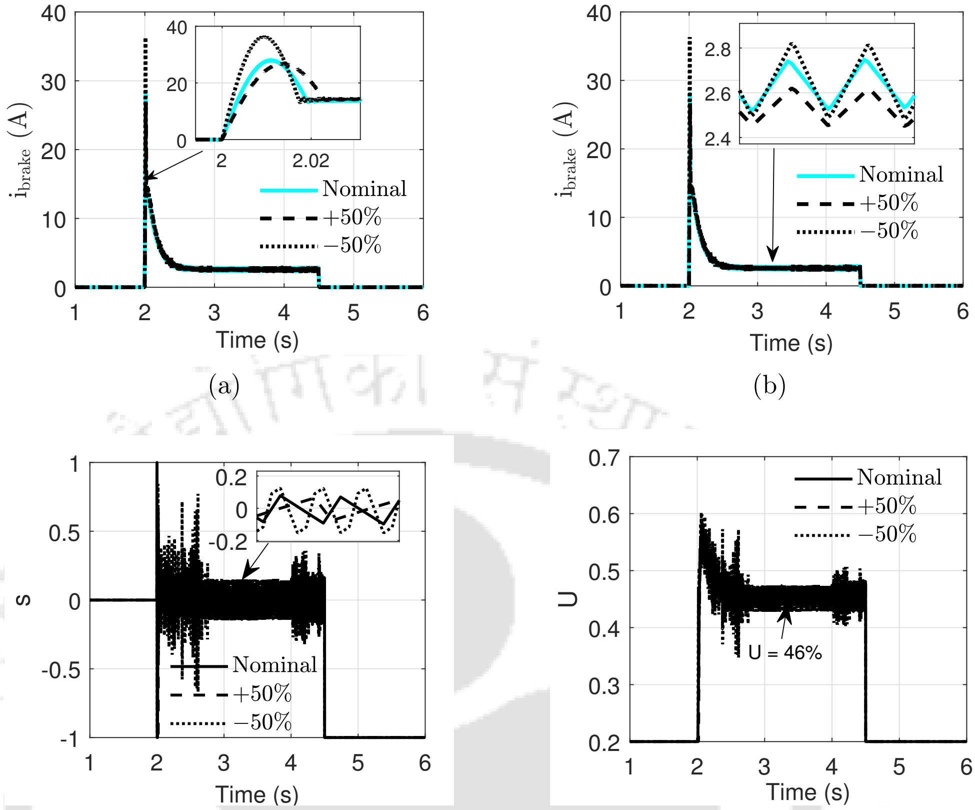

(a) (b) (c) (d)

Figure 4.11: Simulation results with parameter variation (a) transient i_{brake} response (b) steady-state i_{brake} response (c) sliding surface (d) control input.

to its nominal value, and inductance decreased by 50% to its nominal value. During the transition period, there is a very title variation in the braking current with a 50% increase in inductance from its nominal value as seen from the zoomed subplot, but for a decrease in inductance, there is some increase in the transient spike of the braking current as compared to its nominal value. Figure 4.11 (b) shows the same plot as Figure 4.11 (a), but the zoomed subplot is for steady state condition. It is observed that there is a very small variation of the braking currents with ±50 variation in the inductance of the inductor during steady state. Similarly, plots Figure 4.11 (c) and (d) correspond to the sliding surface and control input, respectively. It is observed from these plots that there is a negligible variation in the control input and sliding surface plots for change in the value of the inductor. Hence, it can be concluded the proposed SM controller is robust to parameter variations.

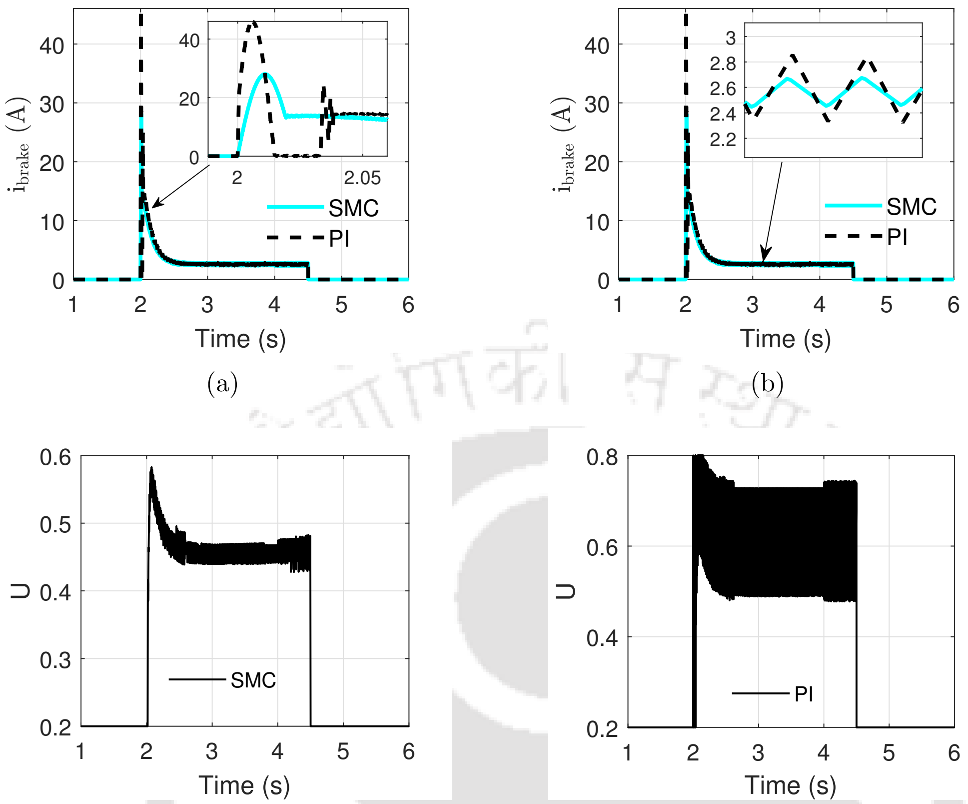

(a) (b)

(c) (d)

Figure 4.12: Simulation results for comparison (a) transient i_{brake} response (b) steady-state I_{brake} response (c) control input response of SM controller (d) control input response of PI controller.

4.4.3 Comparison of SM Controller with PI Controller

A comparison of the transient and steady-state response is shown in Figure 4.12 (a) and (b). In Figure 4.12 (a), the braking current during the transient is shown in the zoom plot, whereas in Figure 4.12 (b), the braking current during the steady state is shown in the plot. In Figure 4.12 (a), the dynamic response of the i_{brake} response waveform with SM controller and PI controller are shown. Here at 2 s, when the regenerative braking circuit is turned on, the i_{brake} with SM control settles at 2.02 s to reach steady-state condition while the PI takes 2.04 s. Also, the transient peak overshoot of the i_{brake} waveform with PI is 73% higher than the SM controller waveform. Then Figure 4.12 (b) shows the steady-state waveform of i_{brake}. Here, the peak-to-peak current ripple is 0.22 A for the SM controller and 0.51 A for the PI controller. The control input due to the SM controller is shown in Figure 4.12 (c), and Figure 4.12 (d) plots the control input due to the PI controller. From Figure 4.12, it can be seen that SMC has a faster-settling response and better steady-state response. Figure 4.12 (c) and (d) shows control input *i.e.* for the SM controller and PI controller; it is observed that the duty cycle has variation in the SM controller as compared to the PI controller.

4.5 Hardware Implementation

The overall hardware set-up is shown in Figure 4.13 (a), and its schematic layout of the hardware connection is shown in Figure 4.13 (b). The details of hardware set-up explained in Section 3.5 of Chapter 3 also apply to this chapter as it is the same setup. The system consists of two power drivelines, one for motoring mode and one for generating mode. Refer to Figure 3.18 in Section 3.5 that shows the block diagram of the hardware set-up for the motoring mode power train. Figure B.1 of Appendix B shows its detailed schematic diagram with circuit connection. Furthermore, for the regenerating mode, refer to Figure 3.19 in Section 3.5 that shows the block diagram representation of the hardware set-up for the regenerative braking mode power train and its detailed schematic diagram with circuit connection is given in Figure B.4 of Appendix B. The implementation of the hardware technique for the mode selection is explained in Section 3.5.1.

4.5.1 Implementing the SM Controller in Hardware

In Section 4.3, the SM control law was designed, and Figure 4.7 presented the block diagram implementation of it on the braking circuit configuration. The SM controller is a full-state feedback controller, as seen from Figure 4.13 (b) the instantaneous values of I_{brake}, V_{bat} and V_{in} are sensed from the converter with the help of current and voltage sensors and then send to the microcontroller via an ADC connection shown in Figure B.6. The microcontroller used here is the STM32F4 Discovery board, as shown in Figure B.4.

Figure B.8 in Appendix B shows the implementation of the controller algorithm with Waijung block set models in MATLAB/Simulink environment. The Matlab/Simulink Waijung block set creates the code for the controller. Waijung is an embedded coder target that enables code generation for the STM32F4 Discovery kit, i.e., it easily deploys the MAT-

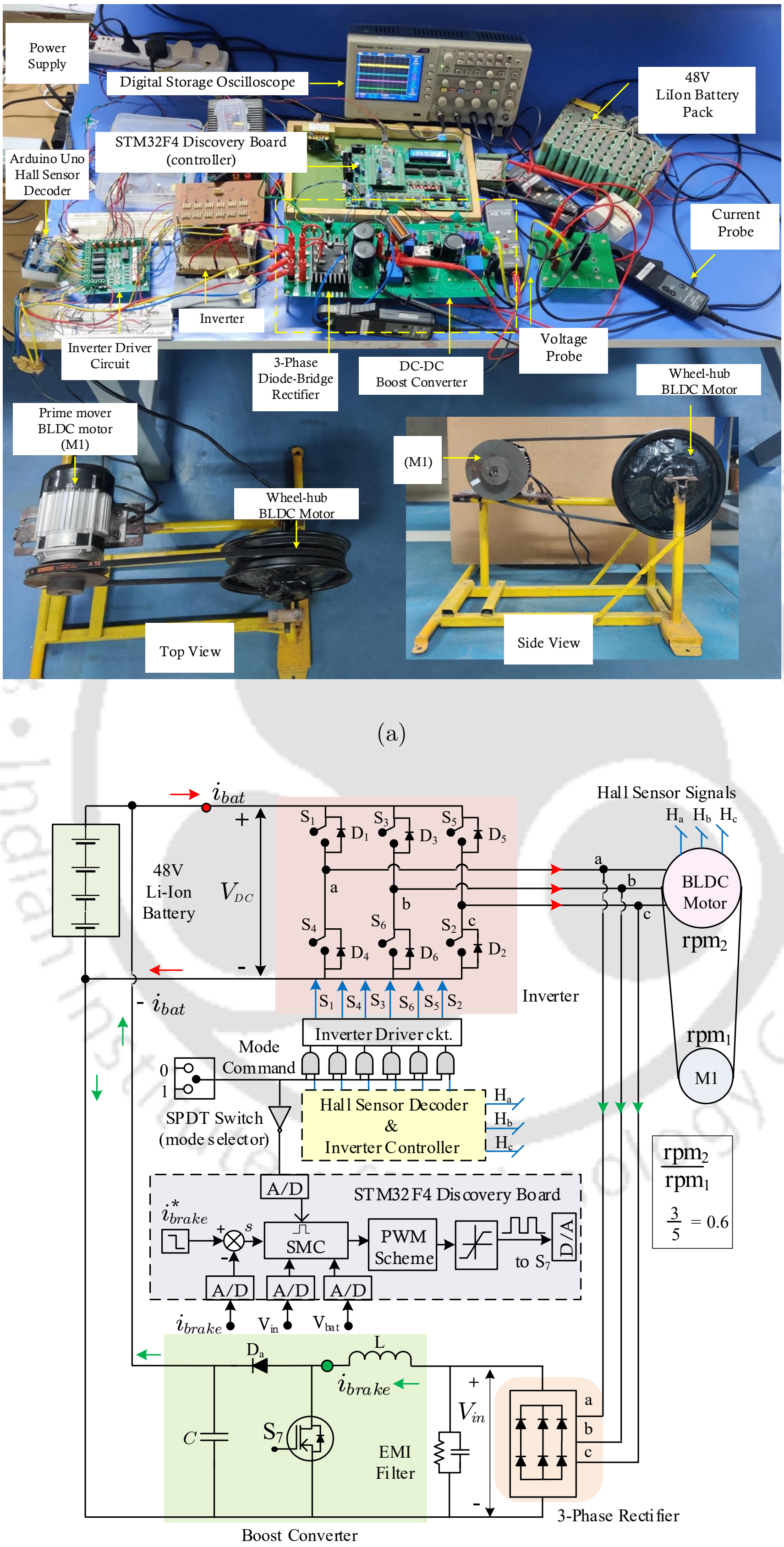

(a)

(b)

Figure 4.13: Hardware set-up (a) laboratory experimental test set-up. (b) simple equivalent circuit connection of the experimental test set-up.

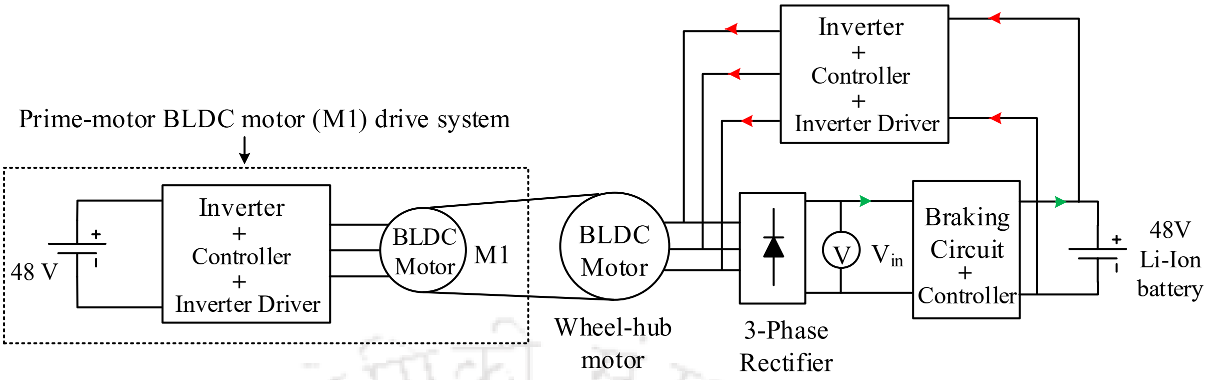

Figure 4.14: Block diagram representation of the experimental set-up to measure the induced voltage of the machine.

LAB/Simulink models to the hardware controller.

4.5.2 Hardware Results

The validation and working of the hardware set-up of the proposed braking system were already described in the experiments 3.5.2 and 3.5.3 of Chapter 3. Here we will only validate the working of the SM controller, i.e., we are interested in the experiment to show the dynamic behavior of the proposed braking system.

Figure 4.14 shows the block diagram representation of the experimental setup. Here, both the motoring and regenerative mode power-train are connected. The experiments aim to demonstrate the switching between two modes and check the SM controller's performance in the transient condition. Figure 4.15 shows a few DSO-captured images from the experiments, which are further explained below.

In Figure 4.15 (a), initially, the wheel hub motor is freely rotated at 270 rpm, and both the motoring mode circuit and the generator mode circuit are inactive. Then, after some moment has elapsed, the regenerative braking circuit is turned ON by manually switching the SPDT switch. The DC/DC current controller regulates itself to track the reference current, set at 2.5 A. It can be observed from the speed waveform that as the braking circuit draws a 2.5 A current, the speed drops to 255 rpm from 270 rpm. The 2.5 A current generates a reverse torque, which opposes the free mechanical torque, decreasing the motor speed. The boost converter sees an input voltage of 29 V for 255 rpm. The duty cycle of the PWM

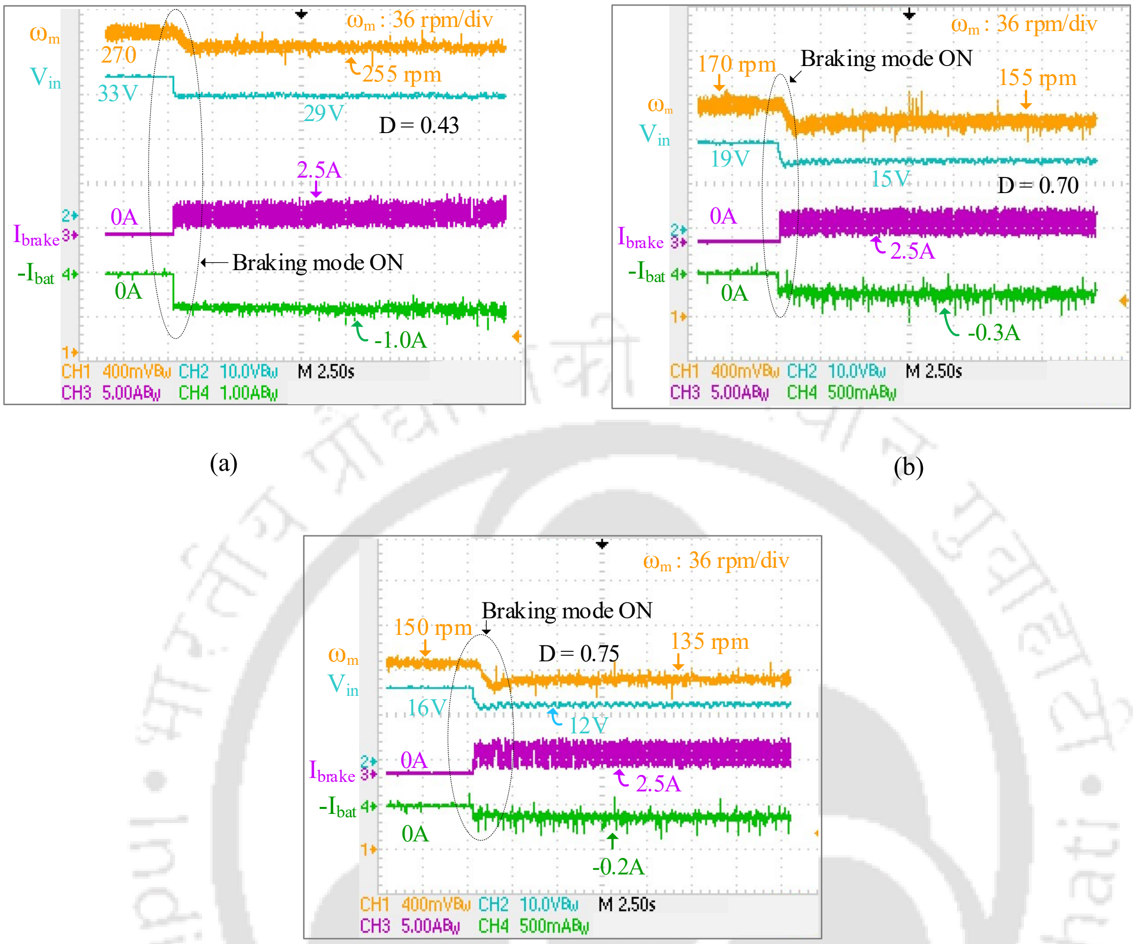

(a)

(b)

(c)

Figure 4.15: Experimental results showing braking action while drawing 2.5 A braking current for motor speed drop (a) from 270 rpm to 255 rpm (b) from 170 rpm to 155 rpm (c) from 150 rpm to 135 rpm.

was measured to be 0.50 for input voltage 29 V and battery voltage 44 V. Similarly, keeping everything else the same Figure 4.15 (b) and Figure 4.15 (c) are the captures for different motor speeds. It is inferred from Figure 4.15 (a), Figure 4.15 (b) and Figure 4.15 (c) that for the same braking current, the higher motor speed results in higher recovery of energy. A higher charging current flow is possible with the higher input voltage since the battery charging current increases with the decrease in the duty cycle for the same braking current.

Next, Figure 4.16 (a) shows the capture of a case of a step-change in the braking current reference. It is seen from the motor speed plot that as the braking current increases from 2.5 A to 3.5 A, the motor speed decreases from 259 rpm to 244 rpm. The SM controller

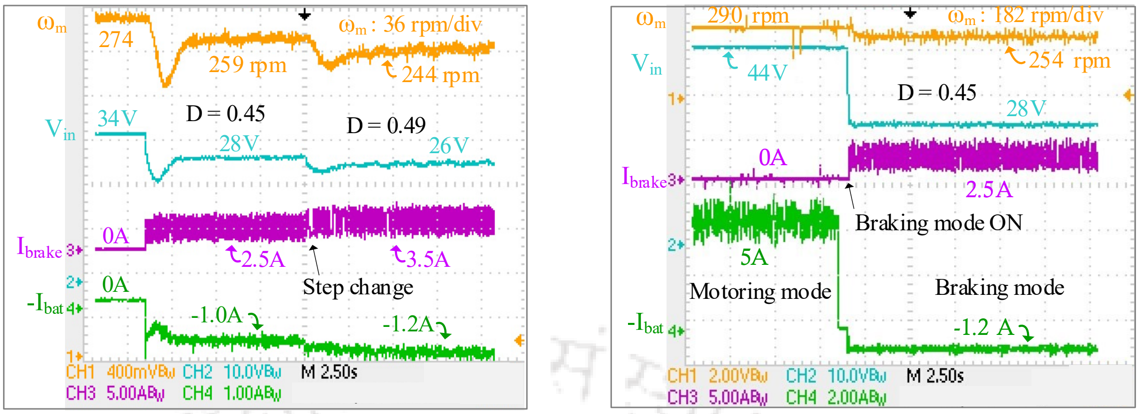

(a) (b)

Figure 4.16: Experimental result showing the motoring and braking mode.

regulates the duty cycle from 0.45 to 0.49 as the voltage input drops from 28 V to 26 V to boost it to the source battery voltage level of 44 V. This figure validates the SM controller's performance to track the change in reference current.

Finally, Figure 4.16 (b) captures the overall control scheme. It shows the successful transition between the motoring and regenerative braking modes. Initially, the M2 is run in the motoring mode at no-load conditions, and a 0.50 duty ratio is given to the inverter pulses. As seen from the figure, during the motoring mode, the motor driveline draws a positive battery current of 5 A and zero braking current. Once the regenerative braking circuit command is given, the braking current starts flowing, and the 2.5 A braking current develops the braking torque, which drops from 290 rpm to 254 rpm. The SMC controller computes the duty cycle of 0.45 for V_{in} equal to 28 V. The hardware results, Figure 4.15 and 4.16 validate the proposed regenerative braking circuit's control strategy and controller design.

In conclusion, the experimental results validate the fast switching technique between the two driving modes, i.e., motoring and regenerating. The hardware implementation of the SM controller performs satisfactorily by tracking the reference current and providing the required braking torque. Overall, the transient response from Figure 4.15 to Figure 4.16 shows that the compensator gives us a good transient response, steady-state performance, and stability.

4.6 Summary

The present Chapter has designed a sliding mode controller for the regenerative braking circuit. The Chapter further evaluates the robustness of the proposed SM controller in the presence of model uncertainties, i.e., for parameter variation. It is observed that the proposed SM controller is robust to parameter variation. Further, a comparison of the proposed SM controller is done with the designed PI controller in MATLAB/Simulink. It is observed that the performance of the SM controller is better than the PI controller, both in the transient and steady states. Further, the performance of the proposed SM controller is also experimentally verified on the laboratory test set-up. Both the simulation and hardware results validate the performance of the proposed SM controller in controlling braking and battery currents. The results show successful braking action and simultaneously charging the battery at a very low-speed range of 24 km/h to 15 km/h, as expected on hilly roads.

5

Application of a Smart Hall-Effect Sensor System for 3-Phase BLDC Drives

Contents

5.1 Introduction

In recent times, the presence of Brushless DC (BLDC) motors is felt in a wide range of applications, like home appliances, automotive, aerospace, consumer, medical, automated industrial equipment, actuators for industrial robots, and instrumentation. Its application in EVs, especially for low-power two-wheelers and three-wheeler applications, has grown exponentially in the last decade. These motors consist of a stator and a rotor, wherein the permanent magnet rotates, and current-carrying conductors are fixed, constituting the stator part. Usually, in the conventional brushed-type DC motor, the brushes make physical contact with a commutator on the rotor to provide an electric path between a DC electric source and the rotor armature winding. However, the BLDC motor instead uses an electronic circuit to aid its excitation and commutation process. The BLDC motors are pretty durable and long-lasting; also, they require less maintenance due to permanent magnet rotors and the absence of brushes for commutation. Due to the elimination of the brushes, i.e., the mechanical contacts from the commutation process, the BLDC motors are noise-free and more reliable in operation. The BLDC motor has gradually replaced the DC motors in many applications because of its simplicity and robustness.

A typical arrangement of BLDC motor drives for an EV application consists of a DC power supply, an inverter circuit with solid-state switches, a driver circuit, and a control system. Figure 5.1 shows the equivalent circuit of the BLDC motor and the 3-phase inverter circuit. It can be seen from the motor drive system that the input to the control system consists of three digital signals from the Hall effect sensors, which provide the rotor position and a current feedback signal for traction control. The knowledge of rotor position is vital to commutate the current in the motor stator windings. In Figure 5.1 S_1, S_3, and S_5 are the high side switches of the inverter and S_2, S_4 and S_6 the low side switches. These switches are turned on by the gate pulses generated from the control block upon receiving the signals from the position sensors.

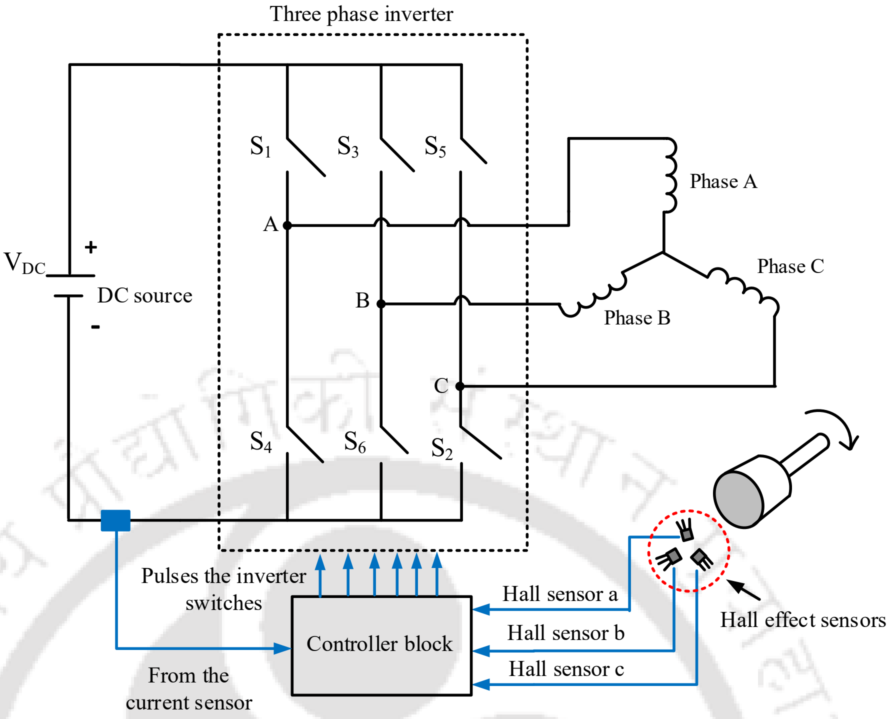

Figure 5.1: Schematic showing the electric drive system of a BLDC motor.

5.1.1 Rotor Position Detection in the 3-Phase BLDC Motor

The rotor position of a 3-phase BLDC motor can be detected using three Hall effect sensors [109, 110] or by zero crossing back-EMF technique for sensorless BLDC motors [111–113]. Sensorless techniques rely on voltage or current sensors, contributing to increased costs due to the requirement for additional filtering and amplifying circuits. In contrast, Hall effect sensors offer a straightforward installation process and present a cost-effective means of locating rotor position. Three Hall effect sensors are employed to detect the rotor position in a 3-phase BLDC motor. These sensors are digital; each indicates whether it is under the north or south pole by giving HIGH or LOW signals, respectively. These Hall effect sensors are also known as position sensors. The three-position sensors will carry binary information of eight combinations, i.e., $2^3 = 8$. These sensors are placed 120° spaced apart from each other in the stationary part of the motor, and the motor starts to rotate, then each of the Hall sensors is HIGH for 180° and LOW for 180° in a complete 360° electrical cycle. For every 60° rotation, the three different signal combinations of the three Hall effect sensors will give one new state. Hence, there are six states in one complete electrical cycle.

Table 5.1: The six states from 3 Hall effect sensors

States	Hall sensor a	Hall sensor b	Hall sensor c	Switches to be ON	The active lines of the stator winding
I	1	0	0	S_1,S_6	AB
II	1	1	0	S_1,S_2	AC
III	0	1	0	S_3,S_2	BC
IV	0	1	1	S_3,S_4	BA
V	0	0	1	S_5,S_4	CA
VI	1	0	1	S_5,S_6	CB

All ones and zeroes signal combinations are not possible in this arrangement. These six states of the three position sensors form the six commutation sequences for firing the 3-phase inverter power switches. As an example, Table 5.2 shows one possible combination of the six states with the corresponding inverter switch and the active stator lines to be active. Figure 5.2 shows the waveforms of the Hall sensor signals, switching signals, and the BLDC motor's switching sequences during the motoring mode. Here E_a, E_b and E_c are the phases of armature back EMF's and i_a, i_b and i_c are the corresponding current. Each sensor is active for 120°, and the combination of the three sensor's positions gives one active state for 60°. The six states and the corresponding active switches are shown in Figure 5.2.

For the motor to rotate, the current commutation is needed to magnetize the stator armature coils such that the poles produced on it at every instant are always non-aligned to the permanent magnet rotor poles. This will produce torque in a 3-phase BLDC motor [110]. The Hall effect sensors are usually positioned such that the magnets change their value before the rotor is in the next commutation position, allowing for the next commutation to be made before the rotor becomes stuck at one position. The controller of the control system receives the signal from the position sensors; the algorithm inside the controller decodes the Hall sensor signals and turns on two switches out of the six inverter switches at a time based on the relation given in Table 5.1. For example, if the controller reads the '100' state, the inverter switches S_1, and S_6 will be turned ON, and if it reads '110', then S_1, and S_2 will be turned ON. Similarly, for other states, the required switches are turned ON.

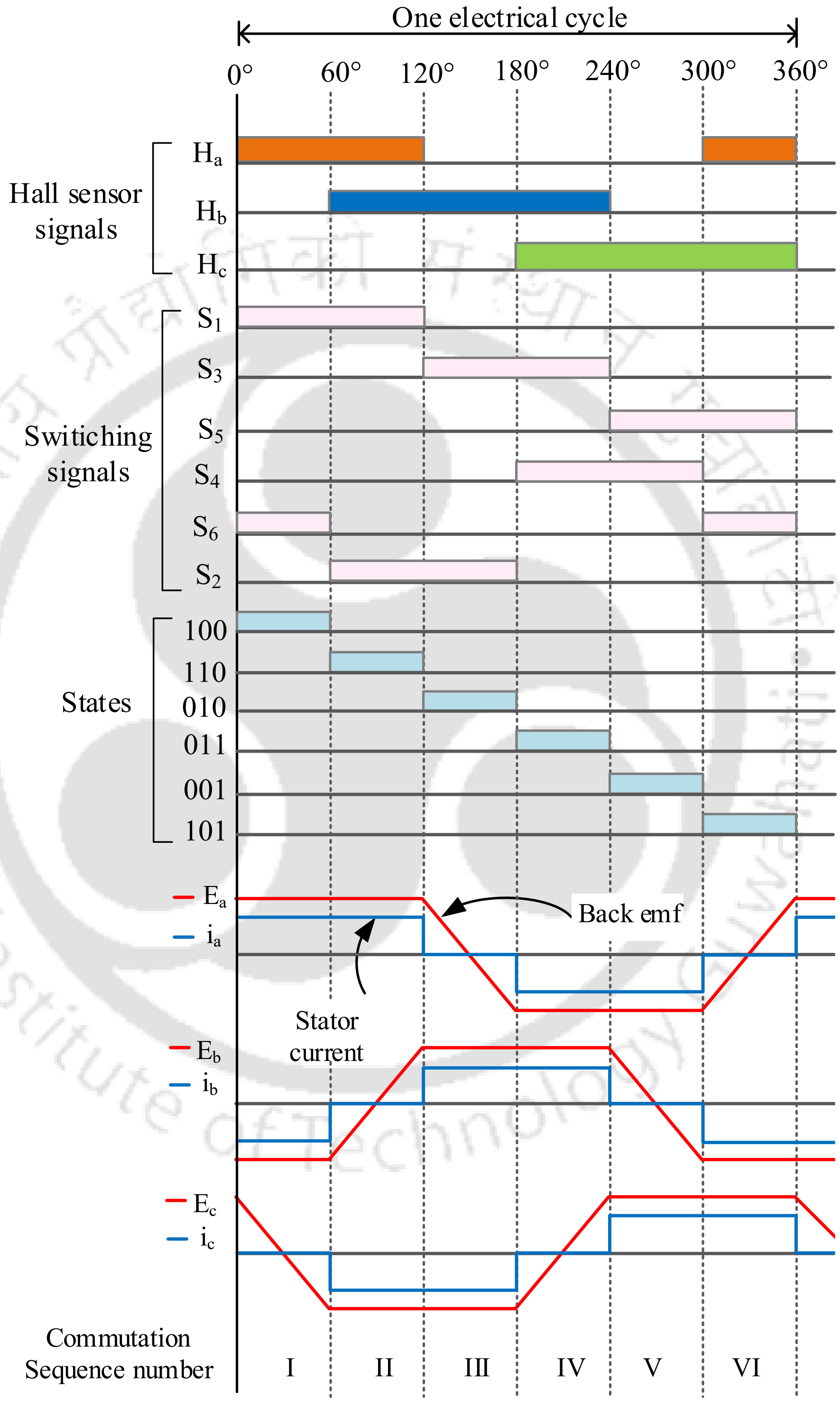

Figure 5.2: Hall sensor signals, switching signals, back EMFs, and armature current waveforms.

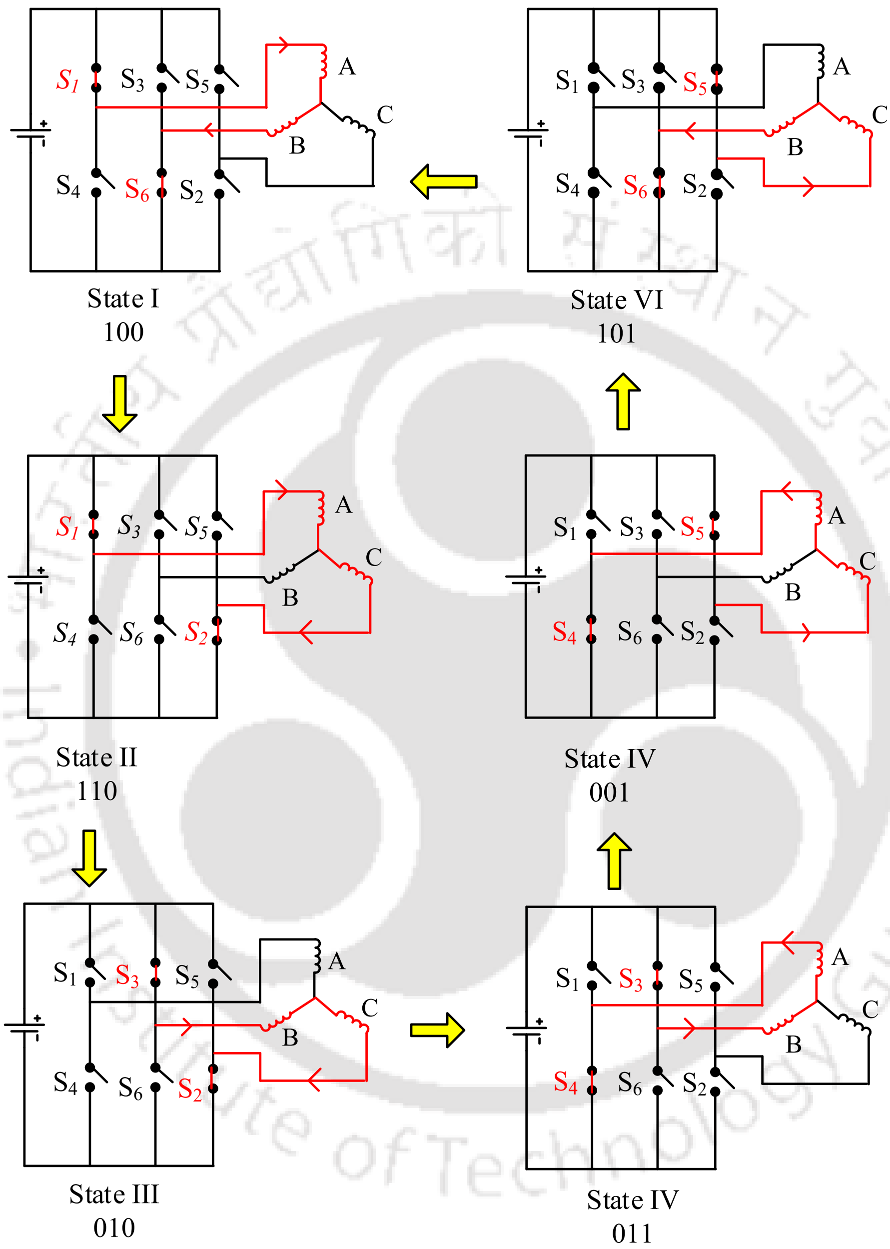

Figure 5.3: The six commutation stages of a 3-phase BLDC motor.

Figure 5.2 shows the related signal waveform of Table 5.1 for one electrical cycle of the 3-phase BLDC motor in steady-state motoring mode. Combining the information from Figure 5.2 and Table 5.1, the six-step commutation process of a 3-phase BLDC motor is chronologically shown in Figure 5.3 with the equivalent inverter circuit and BLDC motor circuit. From the figure, it is seen that at every state, a new pair of inverter switches are triggered, which means for every state, two phases of the stator winding are active, and the third one is floating. The red color lines in Figure 5.3 are two active lines. This process is called 120° commutation for BLDC motors with trapezoidal induce voltage waveform. Hence, from the brief introduction and understanding of the working of the Hall sensor for a BLDC motor drive system, it is inferred that it is crucial to have the correct rotor position knowledge to develop a functioning motor driver circuit.

In this Chapter, we are interested in the faults associated with the Hall effect sensor. As explained above the whole operation of the BLDC drive depends upon the signals obtained from the Hall sensors. Sometimes, the Hall sensors might produce unwanted glitches or entirely go dead due to ageing, extreme heat, jerking, loose wire connections, etc., leading to a wrong switching sequence of the inverter switches. This situation can cause the motor speed to oscillate and vibrate due to the fluctuations in motor current, which again is caused by uneven excitation of the inverter switches. Hence, even though Hall effect sensors are reliable, less inexpensive, and easy to integrate into the motor drive system, their reliability can be further increased with a simple protection layer in terms of a good fault diagnosis and its remedy.

The nature of the fault in the Hall effect sensor system may vary; for example, case one where all three Hall sensors are healthy, but a fault may arise due to the misalignment in the sensor position or due to some delay or damage in the signal conditioning circuit, and, the second case is dealing with the unhealthy Hall sensor, i.e., one or more of the Hall sensor is damaged. There is complete obstruction of the signal in the latter case. Various FD and SR methods have been proposed in the past and present to improve the reliability of Hall-sensor-based BLDC motor drives. A brief comprehensive literature review on various methods to detect the fault and mitigating has been given in Sub-Section 1.3.3 of Chapter 1. Unlike the previous work, which demands substantial computational resources for implementing coordinate transformations, state and vector observers, or requiring additional circuits, here in this chapter, we present a simple and smart Hall effect sensor system that detects the fault and keeps the BLDC motor working despite one hall effect sensor being damaged. The algorithm is simple, making it well-suited for low-cost microcontrollers.

This chapter provides a scheme to increase the reliability of the Hall sensors system, enabling the motor to run smoothly despite one damaged sensor, i.e., rotor positions will be decoded from the remaining two working sensors of the 3-phase BLDC drive system. This scheme gives intelligence to the sensor unit and redundancy to the 3-phase BLDC drive system. The remaining chapter is organized as follows: the problem statement is given in Section 5.1.2. Then, in Section 5.2, the proposed smart Hall-effect sensor system is explained. Followed by its implementation in MATLAB/Simulink environment in Section 5.3. Finally, the chapter ends in Section 5.3 with the summary of the chapter.

5.1.2 Problem Statement

The problem associated with one of the Hall effect sensors getting damaged is further explained below. Suppose the two-wheeler using a BLDC motor is running, and suddenly, one of the Hall effect sensors out of three gets damaged. Then, the remaining two sensor signals will carry binary information of four possible combinations, i.e., $2^2 = 4$. The damaged Hall sensor will not respond to the rotor poles and will show a null value. In such a situation, the three-Hall sensor combination will show a state '000'. Table 5.2 shows the four states from two effective Hall effect sensors if Hall sensor 'a' gets damaged. During this condition, the microcontroller of the control block will always see a low for the Hall sensor 'a' signal; hence, the available four combinations from the controller will be 000, 010, 011, and 001. Figure 5.4 (a) shows the waveform of sensor signals and the state duration at this fault condition.

Similarly, Table 5.3 shows the four states from two effective Hall effect sensors if Hall

Table 5.2: The four states when Hall sensor ‘a’ is not working

States	Hall sensor a	Hall sensor b	Hall sensor c
I	0	0	0
II	0	1	0
III	0	1	1
VI	0	0	1

Table 5.3: The four states when Hall sensor ‘b’ is not working

States	Hall sensor a	Hall sensor b	Hall sensor c
I	1	0	0
II	0	0	0
III	0	0	1
VI	1	0	1

Table 5.4: The four states when Hall sensor ‘c’ is not working

States	Hall sensor a	Hall sensor b	Hall sensor c
I	1	0	0
II	1	1	0
III	0	1	0
VI	0	0	0

sensor ‘b’ gets damaged. During this condition, the microcontroller of the control block will always see a low for the Hall sensor ‘b’ signal; hence, the available four combinations from the controller will be 000, 001, 101, and 100. Figure 5.4 (b) shows the waveform of sensor signals and the state duration at this fault condition. Table 5.4 shows the four states from two effective Hall effect sensors if Hall sensor ‘c’ gets damaged. During this condition, the microcontroller of the control block will always see a low for the Hall sensor ‘c’ signal; hence, the available four combinations from the controller will be 000, 100, 110, and 010. Figure 5.4 (c) shows waveform sensor signals and the state duration at this fault condition.

If we investigate and compare the original signal waveform in Figure 5.2 with Figure 5.4. We can see that when all three Hall sensors are working, each state’s duration is 60° degrees

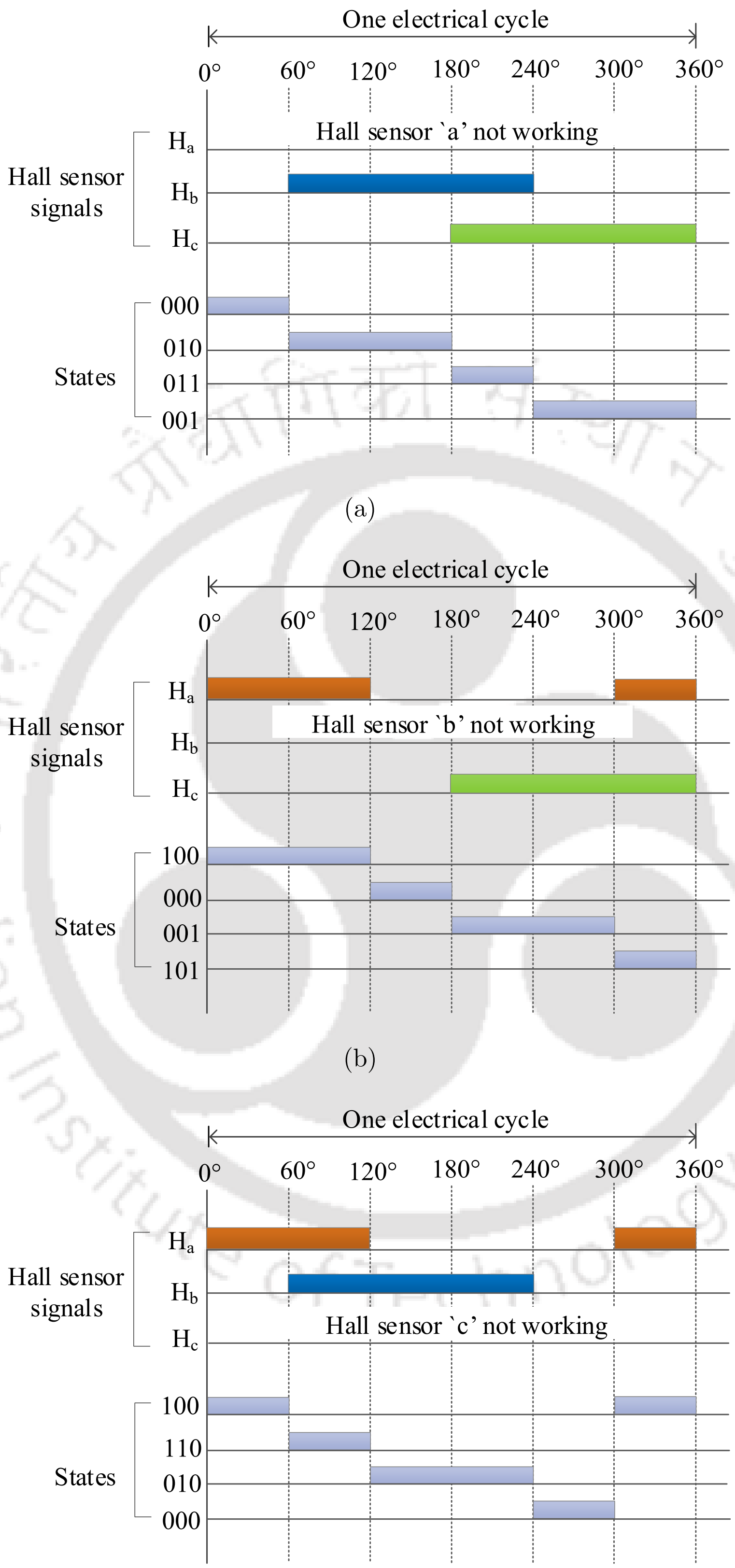

(a)

(b)

(c)

Figure 5.4: Signal waveforms of the four states with only two Hall Effect sensors are working.

as shown in Figure 5.2. However, during fault conditions, we have two states, '000' and '011', for 60° duration each and two states, '010' and '001', for 120° duration each when Hall sensor 'a' is damaged as shown in Figure 5.4 (a). Similarly, for Hall sensor 'b', the two states, '000' and '101', for 60° duration each, and two states, '001' and '100', for 120° duration each when Hall sensor 'b' is damaged as shown in Figure 5.4 (b). Further, for Hall sensor 'c', the two states, '000' and '110', are for 60° duration each, and two states, '100' and '010', are for 120° duration each when Hall sensor 'c' is damaged as depicted in Figure 5.4 (c).

The challenge here is to keep running the BLDC motor smoothly despite one Hall sensor not working. If we can find a way to split the two 120° duration states as shown in Figure 5.4 into two states of 60° each, then by doing so, six independent states can be achieved, which can further be used, like the six firing states for the inverter, so that the BLDC motor keeps running even with only two Hall effect sensors active. In the following section, a smart hall sensor signal decoder system will be presented that will detect the fault, decode the six commutation states from two active hall sensors and allow the BLDC motor to continue running in emergency mode before replacing the damaged hall effect sensor.

5.2 The Proposed Smart Hall-Effect Sensor System

As outlined in the previous section, the goal of the proposed work is to operate the BLDC motor under a fault condition, i.e., when one of the Hall sensors is not working. Algorithm 1 shows the pseudo algorithm of the proposed smart Hall effect sensor system. It is smart because it enables the Hall sensor decoder system to detect the fault independently and decode the six states from the available four states to continue the motor running despite the fault. As seen from the logic of Algorithm 1, the first task of the proposed algorithm is to identify the fault, the second is to check which Hall effect sensor is damaged, and the third is to decode Hall sensor signals into the six commutation states from available four states. Below is a description of what the algorithm does.

The smart Hall sensor signal decoder keeps tracking the '000' state at every iteration of the program. Suppose an invalid state '000' is not detected. In that case, the normal function

Algorithm 1: The algorithm of the proposed smart Hall effect sensor system.

```
initialization;
if State $\neq$ "000", i.e. normal state then
    • All Hall sensors working;
    • Call the scheme in Figure 5.2;
else
    if next state = "010" then
        • Hall sensor 'a' is damaged;
        • Call the scheme in Figure 5.5;
    end
    if next state = "001" then
        • Hall sensor 'b' is damaged;
        • Call the scheme in Figure 5.6;
    end
    if next state = "010" then
        • Hall sensor 'c' is damaged;
        • Call the scheme in Figure 5.7;
    end
end
```

is called, which decodes the six commutation states for the normal switching operation from the three Hall sensor signals as per the relationship in Table 5.1. When an invalid state '000' is detected, then a new function is called, which will do two things: first, a counter is initiated to measure the HIGH period of the '000'; as soon as the '000' goes LOW, the counter stops, and it will store the value. Second, the algorithm will identify the damaged Hall sensor; to do this, it will check the next state. Suppose the next state is '010'. Then it calls for the function to execute the algorithm with the Hall sensor 'a' damaged, whereas if the next state is '001', then the function to execute the algorithm with the Hall sensor 'b' damaged is called, and if the next state is '100' then it calls for the function which executes the algorithm for Hall sensor ‘c’ damaged.

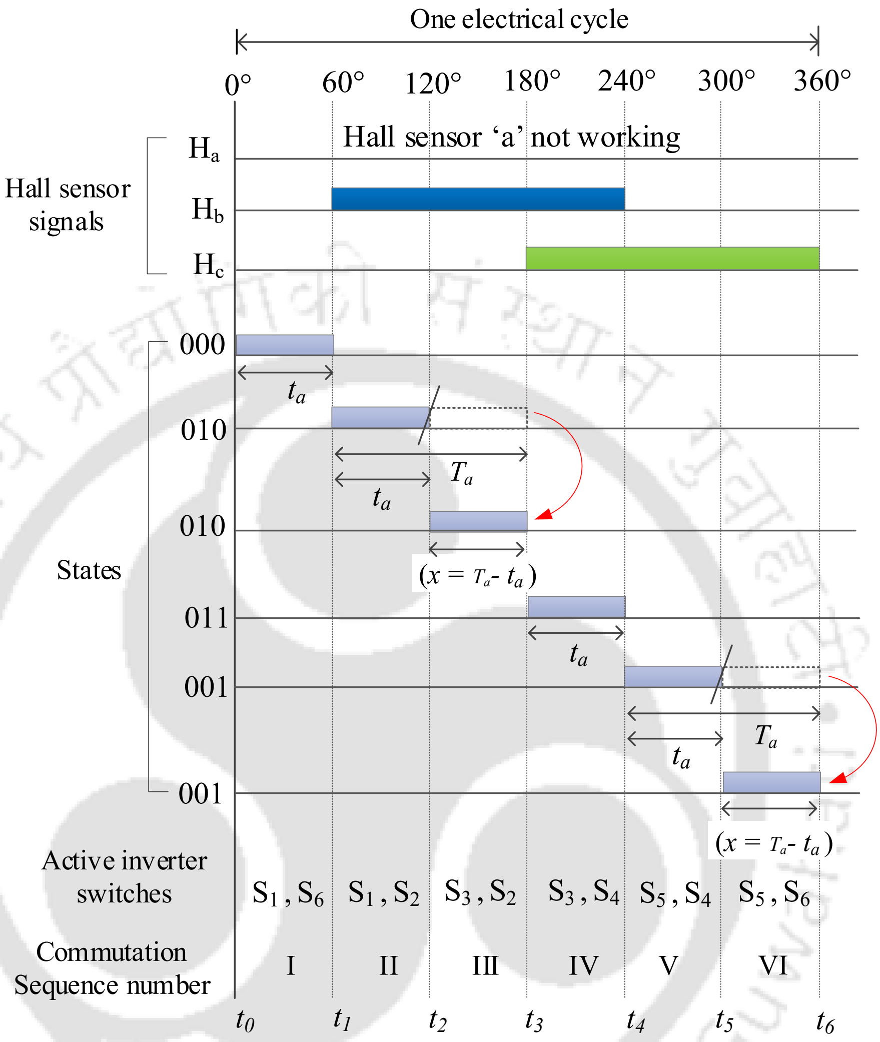

Figure 5.5: The pictorial representation of the theory behind obtaining six states from the four states when Hall sensor ‘a’ is not working.

Table 5.5: The six states from 2 Hall effect sensors when Hall sensor ‘a’ is not working

States	Hall sensor a	Hall sensor b	Hall sensor c	Switches to be ON	The active lines of the stator winding
I	0	0	0	S_1,S_6	AB
II	0	1	0	S_1,S_2	AC
III	0	1	0	S_3,S_2	BC
IV	0	1	1	S_3,S_4	BA
V	0	0	1	S_5,S_4	CA
VI	0	0	1	S_5,S_2	CB

For further explanation, consider the case where Hall sensor ‘a’ is damaged; the controller will read the ‘000’ state when the fault occurs. Referring to Figure 5.5, let us say that at t_0, the ‘000’ state goes HIGH, then inverter switch S_1 and S_6 are turned ON, and simultaneously a counter is initiated; it will start counting until t_1, when the ‘000’ goes LOW then the counter value is saved to a new variable ‘t_a’. At t_1, when ‘010’ is HIGH, the inverter switches S_1 and S_2 are turned ON, and a timer with the counter value ‘t_a’ is initiated. When the timer is completes its counting, i.e. at t_2, the inverter switches S_3 and S_2 are turned ON. Then the next state, ‘010’, will be broken down into two states, where the first half will be high for the duration equal to ‘t_a’ seconds, and the second half will be HIGH for the duration equal to ‘$T_a - t_a$’ seconds, where ‘T_a’ is the high total duration of state ‘010’. Here ‘t_a’ is 60° in terms of electrical degree, and ‘T_a’ is 120° as illustrated in Figure 5.5. Similarly, at ‘t_3’ when the second definite state ‘011’ is HIGH, then inverter switch S_3 and S_4 are turned ON, and simultaneously a counter is initiated; it will start counting until ‘t_4,’ i.e. when the ‘011’ goes LOW then the counter value is saved to a new variable ‘t_a’. At ‘t_4’, when ‘001’ is HIGH, the inverter switches S_5 and S_4 are turned ON, and a timer with the counter value ‘t_a’ is initiated. When the timer is completed, i.e. at ‘t_5’, the inverter switches S_5 and S_6 are turned ON. In other words, if the state “011” is high for ‘t_a’ seconds, then the next state ‘001’ will be broken down into two states, where the first half will be high for the duration equal to ‘t_a’ seconds and the second half will be HIGH for the duration equal to ‘$T_a - t_a$’ seconds, where ‘T_a’ is the high total duration of state ‘011’. Here ‘t_a’ is 60° in terms of electrical degree, and ‘T_a’ is 120° as illustrated in Figure 5.5.

In this fashion, the four states from two active Hall sensors and one damaged Hall sensor are broken down into six states needed for the inverter circuit to commute the motor, and the electric two-wheeler containing the motor continues to run with only two Hall sensors without stopping on the run. Table 5.5 shows the final commutation states with the respective active inverter switch and the active stator lines when Hall sensor ‘a’ is damaged.

The same explanation applies when the Hall sensor ‘b’ and ‘c’ is not working. If Hall sensor ‘b’ is damaged, then ‘000’ is preceded by ‘100’ and followed by “001” as shown in

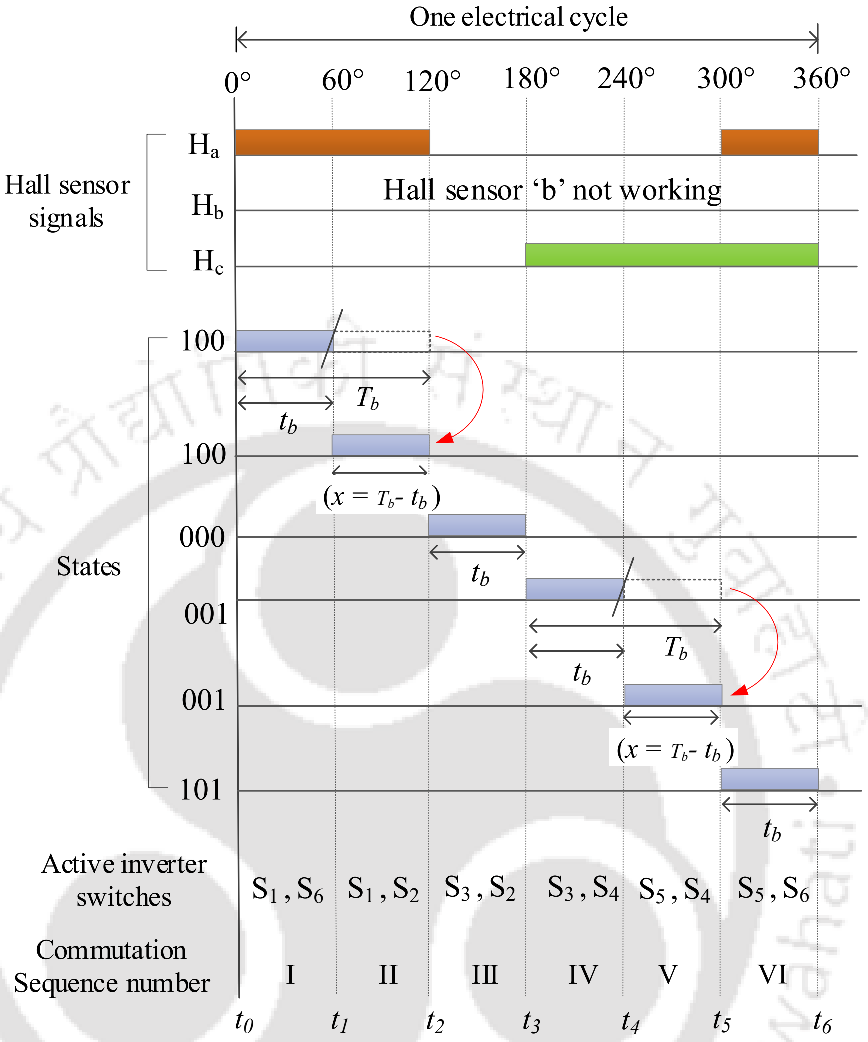

Figure 5.6: The pictorial representation of the theory behind obtaining six states from the four states when Hall sensor 'b' is not working.

Table 5.6: The six states from 2 Hall effect sensor when Hall sensor 'b' is not working

States	Hall sensor a	Hall sensor b	Hall sensor c	Switches to be ON	The active lines of the stator winding
I	1	0	0	S_1,S_6	AB
II	1	0	0	S_1,S_2	AC
III	0	0	0	S_3,S_2	BC
IV	0	0	1	S_3,S_4	BA
V	0	0	1	S_5,S_4	CA
VI	1	0	1	S_5,S_6	CB

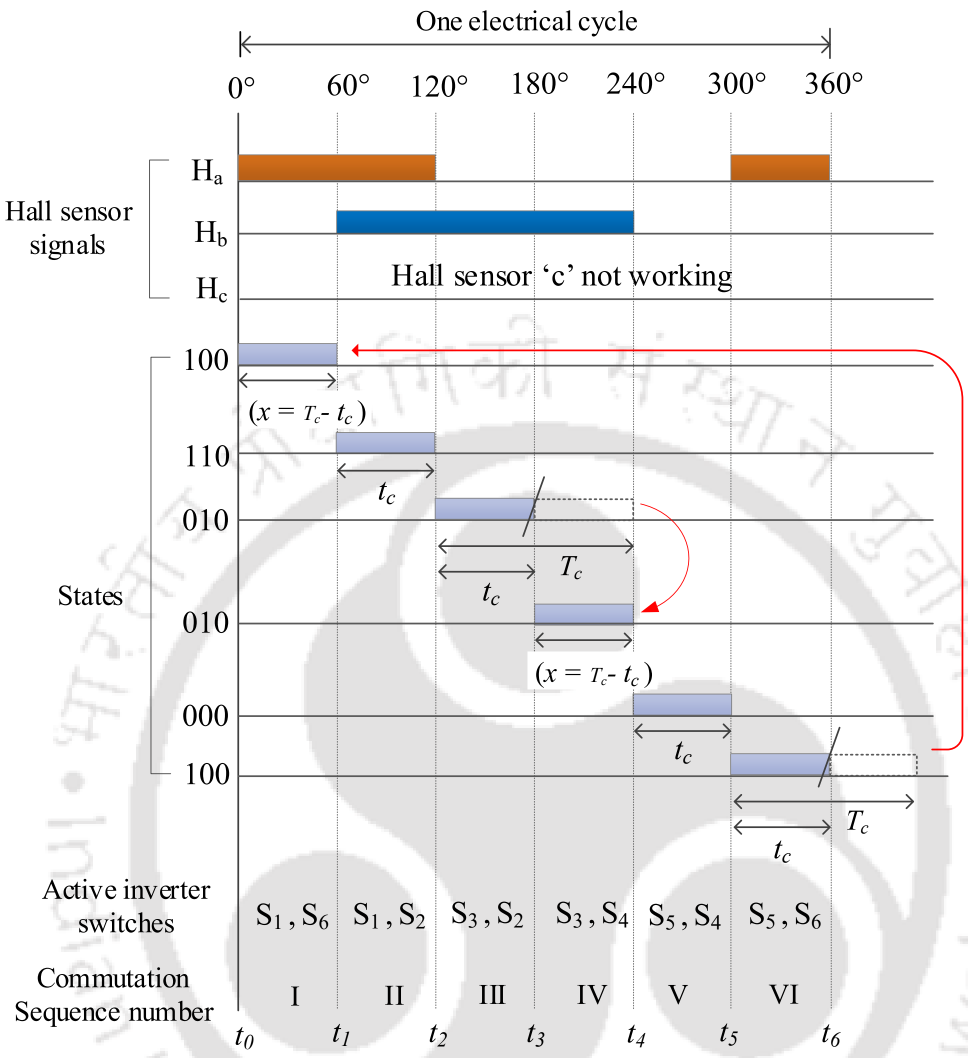

Figure 5.7: The pictorial representation of the theory behind obtaining six states from the four states when Hall sensor 'c' is not working

Table 5.7: The six states from 2 Hall effect sensor when Hall sensor 'c' is not working

States	Hall sensor a	Hall sensor b	Hall sensor c	Switches to be ON	The active lines of the stator winding
I	1	0	0	S_1,S_6	AB
II	1	1	0	S_1,S_2	AC
III	0	1	0	S_3,S_2	BC
IV	0	1	0	S_3,S_4	BA
V	0	0	0	S_5,S_4	CA
VI	1	0	0	S_5,S_6	CB

Table 5.3 and Figure 5.4 (b). If Hall sensor 'c' is damaged, then '000' is preceded by '010' and followed by "100" as shown in Table 5.4 and Figure 5.4 (c). The controller will identify which Hall is damaged and then call for the dedicated function. Figure 5.6 illustrates the concept, and Table 5.6 tabulates the commutation states with the respective active inverter switches and stator lines when Hall sensor 'b' is not working. Similarly, Figure 5.7 illustrates the concept, and Table 5.6 sums it up and tabulates the commutation states with the respective inverter active switches and stator lines when Hall sensor 'c' is not working. The algorithm's working explanation remains the same as what it was when the Hall sensor 'a' was damaged.

5.3 Implementing the Smart Hall Effect Sensor System

The proposed smart Hall effect sensor system is implemented by simulating a BLDC motor drive system in the MATLAB/Simulink environment. Figure 5.8 shows the simulation set-up arrangement. The inbuilt BLDC motor block is fed from a DC source via a 3-phase inverter constituting the motor drive system. As seen from Figure 5.8, the three Hall sensor signals from the motor are fed to the Hall sensor decoder block, which is a MATLAB function block inside which the code for the smart Hall effect sensor is written. The output of the functional block is the decoded six-switch signal of the inverter. In order to emulate the damaged Hall effect signal, another MATLAB function block is used, as shown in the figure, which generates a LOW signal to simulate the sensor faults. Irrespective of which Hall sensor gets damaged, the main program inside the function block remains the same, as shown in Algorithm 1.

5.3.1 Simulation Results

Figure 5.9 is the simulation results plotting the three Hall sensor signals, the six inverter switch pulses, and the BLDC motor speed response. The simulation is run for a total of 0.5 s, the first half of the simulation, i.e., from 0 s to 0.2 s, the BLDC motor is excited with a 25V DC input voltage and a load of 1 Nm. All three Hall sensor signals are fed into the MATLAB function block, which decodes the inverter switching sequence. The motor

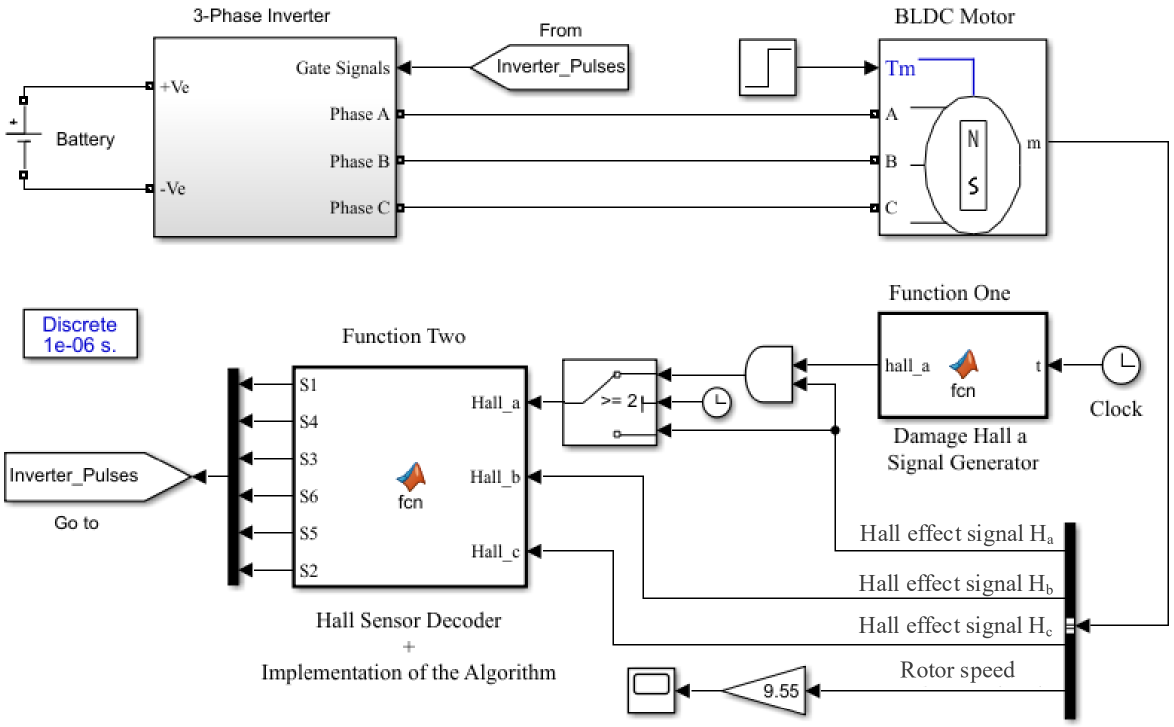

Figure 5.8: Simulation set-up of the BLDC motor drive system to simulate the condition when Hall sensor ‘a’ is damaged in a MATLAB/Simulink environment.

achieves a speed of 200 rpm, as seen in the speed plot. At 0.2 s, the Hall sensor ‘a’ block output is set to a LOW signal to emulate the damaged Hall sensor. When the error signal is fed to the intelligent function block, the algorithm detects it and then implements the scheme as described and explained in Section 5.2 and illustrated in Figure 5.5.

When the error occurs at 0.2 s, it will take a few moments for the algorithm to find the damaged sensor, destabilizing the decoding process, which is reflected in the speed plot of the rpm; there is a dip seen right after the error. However, after a few iterations, the intelligent Hall sensor system can stabilize the decoding, and the motor speed returns to its normal speed. During this adjustment period, there will be glitches in the sequence of the inverter switch. The effect on the switches is shown in the Figure 5.9. When the ‘000’ occurs, it takes a few iterations to process the damaged sensor and start the new decoding process. Similarly, Figure 5.10 and Figure 5.11 shows the simulation results to emulate when hall sensor ‘b’ and ‘c’ are damaged, respectively.

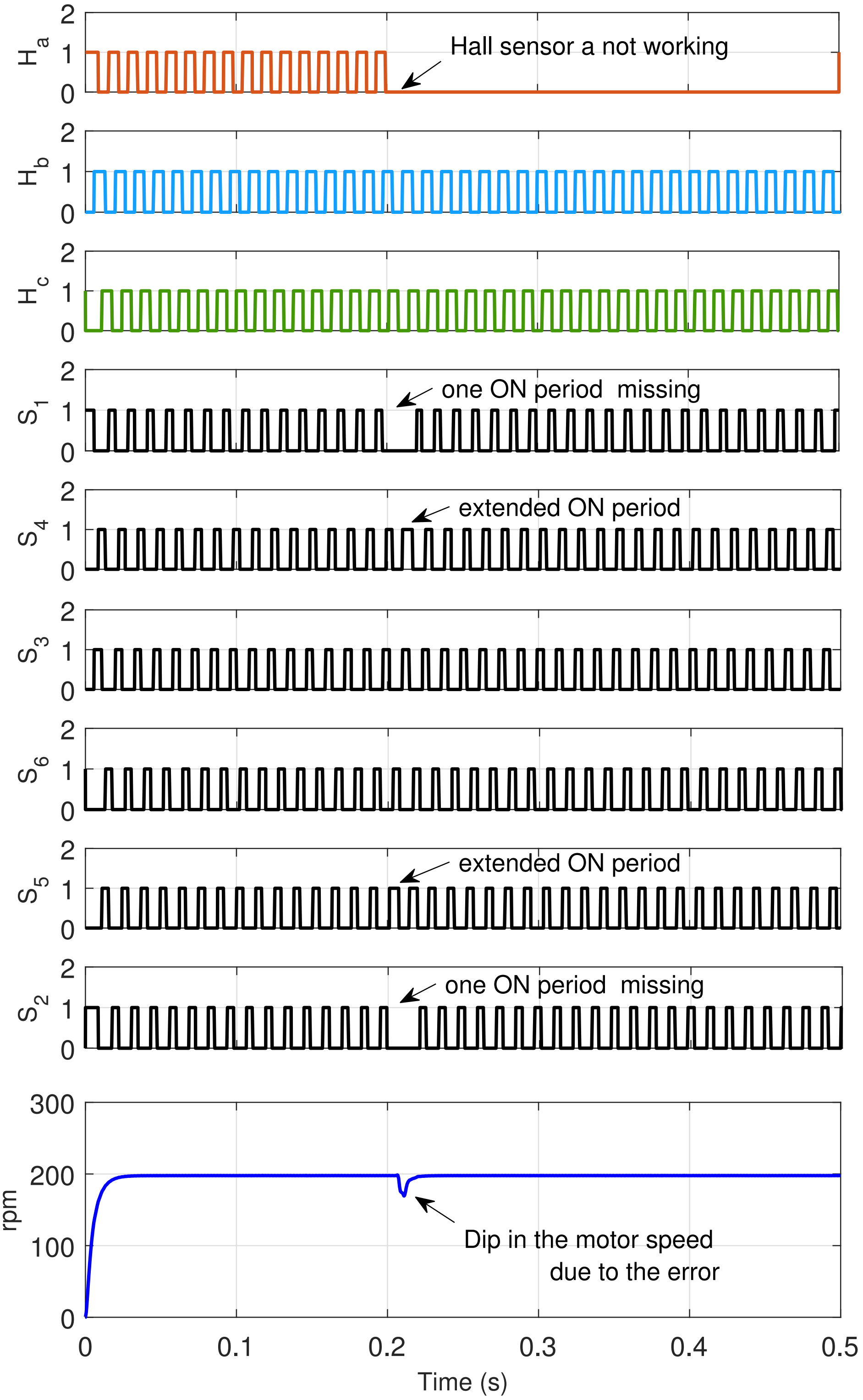

Figure 5.9: Simulation response waveform showing Hall sensor ‘a’ damage and working of the proposed algorithm.

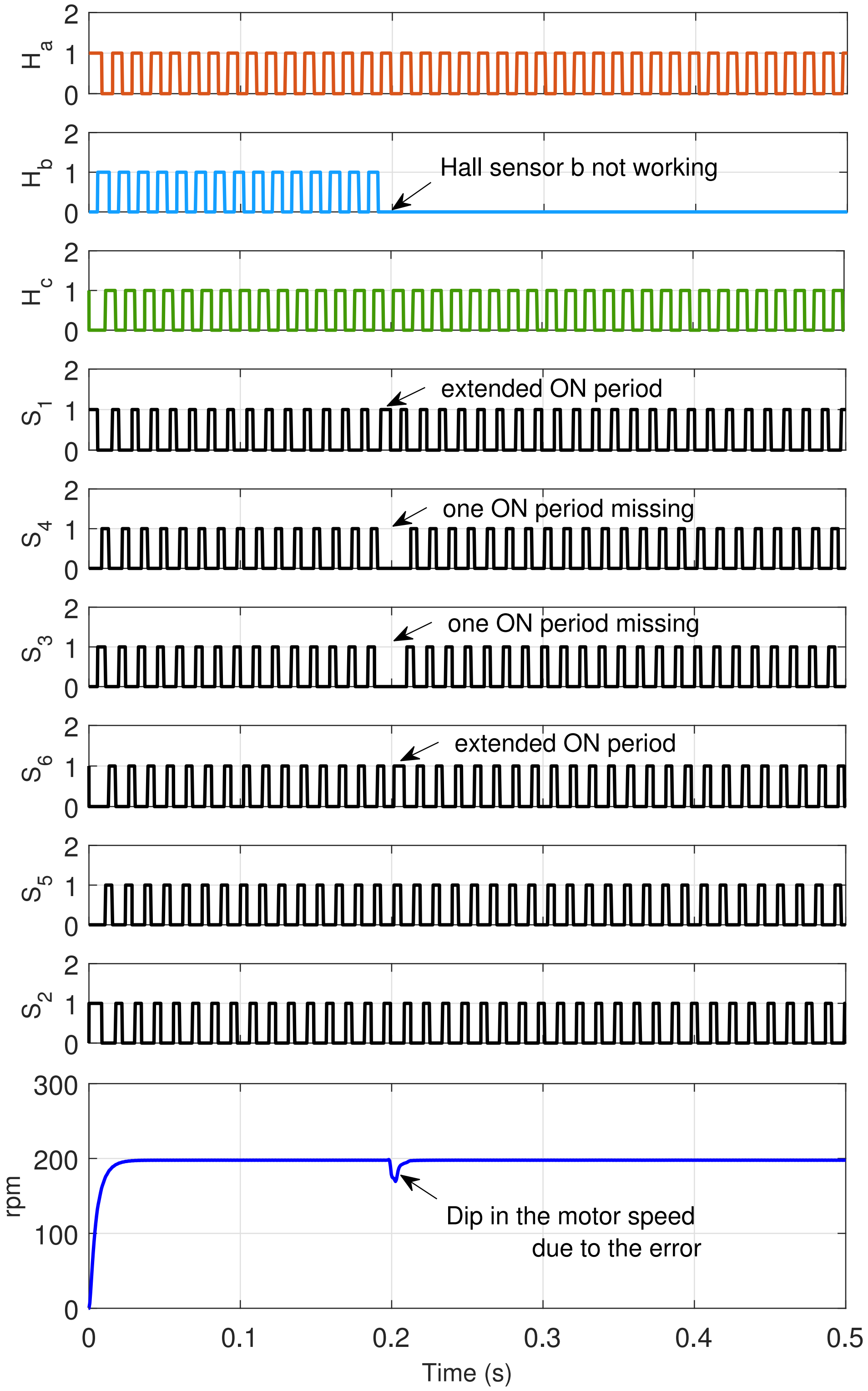

Figure 5.10: Simulation response waveform showing Hall sensor ‘b’ damage and working of the proposed algorithm.

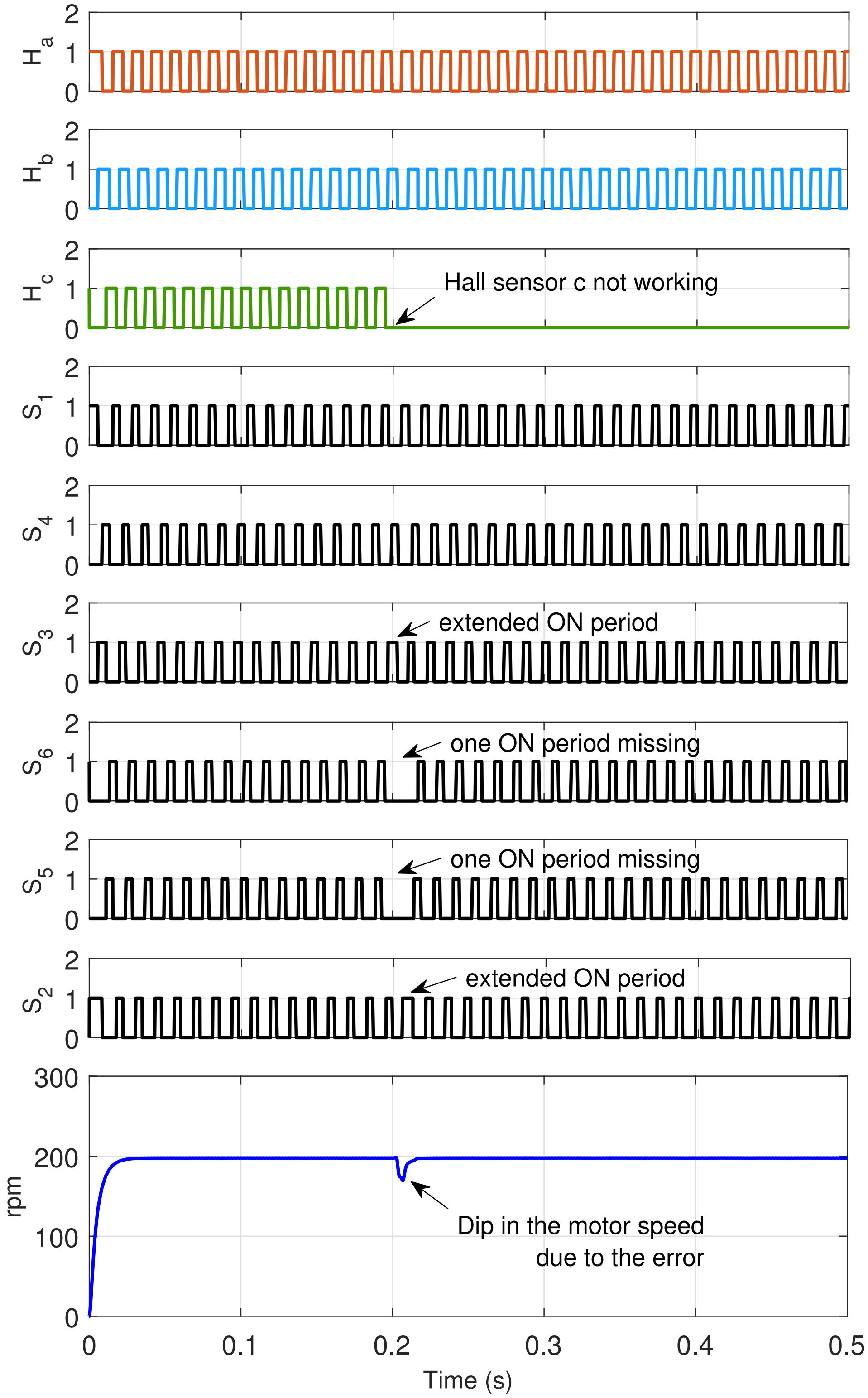

Figure 5.11: Simulation response waveform showing Hall sensor 'c' damage and working of the proposed algorithm.

The Simulation results validate the working of the proposed algorithm to detect the Hall sensor fault and reconstruct the required six signals for the inverter switches from two active hall sensors. The work can be extended in the future to detect two hall sensor faults.

5.4 Summary

The work in this chapter describes the concept of a smart Hall effect sensor system for sensing the rotor position in a 3-phase BLDC motor. The smart sensor system proposed allows the motor to continue working even when one Hall sensor is damaged and not working. The scheme is simple but effective and is particularly suitable for light two-wheelers or robotic arms. The simulation results validate the effectiveness of the proposed algorithm. The future scope of the work is to implement the theory presented in this chapter in a real-time hardware system.

6

Conclusion and Future Scope

Contents

6.1 General Remark

Electric Vehicles, especially electric two-wheelers, are booming in the Indian automobile market. However, their presence is felt less in the cities of the hilly region where the road has frequent up and down slopes. Although EVs have many benefits over ICE vehicles, like being more efficient, reliable, safer, smarter, and environmentally friendly. However, their range is still a major challenge. The range of the EVs further goes down when operating on hilly roads because the road's gradient makes the hilly roads draw a high current, leading to increased power consumption and a quick drop in the battery energy, and eventually a decrease in the range of the EVs. If we only consider the battery power consumption, i.e., kWh per hour, the hilly region roads become unfriendly to EVs. Because of this, the presence of electric two-wheelers is minimal in the hilly region of the country.

Overall, the thesis endeavors to provide readers from diverse backgrounds with a comprehensive understanding of how hilly roads impact electric two-wheelers. It aims to familiarise readers with the challenges of navigating these rugged terrains and offers suggestions to address these issues, making electric vehicles more practical for such conditions. The central focus of the thesis is to present practical solutions for the difficulties faced by electric two-wheelers on hilly roads, thereby enhancing their feasibility in challenging terrain.

6.2 Contribution of Thesis

Chapter 2 presented a simple and cost-effective procedure to find the two-wheeler's speed variation pattern with the road gradient for hilly roads. The data are further used for analysis in developing and designing the electric scooter regenerative braking systems. The few highlights of this Chapter are:

- The drive cycle data was collected from Shillong City in an ICE scooter. The data was collected using a smartphone, iPhone 7, and an App. The app "Speedometer 55 Pro" actively tracks and records data; the data logged are speed, altitude, distance, and time at a 1 Hz sampling rate, which is saved in the black box of the app and later transferred to a computer for analysis.

- The data was processed in MATLAB, and then a simple method was used to derive the hill angle (θ) using spatial location information and a basic trigonometric formula. Further, from the derived hill angle, the road load characteristic was studied for synthesizing the electric scooter's power and torque requirement for such hilly roads.

- The results found that for an electric scooter to be suitable for such a high torque-demanding road, it should have a high-power motor and high current capacity battery banks. With proper design of the motor core, winding conductor for high current capacity, and using a battery with high power and energy, it is possible to develop scooters that may find much acceptance in the hilly region. The results also indicate an opportunity to harness the kinetic energy back to the battery source by applying regenerative braking.

Chapter 3 proposes a new modular regenerative braking circuit and a control scheme for low-speed and extended braking period applications. The proposed regenerative braking circuit can also be integrated into an existing electric scooter, which does not have a regenerative braking system. This is mainly due to the modular nature of the proposed regenerative braking system. Its application is not limited to BLDC motors but can be used for all three-phase motors. The main contributions of this chapter are:

- Detailed mathematical modeling of the proposed regenerative braking circuit and analysis of its steady-state and dynamic-state performance were presented. Its small-signal model was used to study the dynamic nature and derive its desired open-loop Transfer Function.

- For the closed-loop controller design, the Bode plot technique was used. Further, a Type-II compensator current controller for regulating the proposed regenerative braking circuit was designed.

- The proposed system had two modes of operation for the BLDC motor, i.e., motoring and regenerative braking. A control technique was designed to offer a fast switching between the two driving modes by enabling or disabling the gate pulses to the inverter or the boost converter.

- This switching method increases reliability and reduces the cost of the circuit by eliminating power switches to switch between motoring and regenerative braking modes. Since the proposed regenerative system uses the same source battery for both driving modes, i.e., motoring and regenerative braking, thus reducing the cost and weight of additional energy sources.

- The feasibility and the working of the proposed regenerative braking circuit are validated through simulations in MATLAB/Simulink. Further, the results are also experimentally verified on a developed prototype of a scaled-down laboratory test set-up. The results show successful braking action and battery charging at a very low speed in the range of 25 km/h to 15 km/h, as required on hilly roads.

Chapter 4 is the continuation of Chapter 3; the only significant difference is that, here, in this chapter, the close-loop feedback controller of the braking circuit is new. The main contributions of this chapter are:

- A Sliding Mode control current controller was designed to regulate the proposed regenerative braking circuit.

- Further evaluation of the robustness of the proposed SM controller in the presence of model uncertainties, i.e., for parameter variation, was done. It is observed that the proposed SM controller is robust to parameter variation. A comparison of the proposed SM controller with the PI controller was studied in MATLAB/Simulink. The results show that the performance of the SM controller is better than the PI controller, both in the transient and steady states.

- Further, the performance of the proposed SM controller is also experimentally verified on the laboratory test set-up. Both the simulation and hardware results validate the performance of the proposed SM controller in controlling braking and battery currents.

Chapter 5 proposes a simple and smart Hall effect sensor system for the BLDC motor drive system. The main contributions of this chapter are:

- The proposed smart Hall effect sensor system is an enhanced algorithm that is capable of detecting the fault independently and decoding the six states from the available four states to continue the motor running despite the fault, making the Hall sensor decoder of a BLDC motor more reliable.
- The proposed scheme allows the BLDC motor to work even when one Hall sensor is damaged and not working.
- The simulation results validate the effectiveness of the proposed algorithm. The scheme is simple but effective and is particularly suitable for light two-wheelers or robotic arms.

Overall, the contributions of this thesis can be summarized as follows:

Major Contributions of the Thesis

(i) Presented a new modular regenerative braking circuit and control scheme for low-speed, extended braking applications, compatible with all three-phase motors (BLDC or PMSM).

(ii) Designed and developed a robust Sliding Mode current controller for regulating the proposed regenerative braking circuit, with its implementation and hardware validation.

(iii) Proposed a simple, cost-effective method to determine the speed variation pattern of two-wheelers based on road gradients in hilly areas. This data is used for analysis in designing the electric scooter's regenerative braking system.

(iv) Developed a simple and smart Hall effect sensor system that detects the fault and keeps the BLDC motor working despite the damage to Hall effect sensors.

Minor Contributions of the Thesis

(i) The thesis includes detailed Modeling of the Electric two-wheelers in the Hilly region.

(ii) It also includes details about the benefits and limitations of Electric Vehicles.

(iii) The thesis provides the challenges associated with the electric two-wheelers in the Hilly region.

(iv) The thesis includes a control technique that was designed to offer a fast switching between the two driving modes by enabling or disabling the pulse to the inverter or the boost converter.

6.3 Limitation of Thesis and Scope for Future Work

Below are the limitations and work that may be carried forward in the future

- Due to the lack of high-power electric scooters with high battery capacity available in 2017, the data collection work in Chapter 2 was carried out in an ICE scooter. However, today, in 2023, many companies have come up with high battery capacity and motor ratings. In the future, real-time hill angle and power consumption data can be collected with Electric scooters instead of ICE scooters.
- In chapters 3 and 4, the working of the regenerative braking circuit was demonstrated on a low-scale laboratory set-up. Future work can be done by installing the proposed regenerative braking in a real electric scooter.
- The energy efficiency study of the proposed regenerative braking system can be analyzed and studied, which was not done in this thesis.

- The hardware implementation of the smart hall effect sensor system presented in Chapter 5 can be further explored. The algorithm can be extended in the future to detect two Hall sensor faults.

A

Appendix A

A.1 State-Space Equations

In literature, there are several techniques available for PWM converter modelling. State-space averaging and small-signal linearization are commonly accepted techniques in modelling PWM converters.

A.1.1 State-Space Averaging

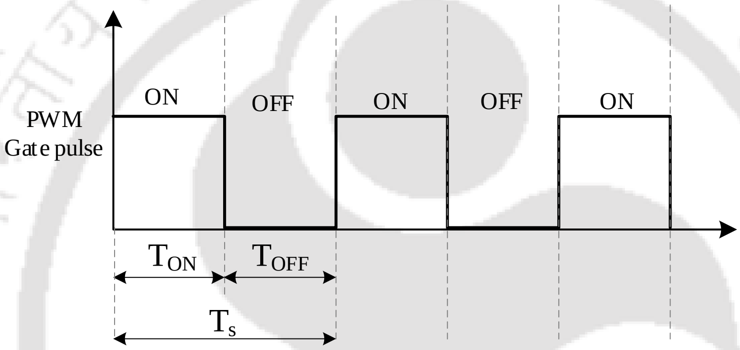

Figure A.1: Equivalent waveforms of the PWM gate pulse given to the converter switch.

In a PWM converter, when the switch is ON, the converter operates in the first topology, and when the switch is OFF, the converter operates in the second topology. The circuit configuration in two operating modes are different and in each mode the converter circuit is linear time-invariant. Both ON and OFF states form one switching cycle of the control signal (PWM gate signal) as shown in waveform Figure A.1. The converter switch is ON during dT_s interval and OFF during $(1-d)T_s$ interval. Where 'd' is the duration of the switch ON period commonly know as the duty ratio. Thus, the PWM converter can be described by a set of state-space equations in each mode and is given below:

$$\text{When Switch is ON,} \quad (0 < t < dT_s) : \begin{cases} \dot{\mathbf{x}}(t) = \mathbf{A}_{on}\mathbf{x}(t) + \mathbf{B}_{on}\mathbf{u}(t) \\ \mathbf{y}(t) = \mathbf{C}_{on}\mathbf{x}(t) + \mathbf{D}_{on}\mathbf{u}(t) \end{cases}$$

$$\text{When Switch is OFF } (dT_s < t < T_s): \quad \begin{cases} \dot{\mathbf{x}}(t) = \mathbf{A}_{off}\mathbf{x}(t) + \mathbf{B}_{off}\mathbf{u}(t) \\ \mathbf{y}(t) = \mathbf{C}_{off}\mathbf{x}(t) + \mathbf{D}_{off}\mathbf{u}(t) \end{cases}$$

where $\mathbf{A}_{on}, \mathbf{B}_{on}, \mathbf{C}_{on}, \mathbf{D}_{on}$ denotes the state-space matrices for the ON state of the converter and $\mathbf{A}_{off}, \mathbf{B}_{off}, \mathbf{C}_{off}, \mathbf{D}_{off}$ denotes the OFF state. $\mathbf{x}(t)$ denotes state variable vector, $\mathbf{u}(t)$ denotes input variable vector, and $\mathbf{y}(t)$ denotes output variable vector.

The averaged state-space equation for the entire switching period T_s is given by:

$$\begin{aligned} \dot{\mathbf{x}} &= \mathbf{A}\mathbf{x} + \mathbf{B}\mathbf{u} \\ \mathbf{y} &= \mathbf{C}\mathbf{x} + \mathbf{D}\mathbf{u} \end{aligned} \tag{A.1}$$

where

$$\begin{aligned} \mathbf{A} &= \mathbf{A}_{on}d + \mathbf{A}_{off}(1-d) \\ \mathbf{B} &= \mathbf{B}_{on}d + \mathbf{B}_{off}(1-d) \\ \mathbf{C} &= \mathbf{C}_{on}d + \mathbf{C}_{off}(1-d) \\ \mathbf{D} &= \mathbf{D}_{on}d + \mathbf{D}_{off}(1-d) \end{aligned} \tag{A.2}$$

Equation (A.1) is the averaged state-space model that describes the dynamics of the converter, it is obtained by averaging the state-space equations of two switching intervals.

A.2 Small Signal Perturbation and Linearization

A small perturbation signal is introduced in the input variables and duty cycles, causing perturbation in the steady-state value of inductor currents, capacitor voltages and output voltages. This is done considering the feedback circuit is disabled. Perturbation is the low-frequency sinusoidal waveform superimposed on the DC nominal value. The averaged state variable vector, input variable vector, output variable vector and control variables can be written as:

$$\mathbf{x} = \mathbf{X} + \hat{\mathbf{x}} \qquad \mathbf{y} = \mathbf{Y} + \hat{\mathbf{y}} \qquad \mathbf{u} = \mathbf{U} + \hat{\mathbf{u}} \qquad d = D + \hat{d}$$

where $\mathbf{X}$, $\mathbf{Y}$, $\mathbf{U}$, D are the nominal DC values of $\mathbf{x}$, $\mathbf{y}$, $\mathbf{u}$, d and $\hat{\mathbf{x}}$, $\hat{\mathbf{y}}$, $\hat{\mathbf{u}}$, $\hat{d}$ are the perturbation in $\mathbf{X}$, $\mathbf{Y}$, $\mathbf{U}$, D.

The superimposing of the perturbation in duty cycle affects the average stat-space matrices $\mathbf{A}, \mathbf{B}, \mathbf{C}, \mathbf{D}$. The state-space matrices under perturbation can then be written as

$$\mathbf{A} = \mathbf{A}_{on}(D + \hat{d}) + \mathbf{A}_{off}(1 - \mathrm{D} - \hat{\mathrm{d}})$$

$$\mathbf{A} = \mathbf{A}_{on}D + \mathbf{A}_{on}\hat{d} + \mathbf{A}_{off} - \mathbf{A}_{off}D - \mathbf{A}_{off}\hat{d}$$

$$\mathbf{A} = \mathbf{A}_{on}D + \mathbf{A}_{off}(1 - D) + (\mathbf{A}_{on} - \mathbf{A}_{off})\hat{d}$$

$$\mathbf{A} = \mathbf{A}_{av} + (\mathbf{A}_{on} - \mathbf{A}_{off})\hat{d}$$

Similarly,

$$\mathbf{B} = \mathbf{B}_{av} + (\mathbf{B}_{on} - \mathbf{B}_{off})\hat{d}$$

$$\mathbf{C} = \mathbf{C}_{av} + (\mathbf{C}_{on} - \mathbf{C}_{off})\hat{d}$$

$$\mathbf{D} = \mathbf{D}_{av} + (\mathbf{D}_{on} - \mathbf{D}_{off})\hat{d}$$

Now, substituting all the above perturbed variables in the averaged state-space equations (A.1), gives

$$\begin{cases} \frac{d[\mathbf{X}+\hat{\mathbf{x}}]}{dt} = [\mathbf{A}_{av} + (\mathbf{A}_{on} - \mathbf{A}_{off})\hat{d}][\mathbf{X} + \hat{\mathbf{x}}] + [\mathbf{B}_{av} + (\mathbf{B}_{on} - \mathbf{B}_{off})\hat{d}][\mathbf{U} + \hat{\mathbf{u}}] \\ \\ \mathbf{Y} + \hat{\mathbf{y}} = [\mathbf{C}_{av} + (\mathbf{C}_{on} - \mathbf{C}_{off})\hat{d}][\mathbf{X} + \hat{\mathbf{x}}] + [\mathbf{D}_{av} + (\mathbf{D}_{on} - \mathbf{D}_{off})\hat{d}][\mathbf{U} + \hat{\mathbf{u}}] \end{cases} \tag{A.3}$$

The derivation of constant is zero, the above expression can be written as:

$$\begin{cases} \frac{d\hat{\mathbf{x}}}{dt} = \mathbf{A}_{av}\mathbf{X} + \mathbf{B}_{av}\mathbf{U} + \mathbf{A}_{av}\hat{\mathbf{x}} + \mathbf{B}_{av}\hat{\mathbf{u}} + [(\mathbf{A}_{on} - \mathbf{A}_{off})\hat{d}]\mathbf{X} \\ \qquad + [(\mathbf{B}_{on} - \mathbf{B}_{off})\hat{d}]\mathbf{U} + [(\mathbf{A}_{on} - \mathbf{A}_{off})\hat{d}]\hat{\mathbf{x}} + [(\mathbf{B}_{on} - \mathbf{B}_{off})\hat{d}]\hat{\mathbf{u}} \\ \mathbf{Y} + \hat{\mathbf{y}} = \mathbf{C}_{av}\mathbf{X} + \mathbf{D}_{av}\mathbf{U} + \mathbf{C}_{av}\hat{\mathbf{x}} + \mathbf{D}_{av}\hat{\mathbf{u}} + [(\mathbf{C}_{on} - \mathbf{C}_{off})\hat{d}]\mathbf{X} \\ \qquad + [(\mathbf{D}_{on} - \mathbf{D}_{off})\hat{d}]\mathbf{U} + [(\mathbf{C}_{on} - \mathbf{C}_{off})\hat{d}]\hat{\mathbf{x}} + [(\mathbf{D}_{on} - \mathbf{D}_{off})\hat{d}]\hat{\mathbf{u}} \end{cases} \tag{A.4}$$

Now ignoring the non-linear terms we separate the DC terms and AC terms, the above expression is then written as:

$$dc\begin{cases} 0 = \mathbf{A}_{av}\mathbf{X} + \mathbf{B}_{av}\mathbf{U} \\ \mathbf{Y} = \mathbf{C}_{av}\mathbf{X} + \mathbf{D}_{av}\mathbf{U} \end{cases} \quad ac\begin{cases} \frac{d\hat{\mathbf{x}}}{dt} = \mathbf{A}_{av}\hat{\mathbf{x}} + \mathbf{B}_{av}\hat{\mathbf{u}} + [(\mathbf{A}_{on} - \mathbf{A}_{off})\mathbf{X} + (\mathbf{B}_{on} - \mathbf{B}_{off})\mathbf{U}]\hat{d} \\ \hat{\mathbf{y}} = \mathbf{C}_{av}\hat{\mathbf{x}} + \mathbf{D}_{av}\hat{\mathbf{u}} + [(\mathbf{C}_{on} - \mathbf{C}_{off})\mathbf{X} + (\mathbf{D}_{on} - \mathbf{D}_{off})\mathbf{U}]\hat{d} \end{cases} \tag{A.5}$$

The solution of DC part is given as:

$$\mathbf{X} = -\mathbf{A}_{av}^{-1}\mathbf{B}_{av}\mathbf{U} \qquad \mathbf{Y} = (-\mathbf{C}_{av}\mathbf{A}_{av}^{-1}\mathbf{B}_{av} + \mathbf{D}_{av})\mathbf{U} \tag{A.6}$$

Using (A.6) steady-state value of inductor currents, capacitor voltages and output voltages can be calculated.

By applying Laplace transform to the ac part, gives:

$$\begin{cases} s\hat{\mathbf{x}}(s) = \mathbf{A}_{av}\hat{\mathbf{x}}(s) + \mathbf{B}_{av}\hat{\mathbf{u}}(s) + [(\mathbf{A}_{on} - \mathbf{A}_{off})\mathbf{X} + (\mathbf{B}_{on} - \mathbf{B}_{off})\mathbf{U}]\hat{d}(s) \\ \hat{\mathbf{y}}(s) = \mathbf{C}_{av}\hat{\mathbf{x}}(s) + \mathbf{D}_{av}\hat{\mathbf{u}}(s) + [(\mathbf{C}_{on} - \mathbf{C}_{off})\mathbf{X} + (\mathbf{D}_{on} - \mathbf{D}_{off})\mathbf{U}]\hat{d}(s) \end{cases} \tag{A.7}$$

resulting in the solution of ac part is given as:

$$\hat{\mathbf{x}}(s) = (s\mathbf{I} - \mathbf{A}_{av})^{-1}\mathbf{B}_{av}\hat{\mathbf{u}}(s) + (s\mathbf{I} - \mathbf{A}_{av})^{-1}[(\mathbf{A}_{on} - \mathbf{A}_{off})\mathbf{X} + (\mathbf{B}_{on} - \mathbf{B}_{off})\mathbf{U}]\hat{d}(s) \tag{A.8}$$

$$\begin{aligned} \hat{\mathbf{y}}(s) = [\mathbf{C}_{av}(s\mathbf{I} - \mathbf{A}_{av})^{-1}\mathbf{B}_{av} + \mathbf{D}_{av}]\hat{\mathbf{u}}(s) + \mathbf{C}_{av}(s\mathbf{I} - \mathbf{A}_{av})^{-1}[(\mathbf{A}_{on} - \mathbf{A}_{off})\mathbf{X} + (\mathbf{B}_{on} - \mathbf{B}_{off})\mathbf{U}]\hat{d}(s) \\ + [(\mathbf{C}_{on} - \mathbf{C}_{off})\mathbf{X} + (\mathbf{D}_{on} - \mathbf{D}_{off})\mathbf{U}]\hat{d}(s) \end{aligned} \tag{A.9}$$

The transfer functions between the state variables and input variables are obtained using (A.8) by considering $\hat{d} = 0$ and is given by

$$\hat{\mathbf{x}}(s) = (s\mathbf{I} - \mathbf{A}_{av})^{-1}\mathbf{B}_{av}\hat{\mathbf{u}}(s) \tag{A.10}$$

The transfer functions between the state variables and duty ratios are obtained using (A.8) by considering $\hat{\mathbf{u}} = 0$ and is given by

$$\hat{\mathbf{x}}(s) = (s\mathbf{I} - \mathbf{A}_{av})^{-1}[(\mathbf{A}_{on} - \mathbf{A}_{off})\mathbf{X} + (\mathbf{B}_{on} - \mathbf{B}_{off})\mathbf{U}]\hat{d}(s) \tag{A.11}$$

The transfer functions between the output variables and input variables are obtained using (A.9) by considering $\hat{d} = 0$ and is given by

$$\hat{\mathbf{y}}(s) = [\mathbf{C}_{av}(s\mathbf{I} - \mathbf{A}_{av})^{-1}\mathbf{B}_{av} + \mathbf{D}_{av}]\hat{\mathbf{u}}(s) \tag{A.12}$$

The transfer functions between the output variables and duty ratios are obtained using (A.9) by considering $\hat{\mathbf{u}} = 0$ and is given by

$$\begin{aligned}\hat{\mathbf{y}}(s) = \{&\mathbf{C}_{av}(s\mathbf{I} - \mathbf{A}_{av})^{-1}[(\mathbf{A}_{on} - \mathbf{A}_{off})\mathbf{X} + (\mathbf{B}_{on} - \mathbf{B}_{off})\mathbf{U}]\hat{d}(s) \\ &+ [(\mathbf{C}_{on} - \mathbf{C}_{off})\mathbf{X} + (\mathbf{D}_{on} - \mathbf{D}_{off})\mathbf{U}]\hat{d}(s)\end{aligned} \tag{A.13}$$

B

Appendix B

B.1 Specifications for Simulation

Table B.1: Specification of the boost converter

Parameter	**Values**
Input Voltage, V_{in}	24 Volt
Output Voltage, V_{bat}	48 Volt
Inductance, L	0.56 mH
Output Capacitance, C	2700 μF
Input Side Internal Resistance, R_{in}	0.05 Ω
ESR of Capacitance, r_c	0.01 Ω
Internal Resistance of Battery, R_{int}	0.33 Ω

Table B.2: Specifications of the BLDC motors

Parameter	**Values**
Stator Resistance, R_s	0.11 Ω
Stator Inductances, L_s	0.25 mH
Voltage Constant, K_v	122 $V_{l-l}/krmp$
Torque Constant, K_t	1.165 Nm/A
Inertia, J	0.35
No. of Pole Pair	24

B.2 Six Commutation States of BLDC Motor

Table B.3: The six states from 3 hall effect sensors

States	H_a	H_b	H_c	Switches to be ON	The Active Lines of the Stator Winding
I	1	0	0	S_1,S_6	AB
II	1	1	0	S_1,S_2	AC
III	0	1	0	S_3,S_2	BC
IV	0	1	1	S_3,S_4	BA
V	0	0	1	S_5,S_4	CA
VI	1	0	1	S_5,S_6	CB

B.3 Specifications for Experimental Hardware Set-up

The overall hardware set-up is shown in Figure 3.17 (a), and its schematic layout of the hardware connection is shown in Figure 3.17 (b) of Chapter 3. The experimental setup is designed for a reduced power scale. The proposed regenerative braking system consists of two power drivelines one for the motoring mode and the other for the regenerating mode as explained in Sub-Section 3.5. Here in this Section of the Appendix the hardware specification are given for the most relevant components used for building the power circuit to drive the BLDC motor and to charge the battery during regenerative braking period.

Table B.4: Specifications of the motoring mode electric drive system

Component	**Ratings**	**Makers**	**Model**
Inverter IGBT Module	1200V/100A	Fuji	6MBI100S-120
Driver Circuit FOD	10V-20V/2A	Fairchild	FOD3180
Logic Gates (NAND, OR, AND & Hex Inverter)	5.5V / 0.5mA	On Semiconductor	SN54/74LS04
Controller	8-bit, 16 MHz, 3.3V (Power)	Arduino	UNO R3
Hall Effect Position Sensors	4.0V-24V (Power), 20mA	Honeywell	SS41
SPDT	20V , 500mA	Same Sky	SLW-1276864-4A-D
BLDC Motor	1.8kW, 48 pole, 60V, 25A	NA	NA
Li-Ion Battery Pack	48V, 12Ah	NA	NA

Table B.5: Specifications of the regenerative mode braking circuit system

Component	**Ratings**	**Makers**	**Model**
N-Channel MOSFET	300V, 38A, 0.085Ω	On Semiconductor	FDA38N30
Hyper-fast Diode	30A, 1200V	On Semiconductor	RHRG30120
Toroidal Inductor	10A, 0.56mH, 0.077Ω	Multi Comp	MCAP Series
DC Link Capacitor	6800μF, 100V	Kemet	Electrolytic
Boost Output Capacitor	2700μF, 400V	Kemet	Electrolytic
3-Phase Bridge Rectifier	$100 - 1600$V, $50 - 100$A	Thinki Semiconductor	SQL50A thru SQL100A
Voltage Transducer	±12V (Power), $10 - 500$V (V_{pn}) 10mA (I_{pn})	LEM	LV 25-P
Current Transducer	$\pm 12V$ (Power) 50A (I_{pn})	LEM	LA 55-P
Op Amps Quad	$\pm 12V$	Texas Instrument	LM324
Controller	32-bit, 168 MHz, $3.3V$ (Power)	ST Microelectronics	STM32F407VGT6

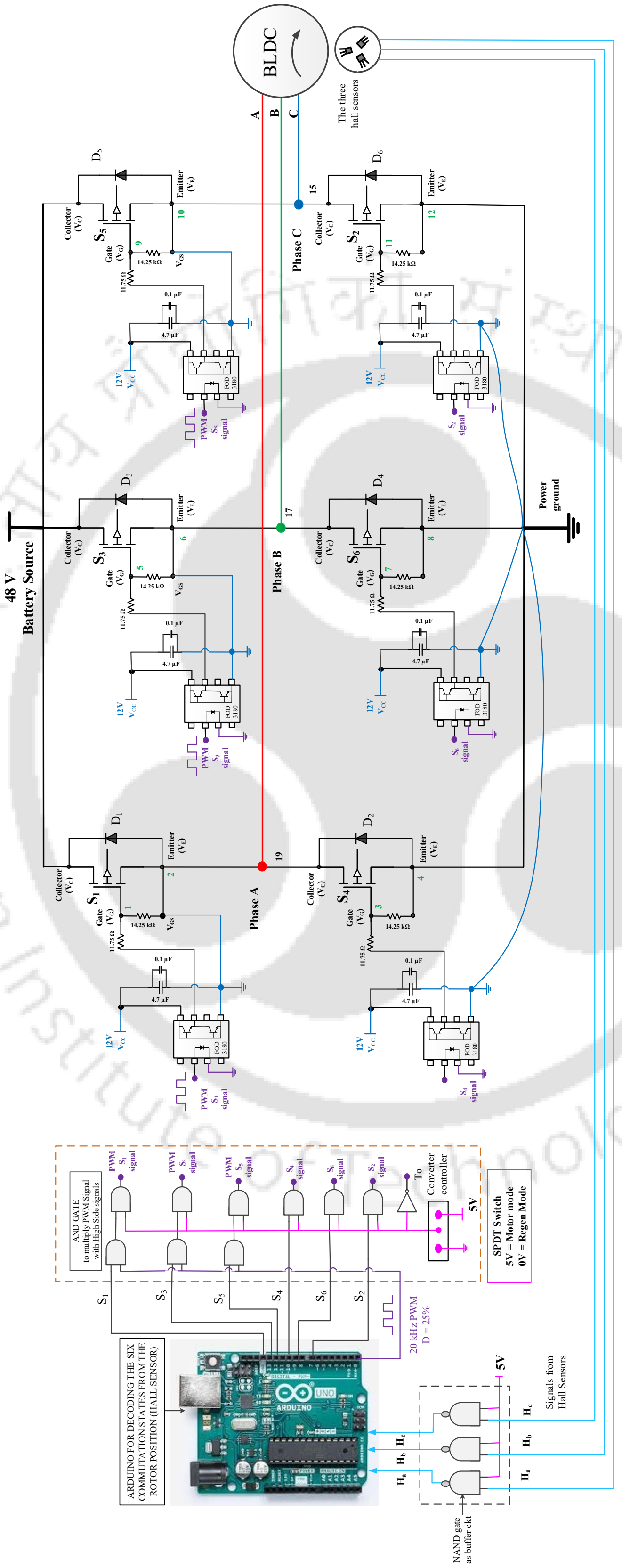

Figure B.1: Schematic diagram showing the experimental set-up circuit connections for the BLDC motor drive.

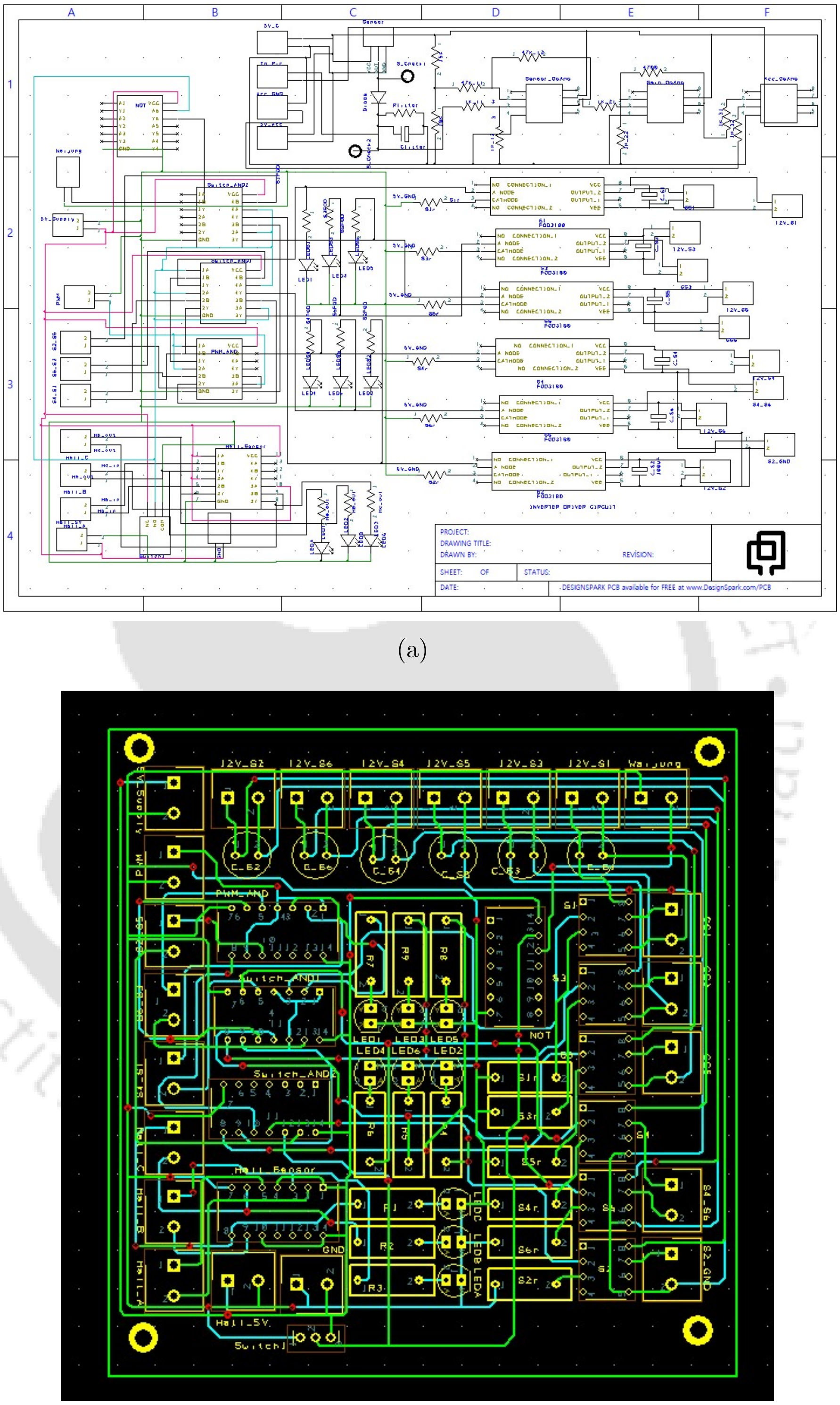

(a)

(b)

Figure B.2: Screenshots of DesignSpark CAD showing (a) schematic design layout of the driver circuit of the 3-phase inverter (b) PCB design layout of the driver circuit along with mode selector circuit

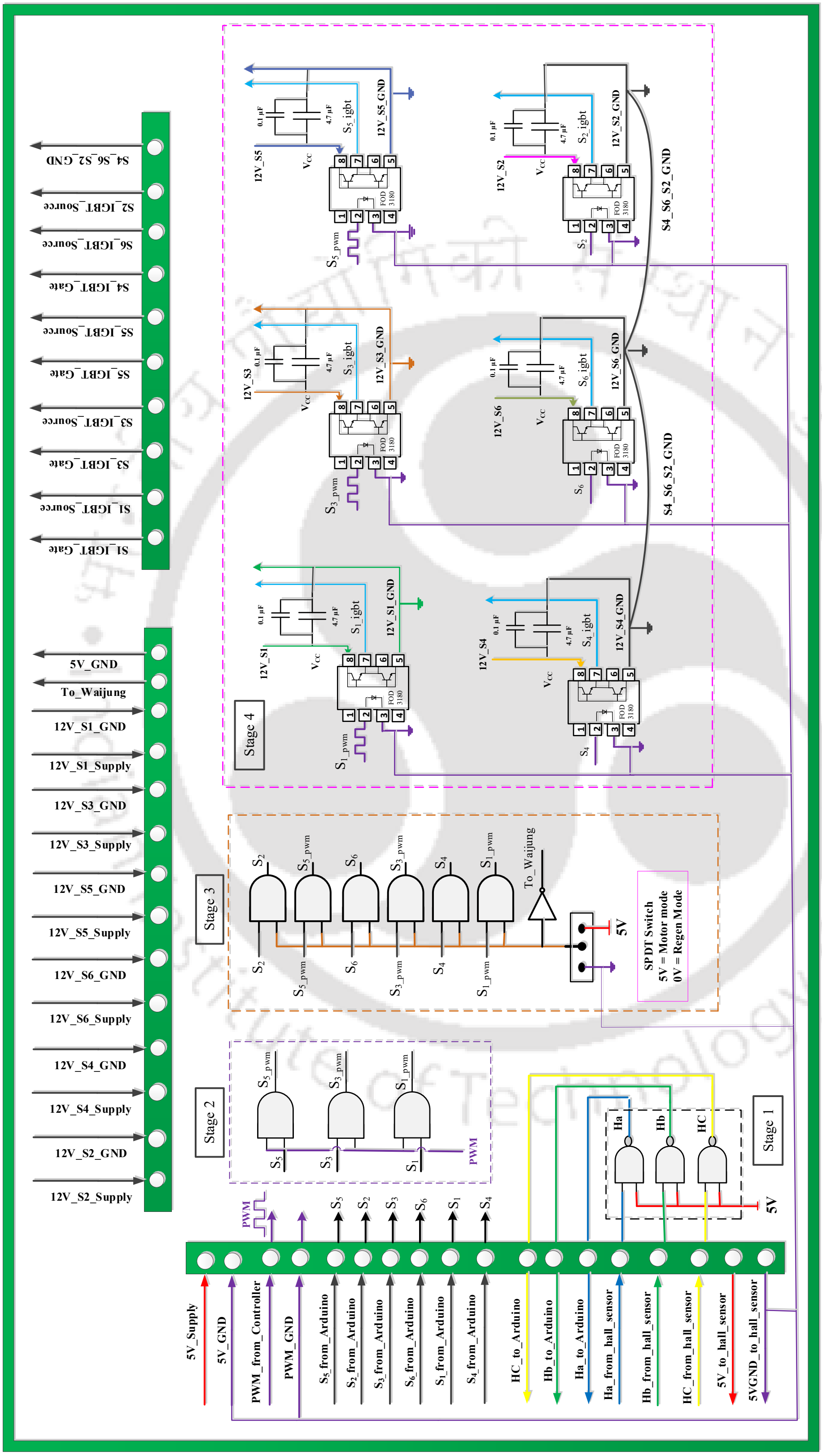

Figure B.3: Schematic diagram representing Figure B.2, showing the logic gate ICs and the FOD connection used as inverter driver circuit.

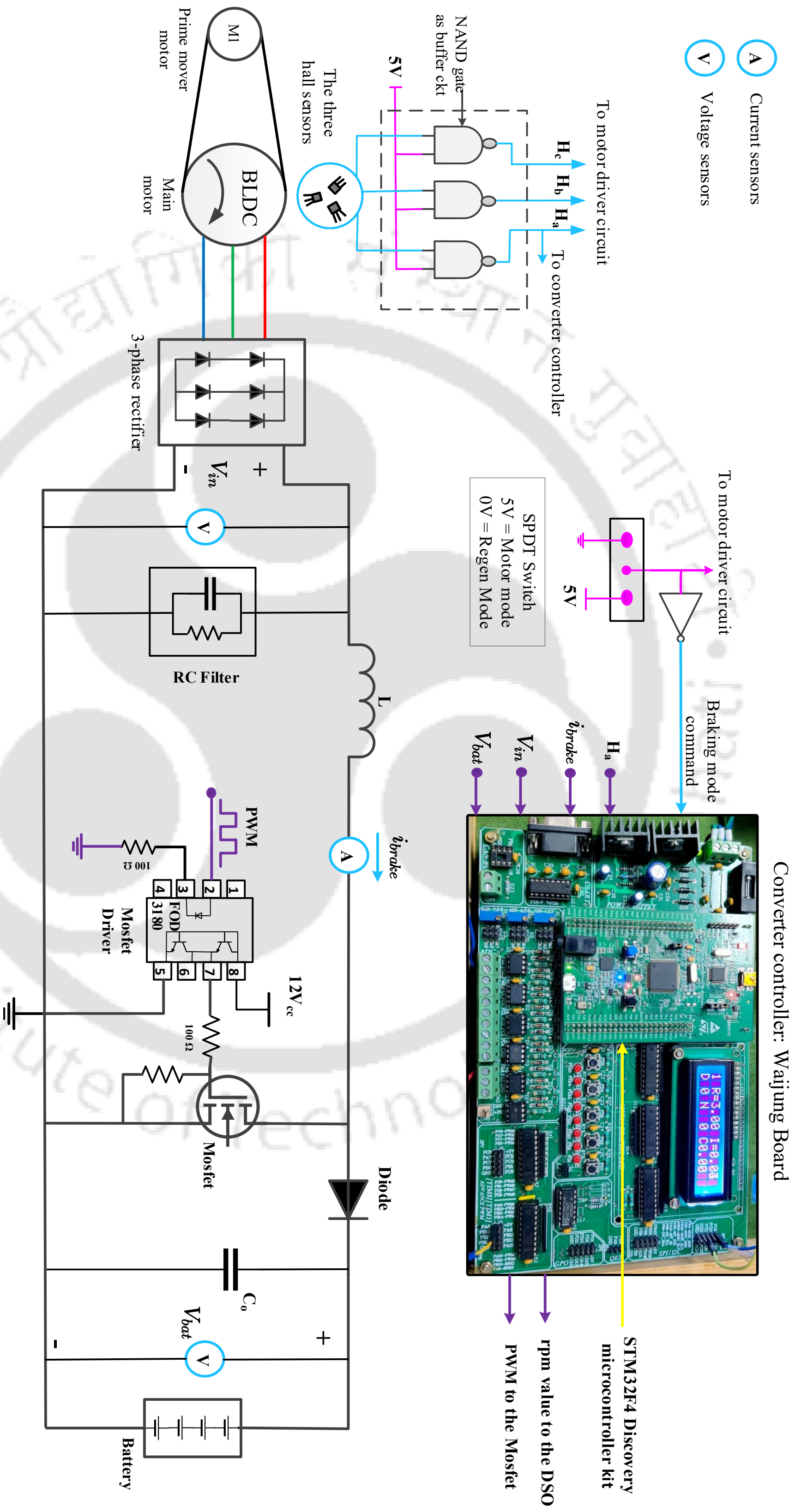

Figure B.4: Schematic diagram showing the experimental set-up circuit connections for the regenerative braking mode.

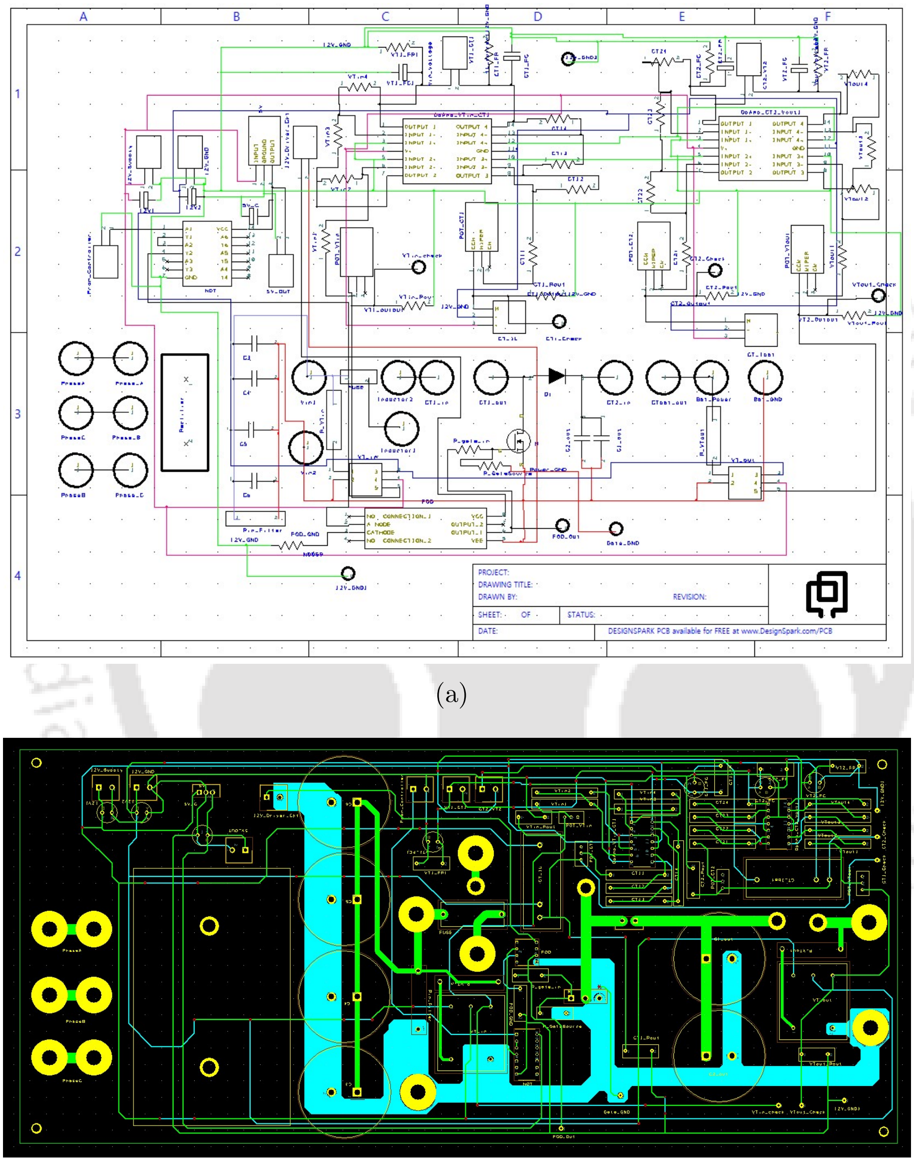

(a)

(b)

Figure B.5: Screenshots of DesignSpark CAD showing (a) schematic design layout of the regenerative braking circuit (b) PCB design layout of the regenerative braking circuit

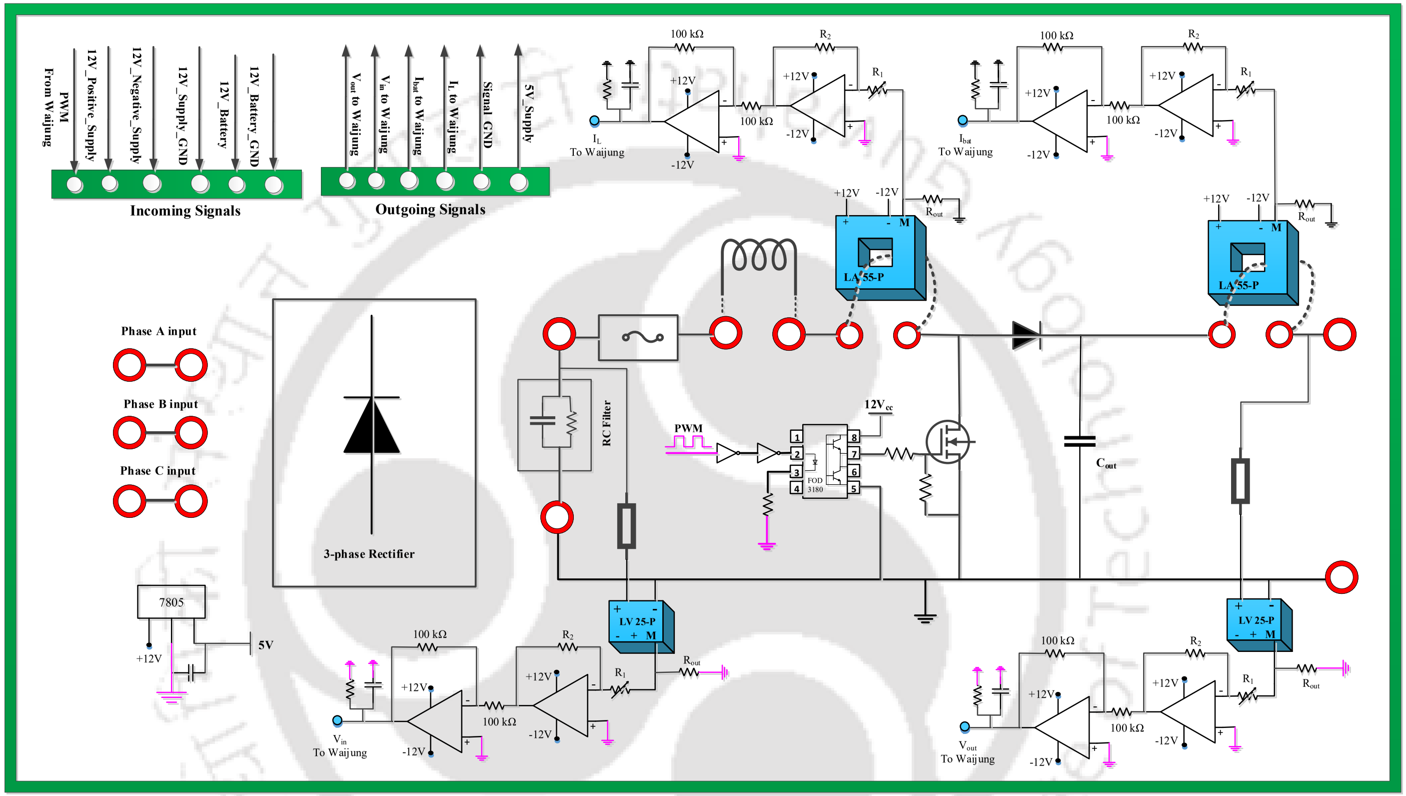

Figure B.6: Schematic diagram representing Figure B.5, showing the sensors and signal conditioning circuits.

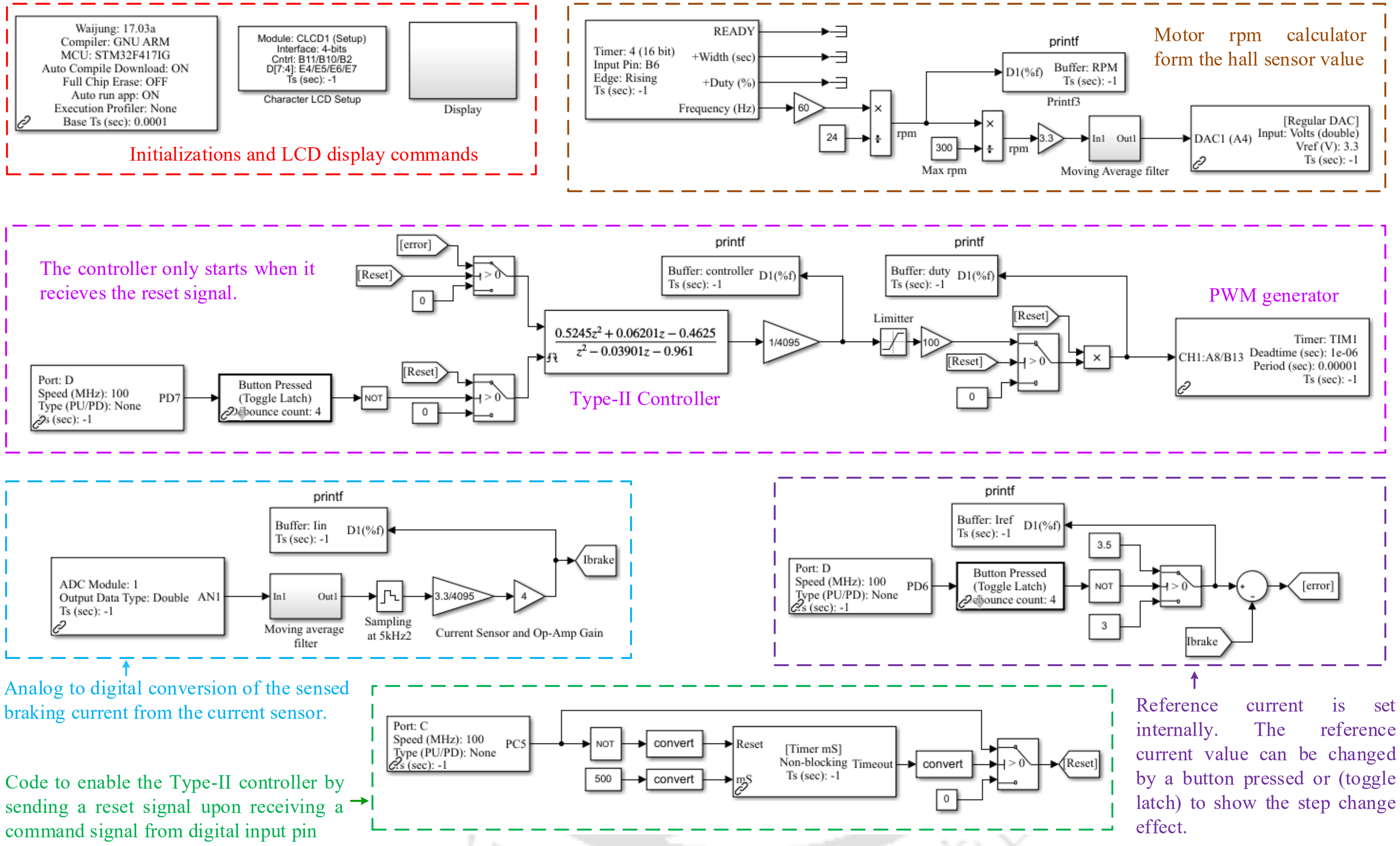

Figure B.7: Simulation page showing the implementation of the controller with Waijung blockset models in MATLAB/Simulink environment.

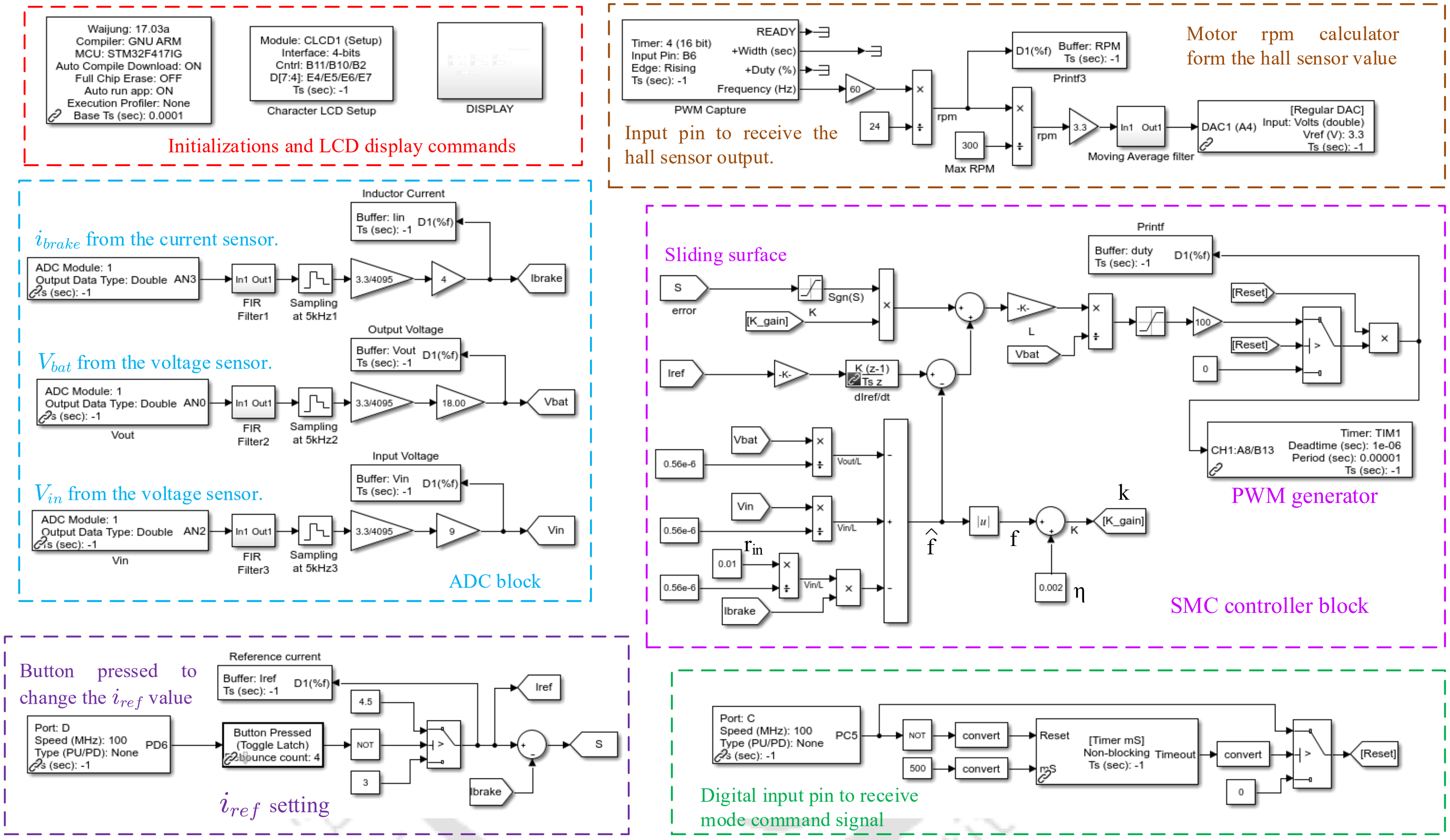

Figure B.8: Simulation page showing the implementation of the SMC controller with Waijung blockset models in MATLAB/Simulink environment.

References

[1] A. Emadi, *Advanced Electric Drive Vehicles.* CRC Press Taylor & Francis Group, 2015.

[2] J. Larminie and J. Lowry, *Electric Vehicle Technology Explained.* John Wiley & Sons, Ltd, Aug. 2012.

[3] L. Paoli and T. Gül, “Electric cars fend off supply challenges to more than double global sales,” *Available at https://www.iea.org/commentaries/electric-cars-fend-off-supply-challenges-to-more-than-double-global-sales*, IEA, Paris 2022.

[4] A. Emadi, “Transportation 2.0,” *IEEE Power and Energy Magazine*, vol. 9, no. 4, pp. 18–29, jul 2011.

[5] IEA, “Global ev outlook 2023, paris,” *Available at https://www.iea.org/reports/global-ev-outlook-2023*, 2023, License: CC BY 4.0.

[6] “Vahan dashboard,” *Available at https://vahan.parivahan.gov.in/vahan4dashboard*, 2023.

[7] “One in three households in india owns a two-wheeler,” *Available at http://www.ice360.in/en/projects/homepageservey/one-in-three-households-in-india-owns-a-two-wheeler-1*, 2016.

[8] K. V. Rupchand, “A proposal for meeting power demands of electric vehicle transportation in india,” in *Proceedings IEEE Power Energy Society General Meeting.*, Jul. 2011, pp. 1–5.

[9] B. Y. Boroujeni and H. C. Frey, “Road grade quantification based on global positioning system data obtained from real-world vehicle fuel use and emissions measurements,” *Atmospheric Environment*, vol. 85, pp. 179–186, Mar. 2014.

[10] M. Bertoluzzo and G. Buja, “Development of electric propulsion systems for light electric vehicles,” *IEEE Transaction on Industrial Informatics*, vol. 7, no. 3, pp. 428–435, Aug. 2011.

[11] M. Ehsani, K. Rahman, and H. Toliyat, “Propulsion system design of electric and hybrid vehicles,” *IEEE Transaction on Industrial Electronics*, vol. 44, no. 1, pp. 19–27, Feb. 1997.

[12] W. Hung, H. Tong, C. Lee, K. Ha, and L. Pao, “Development of a practical driving cycle construction methodology: a case study in hong kong,” *Transportation Research Part D: Transport and Environment*, vol. 12, no. 2, pp. 115–128, Mar. 2007.

[13] L. Berzi, M. Delogu, and M. Pierini, “Development of driving cycles for electric vehicles in the context of the city of florence,” *Transportation Research Part D: Transport and Environment*, vol. 47, pp. 299–322, Aug. 2016.

[14] T. J. LaClair, Z. Gao, J. S. Fu, J. Calcagno, and J. Yun, "Development of a short-duration drive cycle to represent long-term measured drive cycle data," *Transportation Research Record: Journal of the Transportation Research Board*, vol. 2428, no. 1, pp. 63–74, Jan. 2014.

[15] K. Nesamani and K. Subramanian, "Impact of real-world driving characteristics on vehicular emissions," *JSME International Journal Series B*, vol. 49, no. 1, pp. 19–26, Aug. 2006.

[16] K. Nesamani and K. Subramaniann, "Development of a driving cycle for intra-city buses in chennai, india," *Atmospheric Environment*, vol. 45, no. 31, pp. 5469–5476, Oct. 2011.

[17] W. Saleh, R. Kumar, H. Kirby, and P. Kumar, "Real world driving cycle for motorcycles in edinburgh," *Transportation Research Part D: Transport and Environment*, vol. 14, no. 5, pp. 326–333, Jul. 2009.

[18] K. Boriboonsomsin and M. Barth, "Impacts of road grade on fuel consumption and carbon dioxide emissions evidenced by use of advanced navigation systems," *Transportation Research Record: Journal of the Transportation Research Board*, vol. 2139, no. 1, pp. 21–30, Jan. 2009.

[19] K. Rogers and R. Trayford, "Grade measurement with an instrumented car," *Transportation Research Part B: Methodological*, vol. 18, no. 3, pp. 247–254, Jun. 1984.

[20] S. Mangan, J. Wang, and Q. Wu, "Measurement of the road gradient using an inclinometer mounted on a moving vehicle," in *Proceedings. IEEE International Symposium on Computer Aided Control System Design.* IEEE, Sep. 2002, pp. 80–85.

[21] K. Zhang and H. Frey, "Road grade estimation for on-road vehicle emissions modeling using lidar data," *Proceedings of Air & Waste Management Association Annual Meeting*, Jan. 2005.

[22] E. G. Gaeke, "Road grade sensor," US Patent 3 752 251, filling date August 17, 1971 Issue date August 1973 Inventor: Edward G. Gaeke Assignee: General Motors Corporation.

[23] T. Massel, E. Ding, and M. Arndt, "Investigation of different techniques for determining the road uphill gradient and the pitch angle of vehicles," in *Proceedings of the 2004 American Control Conference.* IEEE, 2004.

[24] A. Vahidi, A. Stefanopoulou, and H. Peng, "Recursive least squares with forgetting for online estimation of vehicle mass and road grade: theory and experiments," *Vehicle System Dynamics*, vol. 43, no. 1, pp. 31–55, Jan. 2005.

[25] B. HS, J. Ryu, and C. Gerdes, "Road grade and vehicle parameter estimation for longitudinal control using gps," *IEEE Transaction on Intelligent Transportation Systems-TITS*, Jan. 2001.

[26] H. E. Tseng, L. Xu, and D. Hrovat, "Estimation of land vehicle roll and pitch angles," *Vehicle System Dynamics*, vol. 45, no. 5, pp. 433–443, May 2007.

[27] P. Sahlholm and K. H. Johansson, "Road grade estimation for look-ahead vehicle control using multiple measurement runs," *Control Engineering Practice*, vol. 18, no. 11, pp. 1328–1341, Nov. 2010.

[28] X. Liao, Q. Huang, D. Sun, W. Liu, and W. Han, "Real-time road slope estimation based on adaptive extended kalman filter algorithm with in-vehicle data," in *2017 29th Chinese Control and Decision Conference (CCDC).* IEEE, May 2017, pp. 1–6.

[29] B. Y. Boroujeni, H. C. Frey, and G. S. Sandhu, "Road grade measurement using in-vehicle, stand-alone GPS with barometric altimeter," *Journal of Transportation Engineering*, vol. 139, no. 6, pp. 605–611, Jun. 2013.

[30] P. Kadav and Z. D. Asher, "Improving the range of electric vehicles," in *2019 Electric Vehicle International Conference (EV)*. IEEE, Oct. 2019.

[31] I. Aharon and A. Kuperman, "Topological overview of powertrains for battery-powered vehicles with range extenders," *IEEE Transactions on Power Electronics*, vol. 26, no. 3, pp. 868–876, Mar. 2011.

[32] Z. Li, A. Khajepour, and J. Song, "A comprehensive review of the key technologies for pure electric vehicles," *Energy*, vol. 182, pp. 824–839, Sep. 2019.

[33] S. M. A. S. Bukhari, J. Maqsood, M. Q. Baig, S. Ashraf, and T. A. Khan, "Comparison of characteristics - lead acid, nickel based, lead crystal and lithium based batteries," in *2015 17th UKSim-AMSS International Conference on Modeling and Simulation (UKSim)*. IEEE, Mar. 2015.

[34] E. Chemali, M. Preindl, P. Malysz, and A. Emadi, "Electrochemical and electrostatic energy storage and management systems for electric drive vehicles: state-of-the-art review and future trends," *IEEE Journal of Emerging and Selected Topics in Power Electronics*, vol. 4, no. 3, pp. 1117–1134, Sep. 2016.

[35] J.-Y. Kim, B.-S. Lee, Y.-J. Lee, and J.-K. Kim, "Integrated multi mode converter with single inductor for fuel cell electric vehicles," *IEEE Transactions on Industrial Electronics*, vol. 69, no. 11, pp. 11 001–11 011, Nov. 2022.

[36] C. Riczu and J. Bauman, "Implementation and system-level modeling of a hardware efficient cell balancing circuit for electric vehicle range extension," *IEEE Transactions on Industrial Application*, vol. 57, no. 3, pp. 2883–2895, May 2021.

[37] Y. Xie, C. Wang, X. Hu, X. Lin, Y. Zhang, and W. Li, "An MPC-based control strategy for electric vehicle battery cooling considering energy saving and battery lifespan," *IEEE Transactions on Vehicular Technology*, vol. 69, no. 12, pp. 14 657–14 673, Dec. 2020.

[38] S. Madichetty, S. Mishra, and M. Basu, "New trends in electric motors and selection for electric vehicle propulsion systems," *IET Electrical Systems in Transportation*, vol. 11, no. 3, pp. 186–199, Apr. 2021.

[39] J. de Santiago, H. Bernhoff, B. Ekergård, S. Eriksson, S. Ferhatovic, R. Waters, and M. Leijon, "Electrical motor drivelines in commercial all-electric vehicles: a review," *IEEE Transactions on Vehicular Technology*, vol. 61, no. 2, pp. 475–484, Feb. 2012.

[40] Y. Zhang, Y. Zhang, Z. Ai, Y. L. Murphey, and J. Zhang, "Energy optimal control of motor drive system for extending ranges of electric vehicles," *IEEE Transactions on Industrial Electronics*, vol. 68, no. 2, pp. 1728–1738, Feb. 2021.

[41] N. Huda, S. Kaleg, A. Hapid, M. R. Kurnia, and A. C. Budiman, "The influence of the regenerative braking on the overall energy consumption of a converted electric vehicle," *SN Applied Sciences*, vol. 2, no. 4, Mar. 2020.

[42] B. Long, S. Lim, J. Ryu, and K. Chong, “Energy-regenerative braking control of electric vehicles using three-phase brushless direct-current motors,” *Energies*, vol. 7, no. 1, pp. 99–114, Dec. 2013.

[43] G. Xu, W. Li, K. Xu, and Z. Song, “An intelligent regenerative braking strategy for electric vehicles,” *Energies*, vol. 4, no. 9, pp. 1461–1477, Sep. 2011.

[44] M.-J. Yang, H.-L. Jhou, B.-Y. Ma, and K.-K. Shyu, “A cost-effective method of electric brake with energy regeneration for electric vehicles,” *IEEE Transaction on Industrial Electronics*, vol. 56, no. 6, pp. 2203–2212, Jun. 2009.

[45] D. M. U and B. G. R, “A novel switching scheme for regenerative braking and battery charging for BLDC motor drive used in electric vehicle,” in *2020 IEEE International Power Renewable Energy Conference*. IEEE, Oct. 2020.

[46] T. Soylu and R. Bayır, “Downhill speed control of in-wheel motor during regenerative braking,” *Elektronika ir Elektrotechnika*, vol. 23, no. 6, Dec. 2017.

[47] S. Heydari, P. Fajri, R. Sabzehgar, and A. Asrari, “Optimal brake allocation in electric vehicles for maximizing energy harvesting during braking,” *IEEE Transaction on Energy Conversion*, vol. 35, no. 4, pp. 1806–1814, Dec. 2020.

[48] A. J. Godfrey and V. Sankaranarayanan, “A new electric braking system with energy regeneration for a BLDC motor driven electric vehicle,” *Engineering Science and Technology, an International Journal*, vol. 21, no. 4, pp. 704–713, Aug. 2018.

[49] X. Nian, F. Peng, and H. Zhang, “Regenerative braking system of electric vehicle driven by brushless DC motor,” *IEEE Transaction on Industrial Electronics*, vol. 61, no. 10, pp. 5798–5808, Oct. 2014.

[50] X. Zhang, Y. Wang, G. Liu, and X. Yuan, “Robust regenerative charging control based on T–S fuzzy sliding-mode approach for advanced electric vehicle,” *IEEE Transaction on Transportation Electrification*, vol. 2, no. 1, pp. 52–65, Mar. 2016.

[51] G. Xu, K. Xu, C. Zheng, X. Zhang, and T. Zahid, “Fully electrified regenerative braking control for deep energy recovery and maintaining safety of electric vehicles,” *IEEE Transaction on Vehicular Technology*, vol. 65, no. 3, pp. 1186–1198, Mar. 2016.

[52] J. Dixon, I. Nakashima, E. Arcos, and M. Ortuzar, “Electric vehicle using a combination of ultracapacitors and ZEBRA battery,” *IEEE Transaction on Industrial Electronics*, vol. 57, no. 3, pp. 943–949, Mar. 2010.

[53] M. Ortuzar, J. Moreno, and J. Dixon, “Ultracapacitor-based auxiliary energy system for an electric vehicle: implementation and evaluation,” *IEEE Transactions on Industrial Electronics*, vol. 54, no. 4, pp. 2147–2156, Aug. 2007.

[54] J. W. Dixon, M. Ortuzar, and E. Wiechmann, “Regenerative braking for an electric vehicle using ultracapacitors and a buck-boost converter,” *https://hrudnick.sitios.ing.uc.cl/paperspdf/dixon/42a.pdf*, 2002.

[55] J.-H. Lee, D.-Y. Jung, T.-K. Lee, Y.-R. Kim, and C.-Y. Won, “Regenerative current control method of bidirectional dc/dc converter for EV/HEV application,” *Journal of Electrical Engineering and Technology*, vol. 8, no. 1, pp. 97–105, Jan. 2013.

[56] K. Suresh, C. Bharatiraja, N. Chellammal, M. Tariq, R. K. Chakrabortty, M. J. Ryan, and B. Alamri, "A multifunctional non-isolated dual input-dual output converter for electric vehicle applications," *IEEE Access*, vol. 9, pp. 64 445–64 460, 2021.

[57] F. Naseri, E. Farjah, and T. Ghanbari, "An efficient regenerative braking system based on battery/supercapacitor for electric, hybrid and plug-in hybrid electric vehicles with BLDC motor," *IEEE Transaction on Vehicular Technology*, pp. 3724 – 3738, Sep. 2017.

[58] S. Jung and J. Ko, "Study on regenerative energy recovery of electric vehicle through voltage control using switched capacitor," *IEEE Transaction on Vehicular Technology*, vol. 70, no. 5, pp. 4324–4339, May 2021.

[59] W. Yeo, S. Jung, S. Kim, K. Park, and J. Ko, "A regenerative energy recovery system for electric vehicles charging a battery at a low speed," *Advances Science, Technology Engineering System Journal*, vol. 5, no. 2, pp. 64–73, Jan. 2020.

[60] S. Heydari, P. Fajri, M. Rasheduzzaman, and R. Sabzehgar, "Maximizing regenerative braking energy recovery of electric vehicles through dynamic low-speed cutoff point detection," *IEEE Transaction on Transportation Electrification*, vol. 5, no. 1, pp. 262–270, Mar. 2019.

[61] F. Zhu, Z. Yang, Z. Zhao, and F. Lin, "Two-stage synthetic optimization of supercapacitor-based energy storage systems, traction power parameters and train operation in urban rail transit," *IEEE Transaction on Vehicular Technology*, vol. 70, no. 9, pp. 8590–8605, Sep. 2021.

[62] T. Nama, A. K. Gogoi., and P. Tripathy, "Low power electric two-wheelers for hilly region." in *2018 IEEE International Conference on Power Electronics, Drives and Energy System (PEDES)*. IEEE, Dec. 2018, pp. 1–6.

[63] J. Cao and A. Emadi, "A new battery/ultracapacitor yybrid energy storage system for electric, hybrid, and plug-in hybrid electric vehicles," *IEEE Transaction on Power Electron.*, vol. 27, no. 1, pp. 122–132, Jan. 2012.

[64] M. Camara, H. Gualous, F. Gustin, and A. Berthon, "Design and new control of DC/DC converters to share energy between supercapacitors and batteries in hybrid vehicles," *IEEE Transactions on Vehicular Technology*, vol. 57, no. 5, pp. 2721–2735, Sep. 2008.

[65] A. K. Podder, O. Chakraborty, S. Islam, N. M. Kumar, and H. H. Alhelou, "Control strategies of different hybrid energy storage systems for electric vehicles applications," *IEEE Access*, vol. 9, pp. 51 865–51 895, 2021.

[66] K. G. Sarman, T. Madhu, and A. Prasad, "Prognosis of BLDC drive faults using autoregressive integrated moving average algorithm," *Springer, Wireless Personal Communications.*, pp. 1–15, Mar. 2023.

[67] J. Fan, J. Lee, I. Jung, and Y. Lee, "Online monitoring of power converter degradation using deep neural network," *Applied Sciences*, vol. 11, no. 24, p. 11796, Dec. 2021.

[68] S. R. Vippala, S. Bhat, and A. A. Reddy, "Condition monitoring of BLDC motor using short time fourier transform," in *2021 IEEE Second International Conference on Control, Measurement and Instrumentation (CMI)*. IEEE, Jan. 2021, pp. 1–6.

[69] Y. seok Jeong, S.-K. Sul, S. Schulz, and N. Patel, "Fault detection and fault-tolerant control of interior permanent-magnet motor drive system for electric vehicle," *IEEE Transactions on Industry Applications*, vol. 41, no. 1, pp. 46–51, Jan. 2005.

[70] S. Nandi, H. Toliyat, and X. Li, "Condition monitoring and fault diagnosis of electrical motors—a review," *IEEE Transactions on Energy Conversion*, vol. 20, no. 4, pp. 719–729, Dec. 2005.

[71] Y. Da, X. Shi, and M. Krishnamurthy, "Health monitoring, fault diagnosis and failure prognosis techniques for brushless permanent magnet machines," in *2011 IEEE Vehicle Power and Propulsion Conference*. IEEE, Sep. 2011.

[72] S. Choi, M. S. Haque, M. T. B. Tarek, V. Mulpuri, Y. Duan, S. Das, V. Garg, D. M. Ionel, M. A. Masrur, B. Mirafzal, and H. A. Toliyat, "Fault diagnosis techniques for permanent magnet AC machine and drives—a review of current state of the art," *IEEE Transactions on Transportation Electrification*, vol. 4, no. 2, pp. 444–463, Jun. 2018.

[73] L. Wang, Y. Cheng, and W. Yin, "A sage–husa prediction algorithm-based approach for correcting the hall sensor position in DC brushless motors," *Sensors*, vol. 23, no. 14, p. 6604, Jul. 2023.

[74] A. Goswami, M. Sreejeth, and M. Singh, "Simulation and analysis of hall sensor misalignment in BLDC motor drive," in *2022 IEEE Delhi Section Conference (DELCON)*. IEEE, Feb. 2022, pp. 1–6.

[75] K. Kolano, "Improved sensor control method for BLDC motors," *IEEE Access*, vol. 7, pp. 186 158–186 166, Dec. 2019.

[76] K. Ranjani and M. Sreejeth, "Simulation and analysis of proposed technique for BLDC motor drive running on deduced hall sensor equivalent signals," in *2022 International Virtual Conference on Power Engineering Computing and Control: Developments in Electric Vehicles and Energy Sector for Sustainable Future (PECCON)*. IEEE, May 2022, pp. 1–6.

[77] G. Scelba, G. D. Donato, M. Pulvirenti, F. G. Capponi, and G. Scarcella, "Hall-effect sensor fault detection, identification, and compensation in brushless DC drives," *IEEE Transactions on Industry Applications*, vol. 52, no. 2, pp. 1542–1554, Mar. 2016.

[78] G. Scelba, G. D. Donato, G. Scarcella, F. G. Capponi, and F. Bonaccorso, "Fault-tolerant rotor position and velocity estimation using binary hall-effect sensors for low-cost vector control drives," *IEEE Transactions on Industry Applications*, vol. 50, no. 5, pp. 3403–3413, Sep. 2014.

[79] L. Dong, Y. Huang, J. Jatskevich, and J. Liu, "Improved fault-tolerant control for brushless permanent magnet motor drives with defective hall sensors," *IEEE Transactions on Energy Conversion*, vol. 31, no. 2, pp. 789–799, Jun. 2016.

[80] Q. Zhang and M. Feng, "Fast fault diagnosis method for hall sensors in brushless DC motor drives," *IEEE Transactions on Power Electronics*, vol. 34, no. 3, pp. 2585–2596, Mar. 2019.

[81] A. Mousmi, A. Abbou, and Y. E. Houm, "Binary diagnosis of hall effect sensors in brushless DC motor drives," *IEEE Transactions on Power Electronics*, vol. 35, no. 4, pp. 3859–3868, Apr. 2020.

[82] M. Ebadpour, N. Amiri, and J. Jatskevich, "Fast fault-tolerant control for improved dynamic performance of hall-sensor-controlled brushless DC motor drives," *IEEE Transactions on Power Electronics*, vol. 36, no. 12, pp. 14 051–14 061, Dec. 2021.

[83] M. N. Mishra, "Active tectonic deformation of the shillong plateau, india: Inferences from river profiles and stream-gradients," *Journal of Asian Earth Sciences*, vol. 181, p. 103904, Sep. 2019.

[84] J. Jun, R. Guensler, and J. Ogle, "Smoothing methods to minimize impact of global positioning system random error on travel distance, speed, and acceleration profile estimates," *Transportation Research Record Journal of the Transportation Research Board*, vol. 1972, pp. 141–150, Jan. 2006.

[85] F. Naseri, E. Farjah, and T. Ghanbari, "An efficient regenerative braking system based on battery/supercapacitor for electric, hybrid and plug-in hybrid electric vehicles with BLDC motor," *IEEE Transaction on Vehicular Technology*, pp. 1–1, Sep. 2016.

[86] T. Nama, A. K. Gogoi, and P. Tripathy, "Application of a smart hall effect sensor system for 3-phase BLDC drives," in *2017 IEEE International Symposium on Robotics and Intelligent Sensors (IRIS)*. IEEE, Oct. 2017, pp. 1–6.

[87] R. W. Erickson and D. Maksimovic, *Fundamentals of Power Electronics*, 2nd ed. Springer, 2001.

[88] A. Ioinovici, *Power Electronics and Energy Conversion Systems, Volume 1: Fundamentals and Hard-Switching Converters*. WILEY, Jun. 2013, vol. I.

[89] M. K. Kazimierczuk, *Pulse-width modulated DC-DC Power*. John Wiley & Sons, Oct. 2015.

[90] H. D. Venable, "The k factor : a new mathematical tool for stability analysis and synthesis," in *Tenth Proceeding of POWERCON, San Diego, CA, USA*, Mar. 1983.

[91] A. Ghosh and S. Banerjee, "Design and implementation of type-II compensator in DC-DC switch-mode step-up power supply," in *Proceedings of the 2015 Third International Conference on Computer, Communication, Control and Information Technology (C3IT)*. IEEE, Feb. 2015.

[92] W. Bolton, "Chapter 11 - frequency response," in *Instrumentation and Control Systems*, 3rd ed., W. Bolton, Ed. Newnes, 2021, pp. 257–286.

[93] M. Gopal, *Control Systems: Principles and Design*, 4th ed. McGraw-Hill, 2008, 2008.

[94] S.-C. Tan, Y.-M. Lai, and C.-K. Tse, *Sliding Mode Control of Switching Power Converters*. CRC Press Taylor & Francis, Sep. 2018.

[95] J. Mahdavi, A. Emadi, and H. Toliyat, "Application of state space averaging method to sliding mode control of PWM DC/DC converters," in *IAS '97. Conference Record of the 1997 IEEE Industry Applications Conference Thirty-Second IAS Annual Meeting*. IEEE, Oct. 1997.

[96] R.-J. Wai and L.-C. Shih, "Design of voltage tracking control for DC–DC boost converter via total sliding-mode technique," *IEEE Transactions on Industrial Electronics*, vol. 58, no. 6, pp. 2502–2511, Jun. 2011.

[97] R. Erickson, S. Cuk, and R. Middlebrook, “Large-signal modelling and analysis of switching regulators,” in *1982 IEEE Power Electronics Specialists Conference.* IEEE, Jun. 1982.

[98] G. Verghese, C. Bruzos, and K. Mahabir, “Averaged and sampled-data models for current mode control: a re-examination,” in *20th Annual IEEE Power Electronics Specialists Conference.* IEEE.

[99] C. Tse and K. Adams, “A nonlinear large-signal feedforward-feedback control for two-state DC-DC converters,” in *PESC '91 Record 22nd Annual IEEE Power Electronics Specialists Conference.* IEEE.

[100] C. Tse and K. Adams., “Quasi-linear modeling and control of DC-DC converters,” *IEEE Transactions on Power Electronics*, vol. 7, no. 2, pp. 315–323, Apr. 1992.

[101] Y.-F. Liu and P. Sen, “A general unified large signal model for current programmed DC-to-DC converters,” *IEEE Transactions on Power Electronics*, vol. 9, no. 4, pp. 414–424, Jul. 1994.

[102] G. Escobar, R. Ortega, H. Sira-Ramirez, J.-P. Vilain, and I. Zein, “An experimental comparison of several nonlinear controllers for power converters,” *IEEE Control Systems*, vol. 19, no. 1, pp. 66–82, Feb. 1999.

[103] V. Utkin, J. Guldner, and J. Shi, *Sliding Mode Control in Electro-Mechanical Systems.* CRC Press Taylor & Francis, Dec. 2017.

[104] S. C. Tan, Y. Lai, and C. Tse, “Implementation of pulse-width-modulation based sliding mode controller for boost converters,” *IEEE Power Electronics Letters*, vol. 3, no. 4, pp. 130–135, Dec. 2005.

[105] S.-C. Tan, Y. M. Lai, C. K. Tse, L. Martinez-Salamero, and C.-K. Wu, “A fast-response sliding-mode controller for boost-type converters with a wide range of operating conditions,” *IEEE Transactions on Industrial Electronics*, vol. 54, no. 6, pp. 3276–3286, Dec. 2007.

[106] B. Allaoua, B. Mebarki, and A. Laoufi, “A robust fuzzy sliding mode controller synthesis applied on boost DC-DC converter power supply for electric vehicle propulsion system,” *International Journal of Vehicular Technology*, vol. 2013, pp. 1–9, May 2013.

[107] C. Edwards and S. Spurgeon, *Sliding Mode Control.* CRC Press, Aug. 1998.

[108] H. Sira-Ramirez and M. Ilic, “A geometric approach to the feedback control of switch mode DC-to-DC power supplies,” *IEEE Transactions on Circuits and Systems*, vol. 35, no. 10, pp. 1291–1298, 1988.

[109] K. Chau, C. Chan, and C. Liu, “Overview of permanent-magnet brushless drives for electric and hybrid electric vehicles,” *IEEE Transactions on Industrial Electronics*, vol. 55, no. 6, pp. 2246–2257, Jun. 2008.

[110] C. S. Joice, S. R. Paranjothi, and V. J. S. Kumar, “Digital control strategy for four quadrant operation of three phase BLDC motor with load variations,” *IEEE Transactions on Industrial Informatics*, vol. 9, no. 2, pp. 974–982, May 2013.

[111] T.-H. Kim, B.-K. Lee, and M. Ehsani, “Sensorless control of the BLDC motors from near zero to high speed,” in *Eighteenth Annual IEEE Applied Power Electronics Conference and Exposition, 2003. APEC '03.*, vol. 19, no. 6. IEEE, Oct. 2003, pp. 1635–1945.

[112] W.-J. Lee and S.-K. Sul, “A new starting method of BLDC motors without position sensor,” *IEEE Transactions on Industry Applications*, vol. 42, no. 6, pp. 1532–1538, Nov. 2006.

[113] R. Pindoriya, A. Mishra, B. Rajpurohit, and R. Kumar, “Analysis of position and speed control of sensorless BLDC motor using zero crossing back-EMF technique,” in *2016 IEEE 1st International Conference on Power Electronics, Intelligent Control and Energy Systems (ICPEICES)*. IEEE, Jul. 2016, pp. 1–6.

LIST OF PUBLICATIONS

Journal Publications:

Published

1. T. Nama, P. Mondal, P. Tripathy, R. Adda and A.K. Gogoi, "Design, Modeling and Hardware Implementation of Regenerative Braking for Electric Two-Wheelers for Hilly Roads", in IEEE Access, Vol. 10, pp. 130602 - 130618, Dec 2022.
   DOI:10.1109/ACCESS.2022.3229597.

Under Preparation

1. T. Nama, P. Mondal, P. Tripathy, and A.K. Gogoi, "Robust Regenerative Braking Circuit for Electric Two-Wheelers Driven in Hilly Roads".

Conference Publications:

Published

1. T. Nama, P. Tripathy, and A.K. Gogoi, "Study of Hilly Region Road for Electric Scooters", 2021 IEEE International Transportation Electrification Conference (ITEC-India), Dec 2021.
   DOI: 10.1109/ITEC-India53713.2021.9932478

2. T. Nama, P. Tripathy, and A.K. Gogoi, "Low Power Electric Two-Wheelers for hilly Region", 2018 IEEE International Conference on Power Electronics, Drives and Energy Systems (PEDES), Dec. 2018, pp. 1-6.
   DOI: 10.1109/pedes.2018.8707619.

3. T. Nama, P. Tripathy, and A.K. Gogoi, "Application of a Smart Hall Effect Sensor System for 3-phase BLDC Drives", 2020 IEEE International Conference on Power Electronics, Drives and Energy Systems (PEDES), Oct. 2017, pp. 1-6.
   DOI: 10.1109/iris.2017.8250123.